University of Alberta

High Stress Flow Behaviour and Constitutive Modeling of Dry Granular Materials

by

Abraham Enawgaw Mineneh

A thesis submitted to the Faculty of Graduate Studies and Research in partial fulfillment of the requirements for the degree of

Doctor of Philosophy

in

Geotechnical Engineering

Department of Civil and Environmental Engineering

Fall 2013

Edmonton, Alberta

ABSTRACT

Landslides include various forms of geological mass movements such as falls, slides and flows under the force of gravity. Predictions of landslide kinematics and dynamics require knowledge of flow behaviour and mathematical modeling. Research into the flow behaviour of granular materials has revealed the existence of rate-dependent collisional behaviour at high shear rates and void ratios as well as rate-independent frictional behaviour at low shear rates and void ratios. However, the results of high stress shear experiments on small particles indicate that shear rate has no effect on flow behaviour. Following this finding, most geotechnical analyses of landslides have considered mainly frictional flow behaviour. Since the collisional behaviour of granular materials depends on particle inertia, both shear rate and particle mass (or particle density and diameter) are equally important in its occurrence. In this research, the relevance of rate-dependent collisional behaviour at high stress was re-investigated using simulation experiments on large size particles. The results indicate that rate-dependent flow behaviour is more likely to occur in rapid-flow landslides involving large particles, such as debris avalanches and rock avalanches. The critical state framework which captures the frictional behaviour was extended to capture rate-dependent collisional behaviour by adding shear rate as an additional state variable, based on the pioneering work of Campbell. The extended framework was used for flow classification, study of flow progress, and constitutive modeling. The effect of particle shape on granular flow behaviour and the extended critical state framework was reviewed using simulation experiments.

Selected unified constitutive models proposed by Savage and Louge were evaluated using the extended critical state framework. In this research, new unified constitutive model is developed. The new model combines the frictional and collisional stress contributions using weighting functions called stress coefficients to determine the total stress. The stress coefficients are interdependent and are determined using empirical equations and detailed theoretical analyses. The new model is used to predict the extended critical state framework and implemented in the numerical model for inclined flows. The model performs well in capturing the extended framework and flow profiles of dense granular inclined flows on flat-frictional and rough bases.

ACKNOWLEDGEMENT

First and foremost, I would like to express my deepest gratitude to my advisor, *Prof. Dave H. Chan*, for his support and guidance throughout the research. His patience, generosity and understanding are greatly appreciated.

I would like to acknowledge for the permission granted to reproduce the experimental data from S. B. Savage and M. Sayed, Journal of Fluid Mechanics, Volume 142, 1984, pp 391-430. Copyright © 1984 Cambridge University Press.

I would like also to acknowledge for the permission granted to reproduce the simulation data from L. E. Silbert, D. Ertas¸, G. S. Grest, T. C. Halsey, D. Levine, and S. J. Plimpton, Phys. Rev. E 64, 051302 (2001). Copyright (2001) by the American Physical Society. http://link.aps.org/abstract/PRE/v64/e051302

I would like also to extend my gratitude to the National Science and Engineering Research Council (NSERC) for the financial support of this research.

My sincere thank also goes to my wife, *Mekdes Temechache Altaye*, and my little boy, *Yisehak Abraham Mineneh*, for their understanding and patience. Special thanks also go to my family. To my father *Enawgaw Mineneh* and my mother *Semegnish Mengiste*, many thanks for all care and support you have provided me. Mom! May God Rest You in Peace. To my sisters *Seble Enawgaw* and *Tigist Enawgaw*, my brothers *Solomon Enawgaw* and *Nathnael Enawgaw*, your encouragement and love have helped me to overcome the difficult moments.

Finally many thanks to all fellow researchers who provided me your valuable advices throughout my research work. I would like to also acknowledge *Prof. Kolumban Hutter* for his valuable editorial comments.

Glory to God Almighty!

TABLE OF CONTENTS

LIST OF TABLES

LIST OF FIGURES

ABBREVIATIONS

CIBL	Collisional-Intermediate Boundary Line
CS	Critical State
CSL	Critical State Line
CSSM	Critical State Soil Mechanics
DEM	Distinct Element Model
KTGF	Kinetic Theory of Granular Flow
SFD	Steady Fully Developed inclined flow

SYMBOLS

A_h	Horizontal area of servo-wall
b	Specific body force (body force per mass)
C	Damping constant
CN	Coordination number
D	Damping force
d	Particle diameter
$\bar{d}$	Mass average diameter of particles
$d_{\max}$	Diameter of the largest particle in the simulation
E	Modulus of elasticity
$E_{m=1,3N} = 0$	System of non-linear equations
$E_m(\text{var})$	Residuals of the system of non-linear equations
e	Void ratio
e_{cs}	Critical state void ratio
e_c	Collisional state void ratio
e^*	Random loose packing void ratio
e^m	Minimum close packing void ratio
F_1	Fraction of volume occupied by colliding particles in intermediate state
F_2	Fraction of volume occupied by particle clusters in intermediate state
f_S	Servo-wall stress coefficient in the ring shear model
f_R	Relaxation factor for numerical stability in plane shear
F_i^n	Total contact normal force
ΔF_i^s	Incremental contact shear force
F_i^s	Total contact shear force
F_{SW}	Vertical normal force at the servo-wall in plane shear

	flow
F_{SC}	Vertical normal force at the servo-controlled clump plate in the ring shear model
G	Shear modulus
g	Acceleration of gravity
H	Height of sample or flow
H_{o}	Sample height after consolidation
H_{s}	Sample height at steady state of plane/ring shear flow
H_{d}	Effective sample height of plane/ring shear flow, H_{s} - d
I	Dimensionless inertial number
J	Jacobian matrix
K	Secant stiffness at particles contact
k	Tangent stiffness at particles contact
K^n	Secant normal stiffness at particles contact
k^s	Tangent shear stiffness at particles contact
m	Mass of ball
m_{tb}^L	Portion of the mass of particle b occupying layer L at time step t
M	Slope of CSL in $q-p$ plane
$m_i, i=1,5$	Constants in the empirical equation of kinetic/collisional shear stress coefficient
N	Number of nodes in discretizing inclined flow in the z direction into $N-1$ equal segments
N_t	Total number of time steps
n	A unit vector normal to a contact
p	Mean effective stress
q	Deviatoric stress
q_s	Flux of fluctuation kinetic energy
R_o	Outside diameter of the ring shear cell
R_i	Inside diameter of the ring shear cell

$R_1,\ R_2$	Tolerance values for two convergence criteria in solving system of equations
Sa	Savage number
SF	Sliding fraction
Δt	Time step
t	Time
t_h	Thickness of the ring shear model
T_z	Torque in the ring shear model
T	Translational granular temperature
$\hat{T}$	Dimensionless translational granular temperature
T_c	Collisional state translational granular temperature
U^n	Total contact normal displacement
ΔU_i^s	Incremental contact shear displacement
u	Velocity
$\hat{u}$	Dimensionless velocity
u_z	Vertical velocity
u_r	Relative velocity of particles at a contact
u_{r_z}	Relative velocity between servo-wall and top-boundary particles in plane shear simulation
u_{sl}	Slip velocity at the bottom surface in inclined flow
u'	Fluctuation velocity
$\langle \overline{u}_{xL} \rangle$	Mass-weighted average velocity of layer L in the flow direction
$\sqrt{\langle u_{iL}'^2 \rangle}$	Mass-weighted average fluctuation velocities of layer L in x-, y-, and z- directions
$\sqrt{\langle u_i'^2 \rangle}$	Mass-weighted average fluctuation velocities of the uniform plane shear flow in x-, y-, and z- directions
u_{itb}^L	Instantaneous velocity of particle b occupying layer L at time step t in x-, y-, & z- directions

$\text{var}_{n=1,3N}$	The values of the variables at the nodes ($v_{s_{i=1,N}}$, $\hat{T}_{i=1,N}$, and $\hat{u}_{i=1,N}$)
V_{tb}^{L}	Portion of volume of particle *b* occupying layer *L* at time step t
$\left\langle v_s^L \right\rangle$	Average solid volume fraction of layer L
v_S	Solid volume fraction
v_S^m	Maximum close packing solid volume fraction
v_s^*	Random loose packing solid volume fraction
v_s^c	Collisional state solid volume fraction
v_s^{cs}	Critical state solid volume fraction
ν	Poisson's ratio
x	Axis in the direction of flow
y	Axis normal to the plane of flow
z	Vertical axis (normal to flow)
Z	Dimensionless height, z/H
$\Delta Z = 1/(N-1)$	Dimensionless incremental height in discretizing inclined flow in the z direction into $N-1$ equal segments
ρ	Particle density
$\dot{\gamma}$	Shear rate
$\dot{\gamma}_c$	Collisional state shear rate
$\dot{\gamma}_{cs}$	Critical state shear rate
$\dot{\gamma}_{cs}^*$	Shear rate at quasi-static – intermediate boundary
$\dot{\gamma}d$	Characteristic mean shear velocity
I_{cs}^*	Dimensionless inertial number at quasi-static – intermediate boundary
σ	Total Cauchy stress tensor (frictional + collisional stress components)
σ_x	Total normal stress in flow direction

σ_z	Total vertical normal stress
τ_{xz}	Total shear stress
σ_x^f	Frictional normal stress in flow direction
$\sigma_x^{k/c}$	Kinetic/collisional normal stress in flow direction
σ_z^f	Frictional vertical normal stress
$\sigma_z^{k/c}$	Kinetic/collisional vertical normal stress
τ_{xz}^f	Frictional shear stress
$\tau_{xz}^{k/c}$	Kinetic/collisional shear stress
σ^k	Kinetic stress component
σ_z^a	Applied (or prescribed) vertical normal stress in plane/ring shear simulations
σ_z^m	Measured vertical normal stress at the servo-wall in plane/ring shear simulations
$\hat{\sigma}_z^f$	Dimensionless frictional vertical normal stress
${}_\beta\sigma_z^f$	Modified frictional vertical normal stress component
${}_\beta\sigma_x^f$	Modified frictional normal stress component in flow direction
${}_\beta\sigma_x^{k/c}$	Modified kinetic/collisional normal stress component in flow direction
${}_\beta\sigma_z^{k/c}$	Modified kinetic/collisional vertical normal stress component
${}_\beta\tau_{xz}^f$	Modified frictional shear stress component
${}_\beta\tau_{xz}^{k/c}$	Modified kinetic/collisional shear stress component
μ	Bulk friction coefficient
μ_{cs}	Critical state friction coefficient
μ_c	Collisional state friction coefficient
μ_s	Static inter-particle friction coefficient (at particle

	contacts)
ϕ_{cs}	Critical state friction angle
δ	Angle of friction at the bottom surface in inclined flow
ε	Restitution coefficient
ε_w	Restitution coefficient at the boundary wall
θ	Angle of inclined flow
θ_r	Angle of repose
$\theta_{\max}$	The largest angle for which stable inclined flow is obtained, for $\theta > \theta_{\max}$, inclined granular flow is unsteady
ω_z	Angular velocity in the ring shear simulation
Γ	The void ratio intercept at $\sigma_z^f = 1Pa$ in $e_{cs} - \log \sigma_z^f$ plane
λ	Slope of critical state line in $e_{cs} - \log \sigma_z^f$ plane
Ω	The void ratio intercept at $\sigma_Z = 1Pa$ in CIBL
κ	Slope of the CIBL
Υ	Rate of dissipation of fluctuation kinetic energy per unit volume due to inelastic collisions
ζ	Shear viscosity
β_1	Kinetic/collisional shear stress coefficient
β_2	Frictional stress coefficient
β_3	Kinetic/collisional normal stress coefficient
φ	Specularity coefficient
α	Modified factor to Newton-Raphson method for solving system of non-linear equations

CHAPTER ONE

INTRODUCTION

1.1 Statement of Problems

Flow-like landslides include rapid and massive debris flows, snow avalanches, debris avalanches, and rock avalanches (Hungr et al., 2001). These events are catastrophic to the environment. Many parts of Canada face some form of avalanche or debris flow hazards. Since 1840, debris flows and avalanches in Canada have resulted in more than 600 deaths and caused billions of dollars in damage. They are registered as one of the most significant natural hazards in the country. They are also common problems in the U.S., China, and other parts of the world.

In mitigating these natural hazards, precise prediction of landslide kinematics and dynamics plays a vital role. This requires knowledge of flow physics (as applied to landslides) and expressing it mathematically using a constitutive equation. Although fundamental work has been done with regard to this problem, the understanding of flow processes is still incomplete. It can be said that the extreme regimes of flows (frictional, collisional, viscous, and turbulent) are fairly well understood with respect to flow mechanism, flow behavior, and theories to explain their behavior using mathematical modeling have been developed. However, the biggest challenge is the understanding of intermediate flows, where more than one flow regime (or flow mechanism) exists simultaneously making the flow process more complicated. Understanding flow behaviour and constitutive modeling of intermediate flow characteristics is a current research topic of great interest in the study of granular flows (Da Cruz et al., 2005; Jop et al., 2006; Lu et al., 2007; Lee & Huang, 2010; Berzi et al., 2011). In practice, the mechanism of flow and energy dissipation in granular flow varies with both space

and time, implying that understanding their transitional (intermediate) regime from one mechanism to the other is the key for precise flow prediction.

One of the problems in studying granular flow is to gain an understanding of intermediate flow process in relation to the mechanism of flow and energy dissipation, the characteristics of flow, and to develop a theory to explain the flow process. Similar to the theory of Critical State Soil Mechanics (CSSM) for frictional flow and the Kinetic Theory of Granular Flow (KTGF) for collisional flow, an equivalent theory to explain the behaviour of intermediate flow is required. This has been the subject of considerable interest in granular flow research. For flow-like landslides in particular, most geotechnical models assume a rate-independent, fully frictional behaviour. Rate-dependent flow behaviour of flow-like landslides through the collisional interaction of particles is subjected to question seeking experimental proofs. On the other hand, the better performance of the velocity-dependent Voellmy model over the Coulomb frictional model with regards to dry debris and rock avalanches requires an explanation for the possible source of the rate-dependent shear resistance component.

Understanding the characteristics of intermediate flow is important in developing a unified constitutive model to predict the full ranges of granular flow behavior. There have been encouraging developments in unified constitutive modeling. A common limitation observed in many unified constitutive models (Johnson & Jackson, 1987; Savage, 1998; Louge, 2003; Berzi et al., 2011) is that the total stress is equal to the sum of the frictional and collisional stress components based on the ad hoc assumption of Savage (1982). Therefore, the other problem in modeling granular flows is the lack of a unified constitutive model that is developed based on assumptions tested in physical experiments and numerical simulations.

1.2 Background of the Study

From small-scale industrial processes to large-scale geological mass flows, granular flow has become a current subject of interest. Industrial processes involve small size particles flowing under low stress and density, such as the flow of food grains and pharmaceutical drugs; while geological mass flows involve a mixture of small soil particles and large rock fragments under high stress and density. All forms of geological mass movements are termed as landslides, which are classified according to various systems (Varnes, 1978; Cruden & Varnes, 1996; Hungr et al., 2001). This research is limited to dry granular flows and focused to obtain a better understanding of the flow behaviour and develop a model. Two types of dry granular flow behaviour have been identified in the literature, namely rate-independent frictional and rate-dependent collisional flow behaviours.

The rate-independent quasi-static deformation of granular particles has been successfully studied for several years (Reynolds, 1885; Rowe, 1962; Rowe, 1963; Horne, 1965a; Horne, 1965b). Quasi-static deformation is characterized by frictional rubbing or sliding of particles against each other with a relatively long duration of contact. Quasi-static flow of granular particles has been successfully modeled by the Theories of Soil Plasticity and Critical State Soil Mechanics (Schofield & Wroth, 1968; Wood, 1990).

When granular materials flow at a sufficiently high rate of deformation, the inertia of the particles becomes dominant and causes collisions between particles. The collisional flow behaviour was first observed by Bagnold (1954) and further studied by Bridgewater (1972), Savage and Sayed (1984), Hanes and Inman (1985a, b), Patton et al. (1987), Drake (1988), and Hojin (1989). The collisional behaviour is characterized by the instantaneous contact of particles during collisions, which allows an exchange of momentum between particles to develop resistances against the applied stresses. Empirical models were initially proposed

for collisional flows of granular material (Bagnold, 1954; McTigue, 1978). Later, the kinetic theory of gases was adopted as the Kinetic Theory of Granular Flow (KTGF) to explain the collisional mechanism and to drive constitutive modeling (Ogawa, 1978; Ackerman & Shen, 1981; Jenkins & Savage, 1983; Lun et al., 1984; Jenkins & Richman, 1985).

The study of rate-dependent collisional behaviour was limited to the low stress range. Shear experiments conducted to investigate the relevance of collisional behaviour at high stresses revealed no shear rate effects (Hungr & Morgenstern, 1984; Fukuoka & Sassa, 1991; Cagnoli & Manga, 2004). Thus, the collisional stresses and energy dissipations have been ignored in commonly used flow-like landslide models such as MADFLOW (Chen & Lee, 2000), TITAN2D (Pitman et al., 2003), DAN3D (McDougall, 2006), and RASH3D (Pirulli, 2005). However, the Coulomb frictional model does not perform better than the velocity-dependent Voellmy model in the back analyses of dry debris and rock avalanches (Hungr & Evans, 1996; Evans et al., 2001; Hungr et al., 2007; Pirulli, 2009). This becomes a challenge on the argument of whether the rate-dependent collisional behavior is relevant in granular flows. In addition, the high stress shear experiments which showed no shear rate effect on shear resistance were conducted on small diameter particles. The behaviour at high stress shear experiments on large diameter particles has not yet been investigated.

In the transition of flow between frictional and collisional flow regimes, granular particles will undergo frictional and collisional mechanisms simultaneously. However, despite the studies of the transitional flow behavior (Sayed, 1981; Drake, 1990; Campbell, 2002; Campbell, 2005), there is presently no clear understanding on how the two flow mechanisms can act together. The behaviour of intermediate (or transitional) granular flow has been explored using physical experiments and numerical simulations of granular particles (Savage & Sayed, 1984; Da Cruz et al., 2005; Campbell, 2002; Campbell, 2005; Lu et al. 2007). Modeling of granular flow that accounts for both frictional and collisional stress

contributions becomes the latest research area in the study of granular flows. Pioneer work was done by Savage (1982), who followed an ad hoc assumption of simple stress addition. Several unified models have since been proposed by a number of researchers (Nott, 1991; Savage, 1998; Mills et al., 1999; Ancey & Evesque, 2000; Louge & Keast, 2001; Louge, 2003; Berzi et al., 2011). However, most of these models adopt the same assumption made by Savage (1982).

1.3 Objectives and Methodology

The overall objective of this research is to investigate the flow behaviour of large size dry granular particles under high stresses, and to develop a unified constitutive model which will capture the full ranges of flow behavior from frictional flow to collisional flow. The specific objectives of the research are:

1. Based on low stress experiments, it has been well documented that granular flow exhibits rate-dependent collisional behaviour at high void ratio and shear rate. However, some high stress shear experiments revealed that there was no shear rate effect on the shearing resistance of the material. These experiments were conducted on small diameter particles. Since the collisional mechanism depends on particle inertia, both shear rate and particle mass (density and diameter) are equally important. Therefore, *the first objective* of the present research is to investigate the relevance of rate-dependent collisional behaviour for large size particles under high stresses. Due to limitations of resources to conduct physical experiments, the investigation will be carried out numerically using the discrete element method (DEM). Before the DEM model will be used to study flow behavior at high stresses, it will be first calibrated using physical experiments at low stresses taken from the literature.

2. *The second objective* of the research is to develop a unified framework which is able to capture rate-independent and rate-dependent deformation behaviours of dry granular materials. Campbell (2002) obtained a series of state lines as a

function of dimensionless shear rate on the void ratio versus dimensionless stress plane. Based on these findings, the critical state framework will be extended using characteristic mean shear velocity ($\dot{\gamma}d$) as an additional state variable to capture the rate-dependent intermediate and collisional flows. Numerical experiments using DEM will be used to provide data for the extended framework. The critical state framework has been used to capture strain-softening and strain-hardening behaviours and in assessing flow liquefaction of granular materials. Similarly, the use of the extended critical state framework to capture the frictional, collisional, and intermediate granular flows will be investigated. Similar to undrained and drained behaviors in quasi-static soil deformations, stress-controlled and volume-controlled granular flows produce different flow behaviours. The extended framework will also be used to describe the progression of flow under these two flow conditions.

3. The behaviour of rapid granular flow has been investigated using experiments mostly on spherical particles. Some advances have also been made in the investigation of non-spherical granular behaviour. DEM simulations of this latter type of material depend on how the individual non-spherical particles are precisely modeled. *The third objective* is to investigate the behavior of non-spherical particles using DEM simulations. In this research, the ring shear test will be simulated using the DEM model for non-spherical particles.

4. Several unified models have been proposed by various researchers since the pioneering work of Savage (1982). However, most of the models rely on Savage's (1982) ad hoc assumption, where the frictional and collisional stress contributions were directly added to obtain the unified stress. *The fourth objective* of the research is to review the existing unified constitutive models and evaluate selected models using an extended critical state framework. Additionally, the main limitations of the existing models will be discussed.

5. *The final objective* of this research is to develop a new concept in constitutive modeling which will overcome the ad hoc assumption of Savage (1982) and other limitations of the existing models. The new concept is based on the microscopic description of granular flow mechanisms provided by Sayed (1981) and by considering the analogies in the transition of ice to water. The frictional and collisional stress components will be combined by weighting functions, called stress coefficients, to obtain the unified stresses. The stress coefficients will be determined using empirical equations and detailed theoretical analyses.

1.4 Organization of the Thesis

Literature reviews on previous studies of dry granular flow are presented in Chapter 2. The reviews focus on classification of flow, flow behaviours, and constitutive modeling, with emphasis on geological mass flows. Different classification systems of landslides are summarized and the behaviour of quasi-static, collisional, and intermediate flow regimes of dry granular materials are reviewed in detail. Recent advances in the understanding of steady fully developed (SFD) inclined flows of dense granular particles are also included. The Critical State Soil Mechanics (CSSM) and the Kinetic Theory of Granular Flow (KTGF) for constitutive modeling of quasi-static and collisional flows respectively are reviewed. Finally in Chapter 2, the advances and challenges in constitutive modeling of granular flows are discussed.

Chapter 3 summarizes the DEM simulation experiments conducted using the commercial software PFC3D v4.0. Simulations were conducted for steady plane shear flows, steady ring shear flows, and SFD inclined flows. Model descriptions, procedures of simulation experiments, method of measurement of flow characteristics, and model calibrations are discussed in detail.

The relevance of rate-dependent collisional behaviour in geological mass flows is studied in Chapter 4. The study was conducted by performing plane shear simulations on large size granular particles at high stress. The range of flow depths, flow velocities, and flow densities required for rate-dependent flows were assessed and compared with the ranges of values in real life problems.

The extended critical state frame work is presented in Chapter 5. Based on the findings of Campbell (2002), the series of state lines in void ratio versus normal stress plane are determined as a function of characteristic shear velocity ($\dot{\gamma}d$). The state lines are referred to here as supercritical state lines. The rest of the extended framework components are also determined and the uses of this framework for flow classification, study of flow behaviour, and modeling are investigated. Finally, the behaviour of non-spherical particle flows is reviewed using ring shear simulations, and the effect of particle shape in the extended critical state framework is discussed.

Chapter 6 is devoted to the development of a new constitutive model for dry granular flow. Constitutive models from the literature are reviewed, and selected models are evaluated using the extended critical state framework presented in Chapter 5. A new constitutive model is developed based on the extended critical state framework. The model is validated against inclined plane flow simulation experiments.

CHAPTER TWO

LITERATURE REVIEW

2.1 Types of Granular Flow

2.1.1 Introduction

Granular material encompasses a wide variety of substances, ranging from agricultural and industrial materials such as grains, fertilizers and pills to granular soils and rock fragments. Granular material could be described in general as a conglomeration of discrete macroscopic solid particles that interact with each other through rubbing friction and collision. Although many findings have been made towards the understanding of the physics of granular material, it is still an active research topic due to the complex behaviour of the material. A granular material can behave like a solid by interacting through friction when placed at low void ratios. However, it can also behave like a liquid or like gas particles when deforming by rolling and sliding or colliding with each other, respectively.

An understanding of the flow physics of granular materials can have numerous applications in industrial processes and natural gravity driven flows. Industrial processes usually involve flows of small size particles under low stresses, while geological mass flows occur at higher stresses and involve a wide range of particle sizes. All forms of geological mass movements such as falls, slides, and flows under the force of gravity are collectively termed landslides (Cruden & Varnes, 1996; EPOCH, 1993). The scope of this research is limited to the characteristics and modeling of dry flow type landslides.

2.1.2 Types of Landslides

A prominent classification system of landslides was proposed by Varnes (1978) and later modified by Cruden and Varnes (1996). A similar classification system was also developed by EPOCH (1993) to be used in the European community. The classification systems are based on the criteria of material types and movement mechanisms.

Cruden and Varnes (1996) classified the materials as rock, debris, and earth. Debris material is described as soil with more than 20% of the particles greater than 2 mm, and earth material is described as soil with less than 20% of the particles greater than 2 mm. In addition, they classified the movement mechanisms as fall, topple, slide, spread, and flow. The landslides were then classified based on the types of materials and movements, such as rock fall, debris flow, earth spread, and so on.

Similar classifications of the material and movement types were also followed by EPOCH (1993). They classified the materials as rock, debris, and soil; while, they classified the movement mechanisms as fall, topple, slide (rotational, translational, planar), lateral spreading, flow, and complex. They included rock avalanche in their landslide classification system under the complex type of movement mechanism.

USGS (2004) provided detailed descriptions of the movement mechanisms with schematic illustrations.

2.1.3 Flow Type Landslides

From the different types of landslides illustrated in the previous section, Hungr et al. (2001) presented a systematic classification for flow type landslides. They classified the landslide materials as sorted and unsorted materials. Sorted materials include gravel, sand, silt, and clay. Unsorted materials include debris, earth, mud, peat, and rock. Hungr et al. (2001) further characterized the landslide materials as non-cohesive (gravel, sand, silt, and debris), cohesive (clay, earth, and mud), organic (peat), and fragmented (rock).

Based on the above classification of landslide materials, Hunger et al. (2001) provided detail classifications of the variety of flow type landslides including earth flow, mud flow, debris flow, debris avalanche, and rock avalanche. The classification also included the detail descriptions about the degree of saturation (as dry, moist, or saturated) and the range of flow rate (as slow, rapid, very rapid, or extremely rapid) for each flow type landslide.

A flow velocity scale for landslides was proposed by Cruden and Varnes (1996). According to their scale, slow landslide would flow less than $5x10^{-6}$ m/s, rapid landslide would flow less than 0.05 m/s, and extremely rapid landslide would flow greater than 5 m/s. On the other hand, Hungr et al. (2001) compiled maximum recorded flow velocities for various types of flow type landslides. The results show that earth flow could flow up to 0.1 m/s, debris flow could flow up to 20 m/s, debris avalanche could flow up to 40 m/s, and rock avalanche could flow up to 100 m/s. The classification of sediment water flows by Pierson and Costa (1987), based on sediment concentration and flow velocity as criteria, also suggested similar maximum flow velocities for the above flow type landslides.

Debris flows and debris/rock avalanches are among the catastrophic flow type landslides. They move rapidly and usually feature long run-out distances. Based on high stress shear experiments (Hungr & Morgenstern, 1984; Fukuoka & Sassa,

1991), they have been considered to exhibit only rate-independent frictional behaviour. However, the Coulomb frictional model has not performed better than the velocity-dependent Voellmy model in the back analyses of dry debris and rock avalanches (Hungr & Evans, 1996; Evans et al., 2001; Hungr et al., 2007; Pirulli, 2009). This research focuses on the investigation of rate-dependent flow behaviour in dry debris flows and debris/rock avalanches, and their constitutive modeling.

2.2 Behaviour of Dry Granular Flow

2.2.1 Introduction

Precise predictions of the kinematics and dynamics of flow type landslides play a crucial role in mitigating the resulting hazards. This requires a good knowledge of the physics of flow and the ability to express it mathematically using a constitutive equation. Although fundamental work has been done on this problem, understanding of the flow process is still incomplete. It can be said that the extreme regimes of granular flows (i.e., quasi-static regime, fully-collisional regime, viscous regime, and turbulent regime) are fairly well understood with respect to the mechanism involved, their flow behavior, theories to explain their flow, and mathematical modeling. However, intermediate (or transitional) granular flow, in which two or more types of flow mechanisms coexist, is still an active research topic (Jop et al., 2006). In reality, the mechanism of granular flow varies with both space and time; in other words, the flow mechanism is different at the initiation, deposition, and flowing stages. The mechanism of granular flow is also different at the base, in the middle, and at the surface of the flow. A granular flow is a complex process whereby the mechanism of stress generation and energy dissipation are variable with respect to space and time, depending on the stages of the flow and boundary conditions.

2.2.2 Quasi-static Flow Behaviour

The mechanism of quasi-static deformation of granular particles has been studied extensively for many years (Reynolds, 1885; Rowe, 1962; Rowe, 1963; Horne, 1965a; Horne, 1965b; Drescher and De Josselin De Jong, 1972; Howell et. al., 1999).

During quasi-static shear, particles are driven to each other to form chains of contacts among them resulting in contact forces. With further shearing, different groups of particles are formed which slide over each other and destroy the chain of contacts. This is accompanied by the rotation of individual particles. As the deformation continues, particles reorient themselves to form new contact chains, and the above mechanism of deformation continues by the formation of new groups of particles sliding over each other. This mechanism of deformation and contact force distributions have been visualized using photoelastic techniques (Drescher and De Josselin De Jong, 1972; Howell et. al., 1999).

Quasi-static flow occurs as a result of relative motion between groups of particles. The flow is characterized by a steady-state condition, where stresses and void ratio are constant with time. As per Coulomb's law, shear stress is proportional to the normal stress at sliding surfaces and the friction mechanism is independent of sliding velocity. The normal stress is transferred through the chain of contacts and the shear resistance is entirely derived from the frictional mechanism between particles when they slide over each other. The mechanical energy is dissipated by friction converting into heat. Quasi-static granular flow has been successfully modeled by the theory of soil plasticity and critical state soil mechanics (Schofield & Wroth, 1968; Wood, 1990).

2.2.3 Collisional Flow Behaviour

When granular materials flow at a sufficiently high rate, the inertia of particles becomes dominant, which causes particles to collide during contact. The collisional flow mechanism was first observed by Bagnold (1954) and further investigated in laboratory experiments by Bridgewater (1972), Savage and Sayed (1984), Hanes and Inman (1985a & b), Drake (1988), Hojin (1989), and using discrete element simulations such as Luding et al. (1998), Herrmann et al. (2001), and Campbell (2002, 2005).

In this type of flow, particles make contact only for a very short period of time during collision and may spend time in the air between collisions. A particle may collide with only one other particle (binary collision) or with multiple particles at any instant in time. The resistances to normal and shear stresses are predominantly developed by momentum exchanges through particle collisions. The amount of momentum exchange depends on the relative velocities of the particles at collision, which in turn is governed by the rate of shearing of the material. Hence, unlike the frictional flow mechanism, collisional flow mechanism is rate-dependent. In collisional flow, stresses are proportional to the square of the shear rate and the square of the particle diameter. Since granular particles are inelastic, the kinetic energy of the system gradually dissipates upon collision. Collisional granular flow has been successfully modeled by the kinetic theory of granular flow (e.g., Lun et al., 1984).

The experimental investigations of rate-dependent collisional flow behaviour, however, were limited to small size particles and low stresses. In order to investigate the relevance of rate-dependent behaviour in actual flow landslides, some experiments were conducted at high stress ranges (Hungr & Morgenstern, 1984; Kaibori, 1986; Vibert et al., 1989; Fukuoka & Sassa, 1991; Cagnoli & Manga, 2004).

Hungr and Morgenstern (1984) conducted flume and ring-shear experiments to investigate the flow behaviour of granular materials at high velocities. The flume experiments were conducted for Ottawa sand and polystyrene beads with uniform diameters of 0.7 mm and 1.5 mm, respectively. Flow velocity of up to 6 m/s was achieved in the flume experiments, with a typical flow depth of about 10 cm. Due to low stresses in the flume experiments, supplementary experiments at higher stress range were also conducted using a ring shear apparatus. The ring shear tests were carried out on two types of coarse sand (wet and dry), sand-rock flour mixtures, and polystyrene beads. The diameter of sand particles ranged from 1.5 mm to 3 mm, while the rock flour was crushed pure quartz with a mean grain diameter of 0.044 mm. The tests were conducted for the range of circumferential velocities of 0.1 cm/s to 98 cm/s and normal stresses of up to 200 kPa.

Fukuoka and Sassa (1991) also reviewed previous ring shear tests (Kaibori, 1986; Vibert et al., 1989) and conducted additional high-speed high stress ring shear tests to investigate the effect of shear rate on the shear behaviour of granular material. The type of materials tested included glass beads, Toyoura Standard Sand, and river sand. The particle size was generally less than 2 mm and the tests were conducted for normal stresses of up to 300 kPa and shear velocity of up to 100 cm/s. The glass beads did not show any rate-dependence behavior, and the slight variations of friction angle in the various types of sand were attributed to changes in grain-size distribution due to grain-crushing during the shear test.

Cagnoli and Manga (2004) conducted shear tests as well, but on angular pumice fragments using Cagnoli's shear cell. The material was obtained from the pyroclastic deposits of Medicine Lake Volcano in northern California, U.S. The average density of the material was 550 ± 39 kg/m^3 and particle sizes ranged from 8 mm to 9.5 mm, with an average value of 8.75 mm. At high angular speed experiments, a thick rigid layer of particles was formed above a thin basal layer of colliding particles.

Nevertheless, all of the above high stress range experimental results indicated no rate-dependent flow behaviour of granular particles. This led researchers to believe that the rate-dependent collisional flow mechanism is limited to low dense, low stress granular flows such as in industrial processes, and should therefore not be considered in the geotechnical analysis of flow type landslides (Hungr & Morgenstern, 1984; Sassa, 2000; Cagnoli & Manga, 2004; Wang, 2008). Following such an argument, the collisional stress generation and energy dissipation seemed to be ignored in most commonly used landslide models, such as MADFLOW (Chen & Lee, 2000), TITAN2D (Pitman et al., 2003), DAN3D (McDougall, 2006), and RASH3D (Pirulli, 2005). The frictional and Voellmy's rheologies have been mostly used to back-analyze dry flows and avalanches.

The rheological study of collisional flows (Bagnold, 1954; Lun et al., 1984) indicated that collisional stress is directly proportional to particle density, the square of the shear strain rate, and the square of the particle diameter. Even though the above high stress experimental investigations were conducted at high shear rates, the particles used in the experiments had small sizes (mostly less than 2 mm) or low density (Cagnoli & Manga, 2004). These experiments seemed to examine only the effect of shear rate without considering the effects of particle size and density. Hence, the lack of shear rate effects in the above experiments may be related to the low values of the above material properties, which have equivalent effects with shear rate in the occurrence of rate-dependent collisional flows. Therefore this indicates that there is a need to conduct experiments on large size particles. However, such experiments require very large shear apparatus that is capable to contain a sufficient sample of large size particles. Due to the limitation of resources to conduct physical experiments, plane shear numerical experiments are conducted in this research. The simulation results and discussions are presented in Chapter 4.

Another aspect related to the collisional mechanism in geological mass flows is that the Voellmy model is found to make more accurate prediction of flow

characteristics than the Coulomb frictional model in the back-analysis of a number of dry debris and rock avalanche cases (Pirulli, 2009; Hungr et al., 2007; Hungr & Evans, 1996; Evans et al., 2001). The Voellmy model is based on the simple assumption that the shear stress consists of a dynamic drag component proportional to the square of flow velocity and a frictional component proportional to the normal stress (Perla et al., 1980). The dynamic drag component accounts for all possible sources of velocity dependent resistances and would be responsible for the loss of any remaining kinetic energy not dissipated by friction. In wet geological mass flows, the dynamic shear component of the Voellmy model may be assumed to represent the turbulence of the pore water. In dry geological mass flows, however, the use of this model requires an explanation for the possible source of the rate-dependent shear resistance component.

Although it is still unclear regarding the relevance of the collisional mechanism based on the above discussion, some researchers have already considered the rate-dependent collisional mechanism acting simultaneously with the rate-independent frictional mechanism in the analysis of geological mass flows (Chen, 1988; Bartelt et al., 2006; Takahashi, 2007). Geological mass flow is considered to be a dense granular flow which derives its shear resistance from both frictional sliding and particle collisions. The study and modeling of dense granular flow is a state-of-the-art research area. Many researchers have proposed various constitutive equations that account for both types of resistances (Savage, 1998; Louge, 2003; Berzi et al., 2011).

2.2.4 Intermediate (or Transitional[1]) Flow Behaviour

Quasi-static granular flow exists at a state of low shear rate and void ratio, while collisional flow exists at a state of high shear rate and void ratio. On the other hand, in the progression (or transition) of granular flow from one state to another state, granular particles will undergo both frictional and collisional mechanisms

[1] In this thesis, the term transitional flow is synonyms with intermediate flow.

simultaneously. However, there is no clear understanding on how these two flow mechanisms can act simultaneously in the intermediate flow regime. Even though granular flow has been studied extensively in physical experiments (Savage & Sayed, 1984; Hanes & Inman, 1985a; Hanes & Inman, 1985b; Patton et al., 1987; Ahn et al., 1991; Cassar et al., 2005; Martino & Davies, 2003; Lu et al., 2007; Vidyapati et al., 2012) and in numerical simulations (Da Cruz et al., 2005; Campbell, 2002; Campbell, 2005; Rognon et al., 2007; Hatano, 2007; Hatano, 2010; Vidyapati et al., 2012), the understanding of the detailed flow process in the intermediate regime is still an active research topic. Experimental and simulation studies have been conducted for mono- and poly-disperse spherical particles and angular particles to investigate flow behaviour under different conditions.

2.2.4.1 Mono-disperse Spherical Particles

Savage and Sayed's (1984) annular shear experiments on nearly mono-disperse spherical glass and polystyrene beads could be taken as pioneering work in the investigation of the progression of flow of spherical particles. Their test results on 1 mm polystyrene beads indicated that normal and shear stresses are related to the square of the shear rate at constant high void ratio conditions, supporting Bagnold's (1954) arguments for his grain inertia regime. At constant low void ratio conditions, however, the stresses become weakly dependent (to a lesser power than 2) on the shear rate as the flow progresses by decreasing the shear rate from higher values to lower values. These observations were attributed to the possible increase of enduring contacts between particles at low void ratio and at low shear rate, contributing a rate-independent frictional component to the total stress. Hence, the total stress, which is the sum of collisional contribution and frictional contribution, will depend on a power of the shear rate less than 2. They also observed that the shear to normal stress ratio (friction angle) is not strongly dependent upon the shear rate at a constant void ratio condition but increases slightly as the void ratio increases. Nevertheless, it should be noted that most of the experimental data were concerning a collisional regime and thus the results

implied that the dynamic friction angle (the friction angle in the collisional regime) is nearly rate-independent and greater than the quasi-static friction angle.

Their test results for 1.8 mm glass beads also showed that the stresses are weakly dependent (to a power less than 2) on the shear rate at constant low void ratio condition, while at constant high void ratio condition, the stresses depend to the square of shear rate. The density of the glass beads was about three times as large as that of the polystyrene beads. They also attributed the above observation to the increased importance of the rate-independent frictional stress contribution at low void ratios.

Hanes and Inman (1985a) conducted similar annular shear experiments as Savage and Sayed (1984) on glass beads and well-rounded quartz sand. They presented the test results in the plots of solid volume fraction versus dimensionless vertical and shear stresses, $\sigma_z/(\rho\dot{\gamma}^2 d^2)$ and $\tau_{xz}/(\rho\dot{\gamma}^2 d^2)$, where σ_z is vertical normal stress, τ_{xz} is shear stress, ρ is particle density, $\dot{\gamma}$ is shear rate and d is particle diameter. They observed that the dimensionless stresses for solid volume fractions below about 0.55 are predicted by the kinetic theory (Jenkins & Savage, 1983), indicating that the test data represent the collisional regime. With an increase of a solid volume fraction, however, the measured dimensionless stresses increase rapidly, deviating from the kinetic theory prediction. Hanes and Inman (1985a) attributed the difference to the existence of sliding friction between particles in addition to collisions at high solid volume fraction. This implied the progression of flow from the collisional regime (at a low solid volume fraction) to the intermediate regime (at a high solid volume fraction) with the increase of the dimensionless stress. Hanes and Inman (1985a, b) also obtained their measured dynamic friction angles to be nearly constant (with standard deviations of approximately 10% of the mean) over a range of shear rates and applied normal stresses for a given material. This is in agreement with the results of Savage and Sayed (1984) for collisional flows where stresses are dependent on the square of the shear rate.

On the other hand, Patton et al. (1987) conducted inclined flow experiments on small (0.26mm) and large (2.94mm) glass beads, and plotted the measured friction angles with the square of the Froude number and solid volume fraction. The results showed that the measured friction angles remain constant for low Froude numbers but suddenly increase at high Froude numbers. The constant friction angle at low Froude numbers was the same as the quasi-static friction angle of the glass beads, which indicates that the Coulomb friction mechanism governs flows in this range of Froude numbers. The sudden increase of the friction angle indicated the progression of the flow to the intermediate stage and then the collisional regime. The agitation of particles and collisions in these regimes were also observed. Their results also showed an increase in the friction angle with a decrease in solid volume fraction (or increase in void ratio). This result is in agreement with Savage and Sayed (1984), where the dynamic friction angle increases with the void ratio and it is greater than the quasi-static friction angle. Patton et al. (1987) also plotted the dimensionless stress $\left(\sigma/(\rho\dot{\gamma}^2 d^2)\right)$ with the solid volume fraction and obtained similar results to Hanes and Inman (1985a). Similarly, the inclined flow experiments of Ahn et al. (1991) using glass beads also revealed similar results in that the friction angle increased as the void ratio increased (Savage & Sayed, 1984; Patton et al., 1987).

Cassar et al. (2005) plotted the measured friction angles of spherical glass beads from their inclined flow experiments with a dimensionless number, $I \propto \dot{\gamma} d\sqrt{\rho/\sigma_z}$, and found that the friction angle increases from a quasi-static value to a collisional (or dynamic) value as the flow progresses from quasi-static to intermediate and then to a collisional regime with the increase of the dimensionless number.

Furthermore, the progression of granular flow has been studied in detail using Discrete Element Method (DEM) simulations. One fundamental study was conducted by Da Cruz et al. (2005), who performed a series of steady plane shear flow simulations of rigid disks at various states of normal stress and shear rate.

They first identified a single dimensionless number, called the *inertial number* $I = \dot{\gamma} d \sqrt{\rho / \sigma_z}$, which relates the ratio of the particle inertia to the total normal stress in describing the state of the granular material. They then studied the progression of granular flow by varying this dimensionless inertial number. Small values of I correspond to the quasi-static regime which can be described using soil mechanics theory, while large values of I correspond to the collisional regime which can be captured using the kinetic theory. When I increases in the intermediate regime (i.e., in the progression of flow from the quasi-static to the collisional stage through the intermediate stage), an approximately linear decrease of the solid volume fraction and an approximately linear increase of the friction angle from the quasi-static friction value were measured. The above two behaviours were termed dilatancy and friction laws, respectively. These laws also summarize the experimental findings discussed in the previous paragraphs.

Hatano (2007) performed 3D simulations of plane shear flows as an extension of the 2D simulations conducted by Da Cruz et al. (2005). Hatano (2007) discovered a power relationship between the friction coefficient and the inertial number, in contrast to the linear relationship obtained by Da Cruz et al. (2005).

Another fundamental study on all ranges of granular flow was conducted by Campbell, who performed a series of steady plane shear flow simulations of elastic spheres under constant void ratio (Campbell 2002) and constant normal stress (Campbell 2005). He identified a dimensionless stiffness parameter scaled with a shear rate $\left(K/(\rho d^3 \dot{\gamma}^2)\right)$ and studied the flow progression by presenting his results in the solid fraction – dimensionless vertical normal stress $\left(\sigma_z d / K\right)$ – dimensionless stiffness framework. This framework can be considered an extension of a critical state framework by introducing the dimensionless stiffness (or inverse of dimensionless shear rate) as an additional variable. At high void ratio, stresses are related to the square of the shear rates, like the experimental results of Savage and Sayed (1984). On the other hand at low void ratio, stresses

become weakly dependent on shear rate, confirming the experimental results of Savage and Sayed (1984) on 1.8 mm glass beads. Also under very low void ratio conditions, stresses become nearly independent of shear rate as the flow progresses from an intermediate regime to a quasi-static regime with the decrease of shear rate. Similar behaviour was also observed by Savage and Sayed (1984) in their experiments using 1 mm polystyrene beads.

Campbell's (2002) simulation results suggested that, at constant void ratio, flow progression is possible from quasi-static to an intermediate state with an increase in shear rate. However, direct progression from quasi-static to collisional flow is not evident at a constant void ratio. Campbell's (2005) simulation results also suggested that, at a constant normal stress, granular flow can undergo a full progression from quasi-static to intermediate and to collisional regimes.

Moreover, the simulation results of Campbell (2002) indicated that, at constant low void ratio where flows are in the intermediate regime, the friction angle increases with shear rate from quasi-static value (critical state friction angle) to collisional value (dynamic friction angle). Hatano (2010) presented similar simulation results as Campbell (2002), and also included measurements of granular temperature. Recent experimental and simulation studies in the progression of granular flow were conducted by Vidyapati et al. (2012). They also confirmed the increase of stresses and friction angle as the flow progresses from quasi-static to intermediate regime with the increase of shear rate.

2.2.4.2 Effect of Grain Size Distribution

Savage and Sayed (1984) conducted annular shear tests on a binary mixture of spherical polystyrene particles (30% by weight of small particles having a mean diameter of 0.55 mm, and 70% by weight of large particles having a mean diameter of 1.68 mm) in order to study the effects of non-uniform particle sizes. The weighted mean diameter of the mixture was 1.34 mm. The results generally

indicate that the stresses are weakly dependent on the shear rates compared to the results of mono-disperse polystyrene particles with a similar void ratio. They explained their findings as small particles being able to fit in the interstices of the large ones, which increases the likelihood of the frictional stress contribution to the total stress in the polydisperse particles. Their results also showed that, at lower void ratios where the stresses are weakly dependent on shear rate (intermediate flow regime), the measured friction angles increase with shear rate.

Rognon et al. (2007) conducted 2D discrete simulations of inclined flows for a bidisperse assembly of disks. They found that the *inertial number*, $I = \dot{\gamma} d \sqrt{\rho / \sigma_z}$, which describes the shear state of mono-disperse particles (Da Cruz et al., 2005) could be extended to the *generalized inertial number*, $I = \dot{\gamma} \cdot \bar{d} \sqrt{\rho / \sigma_z}$, by introducing a mass average diameter, $\bar{d}$, of the grains to describe the shear state of the bidisperse particles. Accordingly, they found that the measured friction coefficients of the bidisperse particles related approximately linearly to the generalized inertial number, similar to the results of mono-disperse particles (Da Cruz et al., 2005).

2.2.4.3 Effect of Particle Shape

Savage and Sayed (1984) also carried out the pioneer work on the shear behaviour of angular particles by conducting annular shear experiments of irregular-shaped crushed walnut shells of 1.19 mm average particle diameter. The results showed that the dimensionless stresses versus dimensionless shear rates data at high void ratios are consistent in magnitude with the spherical polystyrene and glass beads data. This may imply that, at high void ratios where particles interact fully by collision, the particle shape does not affect either the flow mechanism or the amount of stress generated. However, at constant low void ratio conditions, the stresses are weakly dependent (to a power less than 2) on shear rate, indicating significant rate-independent, dry frictional contributions to the total stresses.

It should be noted here that at some void ratios where the stresses of angular crushed walnut are weakly dependent (to a power less than 2) on the shear rate, stresses of spherical polystyrene and glass beads are strongly dependent (to the power of 2) on the shear rate. This implies that angular particles require higher void ratios than spherical particles to reach full collisional mechanism. Their results also showed that, at low void ratios where stresses are weakly dependent on shear rates (intermediate regime), the measured friction coefficients (ratio of shear to normal stresses) are less than the quasi-static friction angle. This is in contrast to the observations of spherical particles where the quasi-static friction coefficient is the smallest. They attributed this effect to the interlocking of angular particles at a quasi-static state that develops higher shear stress (and hence a high quasi-static friction angle) in angular particles.

Martino and Davies (2003) conducted inverted cone and plate rheometer tests on cylindrical PVC particles at constant normal stress. Their results showed a decrease in friction angle as the flow of the cylindrical particles progresses from a quasi-static to an intermediate regime with the increase of shear rate.

Extensive torsional shear cell experiments were also conducted by Lu et al. (2007) on angular and spherical quartz sands. Under constant void ratio, results of the angular quartz sand showed that the normal and shear stresses decrease with an increase of shear rate as the flow progresses from a quasi-static to an intermediate regime. The flow continued to progress to the collisional regime with further increase of shear rate. Based on this result they concluded that a full progression of flow (from quasi-static to intermediate to collisional regimes) is possible at constant void ratio which is in contrast to the conclusion reached by Campbell (2002). At constant normal stress, on the other hand, results of angular quartz sand showed that the void ratio decreases with increase in shear rate as the flow progresses from a quasi-static to an intermediate regime. The flow continues to progress to the collisional regime with further increase of shear rate. ‘Shear-

weakening' was the term they used for the inverse relation of stresses and void ratio with shear rate in the intermediate regime.

2.2.4.4 Flow Mechanics in the Intermediate Regime

In the intermediate flow regime, the granular particles interact by rubbing friction (in sliding and rolling over each other) and collisions. Several explanations have been provided regarding the combination of the two mechanisms and their stresses. Sayed (1981) proposed a microscopic description model for an intermediate flow state. The model consists of individual particles interacting with each other by collisions, and clusters of particles which undergo frictional deformation. The clusters are transient, and form and break in random fashion.

Drake (1990) explained the structural features in granular flows using films taken from inclined plane granular flows. He classified the vertical profile of the inclined granular flow into frictional and collisional regions. The frictional region consists of quasi-static and block-gliding zones, while the collisional region consists of grain-layer-gliding, chaotic, and saltational zones. The boundaries between the regions and zones are gradational (or gradual). The block-gliding and grain-layer-gliding zones are located at the boundary between the frictional and collisional regions. In the block-gliding zone, coherent blocks of a few to hundreds of particles exist. Within the blocks, particles are typically in contact with one or more of their neighbors at all times. At block boundaries, distinct collisions between blocks are frequently observed. The grain-layer-gliding zone consists of irregular layers of particles that appear to slide over one another. However, the appearance of sliding and continuous contact between particles is deceptive, because high-speed films revealed that intergranular momentum transfer is predominantly collisional both between and within layers. Drake's (1990) explanation gives some insight into how the two flow mechanisms exist in intermediate flow and may partly support the descriptive model of Sayed (1981) regarding the existence of clusters.

Campbell (2002, 2005) explained the reason for frictional stresses to be rate-independent, collisional stresses to be rate-dependent on the square of the shear rate, and intermediate flow has rate-independent and rate-dependent (linearly to shear rate) stress components. He classified the flow regimes as elastic-quasi-static, elastic-inertial, and inertial. He first stated that internal stresses can be thought of as the product of transported momentum and transport rate, or alternatively the product of force, duration of force, and transport rate. In elastic-quasi-static shear flow, Campbell (2002, 2005) contended that stresses are generated when the shear drives the particles together to form a chain, and then compresses, rotates and finally destroys the chain. The degree of compression and thus the magnitude of the force is determined by the necessity of conforming to shear quasi-statically at the required constant critical void ratio, rendering the force rate-independent. On the other hand, chains form as the shear brings the particles together at a transport rate proportional to the shear rate, but the chains persist for a time proportional to the inverse of shear rate. Hence, the product of force, duration of force, and transport rate (and therefore the stress) is independent of shear rate.

When the shear rate is large enough (in the elastic-inertial regime), the particle momentum becomes significant and the forces generated in the chain will have a baseline quasi-static force component (i.e., the force as shear rate is close to zero) and an inertia force component (which is proportional to the shear rate). Since the chains are generated at a rate proportional to the shear rate and persist for a period proportional to the inverse of the shear rate, the product of force duration and transport rate is again rate-independent. Thus, the stresses in the elastic-inertial regime vary only with the generated chain forces, which have rate-independent and linearly rate-dependent components.

Campbell (2002, 2005) further explained that elastic-quasi-static and elastic-inertial regimes are similar and that their only difference is that the inertial forces are negligible in elastic-quasi-static regime. In pure inertial flows, the particles are

free of the force chains and the momentum transferred is proportional to the impact velocity, which is also proportional to the shear rate. As the rate at which particles are driven together is still proportional to the shear rate, the product of the transported momentum and the transport rate (or stress) is proportional to the square of shear rate.

2.2.5 Inclined Granular Flow Behaviour

Inclined flow characteristics of granular particles have been studied in various flow ranges and conditions, such as under thin and thick flow depths, mild and steep inclination angles, and smooth and rough inclined bases (Daerr & Douady ,1999; Pouliquen, 1999; Daerr, 2001; Ancey, 2001; Silbert et al., 2001; Silbert et al., 2002; Silbert et al., 2003; Mitarai & Nakanishi, 2005; Delannay et al., 2007; Kumaran, 2008). Delannay et al. (2007) reviewed the findings and the state of understanding of inclined granular flows in a systematically organized way. They summarized the flow characteristics under three different flow conditions: flat-frictional base; bumpy rigid base; and erodible base. Figure 2.1(a) represents a bumpy-rough boundary while Figures 2.1(b) represents a flat-frictional boundary. Inclined granular flows are substantially affected by the roughness of the inclined base (Silbert et al., 2002; Mitarai & Nakanishi, 2005; Delannay et al., 2007; Kumaran, 2008).

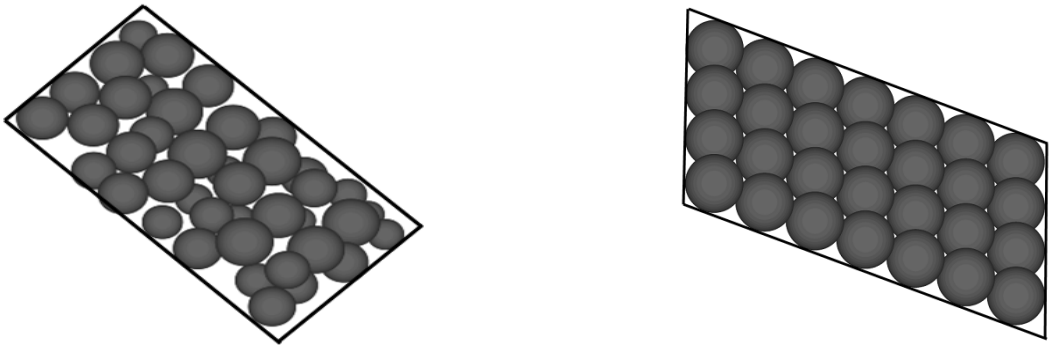

(a) (b)

FIGURE 2.1: Types of bottom boundaries in inclined flow study: (a) bumpy-rough boundary, (b) flat-frictional boundary.

On a flat-frictional base, inclined flows of spherical particles consist of a thin, agitated basal shear layer that supports a thick, less agitated overburden (Louge & Keast, 2001; Delannay et al., 2007). The basal shear layer flows with a finite slip velocity at the base and at a high shear rate (see the velocity profile of the basal shear layer in Figure 2.2b). The basal shear layer is also characterized by smaller density and higher granular temperature than the overburden layer, as in Figures 2.2(a) & (c). Steady fully developed (SFD) flows occur in the range of inclination angles between the measured static and sliding friction angles between a grain and the base (Delannay et al., 2007).

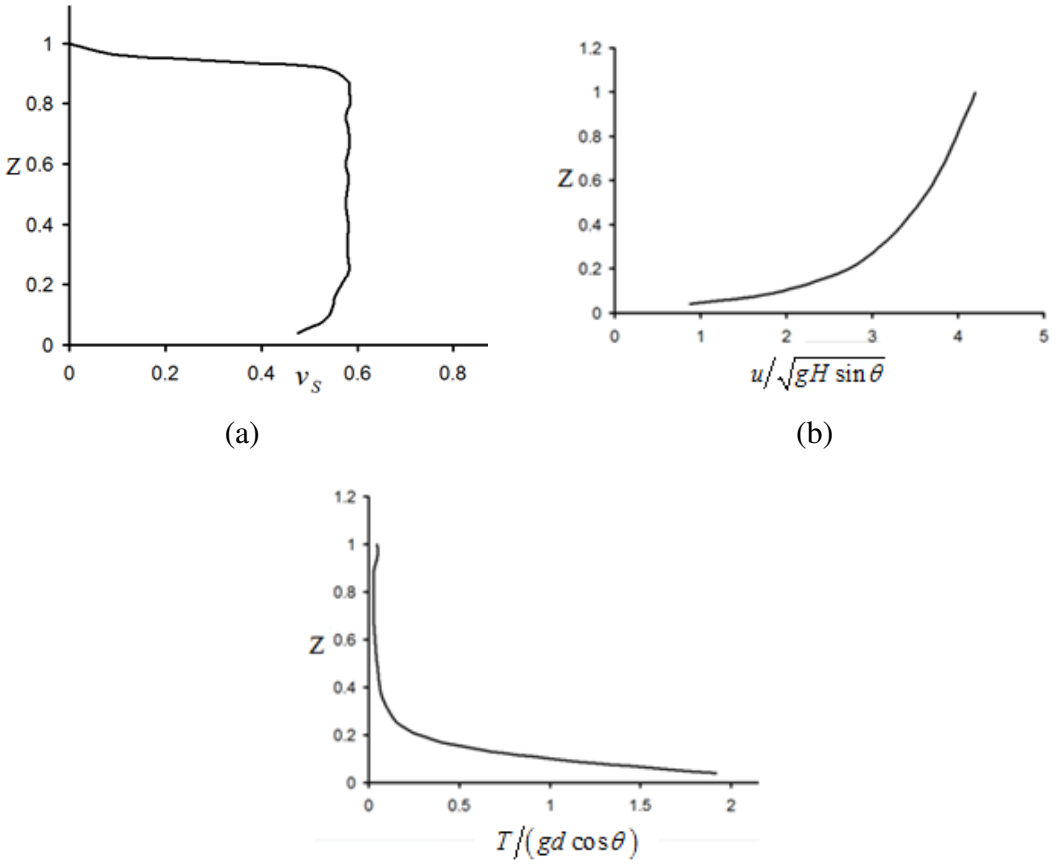

(a) (b)

(c)

FIGURE 2.2: Flow profiles on flat-frictional inclined base: (a) solid volume fraction, (b) dimensionless velocity, and (c) dimensionless granular temperature. Data obtained from 3D simulation of inclined flow (see Sec. 6.4.2.3.3). The flat-frictional base was modeled by attaching spheres of similar diameter with the flowing particles to the base in a rectangular array arrangement.

On a bumpy-rough base, the inclined flow characteristics of a certain spherical particle (with given material parameters) depend on angle of inclination (θ) and dimensionless depth of flow (*H/d*). These variables are used to establish a phase diagram of inclined flow for a classification of flow characteristics (Pouliquen, 1999; Silbert et al., 2001; Silbert et al., 2003). The phase diagram established by Silbert et al. (2001) for mono-disperse particles using 2D and 3D discrete simulations of inclined flows over a bumpy-rough bed is shown schematically in Figure 2.3 for the purpose of discussion. In the phase diagram, three principal regions exist, corresponding to "no flow", "stable flow", and "unstable flow". The three regions are separated by two angles: θ_r, the angle of repose; and $\theta_{\max}$, the maximum stability angle, the largest angle for which stable flow is obtained. They are shown by solid and dashed lines, respectively, in Figure 2.3.

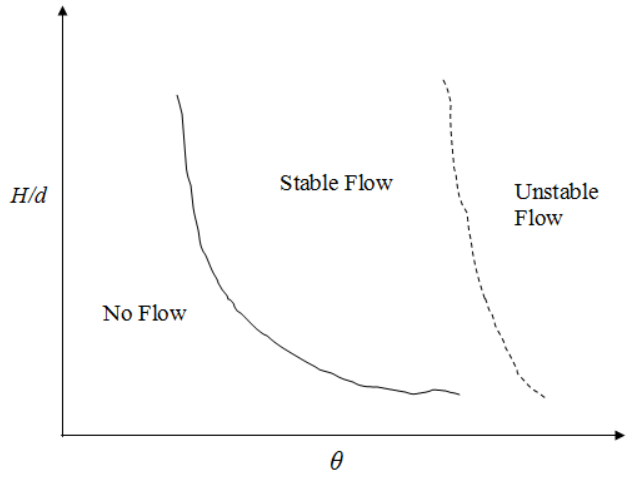

FIGURE 2.3: Schematic representation of phase diagram for mono-disperse granular inclined flows on a bumpy-rough base (based on Silbert et al., 2001).

For $\theta < \theta_r$, granular flow cannot occur, while for $\theta > \theta_{\max}$, granular flow is unsteady. In the region $\theta_r < \theta < \theta_{\max}$, granular particles flow in a stable steady state condition with a constant void ratio throughout the flow depth except for close to the base and surface of the flow. The velocity and granular temperature profiles of flows in this region are studied by Silbert et al. (2001, 2003). At thick

flow depths and steep inclination angles (close to the θ_{max} boundary), the inclined flow of spherical particles has a concave velocity profile and consists of three regions (Louge, 2003), as shown schematically in Figure 2.4. The first is a thin basal layer, where the solid volume fraction is higher and the granular temperature increases sharply with increasing elevation from the bottom boundary. The second is a core region, where the solid volume fraction is nearly constant and the granular temperature decreases from its maximum value at the bottom of the core. The last is a thin collisional surface layer, where the volume fraction abruptly vanishes as the free surface is approached.

Silbert et al. (2003) observed that the solid volume fraction in the core region is independent of flow depth and slightly decreases as the inclination angle increases (moving to the θ_{max} boundary). On the other hand, the velocity profile progresses to a convex shape and the granular temperature values decrease as the inclination angle decreases and/or flow depth decreases (close to the θ_r boundary).

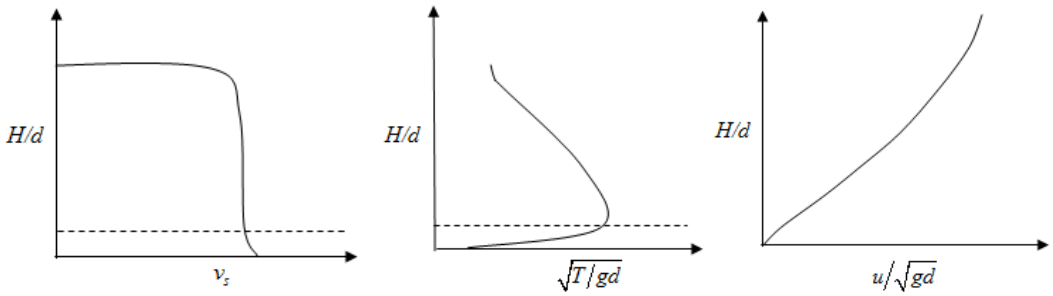

(a) (b) (c)

FIGURE 2.4: Schematic flow profiles for bumpy-rough inclined base: (a) depth profile of solid volume fraction, (b) depth profile of granular temperature, (c) depth profile of velocity (based on Louge, 2003).

2.3 Constitutive Modeling of Dry Granular Flow

2.3.1 Introduction

Like the understanding of granular flow behaviour, the success of constitutive modeling of granular flow has also been limited to extreme flow regimes. Quasi-static granular flows have been successfully modeled by the Theory of Plasticity and Critical State Soil Mechanics (CSSM), while collisional granular flows have been successfully modeled by the Kinetic Theory of Granular Flow (KTGF). Conversely, a concise theory for characterizing and modeling intermediate flow has not yet been established, even though several unified constitutive models have been suggested to capture both rate-independent frictional behaviour and rate-dependent collisional behaviour of granular particles.

2.3.2 Frictional Constitutive Modeling

Quasi-static deformation behaviour of soils is successfully captured by a critical state soil mechanics framework (Schofield & Wroth, 1968; Wood, 1990). At quasi-static deformation, soil reaches a critical state where it flows steadily at a constant void ratio and stress. The locus of void ratios and normal stresses at critical states forms a line called the Critical State Line (CSL). The shear and normal stresses at critical states are also related by Coulomb's friction law using the critical state friction angle, μ_{cs}. Further discussion on the critical state framework is presented in Chapter 5.

Savage and Hutter (1989) formulated the depth-averaged model for dry granular flows down an inclined plane, assuming shear stress and normal stress at the base of flow obeying Coulomb's friction law. The Savage-Hutter (SH) model was extended by Pudasaini and Hutter (2003) to account for complex curved and twisted topography. Following the pioneering work of Savage and Hutter (1989),

the Coulomb friction law has been implemented in several landslide models, such as MADFLOW (Chen & Lee, 2000), TITAN2D (Pitman et al., 2003), DAN3D (McDougall, 2006), and RASH3D (Pirulli, 2005), and used for numerical analyses of laboratory flume experiments (Hungr, 1995; Gray et al., 1999; Wieland et al., 1999; Denlinger & Iverson, 2001; Galas et al., 2007) and flow type landslides (Hungr, 1995; Kelfoun & Druitt, 2005; Sheridan et al., 2003). A concise summary of depth-averaged model is provided in Pudasaini and Hutter (2007).

Voellmy model, which accounts for all possible sources of velocity dependent resistance in addition to frictional resistance, is also used in cases where the frictional model does not offer a better prediction. The Thurwieser rock avalanche in the Italian Alps and the Frank Slide in Canada can be mentioned as good examples (Pirulli, 2009; Hungr et al., 2007). Other studies include Hungr and Evans (1996) and Evans et al. (2001).

2.3.3 Collisional Constitutive Modeling

Bagnold (1954) was the first to propose an empirical constitutive equation for stresses in collisional flows based on experimental results. Later, McTigue (1978) attempted to provide improved constitutive relations. On the other hand, Ogawa (1978) adopted the kinetic theory of gases for the first time to explain the collisional mechanism and to drive constitutive modeling, introducing the variable "granular temperature" as being analogous to gas temperature. Granular temperature is defined as the average of the square of particle fluctuation velocities and measures the fluctuating random motion of particles in a collisional flow. The kinetic theory was also adopted by Savage and Jeffrey (1981), Jenkins and Savage (1983), Lun et al. (1984), Jenkins and Richman (1985), Lun and Savage (1987), Goldhirsch (1999), and Jenkins and Zhang (2002). All of these researchers provided constitutive equations that relate stresses with the variables

of solid volume fraction, shear rate, and granular temperature, and with the material parameters of density, particle diameter, and restitution coefficient.

Savage and Jeffrey (1981) derived the collisional constitutive equations for identical, smooth, hard, and elastic spheres. They introduced a dimensionless parameter, which is the ratio of the characteristic mean shear velocity $(\dot{\gamma}d)$ to the square-root of granular temperature, and expressed the stresses as integrals involving this dimensionless parameter. For moderate and large values of the dimensionless parameter, their theory predicts both shear and normal stresses that are proportional to the square of particle diameter and the square of shear rate.

Jenkins and Savage (1983) extended the analysis of Savage and Jeffrey (1981) for nearly elastic (slightly inelastic) particles by including energy dissipation due to inelastic collisions.

Lun et al. (1984) developed two theories: one for the Couette flow of smooth, inelastic particles having arbitrary coefficients of restitution, and a second for the general flow of particles with coefficients of restitution near 1 (slightly inelastic particles). They followed the method of Savage & Jeffrey (1981) for the Couette flow study, and compared their theory with Ogawa et al. (1980), Shen (1981), Jenkins and Savage (1983), the Chapman-Enskog dense-gas theory, and with annular-shear-cell experiments of Savage and Sayed (1980). Their theory of Couette flow agreed moderately well with the experimental data. Their theory of Couette flow also agreed with Jenkins and Savage (1983) theory, developed for slightly inelastic particles, even when the later was used for highly inelastic particles. Hence, Lun et al. (1984) pursued the "nearly elastic" approximation of Jenkins and Savage (1983) to develop a second theory for general flow fields of particles. The generalized theory incorporates kinetic as well as collisional contributions to the constitutive equations for stress and energy flux and is thus appropriate for dilute as well as dense concentrations of solids. The kinetic

contribution was assumed to be negligible in the analysis of Jenkins and Savage (1983).

The effect of particle roughness (surface friction) in collisions between particles has also been studied by Jenkins and Richman (1985), Lun and Savage (1987), and Jenkins and Zhang (2002). In collisions of rough particles, the collisional impulse has a tangential component due to surface friction and causes rotation of particles. Thus, the mean and the fluctuation motions consist of both the translational and rotational components. Previous studies (Jenkins & Richman, 1985; Lun & Savage, 1987) treated rotational motion in a way similar to translational motion by assigning a "roughness coefficient" to relate the tangential components of the relative velocities of a point of contact before and after collisions (analogous to the "restitution coefficient" which relates the normal components of the relative velocities of a point of contact before and after collisions) and writing balance equations for angular momentum and rotational fluctuation energy. The translational fluctuation energy (or translational granular temperature) is produced by the shear work which is given as the product of collisional shear stress and shear rate. By the same analogy, rotational fluctuation energy (or rotational granular temperature) is produced by rotational work given as the product of collisional angular momentum flux (or collisional couple stress) and the gradient of angular velocity. The fluctuation energies are dissipated by inelastic collisions and surface friction. Later, Jenkins and Zhang (2002) introduced an effective coefficient of restitution that combines the dissipation of fluctuation energy by inelastic and frictional impacts.

2.3.4 Unified Constitutive Modeling

Like the Theory of Plasticity and Critical State Soil Mechanics (CSSM) for quasi-static flows and the Kinetic Theory of Granular Flow (KTGF) for collisional flows, a concise theory for characterizing and modeling intermediate flow has not yet been established. Nonetheless, several unified constitutive models have been

suggested to capture both rate-independent frictional behaviour and rate-dependent collisional behaviour of granular particles (Savage, 1982; Johnson & Jackson, 1987; Nott, 1991; Savage, 1998; Mills et al., 1999; Ancey & Evesque, 2000; Louge & Keast, 2001; Louge, 2003; Lee & Huang, 2010; Berzi et al., 2011).

Pioneering efforts towards a unified constitutive model were made by Savage (1982), who directly added the frictional and collisional stress contributions, each calculated as if they acted alone. Later, Johnson and Jackson (1987) and Nott (1991) extended the unified model proposed by Savage (1982) to the horizontal Couette flows and inclined flows. They assumed that the shear work by the frictional stress component directly dissipated to heat, while the shear work by the collisional stress component produces granular temperature (fluctuation energy), which is then dissipated to heat. However, the above approach is a simplified method based on the ad hoc assumption of stress addition, as it is not clear how the two stress contributions act together in the intermediate flow regime (Johnson & Jackson, 1987).

A more general tensorial expression of a constitutive equation for an intermediate flow regime was given by Savage (1998). He first derived the stress-strain relationship based on an associated flow rule used in the plasticity theory. By introducing strain-rate fluctuation and taking a statistical average, he then obtained a rate-dependent, viscous-like relationship between mean stress and mean strain rate which works even for low deformation rate (quasi-static) flows. Finally, he related the strain rate fluctuation with granular temperature by dimensional analysis and cautiously formulated the functions of flow rule so that the viscous-like constitutive equation reduces to the kinetic theory model of granular flows at high shear rates.

On the other hand, Mills et al. (1999) approached the problem from the microscopic interaction of particles during the flow. They explained the

coexistence of strong and weak contact force networks in dense granular flow, and modeled the flow as a network of transient solid chains (the strong networks) immersed in an assembly of particles behaving as a viscous fluid (the weak networks). The strong contact network supports the whole deviatoric load (like a solid) while the weak contact network contributes to the isotropic pressure (like a fluid). A particle may belong to either of the networks at any given time.

A different approach was presented by Ancey and Evesque (2000), who consider the possible relationship between quasi-static and collisional stress contributions, in contrast to the ad hoc assumption of Savage (1982), and determine their amounts by satisfying the balance of energy.

Louge and Keast (2001) and Louge (2003) developed a unified model for dense dry granular flows on flat-frictional and bumpy-rough inclines, respectively. Like Savage (1982), they expressed the total stress as the superposition of the rate-independent frictional component and rate-dependent collisional component. However, unlike Johnson and Jackson (1987) and Nott (1991), they formulated the fluctuation energy equation by allowing both the frictional and collisional stress components to produce fluctuation energy. They also used the effective restitution coefficient suggested by Jenkins and Zhang (2002) in the fluctuation energy balance. Lee and Huang (2010) also used similar equation for fluctuation kinetic energy to develop a unified model for granular flow.

Most recently, Berzi et al. (2011) followed the assumption of Johnson and Jackson (1987) in the formulation of the fluctuation kinetic energy by taking only the collisional stress contribution to produce granular temperature. However, they used the collisional constitutive equations proposed by Jenkins and Berzi (2010), which incorporates a length scale in the expression for the rate of fluctuation energy dissipation by collisions. This length scale is the size of a cluster of correlated particles (or chain/correlation length). It accounts for the decrease in the collisional energy dissipation due to the presence of a correlated motion of

particles that is likely to occur when the flow is dense. Hence, the Berzi et al. (2011) model differs from the above models (Louge & Keast, 2001; Louge, 2003; Lee & Huang, 2010) in that Berzi et al. (2011) considered the decrease of fluctuation energy dissipation due to the presence of particle clusters in dense flows while the above models considered the additional fluctuation energy production due to the presence of frictional stress contribution in dense flows. Hence, the predictions of both types of models should essentially be similar.

There have been developments of unified constitutive models by extending the hypo-plasticity theory of frictional behaviour to also capture the rate-dependent behaviour of granular materials (Wu, 2006). Elasto-visco-plastic constitutive models have also been proposed based on the Goodman-Cowin theory to capture the elastic, rate-dependent, and plastic behaviours of dry granular flows simultaneously (Wang and Hutter, 1999; Fang et al., 2006).

CHAPTER THREE

SIMULATION EXPERIMENTS

3.1 Introduction

The commercial software PFC3D v4.00, based on the Distinct Element Method (DEM), was used in the simulation experiments of dry particle flows. The particles are assumed to be rigid, contacting each other only at a point, and allowed to slightly overlap at their contact points.

The non-linear Hertz-Mindlin contact model is adopted with viscous damping applied in both the normal and shear directions at particle contacts in order to model inelastic collisions. Forces and relative displacements at a contact are related in case of no viscous damping by (PFC3D User's Manual, 2008)

$$F_i^n = K^n U^n n_i , \tag{3.1a}$$

$$\Delta F_i^s = -k^s \Delta U_i^s \quad \text{and} \quad F_i^s = \min\left(\mu_s \left|F_i^n\right|, \left|\Sigma \Delta F_i^s\right|\right) \Sigma \Delta F_i^s \Big/ \left|\Sigma \Delta F_i^s\right| , \tag{3.1b}$$

where F_i^n and F_i^s are the total contact normal and shear forces, U^n is the total contact normal displacement, K^n is the contact secant normal stiffness, n_i is a unit vector normal to a contact, ΔF_i^s is the incremental contact shear force in a time step, ΔU_i^s is the incremental contact shear displacement, k^s is the contact tangent shear stiffness, and μ_s is the friction coefficient at particles contact. Contact stiffnesses for the Hertz-Mindlin model are given by (PFC3D User's Manual, 2008)

$$K^n = \left(\frac{2\langle G \rangle \sqrt{2\tilde{R}}}{3(1-\langle \nu \rangle)} \right) \sqrt{U^n} \qquad \text{and} \qquad k^s = \left(\frac{2\left(\langle G \rangle^2 3(1-\langle \nu \rangle)\tilde{R}\right)^{1/3}}{2-\langle \nu \rangle} \right) \left| F_i^n \right|^{1/3}, \quad (3.2a)$$

$$\tilde{R} = \frac{2R^{[A]}R^{[B]}}{R^{[A]}+R^{[B]}}, \qquad \langle G \rangle = \tfrac{1}{2}\left(G^{[A]}+G^{[B]}\right), \qquad \langle \nu \rangle = \tfrac{1}{2}\left(\nu^{[A]}+\nu^{[B]}\right), \quad (3.2b)$$

where $R^{[A]}$ and $R^{[B]}$ are radii, $G^{[A]}$ and $G^{[B]}$ are shear moduli, and $\nu^{[A]}$ and $\nu^{[B]}$ are Poisson's ratios of the balls in contact.

In cases involving viscous damping, the damping force is added to the contact force given by Eq. (3.1) and acts to oppose motion. Its normal and shear components are given by (PFC3D User's Manual, 2008)

$$D_i = C_i \left| u_{r_i} \right|, \quad (3.3a)$$

where the subscript *i* refers to the normal and shear components, u_{r_i} is the relative velocity at a contact, and C_i is the damping constant given by (PFC3D User's Manual, 2008)

$$C_i = \frac{2\sqrt{mk_i}\,\ln\varepsilon}{\sqrt{\pi^2+\ln^2\varepsilon}}, \quad (3.3b)$$

where ε is the restitution coefficient, k_i is the contact tangent stiffness, and *m* is the effective system mass, which is taken as the ball mass in case of ball-wall contact, or given by

$$m = \frac{m_1 m_2}{m_1+m_2}, \quad (3.3c)$$

in the case of ball-ball contact, where m_1 and m_2 are masses of particles forming the contact. The viscous damping force is calculated after a sliding check. If the contact is sliding, then the viscous shear force is reduced to zero. The sum of the contact normal force and the viscous normal force is prevented from becoming attractive between the two involved entities. Hence, the magnitude of the viscous normal force is limited to $-\left|F_i^n\right|$ (PFC3D User's Manual, 2008).

3.2 Plane Shear Simulation

3.2.1 Model Description

A series of plane shear simulations were conducted using PFC3D v.4.0 for different states of flow. The 3D plane shear model is presented in Figure 3.1. The sheared particles are bounded by periodic boundaries on the vertical sides and a servo-controlled wall at the top. The model also has top and bottom boundary particles arranged in a rectangular array to simulate the roughness of the boundary surfaces. The bottom boundary particles move only in the *x*-direction at a prescribed shear velocity during shearing. The top boundary particles move only in the vertical direction at an average velocity calculated by taking the measured velocities of all particles in that boundary at each time step. The servo-controlled wall (above the top boundary particles) also moves only in the vertical direction relative to the top boundary particles in order to keep the prescribed vertical normal stress constant. Its relative velocity is calculated at each time step using

$$u_{r_z} = \frac{f_R \cdot A_h}{\Delta t \cdot K_{sum}^n} \cdot \left(\sigma_z^m - \sigma_z^a\right), \tag{3.4}$$

where σ_z^a is the applied (or prescribed) vertical normal stress, $\sigma_z^m = F_{SW} / A_h$ is the measured vertical normal stress at the servo-wall for each time step, F_{SW} is the vertical normal force at the servo-wall, A_h is the horizontal area of the servo-wall,

Δt is the time step, K^n_{sum} is the sum of stiffnesses of the balls contacting the servo-wall at each time step, and f_R is a relaxation factor for numerical stability (PFC3D User's Manual, 2008).

Since gravity is the main factor for heterogeneity, the minimum applied vertical stress in the laboratory experiments is limited by the value required to neglect the effect of gravity on the variation of vertical stress (Savage & Sayed, 1984). However, in simulation experiments, gravity can easily be eliminated (Da Cruz et al., 2005). The plane shear simulations conducted here were also carried out without gravity.

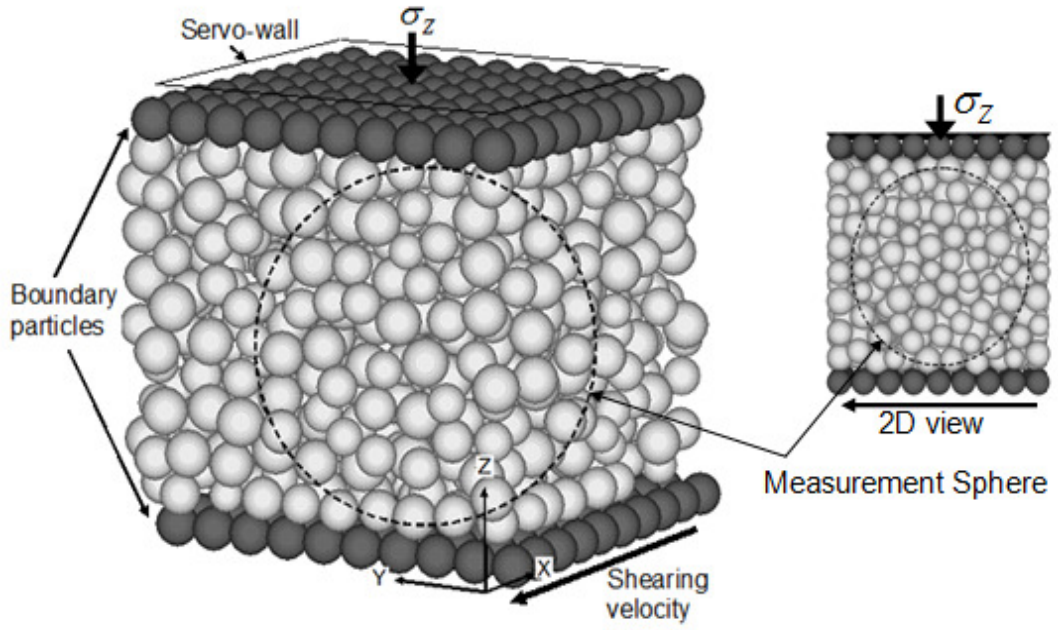

FIGURE 3.1: 3D Plane shear DEM model using PFC3D v. 4.00

3.2.2 Procedures of Plane Shear Simulation

The thickness of the effective shearing zone in a granular flow is around 10*d*, where *d* is the mean particle diameter (Hanes & Inman, 1985a; Hanes & Inman, 1985b; Thompson & Grest, 1991). Thus, a total of 912 particles, including the

boundary particles, were generated in a 9*d* x 9*d* x 10*d* model with the longest dimension in the *z*-axis. The boundary particles, each having size *d*, were arranged in a rectangular array while the rest of particles were randomly placed inside the model. For all plane shear simulations, the initial assembly (or initial random arrangement) of the particles was kept identical in order to eliminate the probable effect of the initial sample condition in comparing results. The particle assembly (or the sample) was then consolidated under a prescribed vertical normal stress until the void ratio was reduced to a specific value. Finally, the sample was sheared by gradually increasing the shear velocity to a prescribed value on the bottom boundary particles. The shearing was then continued for a minimum of 4 seconds similar to actual experiments of Savage and Sayed (1984) under the prescribed shear velocity, in which flow had reached steady state.

3.2.3 Measurement of Flow Characteristics

Stresses, shear rate, void ratio, coordination number, and sliding fraction were measured from a 'measurement sphere' which were sampled at specific time intervals (usually every 10 time steps) after the flow has reached steady state. The detail of the measurement logic can be found in PFC3D v. 4.00 User's Manual (2008). The data from PFC were exported to Excel and the average steady state values were calculated. Since PFC calculates only the contact stresses, the kinetic stresses are calculated using:

$$\sigma_{ij}^{k} = \rho_p v_S \left\langle u_i' u_j' \right\rangle \tag{3.5}$$

where $\left\langle u_i' u_j' \right\rangle$ is the product of fluctuation velocities calculated using Eq. (3.6e) to Eq. (3.6h). In most of the simulations, the servo-wall stress differs from the prescribed vertical normal stress in less than 1.5%. On the other hand, the sum of the vertical normal stresses, one determined from the 'measurement sphere' and the other calculated using Eq. (3.5), differs from the prescribed value in less than

3%, which increases sometimes up to 5% at high void ratios, indicating that the plane shear flow tends to be heterogeneous with increases in void ratio.

Furthermore, translational fluctuation velocities and average velocity in the flow direction were calculated by dividing the plane shear flow into horizontal layers of equal thickness d_{max} (the diameter of the largest particle in the simulation) starting from the bottom but excluding the boundary particles (Lu & Hsiau, 2005; Lan & Rosato, 1995). They are calculated for each layer as follows (Gioia et al., 2006)

$$\left\langle \overline{u}_{xL} \right\rangle = \frac{\sum_t \sum_b m_{tb}^L u_{xtb}^L}{\sum_t \sum_b m_{tb}^L}, \tag{3.6a}$$

$$\sqrt{\left\langle u_{xL}'^2 \right\rangle} = \left[\frac{\sum_t \sum_b m_{tb}^L \left(u_{xtb}^L \right)^2}{\sum_t \sum_b m_{tb}^L} - \left\langle \overline{u}_{xL} \right\rangle^2 \right]^{1/2}, \tag{3.6b}$$

$$\sqrt{\left\langle u_{yL}'^2 \right\rangle} = \left[\frac{\sum_t \sum_b m_{tb}^L \left(u_{ytb}^L \right)^2}{\sum_t \sum_b m_{tb}^L} \right]^{1/2}, \tag{3.6c}$$

$$\sqrt{\left\langle u_{zL}'^2 \right\rangle} = \left[\frac{\sum_t \sum_b m_{tb}^L \left(u_{ztb}^L \right)^2}{\sum_t \sum_b m_{tb}^L} \right]^{1/2}, \tag{3.6d}$$

where $\left\langle \overline{u}_{xL} \right\rangle$ is the average velocity of layer L in the flow direction; $\sqrt{\left\langle u_{xL}'^2 \right\rangle}$, $\sqrt{\left\langle u_{yL}'^2 \right\rangle}$ and $\sqrt{\left\langle u_{zL}'^2 \right\rangle}$ are the average fluctuation velocities of layer L in x, y, and z-directions; m_{tb}^L, u_{xtb}^L, u_{ytb}^L & u_{ztb}^L are the portion of the mass of particle b occupying

layer L at time step t and the instantaneous velocities of the corresponding ball in x-, y-, & z- directions, respectively. The data were sampled at an interval of 10 time steps after the flow has reached steady state. The average velocities in y- and z- directions are essentially zero because the particles are sheared only in the x-direction. However, the corresponding fluctuation velocities are different from zero. Similar results of average and fluctuation velocities were also reported in Natarajan et al. (1995).

The vertical profile of average velocity in the flow direction $\langle \overline{u}_{xL} \rangle$ is approximately linear in all simulation experiments. On the other hand, the fluctuation velocities exhibit a non-uniform profile at higher void ratios. Selected profiles of solid volume fraction, average velocity in the direction of flow, and fluctuation velocities are presented in Figure 3.2 for different flow states. Similar non-uniform variations of fluctuation velocities were also observed in previous works (Lun, 1996; Da Cruz et al., 2004; Liu & Rosato, 2005; Cleary, 2008). In this research, the average fluctuation velocities of a plane shear simulation at steady state were calculated by taking the layers (L) in the central uniform portion of flow and using Eq. (3.6e) to Eq. (3.6g) below.

A PFC3D code written for plane shear simulation is presented in Appendices A.1 and A.3.

$$\sqrt{\langle u_x'^2 \rangle} = \left[\frac{\sum_L \sum_t \sum_b m_{tb}^L \left(u_{xtb}^L - \langle \overline{u}_{xL} \rangle \right)^2}{\sum_L \sum_t \sum_b m_{tb}^L} \right]^{1/2}, \tag{3.6e}$$

$$\sqrt{\langle u_y'^2 \rangle} = \left[\frac{\sum_L \sum_t \sum_b m_{tb}^L \left(u_{ytb}^L \right)^2}{\sum_L \sum_t \sum_b m_{tb}^L} \right]^{1/2}, \tag{3.6f}$$

$$\sqrt{\langle u_z'^2 \rangle} = \left[\frac{\sum_L \sum_t \sum_b m_{tb}^L \left(u_{ztb}^L \right)^2}{\sum_L \sum_t \sum_b m_{tb}^L} \right]^{1/2}, \tag{3.6g}$$

$$\langle u_x' u_z' \rangle = \frac{\sum_L \sum_t \sum_b m_{tb}^L u_{xtb}^L u_{ztb}^L}{\sum_L \sum_t \sum_b m_{tb}^L}, \tag{3.6h}$$

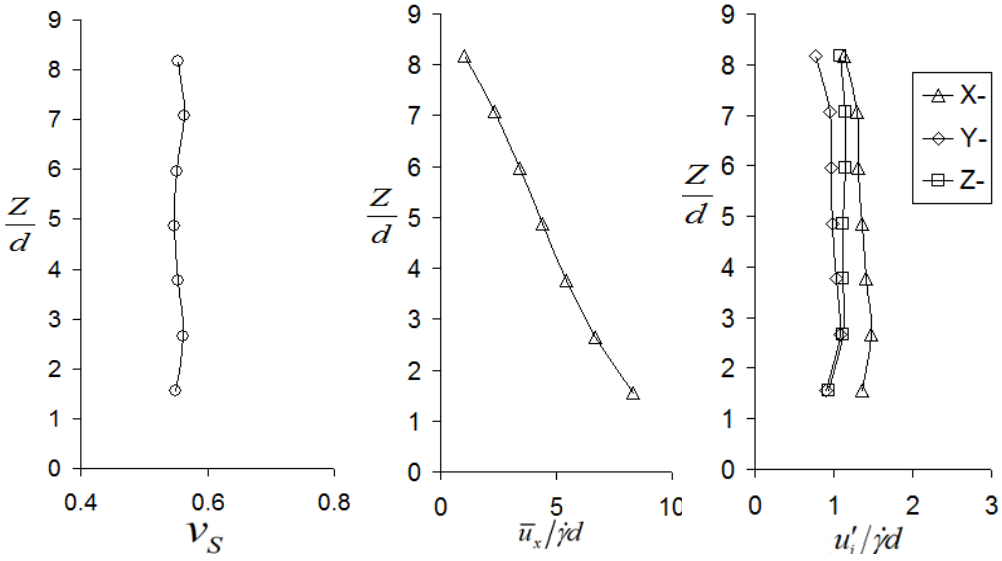

(a) At $\sigma_z = 25kPa$, $e = 0.73$, $\dot{\gamma}d = 0.2564m/s$

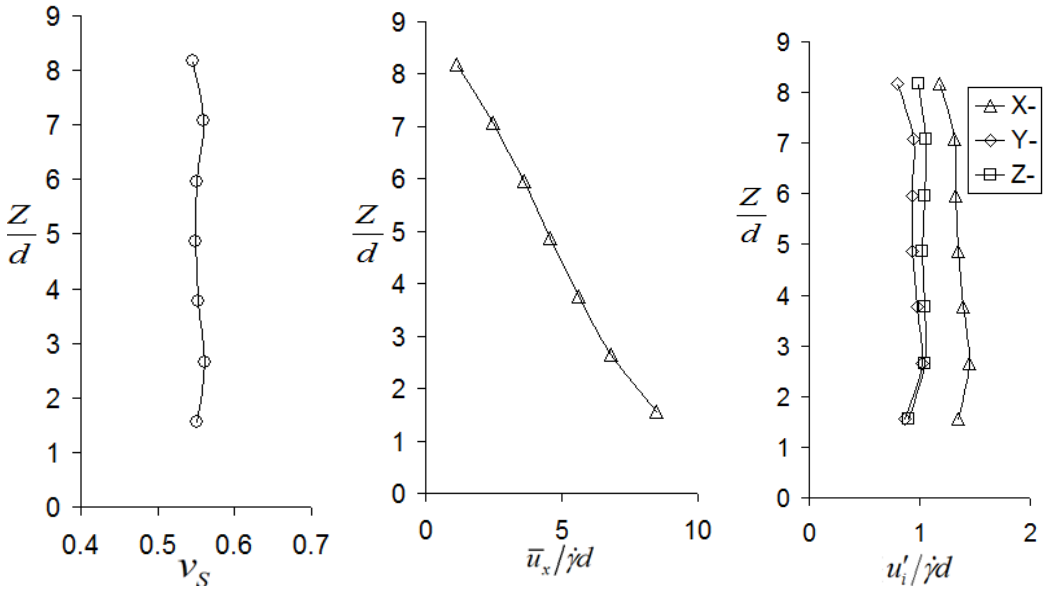

(b) At $\sigma_z = 300kPa$, $e = 0.7295$, $\dot{\gamma}d = 1.2738m/s$

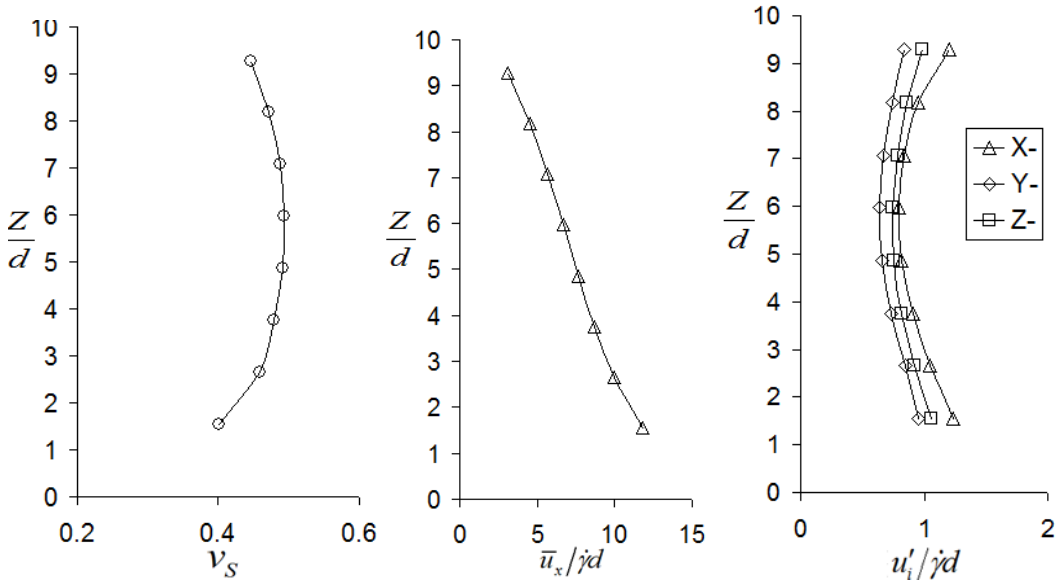

(c) At $\sigma_z = 10kPa$, $e = 0.9986$, $\dot{\gamma}d = 1.265m/s$

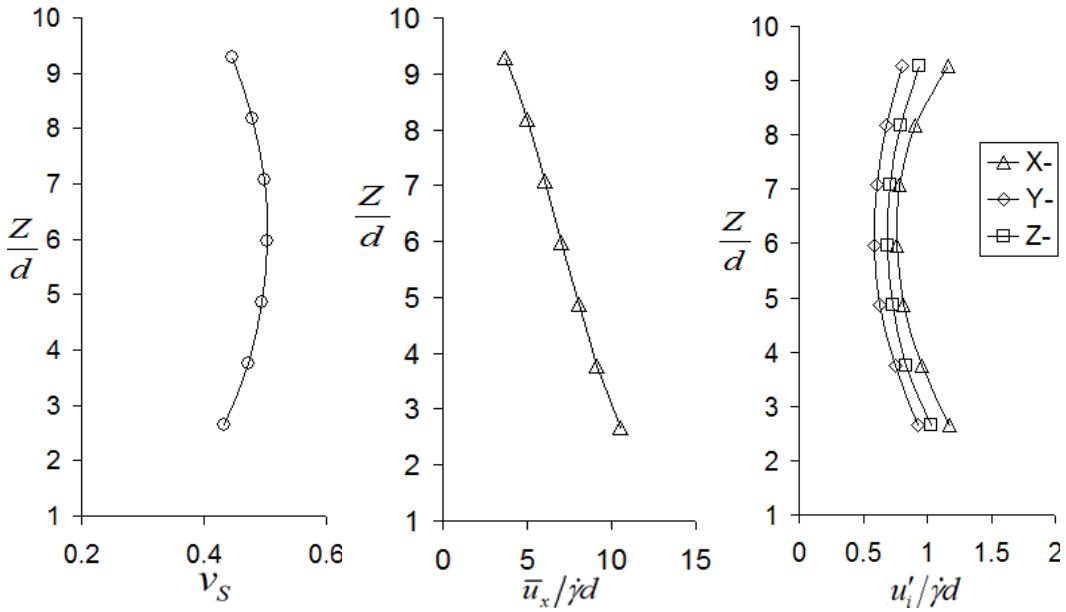

(d) At $\sigma_z = 600kPa$, $e = 0.9926$, $\dot{\gamma}d = 10.95m/s$

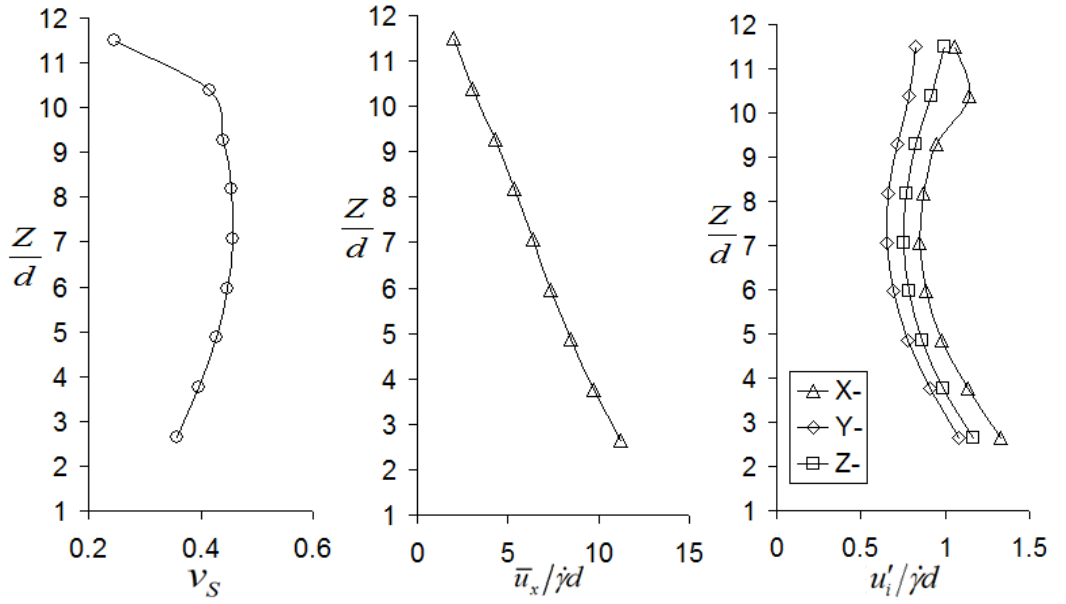

(e) At $\sigma_z = 10kPa$, $e = 1.1996$, $\dot{\gamma}d = 1.6228m/s$

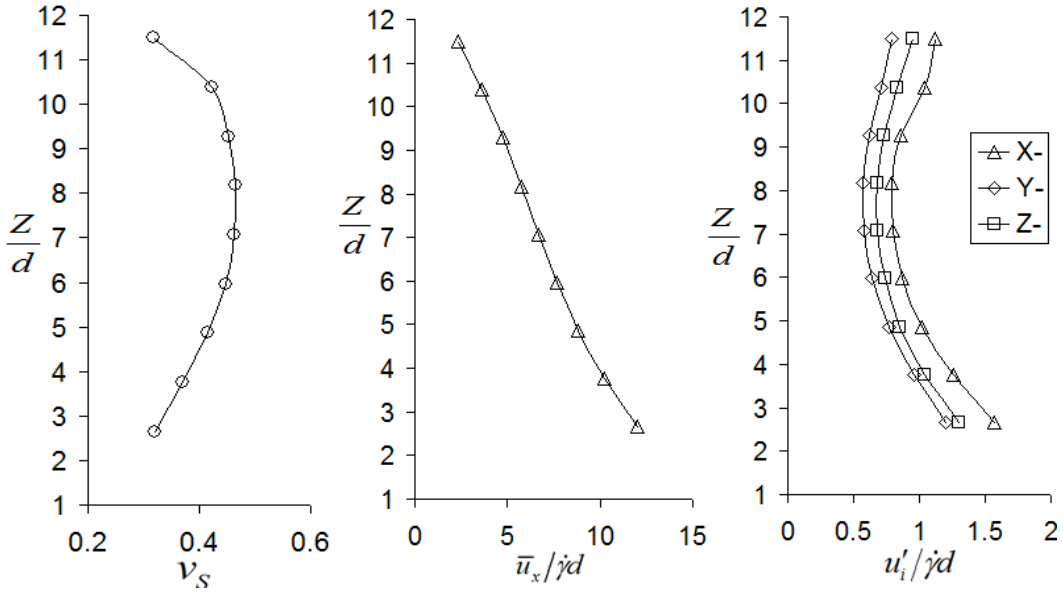

(f) At $\sigma_z = 600kPa$, $e = 1.2038$, $\dot{\gamma}d = 14.6748m/s$

FIGURE 3.2: Profiles of plane shear flow at different flow states. One to two layers close to the boundaries are filtered out in the profiles; σ_z is the vertical normal stress, e the void ratio, $\dot{\gamma}$ the shear rate, and d the mean particle diameter.

3.2.4 Model Calibration

Ring shear experiments can be modeled by DEM simulations of plane shear flows (Johnson & Jackson, 1987). In this research, the DEM plane shear model was calibrated by simulating the annular shear experiments of Savage and Sayed (1984).

While Savage and Sayed (1984) conducted annular shear experiments on different types of granular materials, their experiments on 1 mm mean diameter spherical polystyrene beads are selected in this research to calibrate the DEM model (Savage & Sayed, 1984, Figs. 3a, 8a and 8b). The sizes of the beads were between 0.81 mm and 1.1 mm with a mean diameter of 1 mm, as shown in Figure 3.3. The beads had a particle density (ρ) of 1095 kg/m^3.

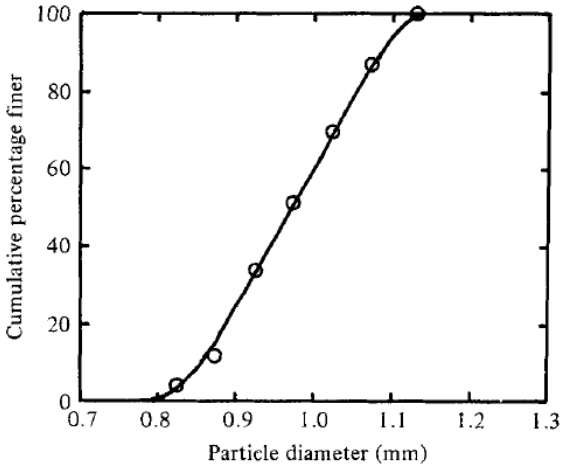

FIGURE 3.3: Grain size distribution of polystyrene beads (taken from Savage & Sayed, 1984)[2]

The particles in the simulations were also generated to achieve the same grain size distribution and particle density as the polystyrene beads. In order to generate particle assemblies of a larger mean diameter, all particles were scaled by the same percentage to keep the grain size distribution curve the same. The values of the parameters used in the simulation to best fit the experimental results are given in Table 3.1. The particle density (ρ), modulus of elasticity (E), and Poisson's ratio (υ) are close to the actual values of the polystyrene material. Restitution coefficient (ε) of actual polystyrene beads is estimated to be approximately 0.8 (Farrell et al., 1986). The restitution coefficient and the static surface friction (μ_s) were determined to best fit the experimental results.

TABLE 3.1: Values of parameters for DEM model

ρ (kg/m^3)	E (Pa)	υ	ε	μ_s
1095	3.25x10^9	0.34	0.75	0.6

[2] Copyright © 1984 Cambridge University Press. Reprinted with the permission of Cambridge University Press.

Rowe (1962) studied the theory and conducted the experiments on the relationship between sliding surface friction and bulk friction in granular particles. The relationship between sliding surface friction and bulk friction was also studied using DEM simulations by Thornton (2000) and Yimsiri (2001). Rowe (1962) indicated that the critical state friction angle of granular material in general is equal to the inter-particle sliding friction angle (also termed as "true friction angle") plus the additional friction angle due to particles rearrangement and fabric development. On the other hand, the DEM simulation studies indicated that the bulk friction angle is larger than the inter-particle friction angle for the later angle smaller than a threshold value (about 20^0). For the inter-particle friction angle greater than the threshold value, the bulk friction angle becomes less than the inter-particle friction angle and the contribution of increasing inter-particle friction angle to the bulk friction angle becomes small. The findings from DEM simulations are partially supported by the experimental data given by Skinner (1969), who performed shear box tests on spherical particles with different coefficients of inter-particle friction angle.

A selected experiment, shown in Table 3.2 row A, was first simulated using 1 mm mean-diameter DEM particles. The simulation result is shown in Table 3.2 row B. The same experiment was then simulated using 4 cm mean particle diameter as shown in Table 3.2 row C. It is observed that the measured shear rates are scaled by the mean particle diameters to give a constant characteristic mean shear velocity$(\dot{\gamma}d)$, which suggests that the shear experiments were collisional. Hence, the rest of the simulations were conducted using 4 cm mean diameter particles to explore the rate-dependent flow behaviour for large size particles.

TABLE 3.2: Comparison of physical and simulation experiments for polystyrene beads

Case	e	$\sigma_z\,(Pa)$	$\rho(kg/m^3)$	d (mm)	$\dot{\gamma}\left(s^{-1}\right)$	$\dot{\gamma}d(mm/s)$
A	0.984	966	1095	1	373.2	373
B	0.999	950	1095	1	380.1	380
C	0.999	984	1095	40	9.537	381

A – experimental result from Savage & Sayed (1984), B – PFC simulation with mean diameter equals to 1 mm, C – PFC simulation with mean diameter equals to 40 mm.

The simulations are compared with the experimental results as shown in Figure 3.4. Some differences were observed between the simulations and experimental results. The experiments at the void ratio of 0.908 were simulated by an assembly of spherical particles with void ratio of 0.825. In addition, the shear rates and the shear stresses at the void ratio of 1.17 were not precisely predicted, especially at higher stress levels. It was noted in the experimental results of Savage & Sayed (1984) that the higher normal stresses at void ratio of 1.17 showed somewhat weaker dependence upon shear rate, which was said to be not explainable according to the authors, S. B. Savage and M. Sayed. Hence, the shear rate and shear stress differences observed at the void ratio of 1.17 in Figure 3.4(a) may be partly attributed to the characteristics of the actual experimental results.

Overall the numerical model is able to capture the main characteristics of the granular assembly, and the variation of shear and normal stresses with the characteristic mean shear velocities compare well with the experimental results. Therefore, the DEM model was used to conduct simulation experiments at higher stresses.

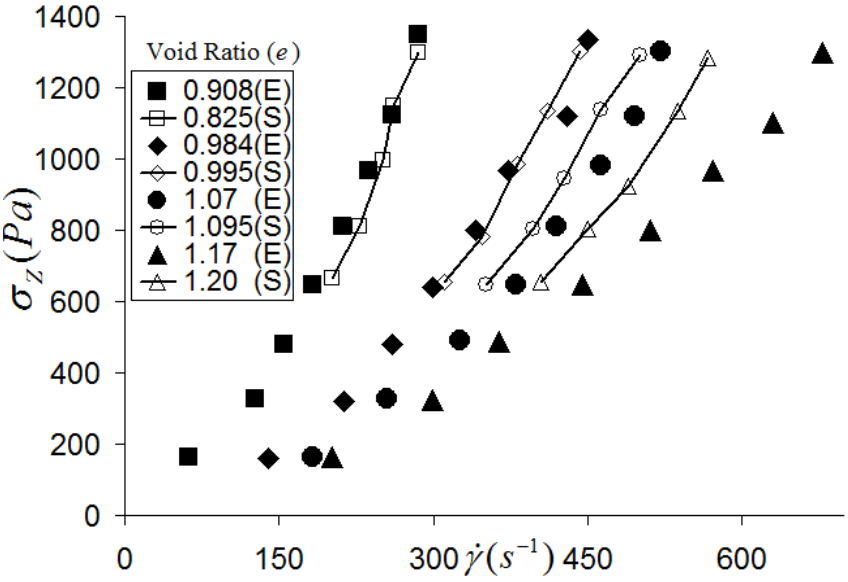

(a) Vertical normal stress versus shear rate

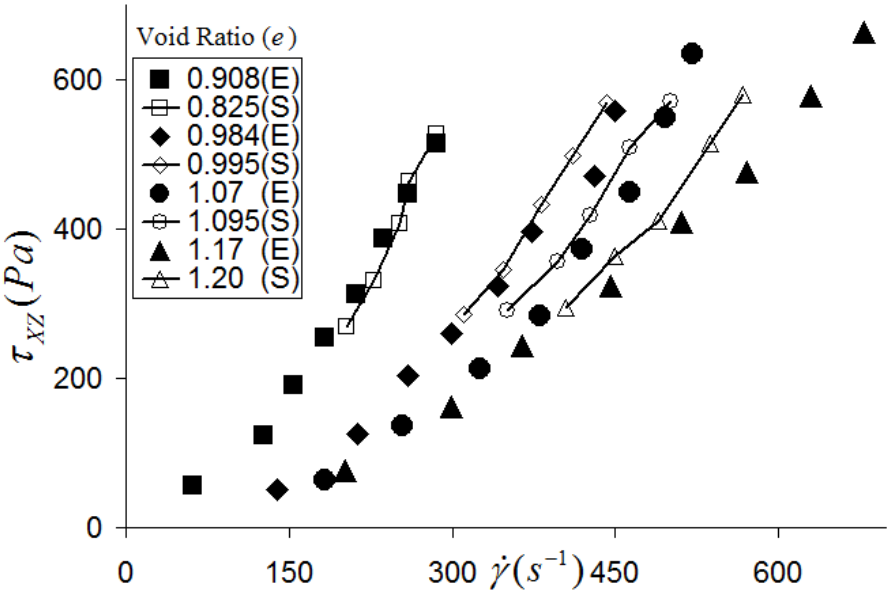

(b) Shear stress versus shear rate

FIGURE 3.4: Comparison of experimental and simulation results; simulation results are denoted by (S), while experimental results taken from Savage & Sayed (1984) are denoted by (E).[3]

[3] Copyright © 1984 Cambridge University Press. Reproduced with the permission of Cambridge University Press.

3.3 Ring Shear Simulation

3.3.1 Model Description

Ring shear simulations were conducted to investigate the effect of particle shape on flow behaviours. A ring shear experiment was modeled using PFC^{3D} Version 4.0, as shown in Figure 3.5.

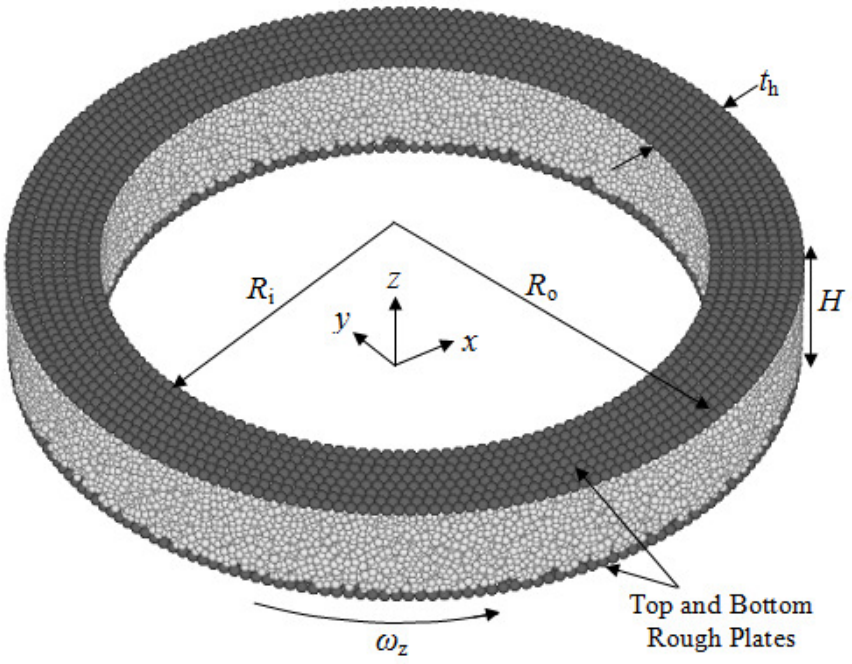

FIGURE 3.5: DEM model for ring shear experiment using PFC3D v. 4.00.

The ring shear was constructed from two concentric cylindrical vertical walls, which are frictionless, with top and bottom horizontal clumps acting as rough boundary plates. The applied vertical normal stress was kept constant during shearing by moving the top servo-controlled clump plate up and down in the vertical direction while the particles were sheared by rotating the bottom clump plate. The velocity at which the servo-controlled clump plate moved vertically was calculated at each time step using the following equation (modified from Campbell, 2005)

$$u_Z = f_S \cdot \omega_z \cdot R \cdot \min\left(\frac{\sigma_Z^m - \sigma_Z^a}{\sigma_Z^a}, \frac{\sigma_Z^m - \sigma_Z^a}{\left|\sigma_Z^m - \sigma_Z^a\right|} \right), \tag{3.7}$$

where σ_Z^a is the applied or prescribed vertical normal stress, $\sigma_Z^m = F_{SC} / A_h$ is the measured vertical normal stress at the servo-controlled clump plate for each time step, F_{SC} is the measured vertical normal force at the servo-controlled clump plate, A_h is the horizontal area of the servo-controlled clump plate, ω_z is the angular velocity of the bottom clump plate in the z direction, R is the average radius of the ring shear $\left(\frac{1}{2}\left(R_o + R_i\right)\right)$, and f_S is a coefficient determined to get the measured vertical normal stress at steady state close to the applied (or prescribed) vertical normal stress. Their difference is mostly less than 1%.

The ring shear simulations were conducted without gravity to eliminate the effect of heterogeneity in the simulations. Simulations were carried out on spherical particles with different average radii of the apparatus, sample heights, and thicknesses. The results are presented in Table 3.3. The particles had similar grain size distribution as the 1 mm mean diameter polystyrene beads used by Savage and Sayed (1984), but with different mean diameters of 1 cm and 0.5 cm. A general observation is that the results are affected for small sample heights (compare the shear stresses for cases 1, 4, 6; 2, 7, 9; and 5, 8), for small radii (compare the shear stresses for cases 5, 6, 7; 1, 2, 3), and for small thicknesses (compare the void ratios and the shear rates for cases 10 to 13). Based on these results, the average radius is selected as 30*d*, the sample height as 10*d* after consolidation, and the thickness as 8*d*. It is known that the thickness of an effective shearing zone in a granular layer is around 10*d*, where *d* is the mean particle diameter (Hanes & Inman, 1985a; Hanes & Inman, 1985b; Thompson & Grest, 1991).

The Savage number (Sa) in Table 3.3 is calculated as

$$Sa = \frac{\rho d^2 \dot{\gamma}^2}{\sigma_Z}. \tag{3.8}$$

TABLE 3.3: Ring shear simulations on spherical particles for different ring shear sizes.

Case	H_oxt_hxRxd (cm)	$\sigma_z(Pa)$	$\tau_{xz}(Pa)$	$\dot{\gamma}(s^{-1})$	e	H_s(cm)	Sa^{-1}
1	7.9x4x15x1	1290.2	512.96	29.83	0.922	8.3	13.2
2	7.98x4x25x1	1289.75	510.56	30.34	0.922	8.3	12.8
3	7.99x4x41.5x1	1290.41	510.42	31.16	0.923	8.3	12.1
4	9.9x4x15x1	1292.14	540.8	29.38	0.922	10.4	13.7
5	11.85x4x12x1	1293.05	559.59	28.74	0.928	12.5	14.3
6	11.88x4x15x1	1294.03	551.38	28.76	0.92	12.5	14.3
7	11.81x4x25x1	1293.28	548.76	29.41	0.92	12.5	13.7
8	14.33x4x12x1	1293.86	568.48	28.06	0.944	15.3	15.0
9	14.29x4x25x1	1294.87	556.11	28.44	0.915	15.1	14.6
10	4.87x2x15x0.5	149795	59902	639.6	0.918	5.19	13.4
11	4.77x3x15x0.5	149753	60182	656.3	0.869	5.07	12.7
12	4.74x4x15x0.5	149828	59808	665.1	0.845	5.01	12.4
13	4.73x5x15x0.5	149814	59729	670.5	0.829	4.97	12.2

Note: H_o refers to sample height after consolidation, H_s refers to sample height at steady state, t_h is thickness of ring cell, σ_z is the vertical normal stress, τ_{xz} is the shear stress, $\dot{\gamma}$ is the shear rate, e is the void ratio, and Sa^{-1} is the inverse of Savage number given in Eq. (3.8).

3.3.2 Procedures of Ring Shear Simulation

A total of 13,330 spherical particles (excluding boundary clumps) were generated at random locations, with sizes ranging from 4.1 mm to 5.5 mm (mean ~ 5 mm), keeping the grain size distribution curve shown in Figure 3.3. Identical initial

assembly (or initial random arrangement) of particles was generated for all simulation experiments in order to eliminate the effect of the initial condition in comparing the simulation results. To simulate angular particles, the spherical particles were replaced by angular particles of the same volume. The sample was then consolidated under a prescribed vertical normal stress and then sheared by gradually increasing the angular velocity to a prescribed value on the bottom clump plate. Shearing continued for a minimum of 2.0 seconds under the prescribed angular velocity until the flow reached the steady state condition.

3.3.3 Measurement of Flow Characteristics

Measurements in the ring shear simulations were taken in a similar way as for the actual ring shear experiments (Savage & Sayed, 1984). The void ratio was calculated by measuring the effective sample height ($H_d = H_s - d$) from the centre of the top clump plate to the centre of the bottom clump plate at steady state, while the shear stress was calculated by measuring the torque (T_z) on the top clump plate, and using

$$\tau_{xz} = \frac{3T_z}{2\pi\left(R_0^3 - R_i^3\right)}, \tag{3.9}$$

where R_i and R_0 are the inside and outside radii of the ring shear apparatus. Finally, the shear rate was calculated from

$$\dot{\gamma} = \frac{\omega_z \cdot R}{H_d}. \tag{3.10}$$

3.3.4 Model Calibration

For the purpose of the calibration of the numerical model, the ring shear experiments conducted by Savage and Sayed (1984) on 1 mm mean diameter spherical polystyrene beads (Savage & Sayed, 1984, Figs. 8a & 8b) were first simulated. The DEM parameters presented in Table 3.1 were used for a ring shear model. The results from the numerical simulations are compared with the physical experiments as shown in Table 3.4. Since higher stresses and larger particles are of interest here, the simulations were conducted using 5 mm mean diameter particles at a vertical normal stress of 150 kPa. The comparison was made based on the Savage number. The Savage number is constant for a constant void ratio in collisional flow.

As in the case of the plane shear model (see Sec. 3.2.4), the ring shear model also approximated the experimental results at a void ratio of 0.908 by the simulations at a void ratio of 0.84. The remaining experimental results were approximated by the simulations at similar void ratios.

TABLE 3.4: Comparison of ring shear simulations with laboratory experiments (Savage & Sayed, 1984, Figs. 8a & 8b) on spherical particles.

Case	d (mm)	$\sigma_z\,(kPa)$	$\tau_{xz}\,(kPa)$	$\dot{\gamma}d\,(m/s)$	e	Sa^{-1}	e*	Sa^{-1}*
1	5	149.75	70.76	5.97	1.2	3.83	1.17	2.5 – 3.4
2	5	149.74	69.57	5.69	1.07	4.22	1.07	4.1 – 4.6
3	5	149.70	67.17	5.01	0.96	5.45	0.984	5.5 – 6.5
4	5	149.83	59.81	3.32	0.84	12.37	0.908	15 – 18

*Range of values from the experiments of Savage and Sayed (1984)

A PFC3D code written for ring shear simulation is presented in Appendix A.4.

3.4 Inclined Flow Simulation

3.4.1 Model Description

Inclined flow simulations were also conducted using PFC3D v.4.0 for 4 mm and 40 mm mean diameter particles. The DEM particles had properties presented in Table 3.1 with similar grain size distribution as the polystyrene beads used by Savage and Sayed (1984). The 3D inclined flow DEM model is presented in Figure 3.6. The sheared particles are bounded by periodic boundaries on the vertical sides and by the boundary particles arranged in a rectangular array at the base. The inclined flow is modeled by assigning acceleration of gravity of $g\sin\theta$ and $-g\cos\theta$ in the x- and z- directions, respectively, instead of tilting the base plane by an angle of θ.

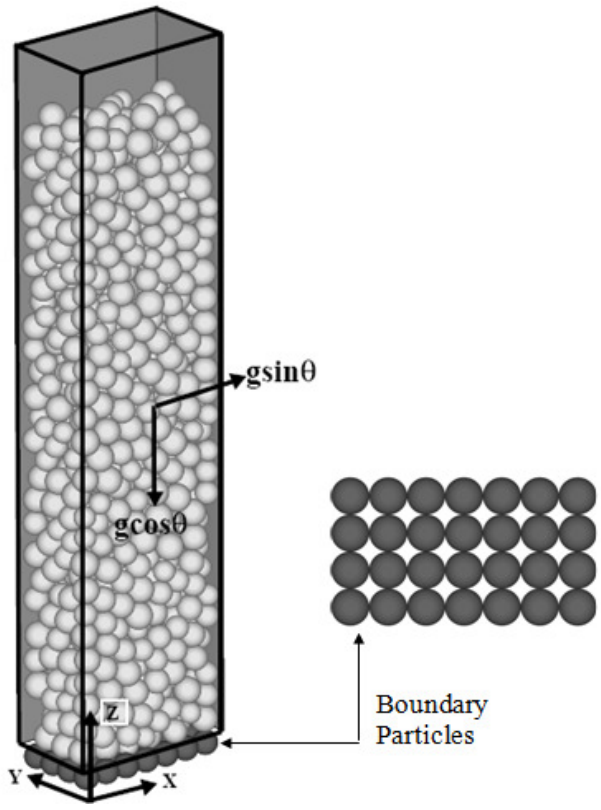

FIGURE 3.6: 3D Inclined flow DEM model using PFC3D v. 4.00.

3.4.2 Procedures of Inclined Flow Simulation

Particles were generated randomly in a 4*d* wide (*y*- direction) by 7*d* long (*x*-direction) model which was bounded by vertical walls. The boundary particles, each having size *d*, were arranged in a rectangular array. The *x*- and *z*- gravity forces were then assigned and the particle assembly (sample) was consolidated under the force of gravity. Finally, the sample was allowed to shear under the force of gravity by replacing the vertical walls with periodic boundaries. The shearing was continued until the flow reached a steady state condition.

3.4.3 Measurement of Flow Characteristics

Profiles of solid volume fraction (or void ratio), flow velocity, and granular temperature were measured by dividing the inclined flow into layers of equal thickness, d_{max} (the diameter of the largest particle in the simulation), starting from the bottom but excluding the boundary particles (Lu & Hsiau, 2005; Lan & Rosato, 1995). Flow velocity and granular temperatures were measured for each layer using Eq. (3.6a) to Eq. (3.6d). Solid volume fraction was measured for each layer using Eq. (3.11) as

$$\left\langle v_s^L \right\rangle = \frac{\sum_t \sum_b V_{tb}^L}{N_t \cdot 4d \cdot 7d \cdot d_{\max}}, \tag{3.11}$$

where $\left\langle v_s^L \right\rangle$ is the average solid volume fraction of layer *L*, V_{tb}^L is the portion of the volume of particle *b* occupying layer *L* at time step *t*, and N_t is the total number of time steps at which the volume summations were made for layer *L*. The volumes of particles were sampled at the interval of 10 time steps after the flow reached the steady state condition.

A PFC3D code written for inclined flow simulation is presented in Appendices A.2 and A.3.

CHAPTER FOUR

RELEVANCE OF COLLISIONAL MECHANISM

4.1 Introduction

As discussed in Chapter 2, the behaviour of dry granular flow has been studied extensively using shear and flume experiments. The investigations have revealed a rate-dependent collisional flow mechanism at high shear rate and high void ratio in addition to the well-known rate-independent frictional mechanism at low shear rate and low void ratio. This leads to the classification of granular flows into frictional, collisional, and intermediate regimes based on the flow mechanisms.

However, the physical experiments were conducted with small size particles and showed rate-dependent collisional flow behaviour only at low stresses. Attempts to observe this behavior at high stresses were not successful. (Detailed discussions of the experiments in the literature are presented in Chapter 2.) As none of the experiments showed rate-dependent flow behavior at high stresses, it was concluded that the rate effect may be limited to low stresses and the collisional mechanism discussed above may not be applicable to geotechnical problems such as debris flows and avalanches. In this regard, many state-of-the-art models for flow type landslide analysis (such as MADFLOW, TITAN2D, DAN3D and RASH3D) consider the basal friction angle as the main resistance parameter. Voellmy model, which accounts for all other possible sources of velocity dependent effects in addition to the frictional resistance, is also used for cases where the frictional model does not provide a good prediction. For instance, the Thurwieser rock avalanche is an example in this case (Pirulli, 2008).

It is postulated in this research that the lack of a shear rate effect at high stresses may be due to the use of small size particles (< 2 mm) in the experiments.

Although the particles were sheared at high rates (which occurs in actual flow slides), the rates were not sufficient to initiate the collisional mechanism for small particles at high stress. As observed in Bagnold's scaling, the stresses in collisional flow are proportional to the square of the shear rate and the square of the particle diameter. Thus, the particle diameter should be large enough in order to produce rate-dependent behaviour at high stress even if the material is sheared at high rate.

Therefore, the main objective of this chapter is to demonstrate the occurrence and relevance of rate-dependent collisional flow behaviour at high stresses for large particles. Using DEM simulations of plane shear flows, the ring shear experiments of Savage and Sayed (1984) on 1 mm mean diameter spherical polystyrene beads are extended to higher stresses for both small and large particles. Comparisons are then made between simulations of small and large particles at high stresses to show how the rate-dependent mechanism will likely occur in practice with the increase of particle diameter. Its relevance in debris flows and avalanches are further investigated by assessing a range of values of vertical stress, flow velocity, and particle diameter required for rate-dependent flows.

4.2 Existence of Collisional Mechanism at High Stresses

Physical shear experiments on large size particles require a much larger shear apparatus than normally available. Therefore, numerical experiments were used in this research. The DEM plane shear model presented in Sec. 3.2 was calibrated by simulating the annular shear experiments of Savage and Sayed (1984) at low stresses before conducting simulation experiments on large size particles at high stresses.

The shearing experiments of Savage and Sayed (1984) are extended to higher stresses for 4 cm mean diameter particles using the calibrated DEM model, with

the results presented in Figure 4.1. They show that stresses continue to depend on the square of the shear rate and particle diameter exhibiting collisional flow behaviour for void ratios equal to 1.2, 1.095, 0.995, and 0.825. The additional simulation experiments conducted at a lower void ratio of 0.7 also show the dependency of stresses on shear rate, even though it is weak compared to the cases of higher void ratios. The less dependency on shear rate is due to the contribution of rate-independent frictional stress at lower void ratios, which changes the flow to intermediate flow. Therefore, the existence of a rate-dependent flow, either collisional or intermediate, at higher stresses is evident here.

Similar variations of stresses with shear rate, as shown in Figure 4.1, were also observed by others (e.g., Campbell, 2002; Ji & Shen, 2005; Yan & Ji, 2009). The results are used here to assess the relevance of rate-dependent behaviour in actual debris flows and avalanches by observing the range of stresses, flow rate, and void ratio.

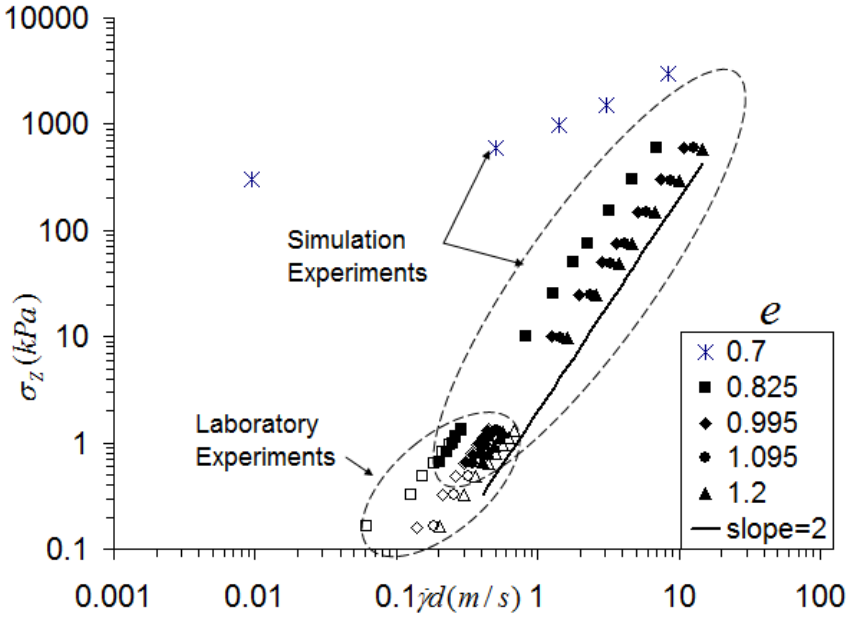

(a) Vertical normal stress versus characteristic mean shear velocity in log scale

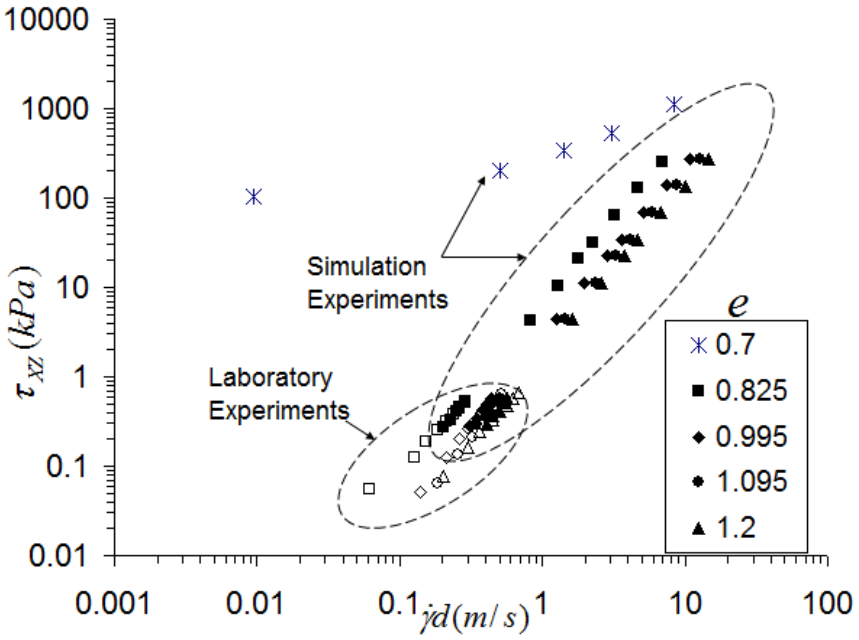

(b) Shear stress versus characteristic mean shear velocity in log scale

FIGURE 4.1: Variation of stresses with the characteristic mean shear velocity; Open symbols represent laboratory experiments from Savage and Sayed (1984)[4]. The solid line in (a) has slope of 1H:2V.

4.3 Relevance of Collisional Mechanism in Flow Type Landslides

In general, the occurrence/relevance of rate-dependent flow behaviour at a given stress or void ratio depends on the particles inertia, i.e., the mass of particles (diameter and density of particles) and the rate of flow.

Small particles require a high flow rate to achieve a given rate-dependent flow state. For example, at the pure collisional flow state of $(e \approx 0.995, \sigma_z \approx 965Pa)$ shown in cases A to C of Table 4.1, 1 mm mean diameter particles require a high shear rate of 373.2 s^{-1} compared to 4 cm mean diameter particles, which require a shear rate of only 9.537 s^{-1}. The required flow rate for small particles will increase even more to achieve a rate-dependent flow state at higher stress. In the above

[4] Copyright © 1984 Cambridge University Press. Reproduced with the permission of Cambridge University Press.

example, for instance, the 1 mm mean diameter particles require a very high shear rate of 1998 s^{-1} to achieve a collisional flow state of the same void ratio but with a higher stress of ~ 25 kPa, as shown in case D of Table 4.1. The required flow rate is much higher than the anticipated values in actual flow type landslides and may explain why the shear rate effect was not observed by Fukuoka and Sassa (1991) and others, such as Hungr and Morgenstern (1984), Kaibori (1986), and Vibert et al. (1989). They used small diameter particles (< 2 mm) in their experiments to observe the shear rate effect at high stresses up to 375 kPa.

In order to see the rate-dependent behaviour in their range of stresses, larger particles should be used. In case E of Table 4.1, for example, the required shear rate decreases to 50 s^{-1} with the increase of the mean diameter to 4 cm, in order to achieve the above-mentioned high stress flow state of $(e \approx 0.995, \sigma_z \approx 25kPa)$. It should be noted that the density of the polystyrene beads $(\rho = 1095kg/m^3)$ is much less than the density of actual soil material $(\rho \approx 2650kg/m^3)$. Case F of Table 4.1 shows that, to achieve the above-mentioned high stress flow state, the required flow rate will further reduce if the actual soil particle density is used.

TABLE 4.1: Comparison of experiments and simulations for polystyrene beads

Case	e	$\sigma_z\,(Pa)$	d (mm)	$\dot{\gamma}\,(s^{-1})$	$\rho\,(kg/m^3)$	Sa^{-1}	$\dot{\gamma}d\,(mm/s)$
A	0.984	966	1	373.2	1095	6.334	373
B	0.999	950	1	380.1	1095	6.008	380
C	0.999	984	40	9.537	1095	6.175	381
D	0.993	24120	1	1998	1095	5.518	1998
E	0.985	24906	40	49.52	1095	5.797	1980
F	0.988	25115	40	31.97	2650	5.795	1278

Case A – based on physical experiment by Savage & Sayed (1984), Cases B-F are based on PFC simulations.

The relevance of the rate-dependent flow behaviour in actual flow landslides can be studied in more detail by examining the depths of flow, velocities, and void ratios required to produce the rate effect. In this section, the relevance of rate-dependent behaviour is assessed in debris, rock, and snow avalanches flowing at a void ratio of 0.995.

The simulation results in $\log\sigma_z - \log(\dot{\gamma}d)$ plot are changed to $\log H - \log(\overline{u}d)$ plot, as shown in Figure 4.2, to assess the ranges of flow depths and velocities at a void ratio of 0.995. This is accomplished as follows.

The depth variations of velocity and density in inclined plane flow have been well studied using laboratory flume experiments (e.g., Johnson, 1987; Drake, 1988; Ahn, 1989; Azanza et al., 1999; Ancey, 2001) and simulation experiments (e.g., Silbert et al., 2001; Silbert et al., 2002; Silbert et al., 2003; GDR MiDi, 2004; Mitarai & Nakanishi, 2005; Delannay et al., 2007). For dense granular flows, it is reasonable to assume a uniform density profile and a linear velocity variation with depth. Hence, the flow depth (H) can be calculated from the vertical-normal stress using

$$\sigma_z = \rho\overline{v}_s gH \ , \tag{4.1}$$

where $\overline{v}_s$ is the depth-average solid volume fraction. On the other hand, the depth-average velocity $(\overline{u})$ which acts at the mid-depth of the flow can be determined from the shear rate using

$$\dot{\gamma} = \frac{\overline{u}}{(H/2)} . \tag{4.2}$$

The maximum mean velocities in debris and rock avalanches could reach up to 40 m/s and 100 m/s, respectively (Pierson & Costa, 1987; Hungr et al., 2001), while for a dense snow avalanche it is estimated to be 50 m/s (Vilajosana et al., 2007).

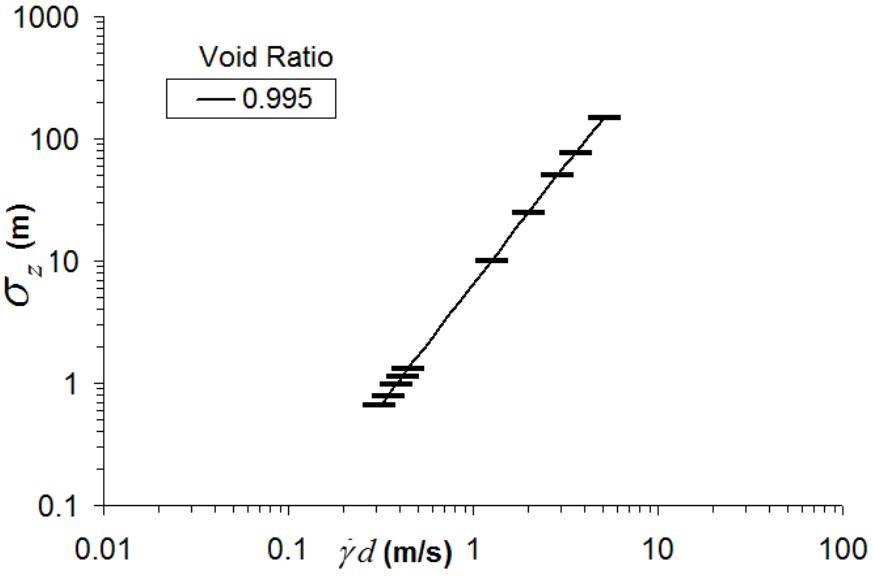

(a)

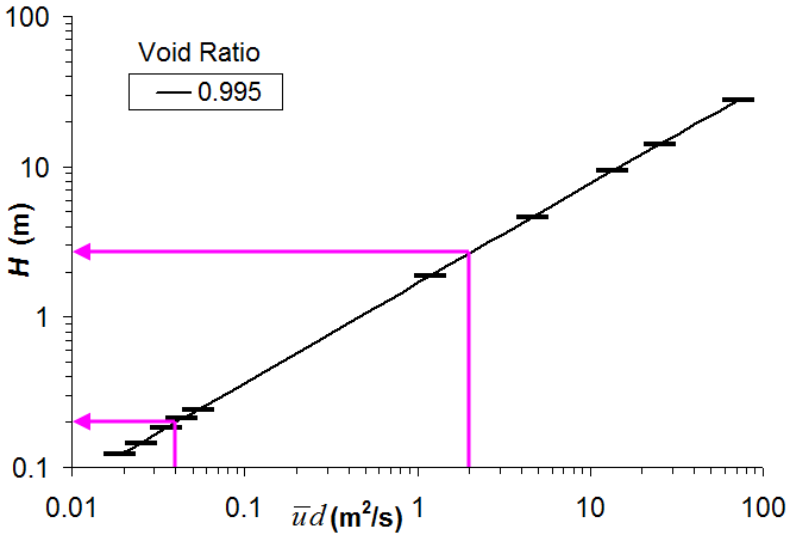

(b)

FIGURE 4.2: Simulation results at a void ratio of 0.995; (a) vertical stress versus characteristic mean-shear velocity, (b) flow depth versus flow velocity times mean diameter

If we consider avalanches with rounded granular materials having similar properties as the polystyrene beads, Figure 4.2 (b) can be used to estimate the flow depths of avalanches flowing at a void ratio of 0.995 for different mean flow velocities. For example, a 5 cm mean diameter rock avalanche flowing at 40 m/s will attain a flow thickness of ~ 3 m, as shown in Figure 4.2 (b). On the other hand, a snow avalanche with 1 mm size particles flowing at the same mean velocity will exhibit flow thickness of only ~ 20 cm, as shown in Figure 4.2 (b). If this snow avalanche is required to flow at higher thickness, the velocity must increase. However, the average flow velocity of snow avalanches is about 40 m/s.

The above examples demonstrate that rate-dependent behaviour is more relevant in avalanches involving large particles. Coarse avalanches may undergo the collisional flow mechanism under reasonable flow depths. With decreased particle size, however, smaller flow depth is required to achieve rate-dependent flow states at a similar void ratio. For very small particles, such as 1 mm size particles as shown in the above example, the required flow depths will be too small to occur in practice, which suggests that the rate-dependent flow may not be relevant for such small granular materials.

CHAPTER FIVE

EXTENDED CRITICAL-STATE FRAMEWORK

5.1 Introduction

In Critical State Soil Mechanics (Schofield & Wroth, 1968; Wood, 1990), quasi-static deformation of soils is captured by a framework which is based on the critical state concept. The critical state framework uses void ratio, mean effective stress and deviatoric stress space to define the state of a material. When it was proposed in the 1960, it was the first model that integrated volume change into the calculation of shear deformation and failure.

The concept of critical void ratio was first introduced by Casagrande (1936). In drained direct shear tests, he observed that dense sands dilated with an increase in shear deformation and the shear strength decreased after reaching a peak value. On the other hand loose sands contracted and the shear strength continued to increase until the shear strain was very large. Both loose and dense sands reached the same constant void ratio and shear strength values at large deformation if they were consolidated under the same initial confining pressure. This final constant void ratio was called the "critical void ratio", and the corresponding state as the "critical state". In critical state, soil continues to deform under constant void ratio, constant mean effective stress, and constant deviatoric stress and a unique relationship exists among these variables.

The "critical state line" of a soil refers to the critical void ratios, mean effective stresses, and shear strengths attained by a material at its critical states. It can be presented in the void ratio (e) – mean effective stress (p) plane and in the deviatoric stress (q) – mean effective stress (p) plane, which constitute the frameworks of critical state soil mechanics. The schematic representation of a

critical state line is shown in Figure 5.1. The equations of the critical state line (CSL) in these two planes are given by

$$e = \Gamma - \lambda \log p \qquad \text{(for CSL in } e\text{-}p \text{ plane)}, \tag{5.1}$$

$$q = Mp \qquad \text{(for CSL in } q\text{-}p \text{ plane)}. \tag{5.2}$$

The constants M, Γ, and λ represent basic soil properties.

At critical state, a soil material continues to deform by transforming the mechanical energy to heat energy by friction. If Figure 5.1(b) is re-plotted in a shear strength versus vertical normal stress plane, the slope of the critical state line will give the internal friction angle of the material at critical state. This critical state friction angle is a material property which can be determined from shear experiments and it is a key input in the constitutive model.

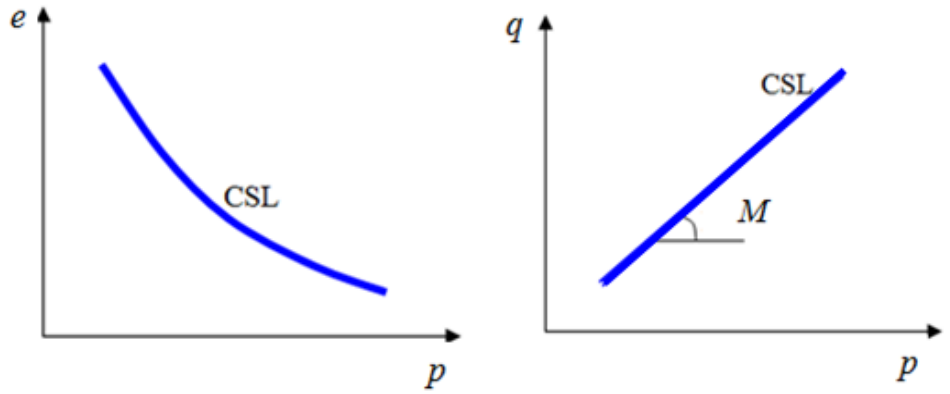

(a) (b)

FIGURE 5.1: Schematic representation of critical state line: (a) in *e-p* plane, (b) in *q-p* plane.

The traditional critical state concept, its framework and models are developed for quasi-static deformation. For granular material under rapid moving conditions, several experiments (e.g., Savage & Sayed, 1984) and simulations (e.g. Campbell, 2005) have suggested, directly or indirectly, that the critical state depends on the

rate of shearing of the material. Hence, the shear rate should be included in addition to the void ratio and stresses in defining the critical state.

When granular material is rapidly sheared, the momentum of the particles will have additional contribution to the shearing resistance of the material. Since momentum is related to the relative velocities of the particles, the shearing resistance then depends on the rate of shearing. The critical state concept and framework can be extended to include the rate of shearing, which will be referred to as the *extended critical state*, for a rapidly flowing granular material.

In the following sections, the extended critical state framework is reviewed by including an additional shear rate variable called the characteristic mean shear velocity $\dot{\gamma}d$ (Lun et al., 1984). Although different parts of the extended framework have been published in the literature, a concise summary of the full extended framework is presented in this chapter based on the results of the numerical simulation experiments conducted in this research. It should be noted that the effect of shear rate was investigated in detail mainly for spherical particles. Hence, the extended critical state framework reflects only spherical granular particle behaviour. In the last section of this chapter, the effect of angularity on the extended framework is discussed.

The extended critical state frame work will be used to evaluate the existing and proposed unified constitutive models in Chapter 6.

5.2 The Extended Critical State Framework

5.2.1 Void Ratio – Vertical Normal Stress Plane

In addition to the critical state line, a series of other state lines were plotted by Campbell (2005) as functions of the dimensionless stiffness (inverse of dimensionless shear rates) in the solid fraction versus the dimensionless vertical

normal stress. These state lines are also presented in Figure 5.2 based on the current simulation results in the void ratio versus the vertical normal stress plane. The effect of shear rate can be observed by comparing Figure 5.1(a) with Figure 5.2(a). The comparison reveals the series of critical state lines as functions of the characteristic mean shear velocity. The classical critical state line in the CSSM belongs to the quasi-static soil deformation and is found to be the lower boundary state line. The series of lines corresponding to different characteristic velocities are referred here as *supercritical state lines*.

The relationship between critical void ratio and vertical normal stress is well established in CSSM for identifying the contractive (wet) and dilative (dry) behaviours (states) of soils in assessing flow liquefaction. Similarly, the extended framework shown in Figure 5.2 is useful for granular flow classification to differentiate quasi-static, collisional, and intermediate flow regimes. The quasi-static flow regime is captured by the critical state line. On the other hand, the supercritical state lines consist of the intermediate (or transitional) and collisional flow regimes. The boundary between these regimes can be identified by first predicting the collisional regimes using the kinetic theory of granular flows (KTGF - dashed, blue lines in Figure 5.2b), and then by drawing a boundary line (CIBL) connecting the points at which the KTGF lines start to deviate from the numerical simulation experiments (dotted, red line) as shown in Figure 5.2(b). It is because the KTGF assumes collisional state even when in the actual case the particles start to develop frictional/sliding contacts below the CIBL. This results in the discrepancy between the KTGF line and the response from numerical experiment.

For quasi-static deformation, the critical state line is usually approximated by a straight line in the $e - \log \sigma_z$ plot, whereas the supercritical state lines can be represented by two curves that meet around the collisional-intermediate boundary line (CIBL). This line would have a general equation of the form similar to the critical state line equation given in Eq. (5.1) except for having a positive slope

$$e = \Omega + \kappa \log \sigma_z , \tag{5.3}$$

where Ω is the void ratio intercept at $\sigma_Z = 1Pa$, and κ is the slope of the line. The values of Ω and κ are estimated to be 0.85 and 0.005, respectively, in this case from Figure 5.2(b). The parameters of the critical state line, Γ and λ, are also estimated to be 0.85 and 0.027, respectively, by fitting a straight line through the critical state points.

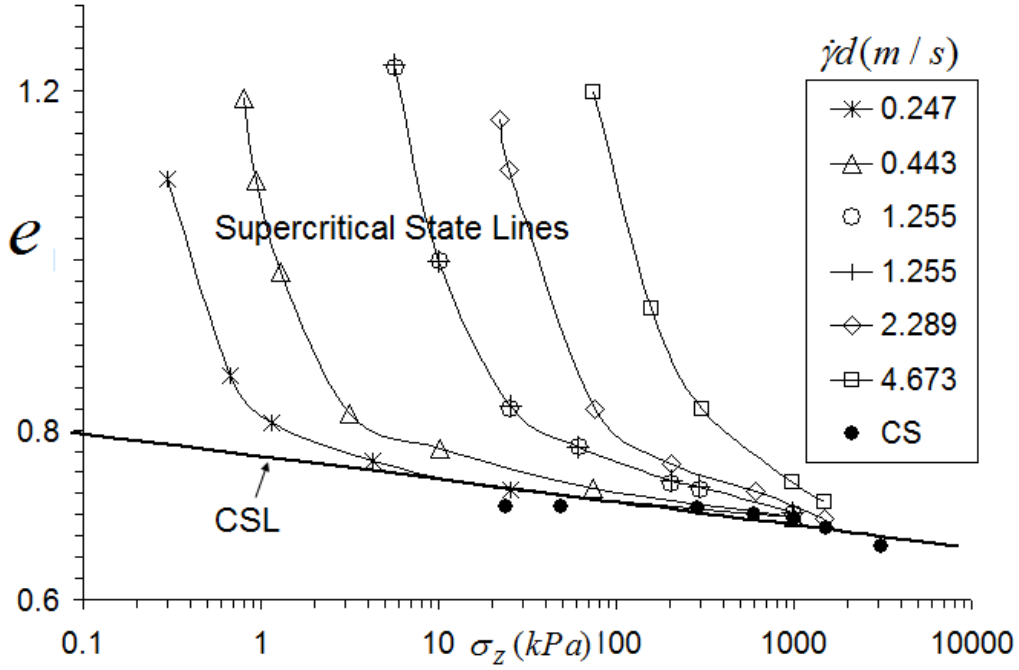

(a)

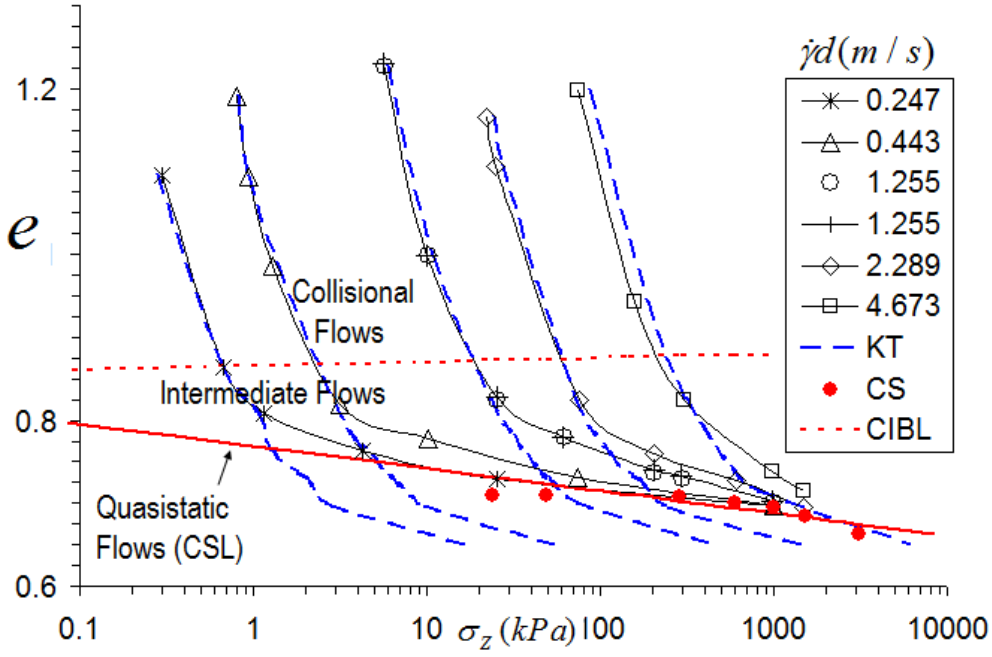

(b)

FIGURE 5.2: Void ratio versus vertical normal stress: (a) critical and supercritical state lines, (b) kinetic theory prediction and flow classification. + are obtained using 1 cm particles while the remaining symbols represent data obtained from 4 cm particles, Kinetic Theory (KT) is based on Lun et al. (1984) equation using $\nu_s^m = 0.61$ and $\varepsilon = 0.81$ (ε of particles was 0.75 in the simulation experiments), CS is the critical state, CSL is the critical state line, and CIBL is collisional-intermediate boundary line.

5.2.2 Shear Stress – Vertical Normal Stress Plane

The supercritical state lines can be plotted as shear stress versus vertical normal stress as shown in Figure 5.3. The regions 'b' and 'c' in Figure 5.3(a) are enlarged and shown in Figures 5.3(b) & (c), respectively.

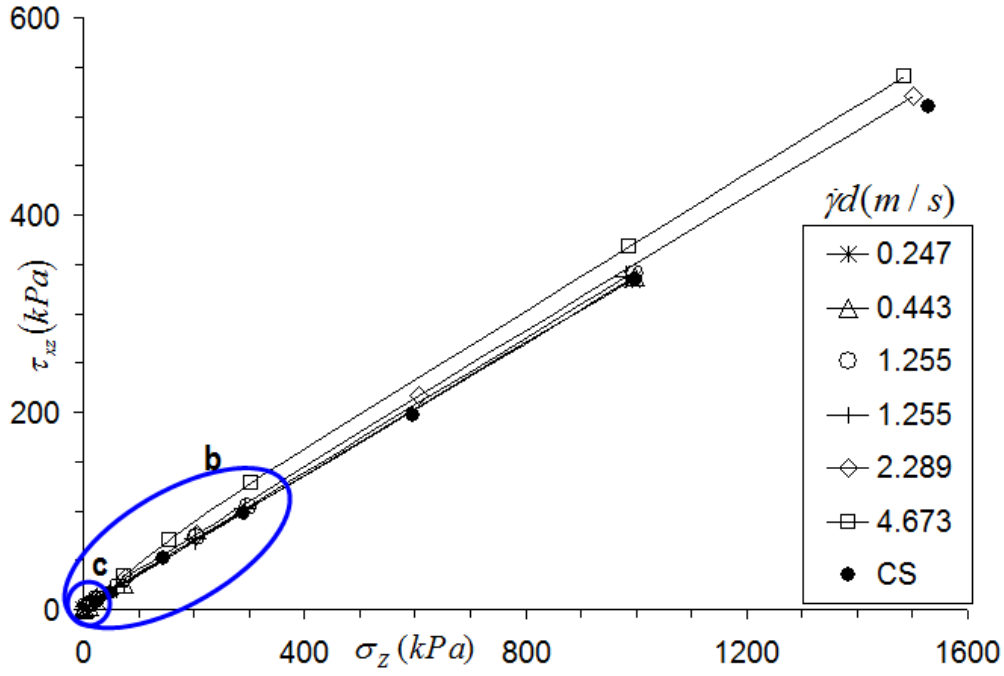
600
400
200
0
$\tau_{xz}(kPa)$
b
c
0
400
$\sigma_z(kPa)$
800
1200
1600
$\dot{\gamma}d(m/s)$
0.247
0.443
1.255
1.255
2.289
4.673
CS

(a)

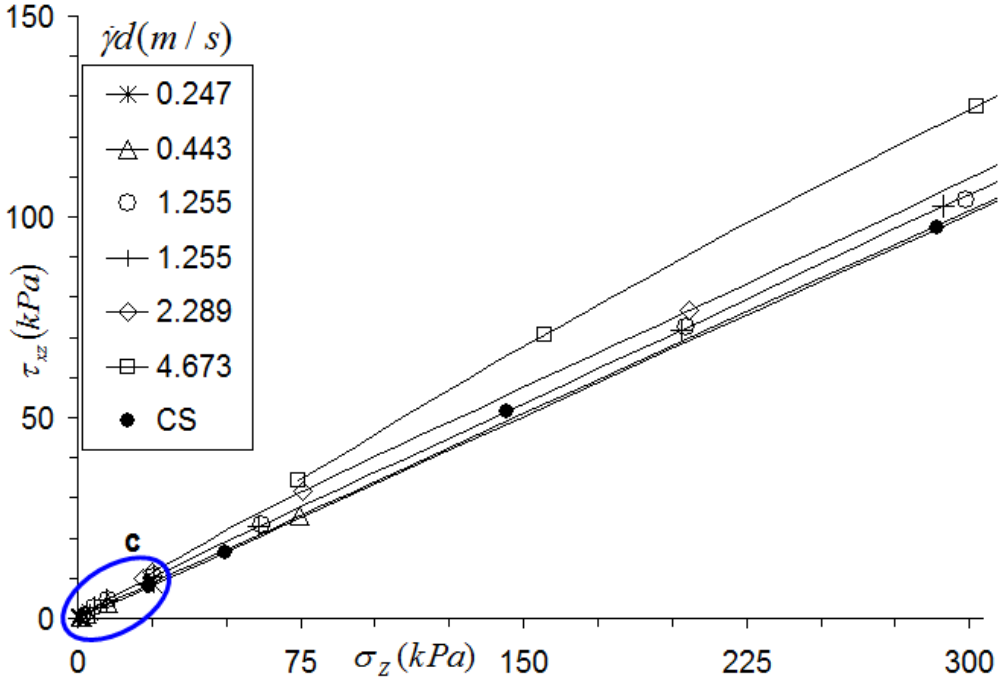
150
100
50
0
$\tau_{xz}(kPa)$
c
0
75
$\sigma_z(kPa)$
150
225
300
$\dot{\gamma}d(m/s)$
0.247
0.443
1.255
1.255
2.289
4.673
CS

(b)

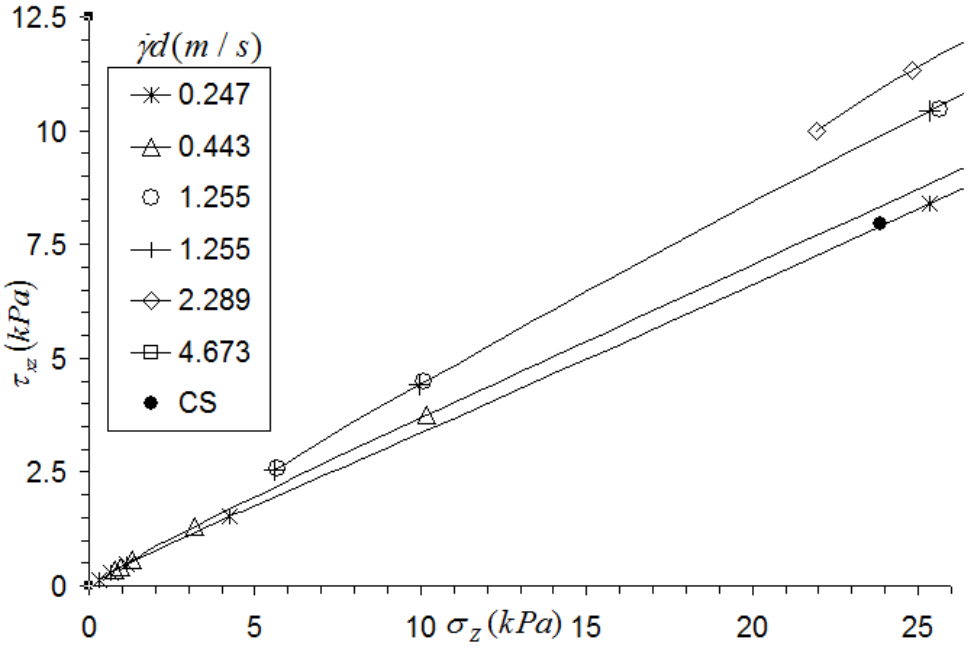

(c)

FIGURE 5.3: (a) Shear stress versus vertical normal stress, (b) the enlarged view of region 'b', (c) the enlarged view of region 'c'.

The series of the state lines are also observed in the above framework as functions of the characteristic mean shear velocity, and the critical state line defines the lower flowing state boundary, as shown in Figure 5.3(a). At constant vertical normal stress, the shear stress or friction angle increases with the characteristic mean shear velocity. The increasing trend of the friction angle is more clearly seen in the friction coefficient versus the characteristic mean shear velocity plot in Figure 5.4(a).

The critical state friction angle can be determined from the slope of the CSL which is approximated by a straight line in the shear stress versus vertical normal stress plot. Conversely, the supercritical state lines are convex with decreasing slopes (or decreasing friction coefficients) as the vertical normal stress increases (see Figure 5.3). In order to clearly see this variation, the friction coefficients are plotted against the vertical normal stresses for different characteristic velocities as shown in Figure 5.4(b). The friction coefficients decrease with increase in the

vertical normal stress except at critical states, where they are more or less constant and attained the lowest value.

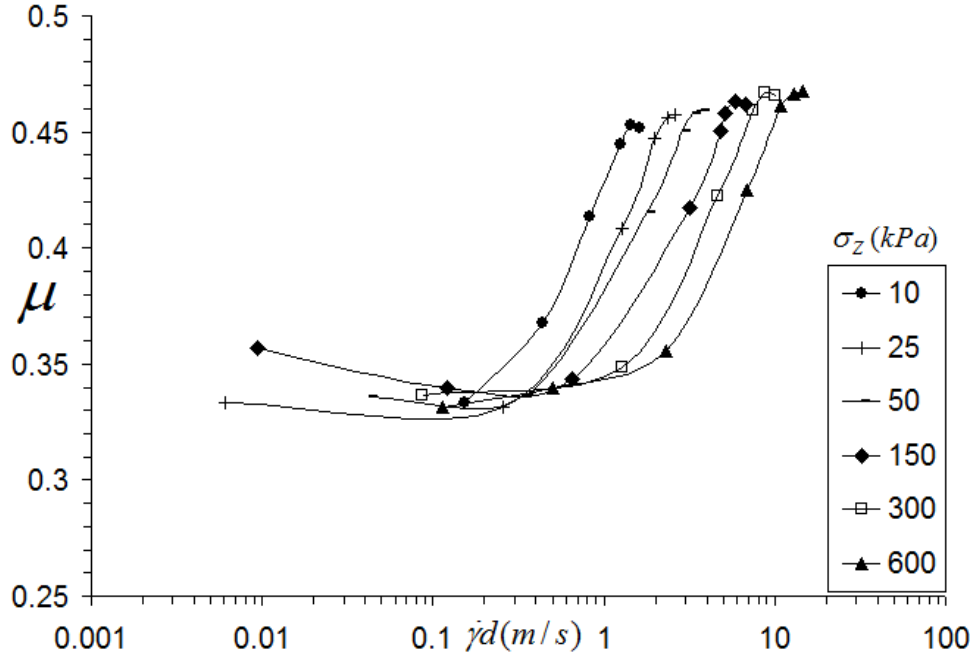

(a)

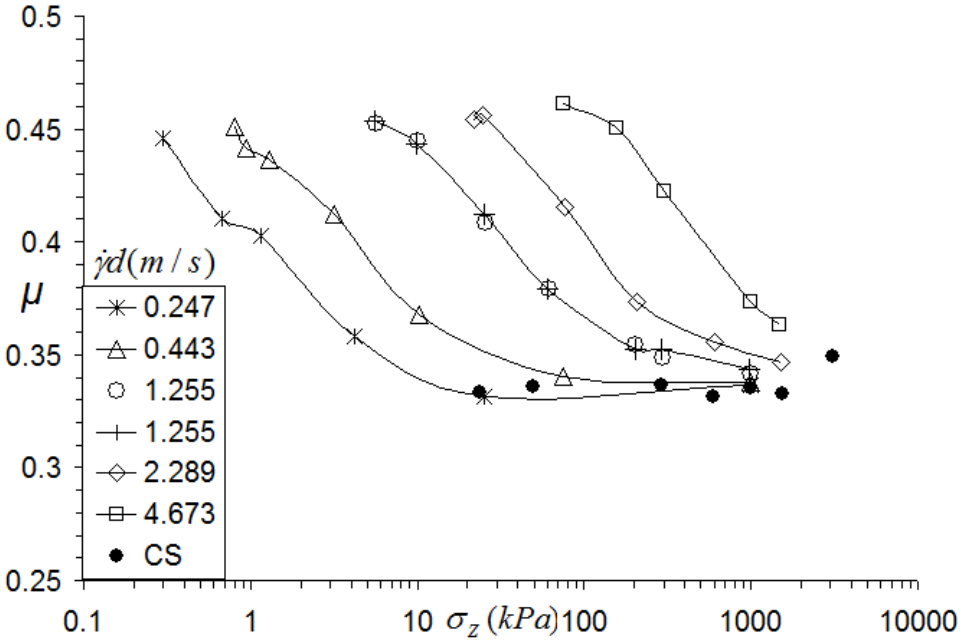

(b)

FIGURE 5.4: Variation of friction coefficient with (a) the characteristic mean shear velocity (b) the vertical stress

The variations of the friction coefficient with respect to the changes in vertical normal stress and characteristic mean shear velocity can be expressed using a single dimensionless variable I, $I = \dot{\gamma} d\sqrt{\rho/\sigma_z}$, as proposed by Da Cruz et al. (2005), see Figure 5.5. The friction coefficient increases from its minimum value μ_{cs} at quasi-static state to its maximum value μ_c at collisional state with the increase of I.

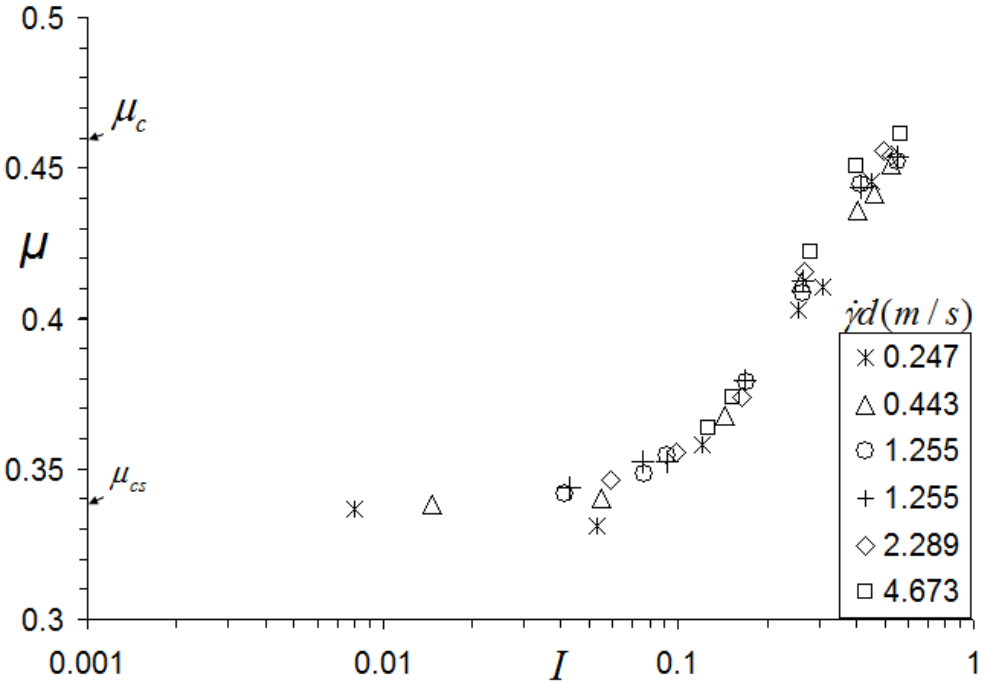

FIGURE 5.5: Friction coefficient versus the dimensionless variable I.

5.2.3 Void Ratio - Granular Temperature Plane

At high void ratios and low stresses, granular material may flow in a collisional state. This process has been studied by adopting a granular kinetic theory based on the kinetic theory of gases (e.g., Lun et al., 1984). In granular mechanics, the granular temperature (T) is a key variable which is introduced to measure the energy state of the material. In pure collisional flow, T is related to the characteristic mean shear velocity and void ratio as

$$T = f(e,\varepsilon)\cdot(\dot{\gamma}d)^2, \tag{5.4}$$

where $f(e,\varepsilon)$ is a function of the void ratio and the restitution coefficient of particles ε.

Since the extended critical state framework comprises the rate-dependent collisional and intermediate regimes, an additional plane is required to include granular temperature in the extended framework. The variation of the granular temperature with respect to void ratio is presented in Figure 5.6 for different characteristic mean shear velocities. It is observed that for a given characteristic mean shear velocity, the granular temperature is more or less constant in the collisional regime for void ratios less than 1.2 (where the simulation experiments were conducted) but increases with the decrease of void ratio in the intermediate regime. Similar variations in the granular temperature were also reported by Lois et al. (2005), Da Cruz et al. (2005), Kumaran (2009), and Reddy and Kumaran (2010). Da Cruz et al. (2005) obtained an increase in the dimensionless fluctuation velocity $(u_x' / \dot{\gamma}d)$ with a decrease in the dimensionless variable I of the intermediate flow regime. He also found that I decreases with decrease in the void ratio in the intermediate regime.

For high void ratios in the collisional regime, Lun et al. 1984 showed (using the kinetic theory) that the granular temperature starts to increase with the increase of void ratio due to the contribution of the kinetic motion of the particles to the fluctuation energy of the material. However, it is considered here that the granular temperature is approximately constant in the collisional flow regime for the range of void ratios that are commonly encountered in flow type landslides.

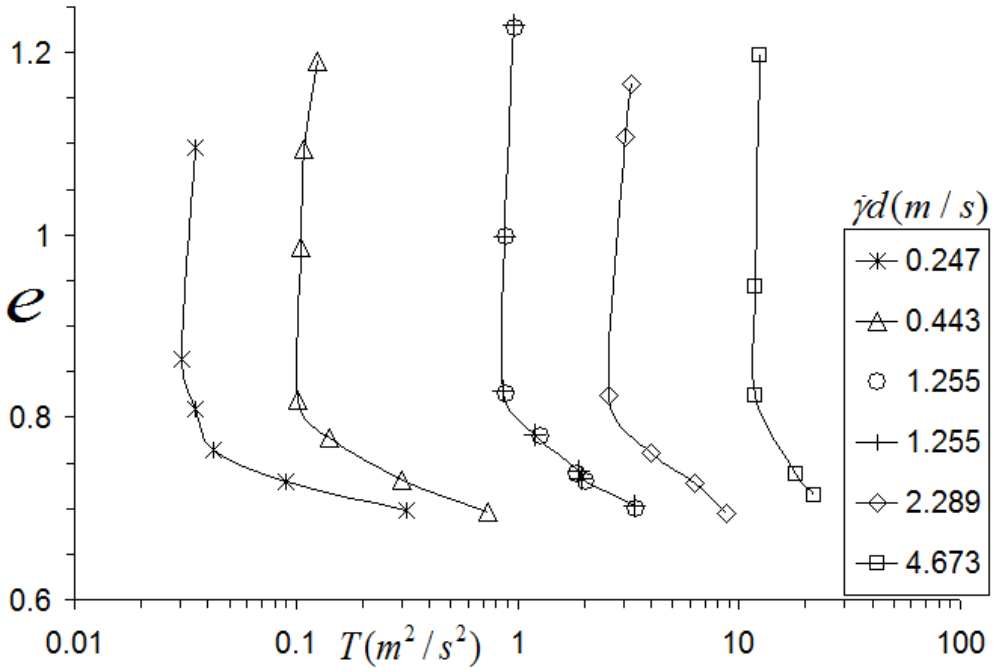

FIGURE 5.6: Variation of granular temperature with void ratio.

5.3 Effect of Particle Shape on Extended Critical State Framework

As presented in the previous sections, the flowing rate of spherical granular particles is the key variable in extending the critical state framework to capture rapid granular flow states (i.e., collisional and intermediate flow states). The stresses and friction coefficient have been observed to increase with the characteristic mean shear velocity, as shown in Figure 5.2(a) and 5.4(a). The pioneering work of Bagnold (1954) suggested that, at a constant void ratio, stresses increase quadratically with the characteristic velocity in the collisional regime. Laboratory ring shear experiments of Savage and Sayed (1984) also supported Bagnold's (1954) results at a high void ratio (in collisional flow regimes); however, their results also showed that the stresses increase weakly with the characteristic velocity (to the power of characteristic velocity less than 2) at a low void ratio (in an intermediate flow regime) due to the contribution of

stresses from the rate-independent frictional mechanism. As presented in Chapter 2, several other shear and flume experiments are also available to show the increase in stresses with the shearing rate for spherical particles in both intermediate and collisional flow regimes.

On the other hand, there are some shear experiments on non-spherical particles that show inverse relationship between stresses and shear rate. For example, Martino and Davies (2003) conducted shear experiments using an inverted cone and plate rheometer on 3.5 mm wide and 4 mm long cylindrical PVC granules under low stresses (< 1 kPa) and shear rates (< 35 s^{-1}). The results showed a decrease in shear stress with an increase in shear rate when the flow progressed from a quasi-static to an intermediate flow regime under a constant vertical normal stress condition. The recent experimental work conducted by Lu et al. (2007) also revealed an inverse relationship of void ratio (in stress controlled condition) and stress (in volume controlled condition) with shear rate for angular particles for intermediate flow. The tests were conducted for small diameter (< 2mm) angular and spherical quartz sand under low stresses (< 15 kPa) using a cylindrical shear cell.

In the subsequent sections, the effect of the decrease in resistance due to an increase in the shearing rate for non-spherical particles will be investigated at high stresses based on DEM simulation of the ring shear experiments. The effect of angularity on the extended critical state framework will also be discussed.

5.3.1 Behaviour of Non-Spherical Particles at High Stress

Angular particles of the type shown in Figure 5.7 were used to study the effect of angularity on granular flow behaviour. The angular particle was created by clumping three spherical particles together with their centroids at (d/8, 0, 0), (7d/8, 0, 0), and (d/2, 0, $\sqrt{3}d$/2), where d is the diameter of the particles. This type of angular particle was selected after some trials with different kinds of angular

particles (formed by clumping two or three spherical particles) to capture the decreasing effect of shear rate on stresses and friction coefficients. The angular particles had sizes ranging from 4.1 mm to 5.5 mm (mean ~ 5 mm), keeping the grain size distribution curve shown in Figure 3.3. They had also properties shown in Table 3.1, similar to the spherical particles. The details of the ring shear simulation have been discussed in Section 3.2.

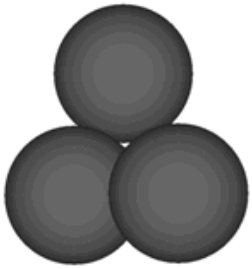

FIGURE 5.7: DEM model of angular particle.

The ring shear simulation results on 5 mm mean diameter angular particles at a constant vertical normal stress of 150 kPa are presented in Figure 5.8. The results of ring shear simulations on the same mean diameter spherical particles are also presented for comparison.

The results show that, for angular particles, the friction coefficient (or the shear stress since the normal stress was held constant) decreases with the increase of the characteristic mean shear velocity as the flow progresses from a quasi-static to an intermediate regime. This result is in agreement with Martino and Davies (2003). The friction coefficient then starts to increase with further increase in the characteristic velocity when the flow continues to progress to the collisional regime. Conversely, the friction coefficient of spherical particles remains nearly constant for a characteristic velocity of up to 0.85 m/s and then starts to increase with the further increase of the characteristic velocity.

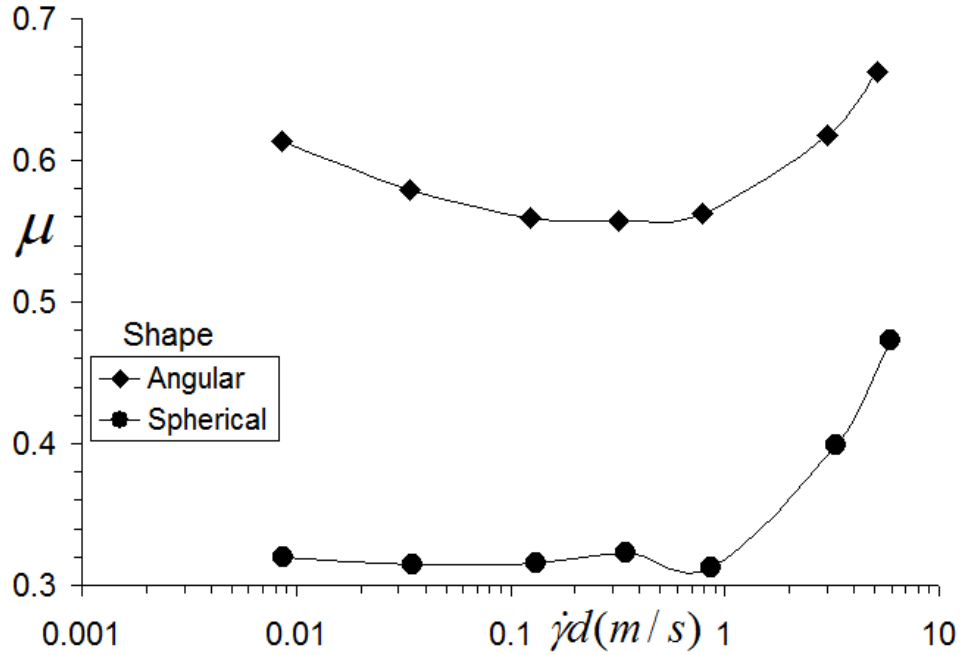

(a)

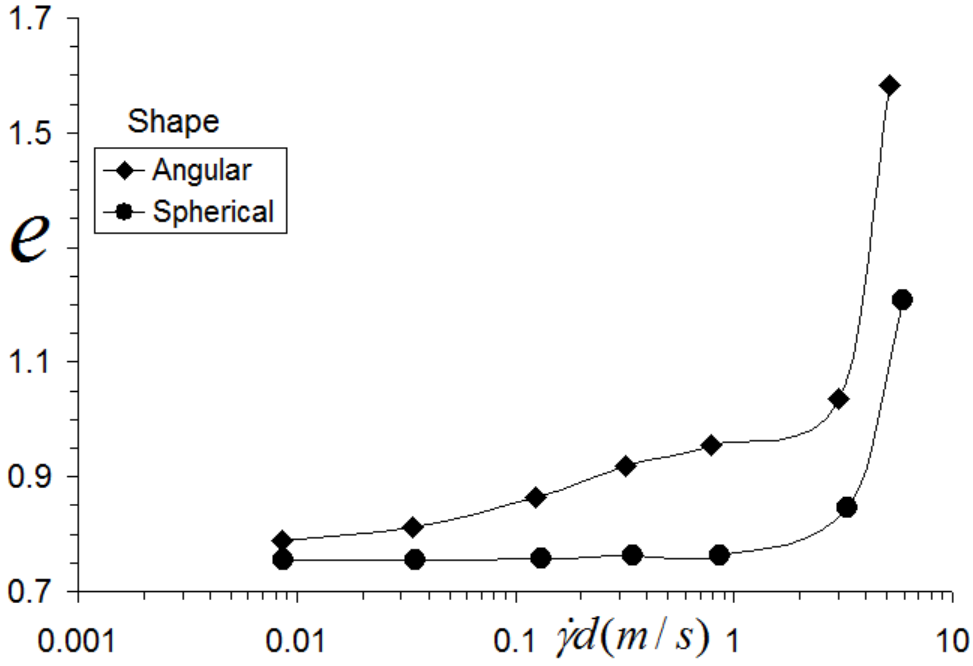

(b)

FIGURE 5.8: Simulation results of ring shear model.

Angular particles attain a higher critical state friction angle than spherical particles due to interlocking effect (Savage & Sayed, 1984). When angular particle flow progresses from quasi-static to intermediate regimes, the decrease in friction angle due to the loss of interlocking (because of the increase of void ratio, as shown in Figure 5.8b) will be higher than the increase in friction angle due to collisional interaction, resulting in the net decrease in friction angle. With further increases in shear rate, however, the flow progresses to the collisional regime with greater contribution of shearing resistance from collisional interaction. At this point, the net friction angle starts to increase.

On the other hand, the void ratio in angular particles increases continuously with the characteristic velocity, as shown in Figure 5.8(b). This may imply that vertical normal stress will continuously increase with the characteristic velocity under constant void ratio. Similar behaviour of stresses and void ratios with shear rates were observed in Savage and Sayed (1984) shear experiments on crushed walnut shell particles and Campbell (2011) plane shear simulations of ellipsoidal particles. However, the above observation is in contrast to the findings of Lu et al. (2007), who reported decrease in the stress (for constant void ratio) and the void ratio (for constant normal stress) with the shear rate in the intermediate regime, followed by their increase with the shear rate in the collisional regime. This difference may be due to:

(a) the angular particles used here could not capture the irregular shapes of actual particles, especially the sharp edges and corners which have significant effects in interlocking, and/or

(b) different type of shear apparatus (cylindrical shearing device) used in the shear experiments of Lu et al. (2007).

The drawback of Lu et al. apparatus is that the shearing velocity varies radially resulting in lower rate of shearing closer to the center (quasi-static condition) and

higher rate of shearing closer to the outer boundary undergoing possible rate-dependent flow mechanisms. Therefore, different flow mechanisms may develop in different regions inside a single experiment which means that the particles are not uniformly sheared. This drawback makes interpretation of the results difficult.

Although Lu et al. (2007) provided a detailed explanation to justify why their results were not affected by the shear apparatus, very few simulation experiments were conducted by modeling their apparatus shown in Figure 5.9 (by modifying the ring shear model setting $R_i = 0$) to investigate the effect of the cylindrical shear apparatus. The radius of the apparatus, (R_0), was selected to be $22d$ in order to test the same amount of particles (13,330) as in the ring shear simulations at the same sample height of $10d$ after consolidation.

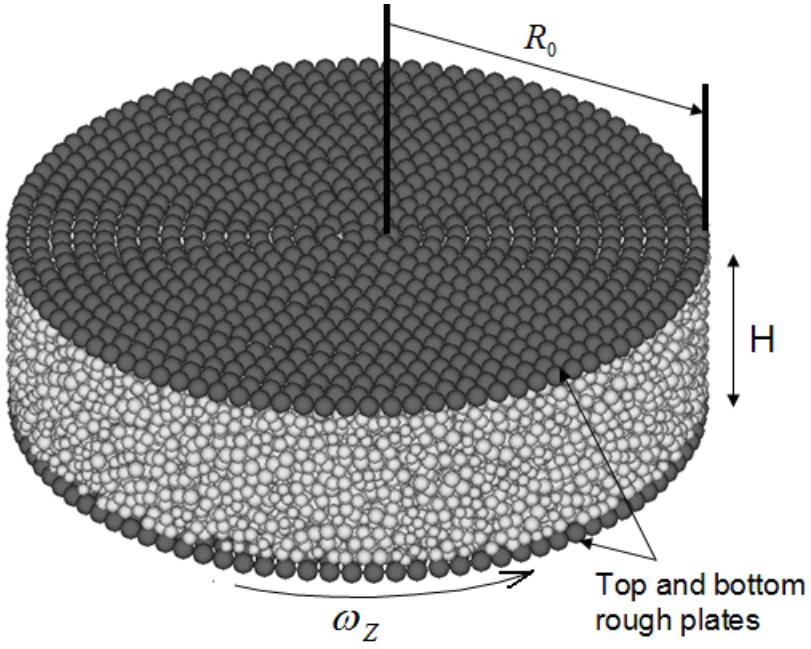

FIGURE 5.9: Cylindrical shear apparatus model.

The simulation results are presented in Table 5.1. It can be seen that the same effect of shear rate on void ratio and friction coefficient is observed as the ring shear simulations. Hence, the simulation results of both the ring and the cylindrical shear models suggest that the void ratio (for constant vertical normal

stress) and the vertical normal stress (for constant void ratio) increase continuously with shear rate at least for the type of angular particles tested in this research, as shown in Figure 5.7. The reason for not observing the decreasing effect of shear rate as reported by Lu et al. (2007) may be due to the difficulty in modeling precisely the actual angular particles, especially the sharp edges and corners. The angular particle model may be improved by constructing it from several smaller spherical particles. This will require a very high-speed computer to run and is left for future study.

TABLE 5.1: Summary of cylindrical shear model results.

Case	$\sigma_z (kPa)$	ω_z (sec^{-1})	$\tau_{xz} (kPa)$	e	μ
1	148.99	0.75	91.61	0.856	0.615
2	149.57	5	88.27	0.886	0.59
3	149.63	15	86.68	0.898	0.579
4	149.43	30	87.66	0.907	0.587

5.3.2 Implications of Decrease in Resistance

Further studies are required to understand the behaviour of different types of non-spherical particles before generalizing their effect on the extended critical state framework. Limited experimental and simulation investigations such as Savage and Sayed (1984) for crushed walnut particles, Martino and Davies (2003) for cylindrical PVC particles, Lu et al. (2007) for irregular-shaped beach sand, Campbell (2011) for ellipsoidal particles, and the simulation results in this research have revealed various flow behaviours depending on the type of non-spherical particles.

In general, the decrease in shearing resistance for non-spherical particles may imply a flow state below the conventional critical state line in both $e - \log \sigma_z$ and

$\tau_{xz} - \sigma_z$ plots. For example, if the shear strength decreases with shear rate as the flow progresses from a quasi-static to an intermediate regime at constant vertical normal stress (as seen in the ring shear simulations conducted in this research), the supercritical state lines in the intermediate regime may fall below the critical state line in the $\tau_{xz} - \sigma_z$ plane as shown in Figure 5.3. Hence, the critical state line will no longer be the lowest boundary state line. On the other hand, if stresses decrease with shear rate as the flow progresses from a quasi-static to an intermediate regime at a constant void ratio (as seen in Lu et al., 2007), the supercritical state lines in the intermediate regime may lie to the left side of the critical state line in the $e - \log \sigma_z$ plot, which makes the CSL line again no longer be the lowest boundary state line.

5.4 Coordination Number and Sliding Fraction

The dependency of stresses and friction coefficient on shear rate in rapid granular flows can be explained by exploring two important micro-level variables called coordination number and sliding fraction. Coordination number is the average number of contacts per particle in a time step. Sliding fraction is the fraction of slipping contacts out of the total contacts in a time step. These variables were calculated in the plane shear simulations of spherical particles conducted in this research. The results are used in this section to explain the dependency of stresses and friction coefficient on shear rate.

In general, stresses in granular flow depend on the amount of particle contacts and contact intensities. The amount of particle contacts is quantified by the variable coordination number, while the contact intensity is directly related to the shear rate of flow.

At constant shear rate, the stresses mainly depend on the coordination number. It is observed in Figure 5.10(a) that, at constant shear rate, the decrease of void ratio

increases the coordination number. The increase of coordination number (due to the decrease of void ratio) in turn increases the stresses as observed in Figure 5.10(b). The increase of contacts (or the coordination number) improves contact chains in the frictional mechanism and increases the amount of momentum transfer in a collisional mechanism, thereby increasing the stresses.

At constant void ratio, on the other hand, the coordination number may increase or decrease with the shear rate depending on the state of granular flow. Aarons and Sundaresan (2006) explained that the increase in shear rate will increase the collision frequency but will also cause more frequent breaking up of the force chains. Thus, the variation of the coordination number with the shear rate depends on the relative importance of these two effects. The increase of the coordination number with the shear rate at constant void ratios in Figure 5.10(a) (except at the void ratio of 0.7) is attributed to the increase in collision frequency with the shear rate, as the flows were mostly collisional and the force chains are not significant. This increase in the coordination number causes the stresses to increase in the same fashion as shown in Figure 4.1. However, the coordination number depends less on the shear rate compared to the stresses (compare the slopes in Figure 4.1a and Figure 5.10a). This might be attributed to the additional contribution to the stresses from the increase of contact intensity (contact force intensity) due to the increase of the shear rate, making the stresses more dependent on the shear rate. At a void ratio of 0.7, however, the coordination number decreases slightly with the increase in shear rate as shown in Figure 5.10(a). It is because the increase of the coordination number due to the increase of collision frequency cancelled the decrease of the coordination number due to more frequent breaking up of the force chains. However, the stresses corresponding to the void ratio of 0.7 increases with the shear rate as shown in Figure 4.1. This increase in stresses might be due to the additional contribution of stresses from the increase of contact intensity (or contact force intensity) due to an increase in the shear rate.

Finally, at constant normal stress, the coordination number is observed to decrease with the increase of shear rate as shown in Figure 5.10(b). The increase of shear rate is accompanied by the increase of void ratio in order to keep the normal stress constant. The increase of void ratio reduces the coordination number so that the normal stress is not allowed to increase due to the increase of shear rate.

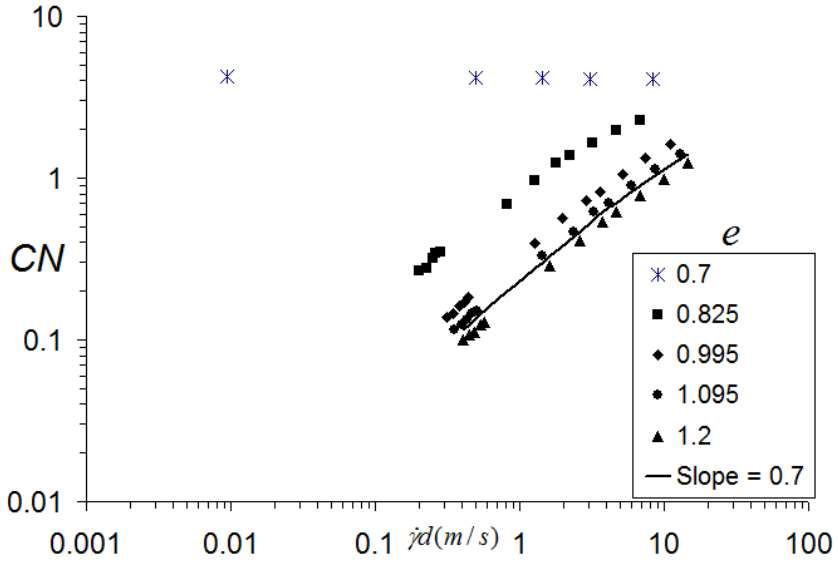

(a)

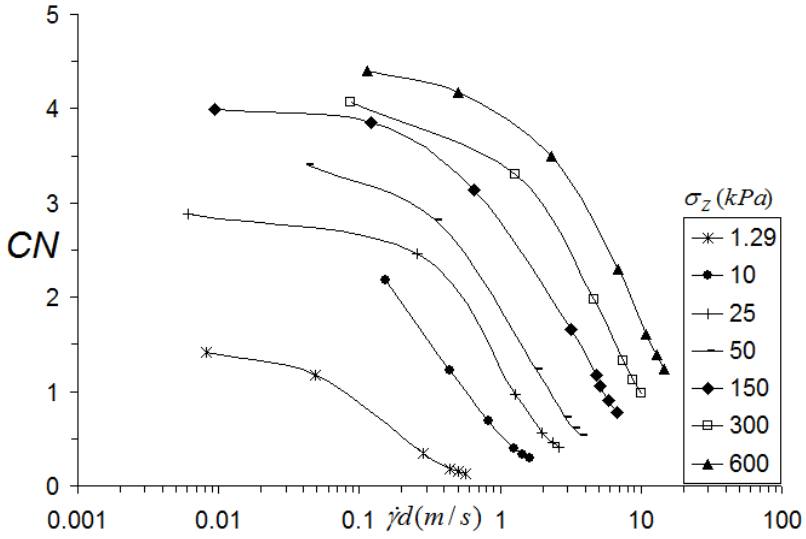

(b)

FIGURE 5.10: Coordination Number (*CN*) versus characteristic velocity: (a) at constant void ratio, (b) at constant vertical normal stress

In addition to the dependency of normal and shear stresses on shear rate as discussed above, the ratio of these stresses (shear stress to normal stress ratio, or friction coefficient) also depends on shear rate. In general, the friction coefficient increases with the progression of flow from the quasi-static regime (lowest value, μ_{cs}) to the collisional regime (highest value, μ_c) due to the increase of shear rate under both constant void ratio and constant normal stress conditions. The graphical presentation of the friction coefficient behaviour is shown in Figure 5.5. This behaviour of friction coefficient might be attributed to the effect of amount of particles sliding in a granular flow.

The variations of the calculated sliding fractions with the shear rates are presented in Figure 5.11 under constant void ratio and normal stress conditions. The variation of the sliding fractions is similar to the friction coefficients under both conditions (e.g. compare Figure 5.4a with Figure 5.11b).

The sliding fraction is stated as an indicator of mobilization of friction by Da. Cruz et al. (2005). The increase in sliding fraction would mean more mobilization of friction in the granular material, thereby increasing the mobilized shear strength. Both the normal and shear stresses are affected equally due to the change in contact numbers and intensities. However, shear stress is increasing at a higher rate than the normal stress due to the increase of sliding fraction, and hence increases the friction coefficient.

The continuous increase in the sliding fraction with shear rate in the quasi-static and intermediate regimes may indicate the breaking up of clusters and blocks of particles, whereby the granular material is being mobilized. After all clusters and blocks of particles are broken down and force networks eliminated, collisional flow will develop where the sliding fraction will no longer increase so that the maximum mobilization of strength is achieved.

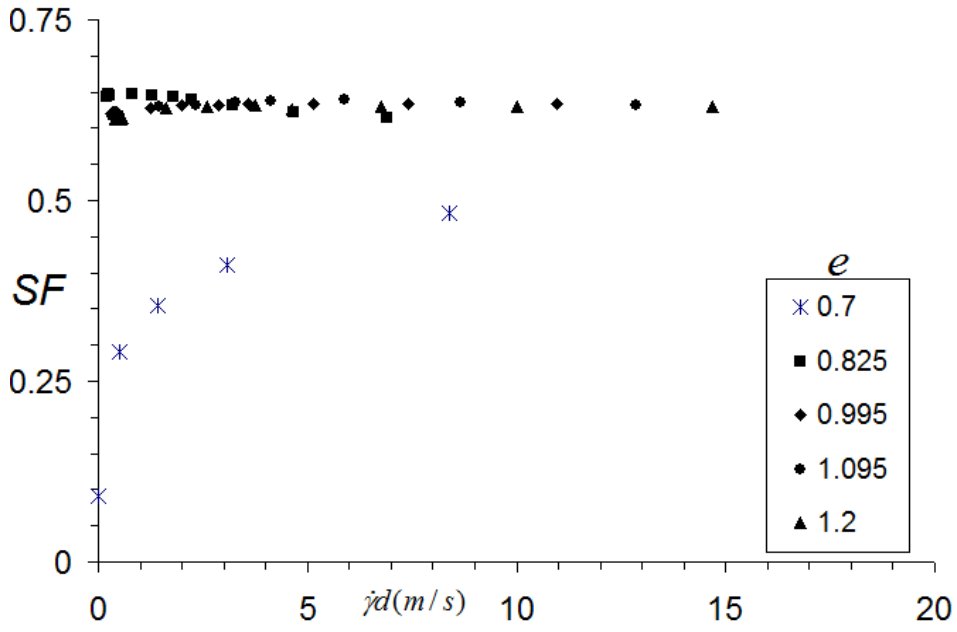

(a)

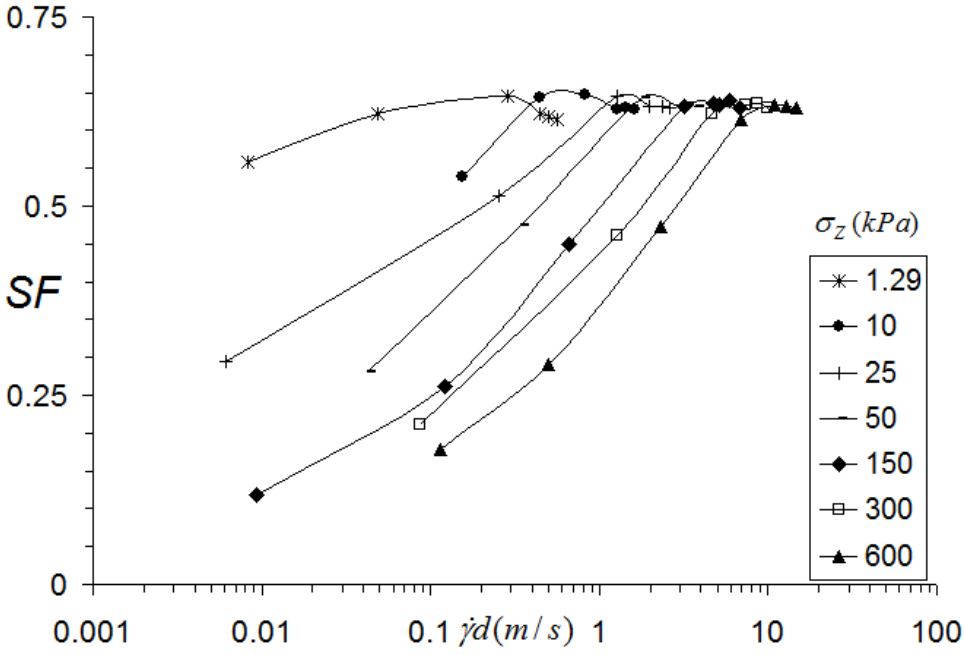

(b)

FIGURE 5.11: Sliding Fraction (*SF*) versus characteristic velocity: (a) at constant void ratio, (b) at constant vertical normal stress.

CHAPTER SIX

CONSTITUTIVE MODELING

6.1 Introduction

Citing the high stress shear experiments (Hungr & Morgenstern, 1984; Fukuoka & Sassa, 1991; Cagnoli & Manga, 2004) discussed in Chapter 2, many geotechnical scientists believe that flow type landslides have frictional flow behavior that can be captured by the Coulomb shear stress to normal stress relationship. Hence, the run-out predictions of many geological mass flows have been performed by implementing the Coulomb friction constitutive law (Savage & Hutter, 1989; Hungr, 1995; Kelfoun & Druitt, 2005; Sheridan et al., 2003). In the cases of the Coulomb equation not performing well, the Voellmy model, which accounts for possible sources of velocity dependent resistance in addition to frictional resistance, has been used to obtain better predictions (Hungr & Evans, 1996; Evans et al., 2001; Hungr et al., 2007; Pirulli, 2009).

Some other researchers are contended with considering geological mass flow being a dense flow which derives its shear resistance from both frictional rubbing and particle collisions. Many of these researchers have proposed constitutive equations that account for both types of resistance contributions (Savage, 1998; Louge, 2003; Berzi et al., 2011).

Although the findings of the shear tests under high stress reveals the limitation of the collisional flow mechanism, based on the analyses in Chapter 4, it is seen that the contribution of the collisional flow mechanism could be significant in very rapid avalanches involving large particles. A mass flow usually goes through the stages of initiation, transition, and deposition. The collisional mechanism could be significant in the transition stage where the flowing velocity is normally high. The

use of Voellmy model as opposed to the Coulomb frictional model for a better flow prediction provides further evidence for the existence of rate-dependent behaviour. It was suggested by Wang (2008) that the turbulence term in the Voellmy model may arise out of the loss of kinetic energy in granular flows which is not accounted for by frictional energy dissipation. Hence, the loss of kinetic energy due to inelastic particle collisions may explain the existence of the turbulence term in Voellmy model. Therefore, there is a need to develop a constitutive model that encompasses frictional sliding and particle collisions from quasi-static and collisional flow regimes.

In the subsequent sections, three selected unified constitutive models proposed by Savage (1982), Savage (1998), and Louge (2003) are evaluated by predicting the extended critical state framework presented in Chapter 5 under high stresses. The constitutive models are discussed in Chapter 2. A new unified model is proposed in this chapter that superposes both frictional and collisional stress contributions using appropriate weighting functions instead of directly adding them as per the assumption of Savage (1982). The proposed unified model is implemented in the numerical model for inclined flows and is used to predict the different types of inclined flow profiles discussed in Chapter 2.

6.2 Evaluation of Existing Unified Constitutive Models

6.2.1 Savage (1982) Model

The prominent approach for unified constitutive modeling of frictional-collisional granular flows was by directly adding the frictional and collisional stress contributions, as originally proposed by Savage (1982). Many researchers followed a similar approach in proposing unified models (Johnson & Jackson, 1987; Louge, 2003; Berzi et al., 2011). However, the approach is a simplified one which is based on an ad hoc assumption of stress addition because it is not clear how the two stress contributions act together. Nevertheless, since this model has

been used extensively in the literature to predict granular flows, it is evaluated here by predicting the extended critical state framework presented in Chapter 5.

According to this model, the total stress is expressed as

$$\sigma_x = \sigma_x^f + \sigma_x^{k/c}, \tag{6.1a}$$

$$\sigma_z = \sigma_z^f + \sigma_z^{k/c}, \tag{6.1b}$$

$$\tau_{xz} = \tau_{xz}^f + \tau_{xz}^{k/c}, \tag{6.1c}$$

where x- and z- axes define the plane of flow and aligned in parallel and normal directions to the flow, respectively, σ_x & σ_z are the total normal stresses, τ_{xz} is the total shear stress, σ_x^f & σ_z^f are the frictional normal stresses, $\sigma_x^{k/c}$ & $\sigma_z^{k/c}$ are the kinetic/collisional normal stresses, τ_{xz}^f is the frictional shear stress, and $\tau_{xz}^{k/c}$ is the collisional shear stress.

The *kinetic/collisional stress contribution* can be determined by using either the Bagnold dispersive stress equation or the kinetic theory of granular particles. The main difference between the two models of kinetic/collisional stress is the presence of the additional variable called 'granular temperature' in the kinetic theory model. Since granular temperature also constitutes the extended critical state framework presented in Chapter 5, the kinetic/collisional stress contribution is determined from the kinetic theory model proposed by Lun et al. (1984) and simplified by Ahn (1989) for two-dimensional steady flows, as follows

$$\sigma_x^{k/c} = \sigma_z^{k/c} = \rho g_1 T, \tag{6.2a}$$

$$\tau_{xz}^{k/c} = \rho g_2 \dot{\gamma} d \sqrt{T}, \tag{6.2b}$$

$$g_1(v_S,\varepsilon) = v_S + 4\eta v_S^2 g_0\,, \tag{6.2c}$$

$$g_2(v_S,\varepsilon) = \frac{5\sqrt{\pi}}{96}\left[\frac{1}{\eta(2-\eta)}\frac{1}{g_0} + \tfrac{8}{5}\frac{3\eta-1}{2-\eta}v_s + \tfrac{64}{25}\eta\left(\frac{3\eta-2}{2-\eta}+\frac{12}{\pi}\right)v_s^2 g_0\right], \tag{6.2d}$$

$$\eta = \tfrac{1}{2}(1+\varepsilon)\,, \tag{6.2e}$$

where T is the translational granular temperature, ρ is the particle density, $\dot{\gamma}$ is the shear rate (or velocity gradient), d is the particle diameter, v_S is the solid volume fraction which is related to the void ratio as $e = (1-v_S)/v_S$, and ε is the restitution coefficient. We use the radial distribution function g_0 proposed by Johnson and Jackson (1987) as shown in Eq. (6.2f) in order to limit the solid volume fraction below its maximum close packing value, v_S^m

$$g_0 = \frac{1}{1-\left(v_S / v_S^m\right)^{1/3}}\,. \tag{6.2f}$$

For homogeneous steady plane shear flow, the expression for granular temperature can be derived from the fluctuation kinetic energy equation. The extended critical state framework is established by determining each flow-state from homogeneous, steady plane shear flow simulations. In such flows, the balance of mass and momentum are automatically satisfied, while the balance of fluctuation kinetic energy is given as

$$\tfrac{3}{2}\rho\frac{dT}{dt} = \tau_{xz}^{k/c}\cdot\dot{\gamma} - \frac{\partial q_s}{\partial z} - \Upsilon\,, \tag{6.2g}$$

where t is time, q_s is the flux of fluctuation kinetic energy, and Υ is the rate of dissipation of fluctuation kinetic energy per unit volume due to the inelastic collisions. Their constitutive equations for the collisional part of the processes are proposed by Lun et al. (1984) and simplified for two-dimensional steady flows by Ahn (1989) as

$$q_s = -\rho d\left(g_3\sqrt{T}\frac{\partial T}{\partial z} + g_4 T^{3/2}\frac{\partial v_s}{\partial z}\right), \tag{6.2h}$$

$$\Upsilon = \frac{\rho}{d} g_5 T^{3/2}, \tag{6.2i}$$

$$g_3\left(v_s,\varepsilon\right) = \frac{25\sqrt{\pi}}{16\eta(41-33\eta)}\left[\begin{array}{l}\dfrac{1}{g_0}+\dfrac{12}{5}\eta\left(1+\eta(4\eta-3)\right)v_s\ldots \\ +\frac{16}{25}\eta^2\left(9\eta\left(4\eta-3\right)+\frac{4}{\pi}\left(41-33\eta\right)\right)v_s^2 g_0\end{array}\right], \tag{6.2j}$$

$$g_4\left(v_s,\varepsilon\right) = \frac{15\sqrt{\pi}}{4}\frac{\left(2\eta-1\right)\left(\eta-1\right)}{(41-33\eta)}\left(\frac{1}{v_s g_0}+\frac{12}{5}\eta\right)\frac{\partial(v_s^2 g_0)}{\partial v_s}, \tag{6.2k}$$

$$g_5\left(v_s,\varepsilon\right) = \frac{48}{\sqrt{\pi}}\eta(1-\eta)v_s^2 g_0. \tag{6.2l}$$

We follow the assumption of Johnson and Jackson (1987) that *only the work of kinetic/collisional shear stress produces granular temperature* while the frictional shear work directly dissipates into heat. Since there is no flux of fluctuation energy in homogeneous steady plane shear flow (see Eq. 6.2h), the fluctuation energy balance reduces to

$$0 = \tau_{xz}^{k/c}\cdot\dot{\gamma} - \Upsilon, \tag{6.2m}$$

and the granular temperature is derived from this as

$$T = \frac{g_2}{g_5}(\dot{\gamma} d)^2 . \tag{6.2n}$$

On the other hand, the *frictional stress contribution* can be determined based on the critical state line equation and the Coulomb friction law as shown in Eq. (6.3)

$$e_{cs} = \Gamma - \lambda \log \sigma_z^f \ , \tag{6.3a}$$

$$\tau_{xz}^f = \mu_{cs} \cdot \sigma_z^f \ , \tag{6.3b}$$

where e_{cs} is the critical state void ratio, λ is the slope of the critical state line in $e_{cs} - \log \sigma_z^f$ plot, Γ is the void ratio at $\sigma_z^f = 1Pa$, and μ_{cs} is the critical state friction coefficient.

The Savage (1982) model is used to predict the extended critical state frame work as shown in Figure 6.1. The values of model parameters used in the predictions are presented in Table 6.1.

TABLE 6.1: Values of parameters used in Savage (1982) model.

v_S^m	ε	Γ	λ	μ_{cs}
0.61	0.81	0.85	0.027	0.34

The parameters Γ, λ, and μ_{cs} were determined from the simulation experiments. On the other hand, the maximum close packing solid volume fraction and the restitution coefficient were determined to best predict the simulation results.

The maximum close packing solid volume fraction mainly influences the prediction of supercritical state lines (Figures 6.1a & b), while the restitution coefficient affects the prediction of the entire framework presented in Figure 6.1.

It should be noted that the restitution coefficient of the DEM-model particles used in the simulation experiments was 0.75.

In general, the unified constitutive equation derived by directly adding the frictional and collisional stress contributions as originally proposed by Savage (1982) predicts the general trends of the critical state lines and friction coefficients, as shown in Figures 6.1(a) to 6.1(c). It should be noted that, similar to the model prediction in Figure 6.1(c), the measured friction coefficients also tend to be constant at high values of I, which are more clearly seen in Figure 5.4.

Conversely, the model has a major limitation in predicting the trend of granular temperature for the transitional regime, as shown in Figure 6.1(d). The granular temperature increases in the transitional regime, while the model predicts it to be constant following the trend in the collisional regime. In explaining the reason for this major limitation, the shear work due to the frictional stress contribution is assumed to dissipate by particle friction while the shear work due to the kinetic/collisional stress contribution is assumed to dissipate by particle collision (Johnson & Jackson, 1987). Hence, only the kinetic/collisional stress component can be used in the equation of fluctuation kinetic energy balance. This will give a granular temperature expression similar to the case of pure collisional flow. Therefore, in the above unified theory, only the expression of stress is changed by adding both stress contributions together, while the granular temperature equation derived from the kinetic theory for pure collisional flow is still used to predict the granular temperature of all flow regimes.

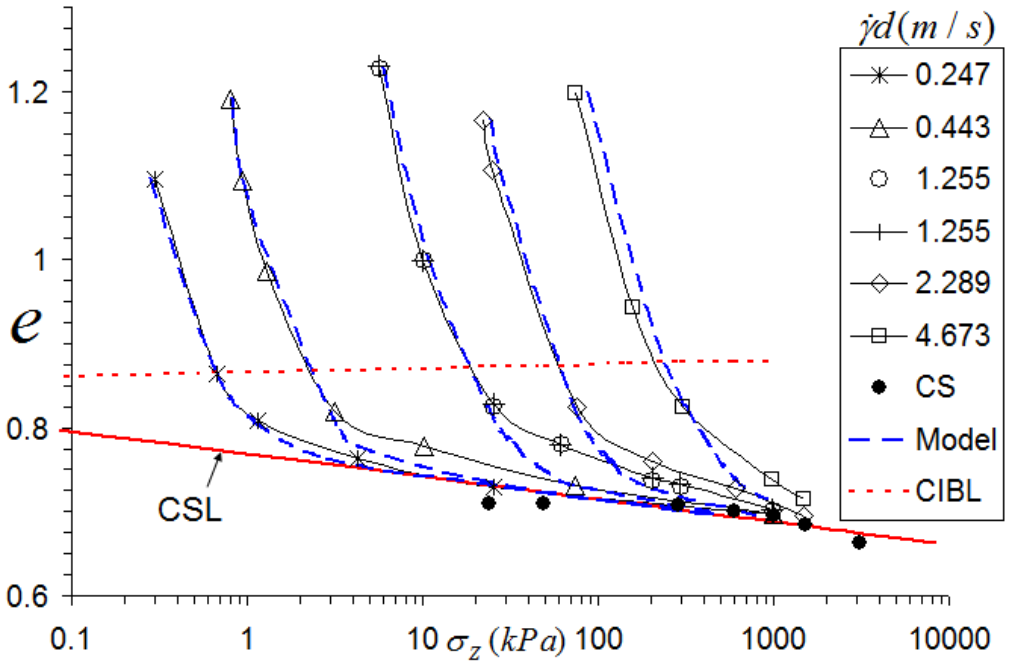
$\dot{\gamma}d(m/s)$
0.247
0.443
1.255
1.255
2.289
4.673
CS
Model
CIBL
CSL
e
1.2
1
0.8
0.6
0.1
1
10
100
1000
10000
$\sigma_z\,(kPa)$

(a)

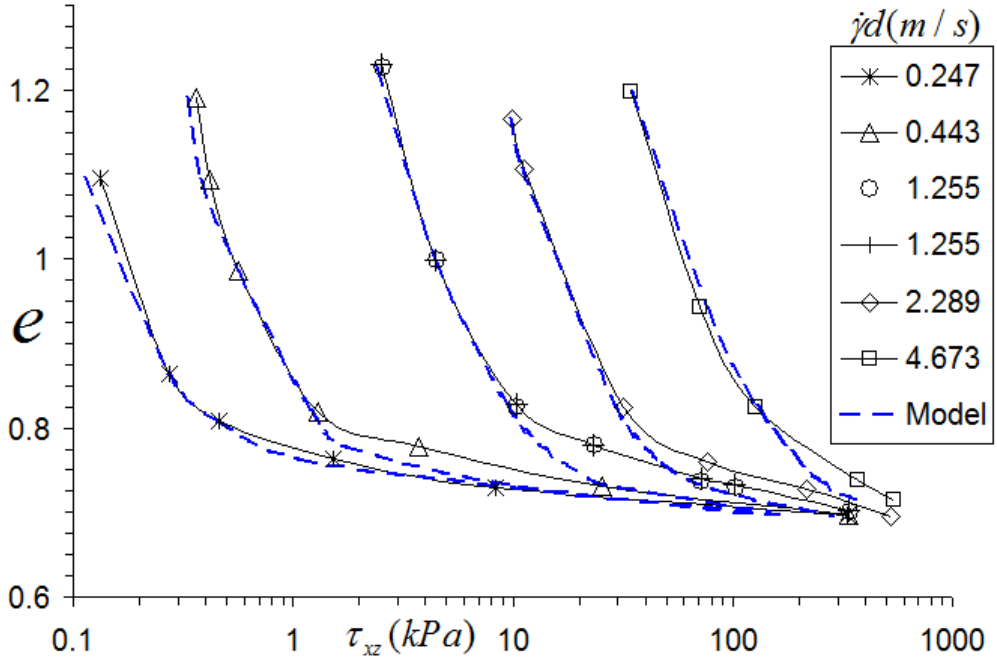
$\dot{\gamma}d(m/s)$
0.247
0.443
1.255
1.255
2.289
4.673
Model
e
1.2
1
0.8
0.6
0.1
1
10
100
1000
$\tau_{xz}\,(kPa)$

(b)

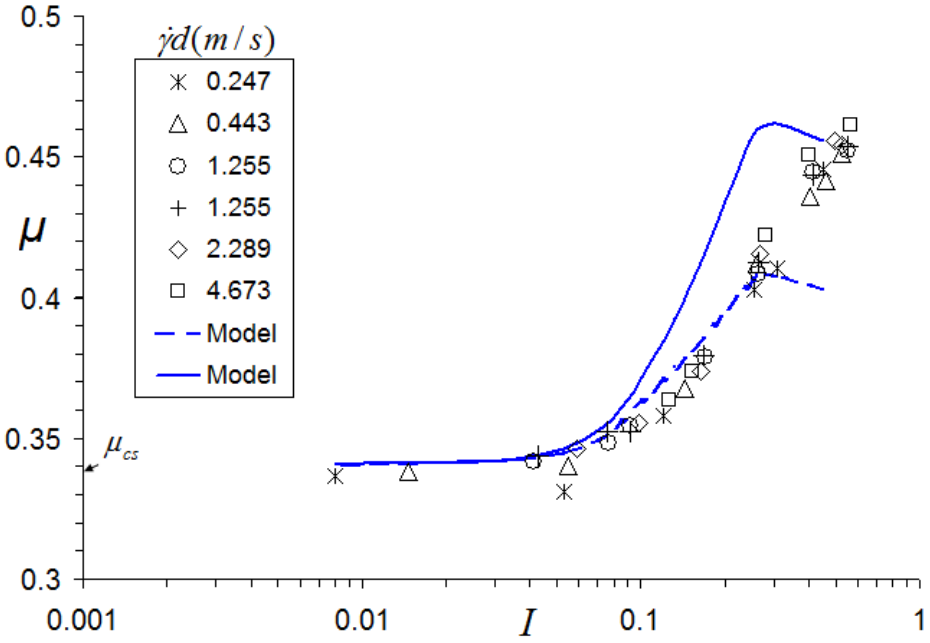

(c)

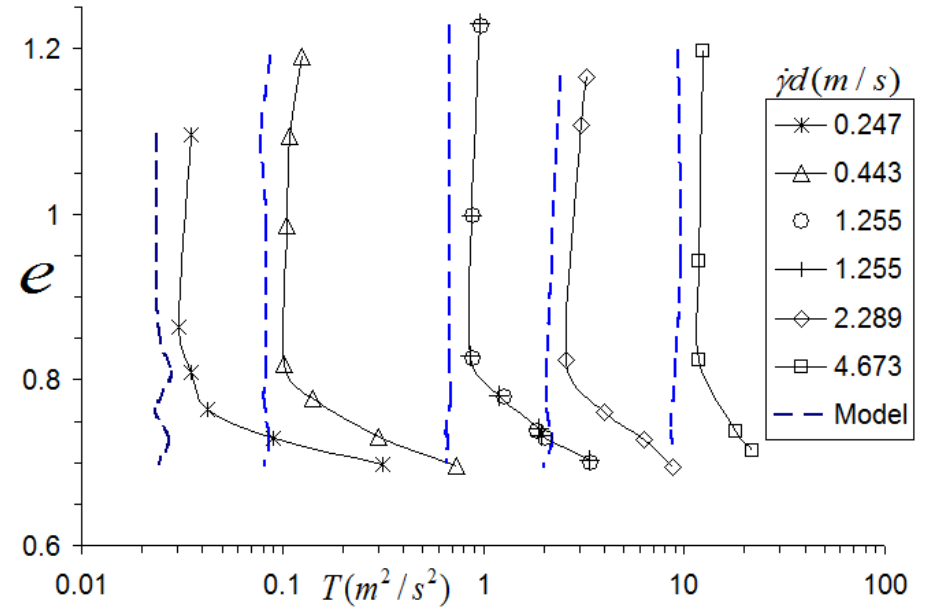

(d)

FIGURE 6.1: Prediction of the Savage (1982) model: (a) void ratio versus vertical normal stress; (b) void ratio versus shear stress; (c) friction coefficient versus dimensionless variable *I*, dashed line is using $\varepsilon = 0.81$ and solid line is using $\varepsilon = 0.75$ while both predictions of friction coefficient are for $\dot{\gamma}d = 0.247$; (d) void ratio versus granular temperature.

6.2.2 Savage (1998) Model

Savage (1998) followed a different approach to derive a unified constitutive model for granular flows. In contrast to the previous model (Savage, 1982), whose prediction is influenced by the restitution coefficient and maximum close packing solid volume fraction, the prediction of the Savage (1998) model is influenced by the critical state friction angle and maximum close packing solid volume fraction. The restitution coefficient has been considered as a main parameter for determining the collisional stress component in most of the unified constitutive models available in the literature (Nott, 1991; Ancey & Evesque ,2000; Louge, 2003; Berzi et al., 2011). Because of this main difference of the Savage (1998) model from the others, it has been selected in this research to study its performance in predicting the extended critical state framework.

Savage (1998) also expressed the total normal stresses as given in Eq. (6.1a) & (6.1b). However, he provided a different equation for the frictional normal stress component, commenting that Eq. (6.3a) is not appropriate for low stress levels. But, the Savage (1998) model is implemented here for high stress level problems, and hence Eq. (6.3a) is used instead in this study. Savage also provided an equation for the kinetic/collisional normal stress component as

$$\sigma_x^{k/c} = \sigma_z^{k/c} = \rho v_S \left(1+2G\right) T \,, \tag{6.4a}$$

$$G = \frac{v_S \left(16-7v_S\right)}{16\left(1-v_S/v_S^m\right)^2} \,. \tag{6.4b}$$

Savage (1998) also derived the equations for the total shear stress and granular temperature as

$$\tau_{xz} = \zeta \cdot \dot{\gamma} = \frac{Ad}{\beta T^{1/2}} \sigma_z \cdot \dot{\gamma}, \tag{6.4c}$$

$$T = \frac{A}{D\beta^2} (\dot{\gamma} d)^2, \tag{6.4d}$$

$$\beta = \frac{(1+2G) A\pi^{1/2}}{G\left[1+\frac{1}{8}\pi\left(G^{-2}+2G^{-1}+1\right)\right]}, \tag{6.4e}$$

where ζ is the shear viscosity, and A & D are coefficients which depend on the critical state friction angle. They were presented graphically by Savage (1998), in which both were observed to increase with the increase of the critical state friction angle.

The predictions of the Savage (1998) model are presented in Figure 6.2, and the values of the model parameters used in the predictions are given in Table 6.2. The maximum close packing solid volume fraction and the critical state friction angle were determined to obtain the best predictions of the simulation results. In contrast to the Savage (1982) model where the restitution coefficient mainly influences the prediction of the entire critical state framework, the critical state friction angle has the main influence in the Savage (1998) model for the predictions of supercritical state lines, friction coefficient, and granular temperature.

TABLE 6.2: Values of parameters used in the Savage (1998) model

v_S^m	ϕ_{cs}	Γ	λ
0.65	23^0	0.85	0.027

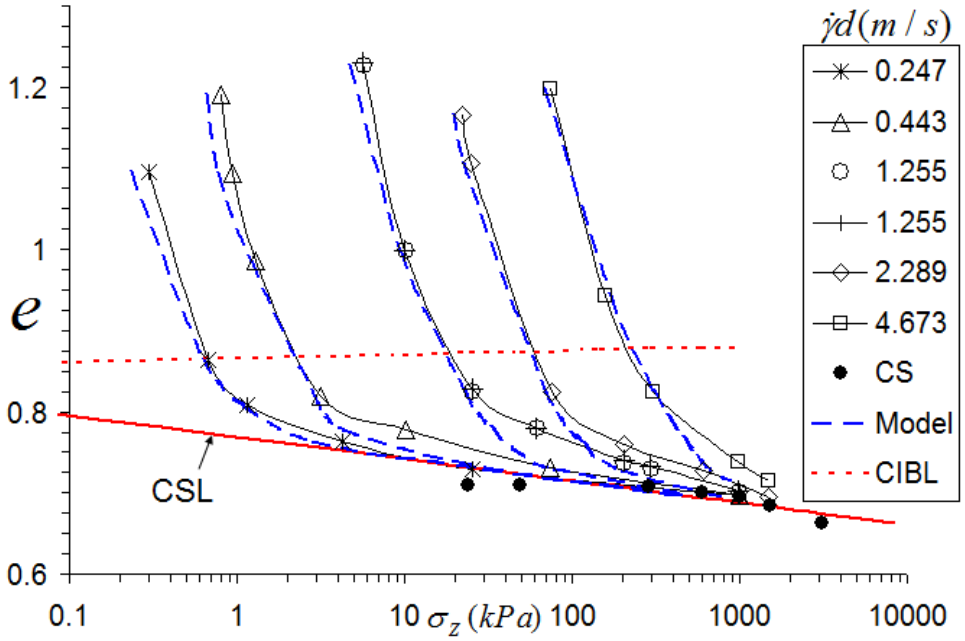
$\dot{\gamma}d(m/s)$
0.247
0.443
1.255
1.255
2.289
4.673
CS
Model
CIBL
CSL
1.2
1
0.8
0.6
e
0.1
1
10
$\sigma_z(kPa)$
100
1000
10000

(a)

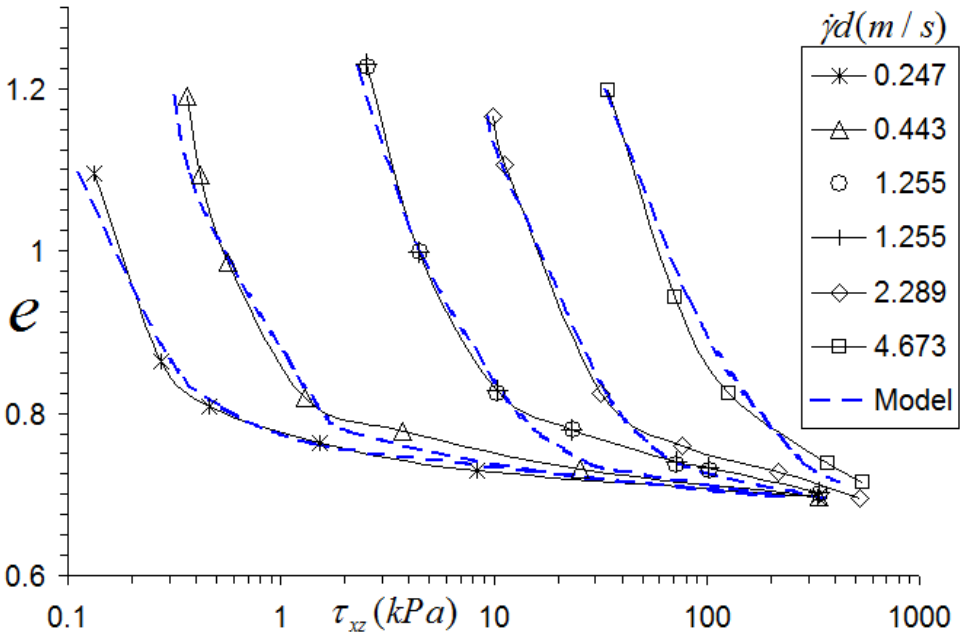
$\dot{\gamma}d(m/s)$
0.247
0.443
1.255
1.255
2.289
4.673
Model
1.2
1
0.8
0.6
e
0.1
1
$\tau_{xz}(kPa)$
10
100
1000

(b)

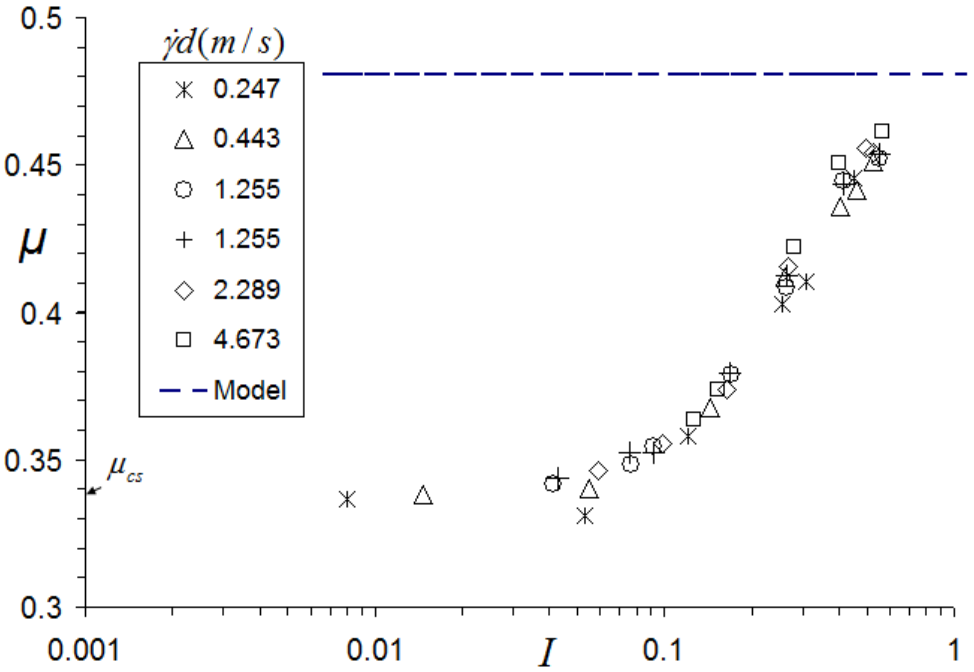

(c)

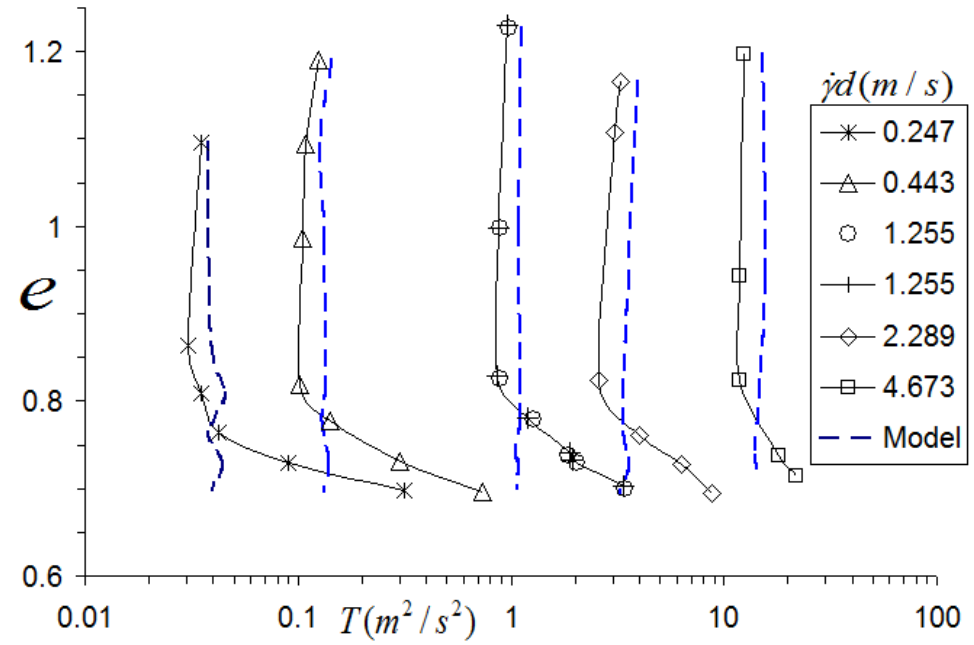

(d)

FIGURE 6.2: Prediction of the Savage (1998) model: (a) void ratio versus vertical normal stress; (b) void ratio versus shear stress; (c) friction coefficient versus dimensionless variable I; (d) void ratio versus granular temperature.

The Savage (1998) model predicts the trends of supercritical state lines, shown in Figures 6.2(a) & (b). However, this model has also a major limitation similar to the Savage (1982) model in predicting the trend of granular temperature for the intermediate regime, as shown in Figure 6.2(d). In addition, the Savage (1998) model gives a constant friction angle independent of the shearing rate, as shown in Figure 6.2(c), which depends only on the critical state friction angle. It can be derived from Eq. (6.4c) & (6.4d) that the ratio of the total shear stress to total normal stress (friction coefficient) is equal to $\sqrt{AD}$, where the parameters A and D are functions of the critical state angle. This implies that, in Savage (1998) model, the friction coefficient doesn't depend on shear rate, and it is a function of its value at critical state.

6.2.3 Louge (2003) Model

The main difference in the Louge (2003) approach for deriving a unified constitutive model is that he considered that the shear works of both frictional and collisional stresses would produce granular temperature before changing to heat and thus he included them in the fluctuation kinetic energy balance. As a normal practice, the kinetic energy produced by the frictional stress work is assumed to dissipate directly to heat. Hence, the frictional kinetic energy balance (using only the frictional stress work) and the fluctuation kinetic energy balance (using only the kinetic/collisional stress work) are written separately (e.g., Johnson & Jackson, 1987).

In his model, the restitution coefficient in the fluctuation kinetic energy balance was then replaced by the effective restitution coefficient (Jenkins & Zhang, 2002) to capture the fluctuation energy dissipation associated with inelastic and frictional impacts during contacts of particles at collisions (see Sec. 2.3.3).

He also used the assumption of stress addition to derive the total stress, as in Eq. (6.1). He invoked the theory of Jenkins (1993) to model the rate-dependent stress

component. However, the Lun et al. (1984) model is used in this research (Eqs. 6.2a & b) instead for the sake of comparison with the above models. The frictional stress component is also modeled in this research using Eq. (6.3).

Based on Louge's (2003) approach, the balance of fluctuation kinetic energy for a homogenous steady plane shear flow given in Eq. (6.2m) would change to

$$0 = (\tau_{xz}^{f} + \tau_{xz}^{k/c}) \cdot \dot{\gamma} - \Upsilon . \tag{6.5a}$$

Substituting Eq. (6.2b), Eq. (6.2i), and Eq. (6.3b) into Eq. (6.5a) will give

$$\rho g_2 \sqrt{T} (\dot{\gamma} d)^2 + \mu_{cs} \sigma_z^f (\dot{\gamma} d) - \rho g_5 T^{3/2} = 0 . \tag{6.5b}$$

Eq. (6.5b) is solved numerically in the prediction of the extended critical state framework. It is interesting to note that Eq. (6.5b) will reduce to Eq. (6.2n) for the case of collisional flow regime in which the frictional stress contribution is negligible. However, the granular temperature result of Eq. (6.5b) will be different from Eq. (6.2n) in the intermediate flow regime where both frictional and collisional stress contributions are important. This could be considered as the main improvement of Louge (2003) model over the Savage (1982) model where the granular temperature expression for collisional flow is used to predict the granular temperatures of the entire granular flow regimes.

Figure 6.3 presents the predictions of the Louge (2003) model for the extended critical state framework. Similar values of model parameters given in Table 6.1 are also used here in the predictions of the Louge (2003) model.

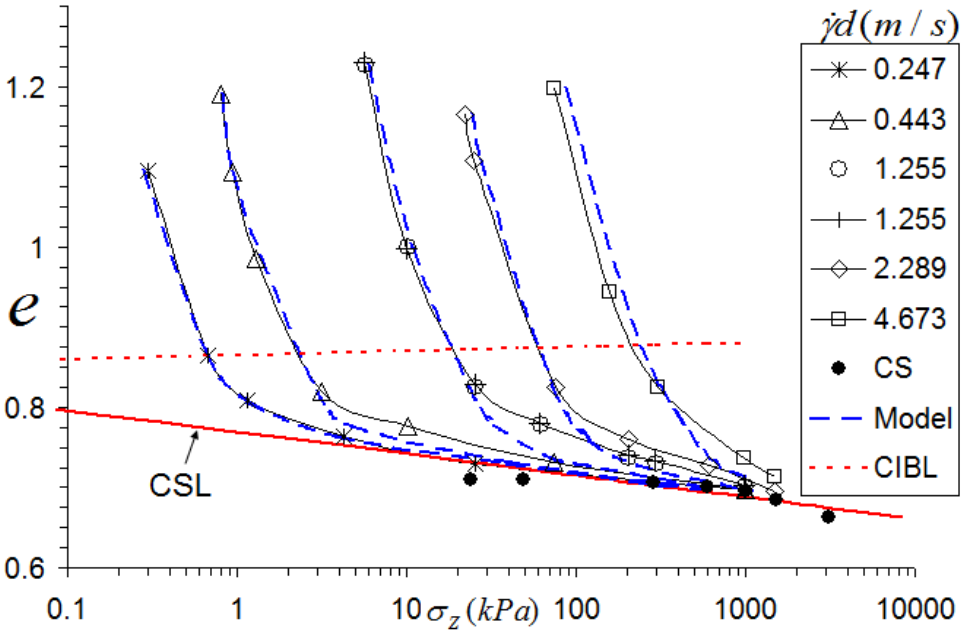
$\dot{\gamma}d(m/s)$
0.247
0.443
1.255
1.255
2.289
4.673
CS
Model
CIBL
CSL
1.2
1
0.8
0.6
e
0.1
1
10
100
1000
10000
$\sigma_z(kPa)$

(a)

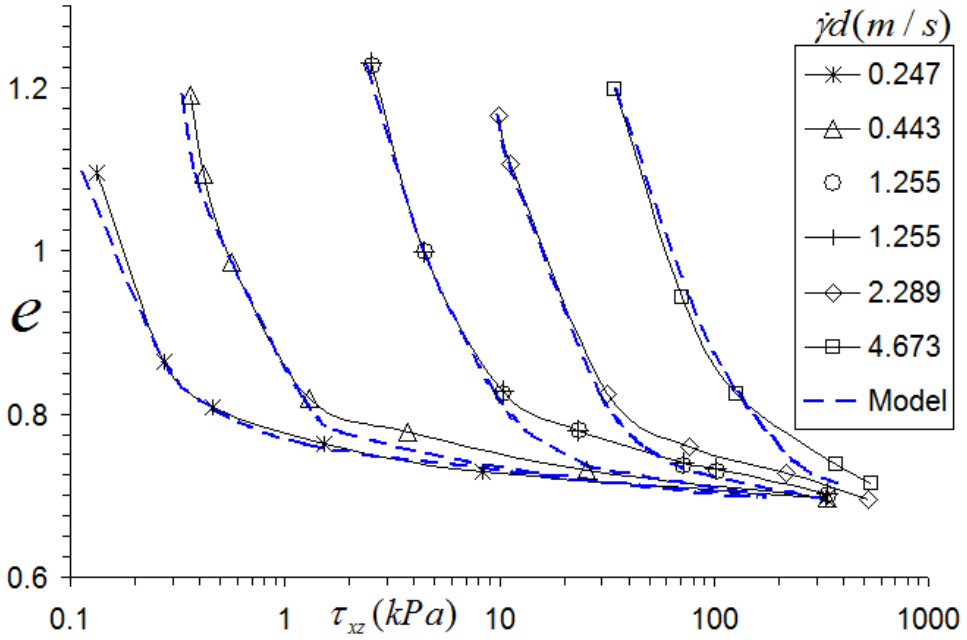
$\dot{\gamma}d(m/s)$
0.247
0.443
1.255
1.255
2.289
4.673
Model
1.2
1
0.8
0.6
e
0.1
1
10
100
1000
$\tau_{xz}(kPa)$

(b)

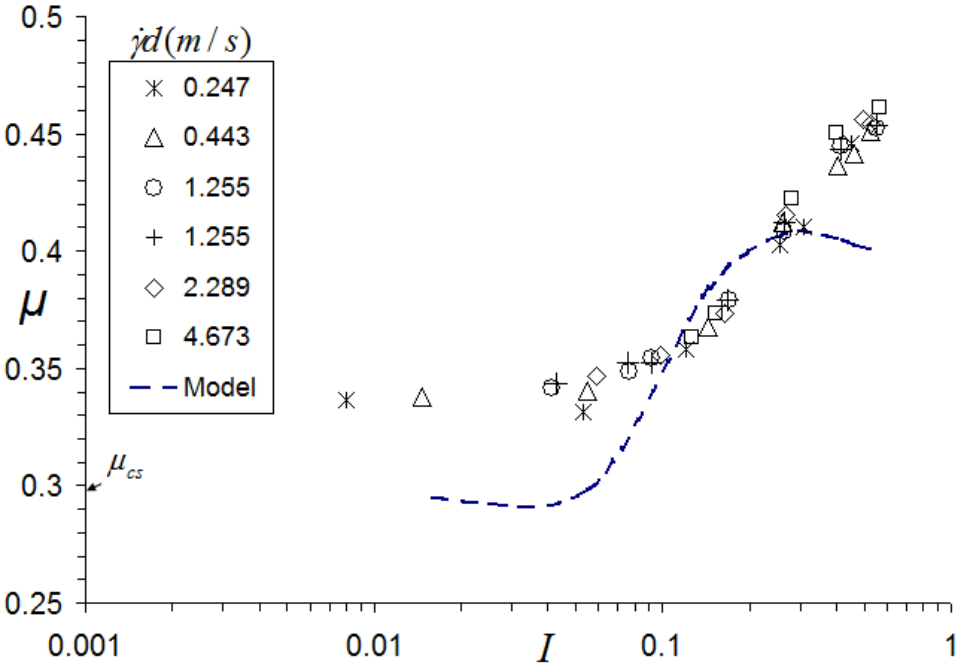

(c)

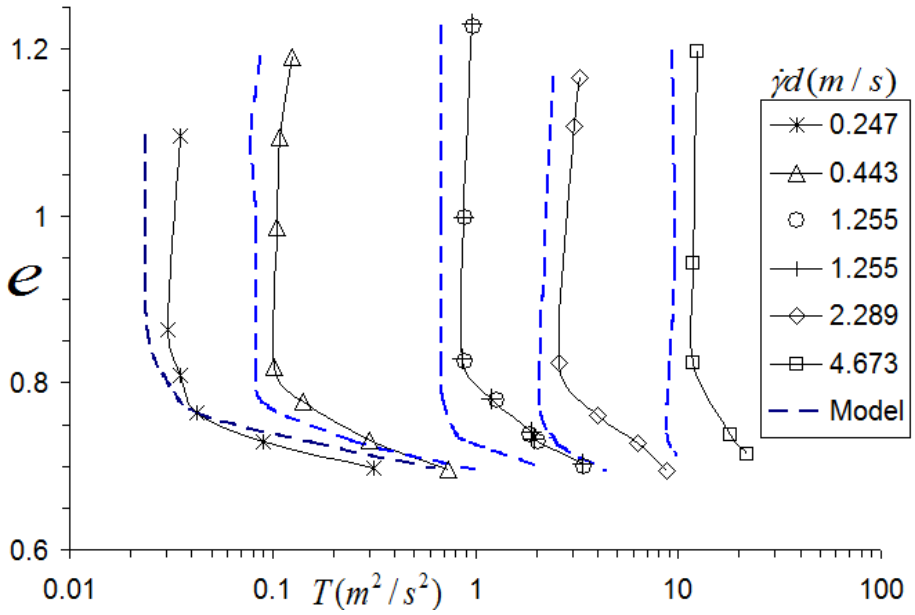

(d)

FIGURE 6.3: Prediction of the Louge (2003) model: (a) void ratio versus vertical normal stress; (b) void ratio versus shear stress; (c) friction coefficient versus dimensionless variable I for $\dot{\gamma}d = 0.443$ m/s; (d) void ratio versus granular temperature.

As shown in Figure 6.3(d), the inclusion of the frictional shear work in the fluctuation kinetic energy equation, as proposed by Louge (2003), enables his model to capture the trend of granular temperature in the intermediate flow regime. This can be considered as the main improvement over the previous two models. The slopes of the granular temperature lines in the intermediate regime decrease with the increase of the characteristic mean shear velocity as shown in Figure 6.3(d). It is interesting to note that this trend is also reflected in the prediction of the Louge (2003) model. Louge and Keast (2001) also showed that the production of fluctuation kinetic energy by the work of frictional shear stress is necessary for the existence of Steady Fully Developed (SFD) flows down a flat-frictional inclined surface for most situations of practical interest.

In general, the Louge (2003) model performs well in capturing the entire extended critical state framework.

6.3 The Proposed Unified Constitutive Model

A prominent approach in developing a unified model has consisted of the direct addition of frictional and collisional stress contributions, as demonstrated by the models presented in the previous sections. The approach is a simplified ad hoc assumption, as it is not clear how the two stress contributions act together.

Different approaches for developing unified models have been also presented in the literature, some of which are discussed in Chapter 2 (Mills et al., 1999; Ancey & Evesque, 2000). Mills et al. (1999) approached the problem from the microscopic interaction of particles during the flow. They explained the co-existence of strong and weak contact force networks in a dense granular flow and modeled the flow as a network of transient solid chains (strong networks) immersed in an assembly of particles behaving as a viscous fluid (weak networks). The strong contact network supports the whole deviatoric load (like a

solid) while the weak contact network contributes to the isotropic pressure (like a fluid). A particle may belong to either of the networks at any given time.

Our approach to the unified constitutive modeling of granular flows is also by exploring the microscopic interaction of particles, similar to Mills et al.'s (1999) approach. However, we consider the co-existence of frictional and collisional mechanisms instead, as proposed in the microscopic description of granular flows by Sayed (1981). As shown in Figure 6.4, the clusters of particles in the intermediate flow regime would undergo a frictional mechanism, yielding the rate-independent stress component while the remaining scattered particles (or colliding particles) interact only by collisions with themselves and with the clusters and contribute the rate-dependent stress component. The clusters of particles exist in the transient form in which they are formed and break up in random fashion. A given particle may be involved in either of the flow mechanisms at a time. As discussed in Chapter 2, the clusters of particles (or blocks) were also observed in the high-speed motion pictures taken from inclined chute flows of spherical particles (Drake, 1990).

In the subsequent sections, a unified constitutive model is developed for a dry granular flow by exploring the particle interactions inside a flow based on the microscopic description proposed by Sayed (1981), as discussed above, and by considering some analogies in the transition of ice to water. The constitutive equation involves an empirical equation for a stress-coefficient which is suggested based on the experimentally observed variations of granular temperature with void ratio at different constant-shear-rates.

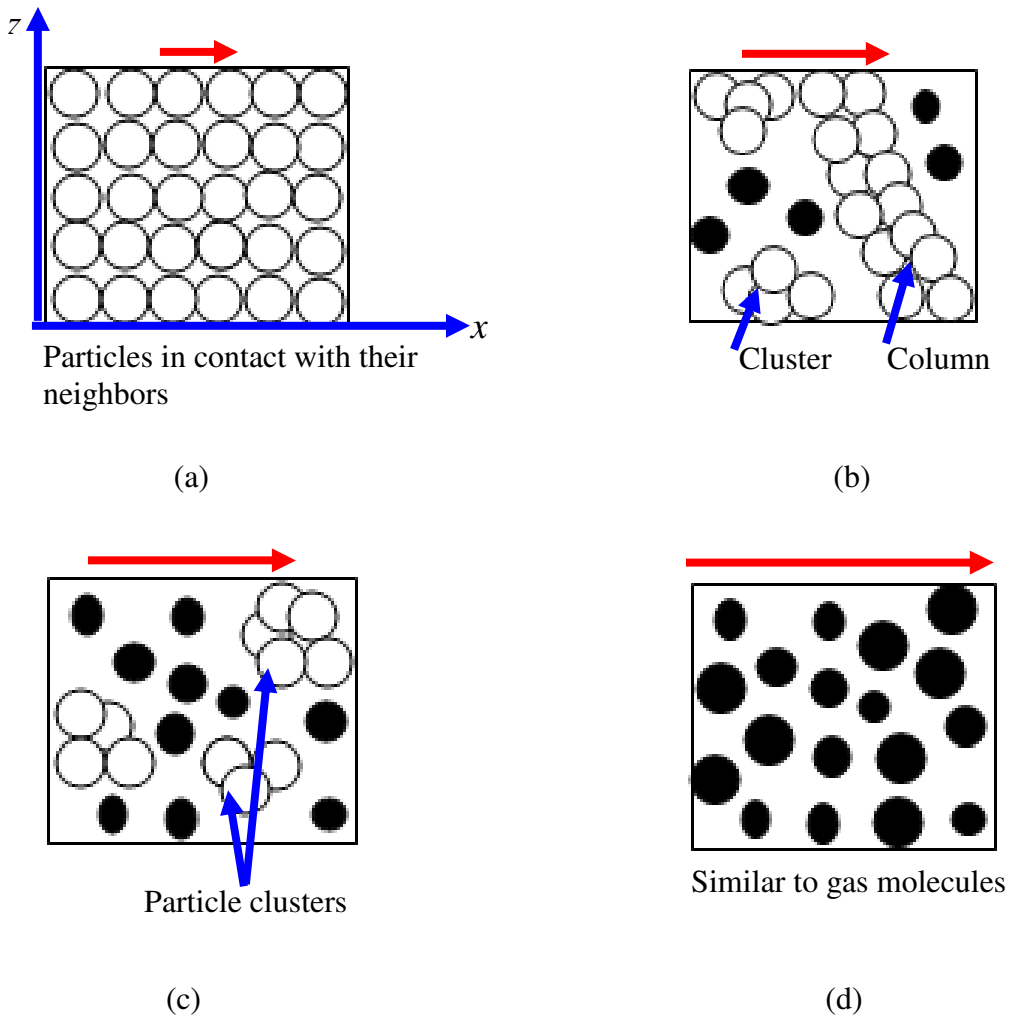

FIGURE 6.4: Proposed microscopic description of granular flow with increase of shear rate and void ratio; (a) quasi-static regime, (b) & (c) intermediate regimes, and (d) fully collisional regime (based on Sayed, 1981).

6.3.1 The Basis of the Proposed Model

A state of granular flow is described by the two state variables of void ratio e, and characteristic mean shear velocity, $\dot{\gamma}d$. If a unit volume of granular particles at an intermediate flow state $(e, \dot{\gamma}d)$ is considered, it can be inferred from the microscopic description of Sayed (1981) discussed above that both frictional and collisional flow mechanisms exist simultaneously in the unit volume. However,

the exact states at which these mechanisms exist (i.e., the critical state void ratio and shear rate, e_{cs} & $\dot{\gamma}_{cs}$, of the frictional state and the collisional void ratio and shear rate of the collisional state, e_c & $\dot{\gamma}_c$) are not clearly known. Since their detailed specification is important for constitutive modeling, it is essential to describe the microscopic description one step further, as follows.

All states of granular flow can be represented in a void ratio – normal stress – mean shear velocity framework, as shown in Figure 5.2. It is obvious that the state of the frictional flow lies on the critical state line (CSL). On the other hand, the state of the collisional flow can be anywhere above the collisional-intermediate boundary line (CIBL). We made our first assumption here that the collisional mechanism in the unit volume of granular particles at the intermediate flow state would exist at the CIBL. We support our assumption by considering the analogous transition of ice to water.

During the transition of ice to water, the supplied heat (external energy) will be fully used to transform ice just to water by breaking up molecular bonds. It will not be used to increase the temperature of the water until all ice changes to water. The state of the water (0 °C as expressed by its temperature) during the phase change is the lowest bound state of water (namely, water exists at temperature of 0 °C and above). By the same analogy, in the intermediate granular flow, the applied external energy, through shear work, will be fully devoted to transform the clusters of particles (like "ice") to independent solid particles (like "water") by breaking up the force network. The individual solid particles will interact only by collision and will attain the lowest bound collisional state, i.e., the state at CIBL. They will progress to the higher collisional state above the CIBL after all particles clusters are transformed to independently interacting particles.

In general, the intermediate flow state is assumed to be composed of the frictional state component at the CSL and the collisional state component at the CIBL, as shown in Figure 6.5.

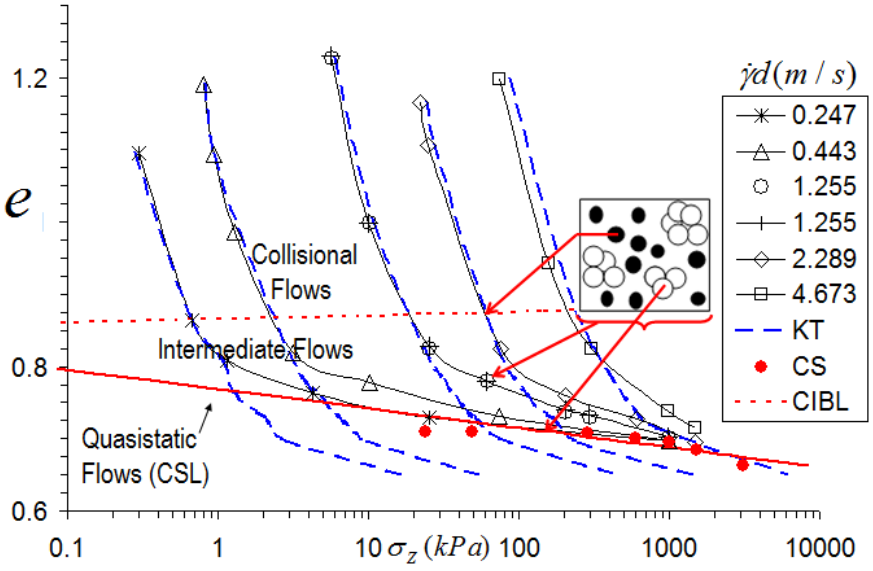

FIGURE 6.5: Intermediate flow state and its quasi-static and collisional components.

6.3.2 Model Formulations

Referring to Figures 6.5 & 6.6, the particle clusters exist at a state of $(e_{cs}, \dot{\gamma}_{cs} d)$ and the colliding particles exist at a state of $(e_c, \dot{\gamma}_c d)$ while all the particles in the unit volume exist at an average intermediate flow state of $(e, \dot{\gamma} d)$. The total stress in the unit volume may then be given by

$$\sigma_x(e, \dot{\gamma} d) = F_2 \cdot \sigma_x^f(e_{cs}) + F_1 \cdot \sigma_x^{k/c}(e_c, \dot{\gamma}_c d), \tag{6.6a}$$

$$\sigma_z(e, \dot{\gamma} d) = F_2 \cdot \sigma_z^f(e_{cs}) + F_1 \cdot \sigma_z^{k/c}(e_c, \dot{\gamma}_c d), \tag{6.6b}$$

$$\tau_{xz}(e, \dot{\gamma} d) = F_2 \cdot \tau_{xz}^f(e_{cs}) + F_1 \cdot \tau_{xz}^{k/c}(e_c, \dot{\gamma}_c d), \tag{6.6c}$$

where F_1 & F_2 are the fractions of volumes (or volumes, because a unit total volume is considered) occupied by particles in the collisional and frictional mechanisms, respectively, the frictional stresses are the stresses in the particle clusters, and the kinetic/collisional stresses are the stresses in the colliding particles. The sum of the volume fractions is equal to unity. In a quasi-static flow, F_1 is zero and the total stress is reduced to the frictional stress. In a fully collisional flow, F_1 is equal to unity and the total stress is reduced to the kinetic/collisional stress.

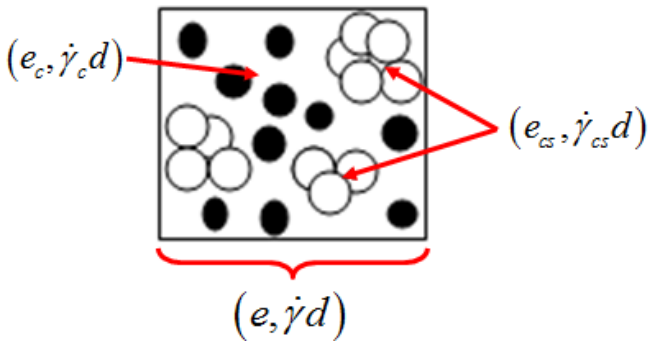

FIGURE 6.6: Representation of a unit-volume of particles at an intermediate flow state.

The governing equations of flow (continuity, momentum, and energy equations) are expressed in terms of flow state variables $(e, \dot{\gamma} d)$. Thus, in order to implement the above proposed model into flow equations, the frictional and kinetic/collisional stress components have to be expressed as functions of $(e, \dot{\gamma} d)$.

The *frictional, vertical normal stress component* can be derived from the critical state line equation provided in Eq. (6.3a) as

$$\sigma_z^f \left(e_{cs}\right) = 10^{\frac{\Gamma - e_{cs}}{\lambda}}. \tag{6.7a}$$

Eq. (6.7a) can be re-written as

$$\sigma_z^f\left(e_{cs}\right)=10^{\frac{\Gamma-e_{cs}}{\lambda}}=10^{\frac{\Gamma-e}{\lambda}}\cdot 10^{\frac{e-e_{cs}}{\lambda}}=\sigma_z^f\left(e\right)\cdot 10^{\frac{e-e_{cs}}{\lambda}}, \tag{6.7b}$$

where

$$\sigma_z^f\left(e\right)=10^{\frac{\Gamma-e}{\lambda}}. \tag{6.7c}$$

Eq. (6.7c) is obtained by substituting e_{cs} with e in Eq. (6.7a). Hence, the *frictional vertical normal stress component* in Eq. (6.6b), $\sigma_z^f\left(e_{cs}\right)$, can be expressed in terms of $\sigma_z^f\left(e\right)$ using Eq. (6.7b) as

$$\sigma_z^f\left(e_{cs}\right)=10^{\frac{e-e_{cs}}{\lambda}}\cdot\sigma_z^f\left(e\right). \tag{6.7d}$$

Then, the *frictional shear stress component* in Eq. (6.6c), $\tau_{xz}^f\left(e_{cs}\right)$, is expressed in terms of $\tau_{xz}^f\left(e\right)$ by taking the product of the critical state friction coefficient and Eq. (6.7d) as

$$\tau_{xz}^f\left(e_{cs}\right)=10^{\frac{e-e_{cs}}{\lambda}}\cdot\tau_{xz}^f\left(e\right), \tag{6.7e}$$

where $\tau_{xz}^f\left(e_{cs}\right)=\mu_{cs}\cdot\sigma_z^f\left(e_{cs}\right)$ & $\tau_{xz}^f\left(e\right)=\mu_{cs}\cdot\sigma_z^f\left(e\right)$. (6.7f)

For the *kinetic/collisional part*, the *vertical normal* and *shear stress components* can be obtained from Lun et al. (1984) kinetic theory (Eq. 6.2a & 6.2b), which are re-written below

$$\sigma_z^{k/c}(e,\dot{\gamma}d)=\rho\cdot g_1(e)\cdot T(e,\dot{\gamma}d), \tag{6.8a}$$

$$\tau_{xz}^{k/c}(e,\dot{\gamma}d)=\rho\cdot g_2(e)\cdot\dot{\gamma}d\cdot\sqrt{T(e,\dot{\gamma}d)}. \tag{6.8b}$$

Eqs. (6.8a) & (6.8b) can also be expressed in terms of the collisional state $(e_c, \dot{\gamma}_c d)$ by substituting e with e_c and $\dot{\gamma}$ with $\dot{\gamma}_c$ as

$$\sigma_z^{k/c}(e_c, \dot{\gamma}_c d) = \rho \cdot g_1(e_c) \cdot T_c(e_c, \dot{\gamma}_c d), \tag{6.8c}$$

$$\tau_{xz}^{k/c}(e_c, \dot{\gamma}_c d) = \rho \cdot g_2(e_c) \cdot \dot{\gamma}_c d \cdot \sqrt{T_c(e_c, \dot{\gamma}_c d)}. \tag{6.8d}$$

Hence, the *kinetic/collisional vertical normal stress component* in Eq. (6.6b), $\sigma_z^{k/c}(e_c, \dot{\gamma}_c d)$, can be expressed in terms of $\sigma_z^{k/c}(e, \dot{\gamma} d)$ using Eq. (6.8a) & (6.8c) as

$$\sigma_z^{k/c}(e_c, \dot{\gamma}_c d) = \frac{g_1(e_c) \cdot T_c(e_c, \dot{\gamma}_c d)}{g_1(e) \cdot T(e, \dot{\gamma} d)} \sigma_z^{k/c}(e, \dot{\gamma} d). \tag{6.8e}$$

Similarly, the *kinetic/collisional shear stress component* in Eq. (6.6c), $\tau_{xz}^{k/c}(e_c, \dot{\gamma}_c d)$, can be expressed in terms of $\tau_{xz}^{k/c}(e, \dot{\gamma} d)$ using Eq. (6.8b) & (6.8d) as

$$\tau_{xz}^{k/c}(e_c, \dot{\gamma}_c d) = \frac{g_2(e_c) \dot{\gamma}_c d \sqrt{T_c(e_c, \dot{\gamma}_c d)}}{g_2(e) \dot{\gamma} d \sqrt{T(e, \dot{\gamma} d)}} \tau_{xz}^{k/c}(e, \dot{\gamma} d). \tag{6.8f}$$

The total stresses in Eq. (6.6) are then expressed as

$$\sigma_x(e, \dot{\gamma} d) = \beta_2 \cdot \sigma_x^f(e) + \beta_3 \cdot \sigma_x^{k/c}(e, \dot{\gamma} d) = {}_{\beta}\sigma_x^f + {}_{\beta}\sigma_x^{k/c}, \tag{6.9a}$$

$$\sigma_z(e, \dot{\gamma} d) = \beta_2 \cdot \sigma_z^f(e) + \beta_3 \cdot \sigma_z^{k/c}(e, \dot{\gamma} d) = {}_{\beta}\sigma_z^f + {}_{\beta}\sigma_z^{k/c}, \tag{6.9b}$$

$$\tau_{xz}(e, \dot{\gamma} d) = \beta_2 \cdot \tau_{xz}^f(e) + \beta_1 \cdot \tau_{xz}^{k/c}(e, \dot{\gamma} d) = {}_{\beta}\tau_{xz}^f + {}_{\beta}\tau_{xz}^{k/c}, \tag{6.9c}$$

where ${}_{\beta}\sigma_x^f$ & ${}_{\beta}\sigma_z^f$ are the modified frictional normal stresses, ${}_{\beta}\sigma_x^{k/c}$ & ${}_{\beta}\sigma_z^{k/c}$ are the modified kinetic/collisional normal stresses, ${}_{\beta}\tau_{xz}^f$ is the modified frictional shear stress, and ${}_{\beta}\tau_{xz}^{k/c}$ is the modified collisional shear stress; while, β_1, β_2 & β_3 are the stress coefficients given by

$$\beta_1 = F_1 \frac{g_2(e_c)\dot{\gamma}_c\sqrt{T_c(e_c,\dot{\gamma}_c d)}}{g_2(e)\dot{\gamma}\sqrt{T(e,\dot{\gamma}d)}}, \tag{6.9d}$$

$$\beta_2 = (1-F_1)\cdot 10^{\frac{e-e_{cs}}{\lambda}}, \tag{6.9e}$$

$$\beta_3 = F_1 \frac{g_1(e_c)\cdot T_c(e_c,\dot{\gamma}_c d)}{g_1(e)\cdot T(e,\dot{\gamma}d)}. \tag{6.9f}$$

The stress coefficients were arbitrarily set equal to unity in the previous constitutive equations (Johnson & Jackson, 1987; Savage, 1998; Louge, 2003). However, the above derivations may show that the stress coefficients are inter-dependent and may have values other than unity.

The stress coefficients depend on the unknowns e_{cs}, e_c, $\dot{\gamma}_c$, and F_1 in addition to the average void ratio and shear rate $(e,\dot{\gamma})$ at which the intermediate flow exists. Thus, additional four equations are required in order to determine the stress coefficients and hence the total stress at a given state of $(e,\dot{\gamma})$. The additional equations are derived in the subsequent paragraphs.

An intermediate flow regime is considered to exist between two limiting solid volume fractions, which are the maximum close packing solid volume fraction, v_s^m, and the random loose packing solid volume fraction, v_s^* (e.g., Ancey & Evesque, 2000; Berzi et al., 2011). The frictional stress contribution vanishes for

solid volume fractions less than v_s^* (Johnson, 1987; Savage, 1998; Berzi et al., 2011). Thus, the random loose packing solid volume fraction demarcates the collisional-intermediate boundary. Even though the collisional-intermediate boundary line (CIBL) discussed in Section 5.2.1 has generally a positive slope, its slope is so small that it can be ignored for the range of stresses in practice. Thus, CIBL can be considered as a horizontal line that passes through a random loose packing solid volume fraction, v_s^*. Therefore, by invoking the assumption stated in Section 6.3.1, the *first equation* can be derived as

$$v_s^c = \min\left(v_s^*, v_s\right), \tag{6.10a}$$

where $$v_s^c = \frac{1}{1+e_c}, \qquad v_s^* = \frac{1}{1+e^*}, \qquad v_s = \frac{1}{1+e}. \tag{6.10b}$$

One can also derive a *second equation* that relates the solid volume fractions in the unit volume of intermediate state in the same way the stresses are related in Eq. (6.6) as

$$v_s = F_2 \cdot v_s^{cs} + F_1 \cdot v_s^c, \tag{6.11a}$$

where $$v_s^{cs} = \frac{1}{1+e_{cs}}. \tag{6.11b}$$

The critical state void ratio could then be derived from Eq. (6.10) & (6.11) as

$$e_{cs} = \frac{1-F_1}{\frac{1}{1+e} - \min\left(\frac{1}{1+e}, \frac{1}{1+e^*}\right)F_1} - 1. \tag{6.12a}$$

For $e \geq e^*$, the kinetic/collisional volume fraction $F_1 = 1$ and the above equation gives a value of $e_{cs} = e$. However, the critical state void ratio is in the range of $e^m \leq e_{cs} \leq e^*$, where $e^m = (1 - v_s^m)/v_s^m$ is the minimum close packing void ratio. Thus, Eq. (6.12a) is limited to

$$e_{cs} = \min\left(e^*, \frac{1 - F_1}{\frac{1}{1+e} - \min\left(\frac{1}{1+e}, \frac{1}{1+e^*}\right) F_1} - 1 \right). \tag{6.12b}$$

A *third equation* can also be derived by considering that the kinetic energy in the unit volume of the intermediate flow state is contributed in the same way as the stresses are contributed in Eq. (6.6). The rate of kinetic energy provided by the total shear stress in the unit volume of the intermediate flow state, $\left[F_2 \cdot \tau_{xz}^f(e_{cs}) + F_1 \cdot \tau_{xz}^{k/c}(e_c, \dot{\gamma}_c d) \right] \cdot \dot{\gamma}$, consists of the rate of the kinetic energy contributions from the colliding particles, $\left[F_1 \cdot \tau_{xz}^{k/c}(e_c, \dot{\gamma}_c d) \right] \cdot \dot{\gamma}_c$, and from the particle clusters, $\left[F_2 \cdot \tau_{xz}^f(e_{cs}) \right] \cdot \dot{\gamma}_{cs}$. Hence, the rate of kinetic energy balance will take the form

$$\begin{aligned} \left[F_2 \cdot \tau_{xz}^f(e_{cs}) + F_1 \cdot \tau_{xz}^{k/c}(e_c, \dot{\gamma}_c d) \right] \cdot \dot{\gamma} \;=\; & \left[F_2 \cdot \tau_{xz}^f(e_{cs}) \right] \cdot \dot{\gamma}_{cs} \;+ \\ & \left[F_1 \cdot \tau_{xz}^{k/c}(e_c, \dot{\gamma}_c d) \right] \cdot \dot{\gamma}_c . \end{aligned} \tag{6.13a}$$

Therefore, the shear rates are related through the shear stresses as

$$\dot{\gamma} = \frac{F_2 \cdot \tau_{xz}^f(e_{cs})}{\tau_{xz}} \cdot \dot{\gamma}_{cs} + \frac{F_1 \cdot \tau_{xz}^{k/c}(e_c, \dot{\gamma}_c d)}{\tau_{xz}} \cdot \dot{\gamma}_c . \tag{6.13b}$$

Alternatively, the kinetic energy balance can be expressed in terms of the stress coefficients using Eq. (6.9d to f) as

$$\dot{\gamma} = \frac{\beta_2 \cdot \tau_{xz}^{f}(e)}{\tau_{xz}} \cdot \dot{\gamma}_{cs} + \frac{\beta_1 \cdot \tau_{xz}^{k/c}(e, \dot{\gamma}d)}{\tau_{xz}} \cdot \dot{\gamma}_c . \qquad (6.13c)$$

e_c can be determined from Eq. (6.10) by assuming that the colliding particles in the unit volume of the intermediate flow state will remain at the state of collisional-intermediate boundary (Sec. 6.3.1). Similarly, $\dot{\gamma}_{cs}$ can be determined by assuming that the particle clusters in the unit volume will remain at the state of quasi-static - intermediate boundary. This boundary can be determined by observing the behaviour of flow progression from quasi-static to intermediate regimes. A progression of granular flow occurs with shear rate in both conditions of constant void ratio and constant normal stress. It can be conveniently presented using a single dimensionless variable, called the *inertial number*, $I = \dot{\gamma}d\sqrt{\rho/\sigma_z}$, as proposed by Da Cruz et al. (2005). For example, the behaviour of the friction coefficient during flow progression is presented in Figure 5.5 using the variable *I*. At quasi-static state, the friction coefficient is rate independent. It starts to increase with shear rate at the boundary of quasi-static and intermediate regimes.

Defining the inertial number corresponding to the quasi-static and intermediate boundary as $I_{cs}^{*} = \dot{\gamma}_{cs}^{*} d\sqrt{\rho/\tau_{xz}}$ using the shear stress, the shear rate of particle clusters $\dot{\gamma}_{cs}$ in Eq. (6.13) can be taken as the shear rate of flow at the quasi-static - intermediate boundary $\dot{\gamma}_{cs}^{*}$.

The *fourth equation* required to complete the formulation of the constitutive model is derived by developing an empirical equation for the shear stress coefficient, β_1, in predicting the granular temperature. A series of plane shear simulations were conducted to produce experimental measurements of granular temperature at different flow states $(e, \dot{\gamma}d)$, as presented in Figure 5.6. The expression for the granular temperature is derived by assuming that only the kinetic/collisional shear work produces fluctuation energy (similar to the

assumption of Johnson and Jackson, 1987), and by substituting the modified kinetic/collisional shear stress of Eq. (6.9c), i.e., $\beta_1 \cdot \rho g_2 \dot{\gamma} d\sqrt{T}$, in the energy equation Eq. (6.2m) as

$$T = \beta_1 \frac{g_2(e)}{g_5(e)} (\dot{\gamma} d)^2 . \tag{6.14}$$

An empirical equation, given by Eq. (6.15), is suggested for β_1 in order to predict the measured granular temperatures presented in Figure 5.6 using Eq. (6.14). It reads

$$\beta_1 = \frac{\left(m_1 + m_2 (\dot{\gamma} d)^{m_3}\right) + \max\left(0, \frac{e^* - e}{|e^* - e|}\right) \cdot m_4 \cdot \exp\left((e^* - e)/m_5\right)}{\left(m_1 + m_2 (\dot{\gamma} d)^{m_3}\right)}, \tag{6.15}$$

where $m_{i=1,5}$ are constants that will be determined by fitting experimental results. For $e \geq e^*$, the stress coefficient $\beta_1 = 1$ and Eq. (6.14) will reduce to a pure collisional flow case (Eq. 6.2n). However, for intermediate flows ($e < e^*$), the expression for β_1 is proposed based on the assumption that the increase of the measured granular temperature is proportional to the ratio of the total stress to the kinetic/collisional stress component. Hence, the empirical equation for β_1 consists of the terms $\exp((e^* - e)/m_5)$ and $m_2(\dot{\gamma} d)^{m_3}$, which are analogous to the frictional and kinetic/collisional stress equations. The constant m_1 is introduced to avoid an undefined value of β_1 at $\dot{\gamma} d = 0$, and hence will be assigned a small value.

Once the kinetic/collisional shear stress coefficient, β_1, is determined from Eq. (6.15), the kinetic/collisional volume fraction F_1 is determined by substituting Eq.

(6.14) and $T_c = g_2(e_c)/g_5(e_c).(\dot{\gamma}_c d)^2$ into Eq. (6.9d) and solving it simultaneously with Eq. (6.13c). This yields

$$\beta_1 = \frac{\left[F_1^{2/3}\min(g_2(e^*), g_2(e))g_5(e)\right]^{1/3}\left[\sqrt{\rho}\dot{\gamma}d\tau_{xz} - \beta_2\tau_{xz}^f(e)I_{cs}^*\sqrt{\tau_{xz}}\right]^{4/9}}{g_2(e)\min(g_5(e^*), g_5(e))^{1/9}\left[\rho\dot{\gamma}^2 d^2\right]^{2/3}}. \quad (6.16)$$

The frictional stress coefficient, β_2, is then determined from Eqs. 6.9(e) and 6.12(b). The kinetic/collisional normal stress coefficient is also determined from Eqs. 6.9(f) and 6.13(c) as

$$\beta_3 = \frac{F_1^{1/3}\min(g_1(e^*), g_1(e))g_5(e)\left[\sqrt{\rho}\dot{\gamma}d\tau_{xz} - \beta_2\tau_{xz}^f(e)I_{cs}^*\sqrt{\tau_{xz}}\right]^{2/3}}{\beta_1 g_1(e)g_2(e)\min(g_5(e^*), g_5(e))^{2/3}\rho\dot{\gamma}^2 d^2}. \quad (6.17)$$

6.3.3 Flow Chart of the Proposed Model

The calculation steps using the proposed model are shown in the following flow chart.

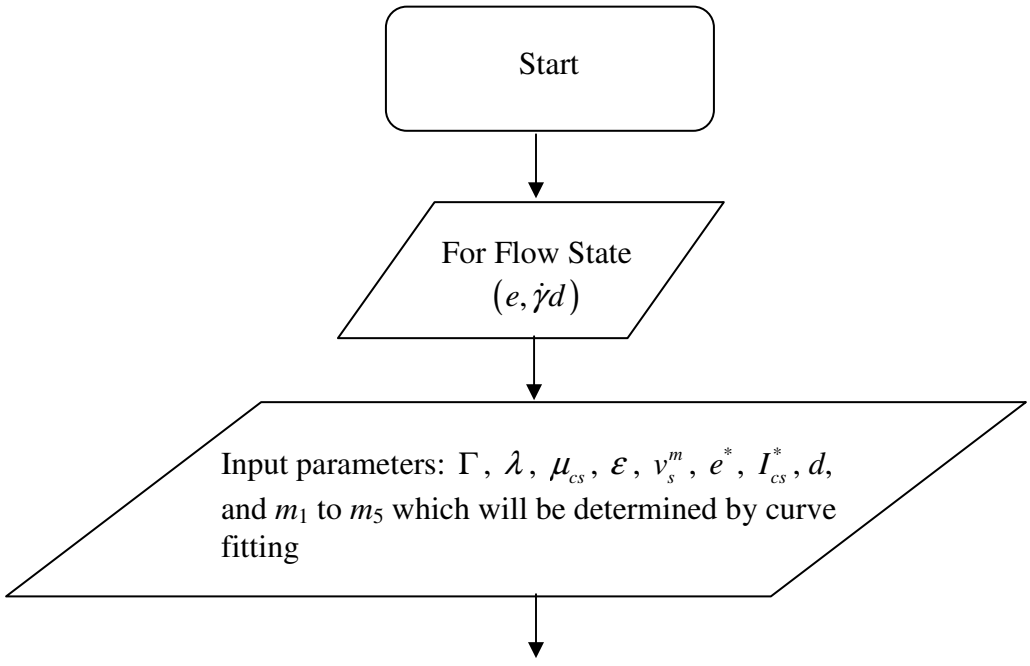

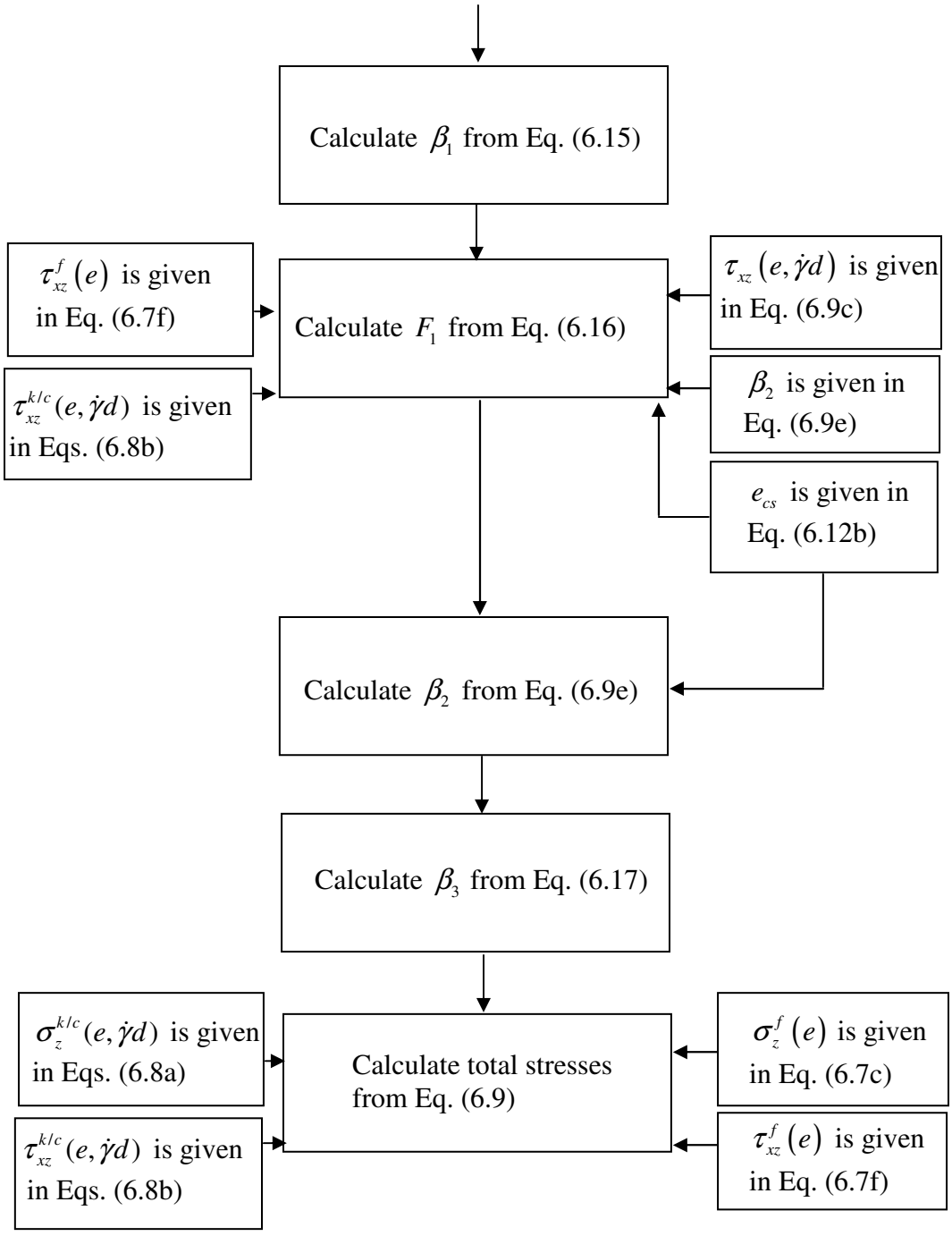
Calculate β_1 from Eq. (6.15)
$\tau_{xz}^{f}(e)$ is given in Eq. (6.7f)
$\tau_{xz}^{k/c}(e,\dot{\gamma}d)$ is given in Eqs. (6.8b)
Calculate F_1 from Eq. (6.16)
$\tau_{xz}(e,\dot{\gamma}d)$ is given in Eq. (6.9c)
β_2 is given in Eq. (6.9e)
e_{cs} is given in Eq. (6.12b)
Calculate β_2 from Eq. (6.9e)
Calculate β_3 from Eq. (6.17)
$\sigma_z^{k/c}(e,\dot{\gamma}d)$ is given in Eqs. (6.8a)
$\tau_{xz}^{k/c}(e,\dot{\gamma}d)$ is given in Eqs. (6.8b)
Calculate total stresses from Eq. (6.9)
$\sigma_z^{f}(e)$ is given in Eq. (6.7c)
$\tau_{xz}^{f}(e)$ is given in Eq. (6.7f)

6.4 Verification of the Proposed Unified Constitutive Model

6.4.1 The Extended Critical State Framework

The proposed unified constitutive model in Sec. 6.3 is used to predict the extended critical state framework presented in Chapter 5. The model parameters used in the calculations are given in Table 6.3.

TABLE 6.3: Values of parameters used in the proposed model.

Γ	λ	μ_{cs}	ε	v_s^m	e^*	I_{cs}^*	m_1	m_2	m_3	m_4	m_5
0.85	0.027	0.34	0.81	0.61	0.85	10^{-5}	0.01	250	0.5	1	0.027

The constants $m_{i=1,5}$ of the empirical equation for β_1 were determined by curve fitting the granular temperature measurements, as shown in Figure 6.7(a). Following the determination of β_1, the proposed constitutive model is used to predict the stresses and friction coefficient in the extended critical state framework. The predictions of the entire extended critical state framework are presented in Figure 6.7.

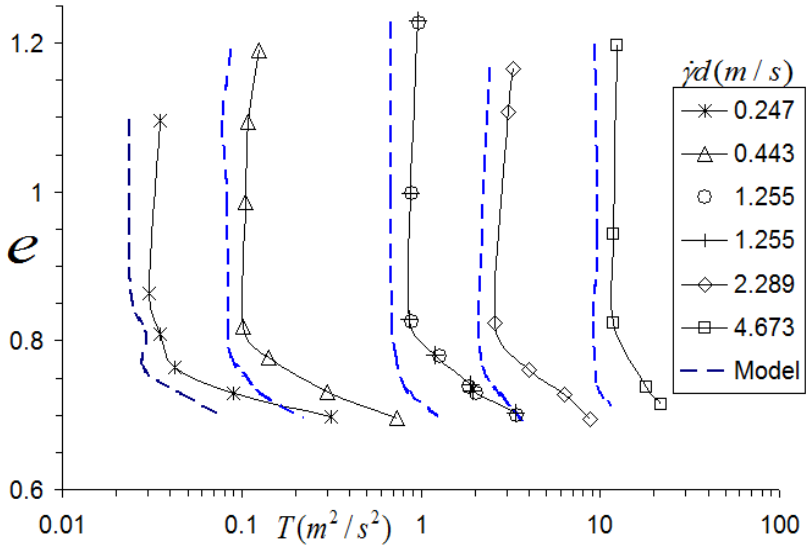

(a)

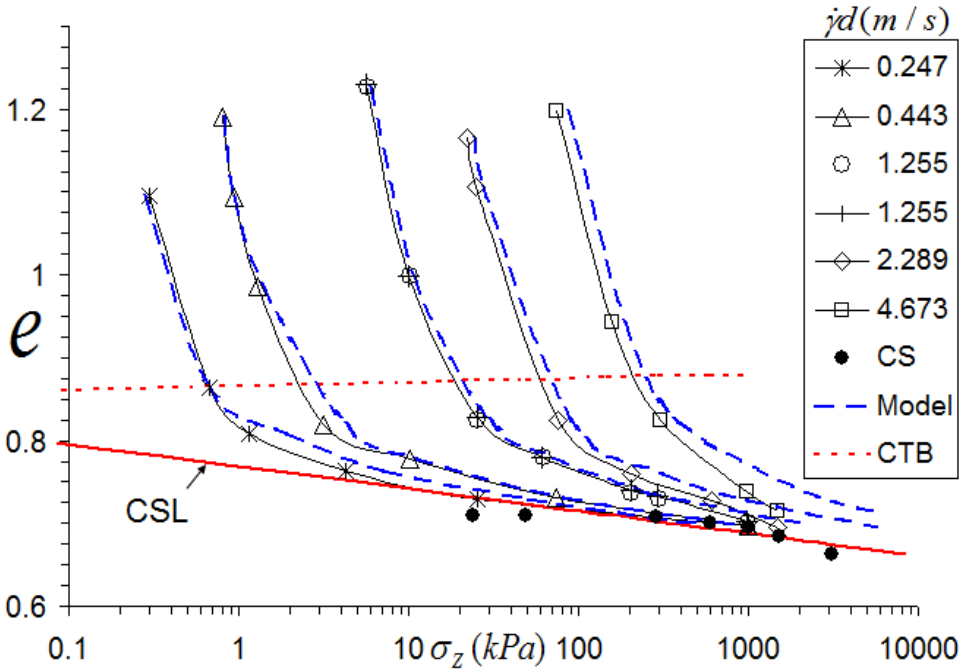
$\dot{\gamma}d(m/s)$
0.247
0.443
1.255
1.255
2.289
4.673
CS
Model
CTB
CSL
e
1.2
1
0.8
0.6
0.1
1
10
100
1000
10000
$\sigma_z(kPa)$

(b)

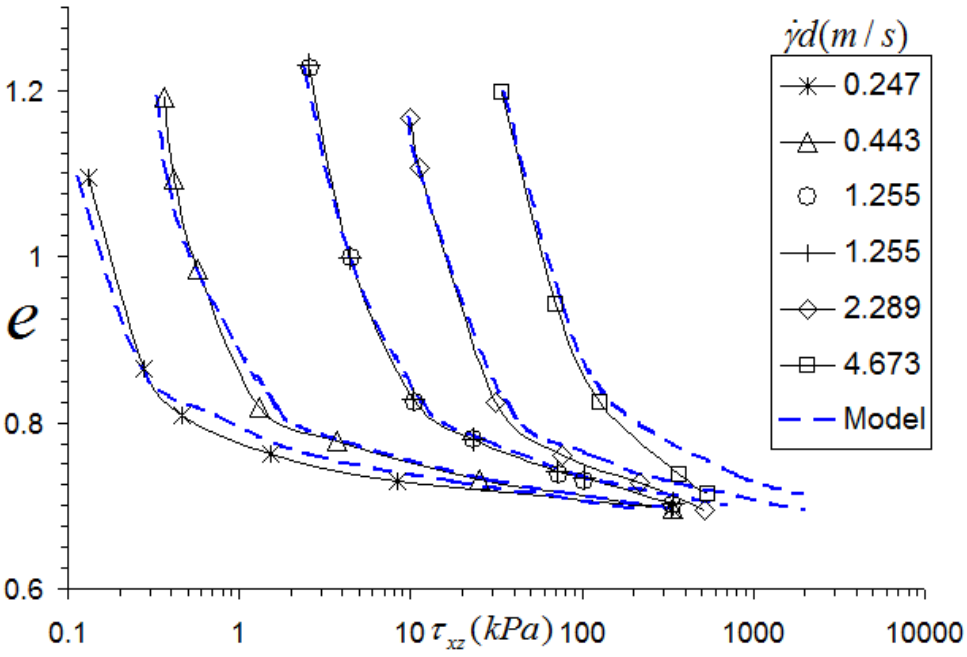
$\dot{\gamma}d(m/s)$
0.247
0.443
1.255
1.255
2.289
4.673
Model
e
1.2
1
0.8
0.6
0.1
1
10
100
1000
10000
$\tau_{xz}(kPa)$

(c)

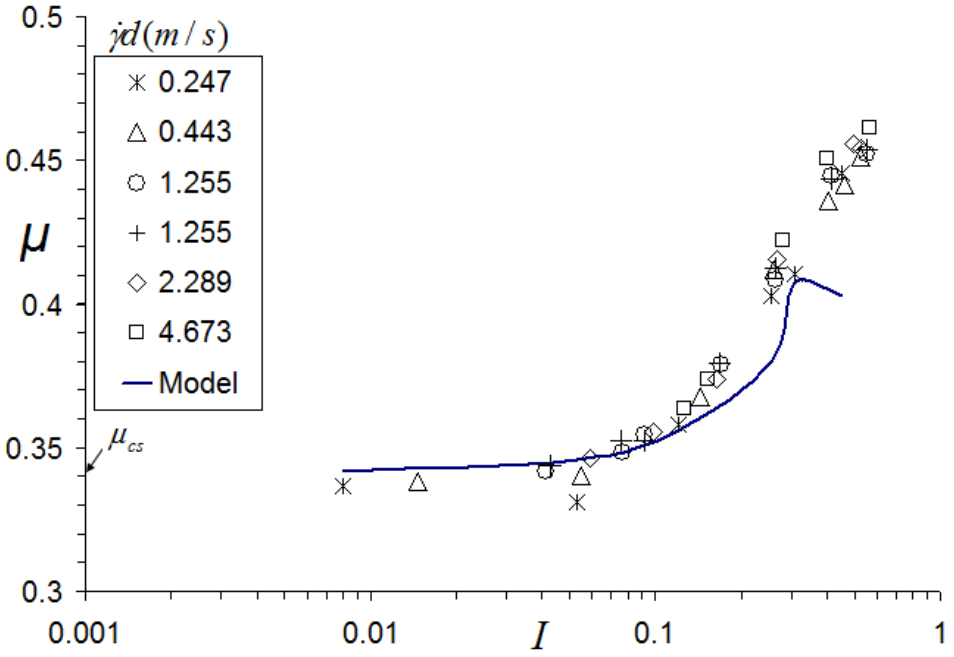

(d)

FIGURE 6.7: Predictions of the proposed constitutive model: (a) granular temperature, (b) vertical normal stress, (c) shear stress, and (d) friction coefficient for $\dot{\gamma}d = 0.247$.

In general, the proposed model captures the extended critical state framework by predicting granular temperature, stresses, and friction coefficient as shown in Figure 6.7. The model predictions have agreed well with the simulation experiments, except some over prediction of normal and shear stresses at high stress levels and high characteristic velocities.

6.4.2 Inclined Flows

6.4.2.1 Governing Equations

Johnson (1987) and Nott (1991) implemented the Savage (1982) model in the governing equations of flow and solved for inclined plane geometry using a finite difference numerical scheme. A similar approach is also followed in this research to implement the proposed constitutive model for inclined flows.

The general forms of the mass, momentum, and fluctuation energy equations are presented, respectively as

$$\frac{d\rho}{dt} + \rho\nabla \cdot u = 0, \tag{6.18a}$$

$$\rho\frac{du}{dt} = \rho b + \nabla \cdot \sigma, \tag{6.18b}$$

$$\tfrac{3}{2}\rho\frac{dT}{dt} = \sigma^{k/c} : \nabla u - \nabla \cdot q_s - \Upsilon, \tag{6.18c}$$

where u is the velocity, b is the specific body force, σ is the total stress, $\sigma^{k/c}$ is the kinetic/collisional stress component (the last terms of Eq. 6.9a to 6.9c), q_s is the flux of fluctuation kinetic energy, and Υ is the rate of dissipation of fluctuation energy per unit volume due to the inelastic collisions. For steady, fully developed (SFD), two-dimensional inclined flows, the derivatives parallel to the inclined plane are zero. Therefore, the continuity equation is automatically satisfied and the momentum and fluctuation energy equations are reduced to

$$\frac{\partial\sigma_z}{dz} = \rho v_s g\cos\theta, \tag{6.19a}$$

$$\frac{\partial\tau_{xz}}{dz} = \rho v_s g\sin\theta, \tag{6.19b}$$

$$0 = \left(\beta_1 \cdot \tau_{xz}^{k/c}\right)\cdot\dot{\gamma} - \frac{\partial q_s}{\partial z} - \Upsilon, \tag{6.19c}$$

where g is the acceleration of gravity and θ is the inclination angle of inclined flow. The constitutive equations for stresses, flux of fluctuation energy, and rate of energy dissipation per unit volume due to inelastic collisions are presented in Eq. (6.9), Eq. (6.2h), and Eq. (6.2i), respectively.

The stress and energy boundary conditions at the bottom solid surface ($Z = 0$) and top free surface ($Z = 1$) are derived by Johnson (1987), as shown below in Eq. (6.20) and Eq. (6.21), respectively. Z is defined as z/H where z is the axis normal to the flow and H is the total flow depth.

At $Z = 0$

$$\tau_{xz} = \frac{\varphi\pi\sqrt{3}\rho v_s \beta_1 \sqrt{T}\,|u_{sl}|}{6v_s^m\left[1-(v_s / v_s^m)^{1/3}\right]} + \left(\beta_2 \cdot \sigma_z^f\right)\tan\delta\,, \tag{6.20a}$$

$$-q_s = -\frac{\varphi\pi\sqrt{3}\rho v_s \beta_1 \sqrt{T}\,|u_{sl}|^2}{6v_s^m\left[1-(v_s / v_s^m)^{1/3}\right]} + \frac{\pi\sqrt{3}\rho v_s T^{3/2}(1-\varepsilon_w^2)}{4v_s^m\left[1-(v_s / v_s^m)^{1/3}\right]}. \tag{6.20b}$$

At $Z = 1$

$$\sigma_z = \frac{\pi}{6}\rho g d\cos\theta\left(\frac{v_s(Z=1)}{v_s^m}\right)^{2/3}, \tag{6.21a}$$

$$\tau_{xz} = \frac{\pi}{6}\rho g d\sin\theta\left(\frac{v_s(Z=1)}{v_s^m}\right)^{2/3}, \tag{6.21b}$$

$$q_s = 0\,. \tag{6.21c}$$

where φ is the *specularity coefficient*[5] at the bottom surface, u_{sl} is the slip velocity at the bottom surface, δ is the angle of friction at the bottom surface, ε_w is the restitution coefficient at the particle to bottom surface collision, and $v_s(Z=1)$ is the solid volume fraction at the free surface. The second term of Eq.

[5] Specularity coefficient represents the fraction of tangential momentum change of particles to their momentum after collision at the bottom boundary.

(6.20a) is the shear stress at the boundary due to collisions between the particles and the bottom surface. In principle, the stresses at the free surface are zero. However, it implies that the density is also zero which contradicts the practical condition. Hence, Equations 6.21(b) & (c) were derived by assuming the stress at the free surface is provided by the weight of the topmost layer of particles (Johnson, 1987). It should be noted that Eqs. (6.20) & (6.21) are modified by introducing the stress coefficients β_1 and β_2 based on the proposed constitutive equation, Eq. (6.9).

Substituting the constitutive equations (Eq. 6.9) and boundary conditions (Eq. 6.20 & Eq. 6.21) into the equations of motion (Eq. 6.19) yields

For 0 < Z < 1 (between the bottom boundary and the free surface)

$$\beta_2 \hat{\sigma}_z^f + \beta_3 g_1 \hat{T} = \tfrac{H}{d} \int_Z^1 v_s dZ + \tfrac{\pi}{6} \left(\tfrac{v_s(Z=1)}{v_s^m} \right)^{2/3}, \tag{6.22a}$$

$$\beta_2 \hat{\sigma}_z^f \tan\phi + \beta_1 g_2 \sqrt{\hat{T}} \left(\tfrac{\tan\theta}{H/d} \right)^{1/2} \frac{d\hat{u}}{dZ} = \tfrac{H}{d} \tan\theta \int_Z^1 v_s dZ + \tan\theta \tfrac{\pi}{6} \left(\tfrac{v_s(Z=1)}{v_s^m} \right)^{2/3}, \tag{6.22b}$$

$$\frac{\partial}{\partial Z} \left(g_3 \sqrt{\hat{T}} \frac{d\hat{T}}{dZ} + g_4 \hat{T}^{3/2} \frac{dv_s}{dZ} \right) + \tan\theta \frac{H}{d} \beta_1 g_2 \sqrt{\hat{T}} \left(\frac{d\hat{u}}{dZ} \right)^2 - \left(\frac{H}{d} \right)^2 g_5 \hat{T}^{3/2} = 0 . \tag{6.22c}$$

At Z = 0 (at the bottom boundary surface)

$$\beta_2 \hat{\sigma}_z^f + \beta_3 g_1 \hat{T} = \tfrac{H}{d} \int_0^1 v_s dZ + \tfrac{\pi}{6} \left(\tfrac{v_s(Z=1)}{v_s^m} \right)^{2/3}, \tag{6.22d}$$

$$\beta_2\hat{\sigma}_z^f \tan\phi + \beta_1 g_2 \sqrt{\hat{T}} \left(\tfrac{\tan\theta}{H/d}\right)^{1/2} \frac{d\hat{u}}{dZ} = \left(\tfrac{H}{d}\tan\theta\right)^{1/2} \frac{\pi\sqrt{3}\varphi\beta_1 v_s g_0 \hat{u}\sqrt{\hat{T}}}{6v_s^m} + \beta_2\hat{\sigma}_z^f \tan\delta, \tag{6.22e}$$

$$g_3 \frac{d\hat{T}}{dZ} + g_4 \hat{T} \frac{dv_s}{dZ} = \tfrac{H}{d}\left(1-\varepsilon_w^2\right)\hat{T}\frac{\pi\sqrt{3}v_s g_0}{4v_s^m} - \left(\tfrac{H}{d}\right)^2 \tan\theta \frac{\varphi\beta_1\pi\sqrt{3}v_s g_0}{6v_s^m}\hat{u}^2. \tag{6.22f}$$

At Z = 1 (at the top free surface)

$$\beta_2\hat{\sigma}_z^f + \beta_3 g_1 \hat{T} = \tfrac{\pi}{6}\left(\tfrac{v_s(Z=1)}{v_s^m}\right)^{2/3}, \tag{6.22g}$$

$$\beta_2\hat{\sigma}_z^f \tan\phi + \beta_1 g_2 \sqrt{\hat{T}} \left(\tfrac{\tan\theta}{H/d}\right)^{1/2} \frac{d\hat{u}}{dZ} = \tan\theta \frac{\pi}{6}\left(\tfrac{v_s(Z=1)}{v_s^m}\right)^{2/3}, \tag{6.22h}$$

$$g_3 \frac{d\hat{T}}{dZ} + g_4 \hat{T} \frac{dv_s}{dZ} = 0. \tag{6.22i}$$

where the dimensionless variables are given by

$$Z = \frac{z}{H}, \quad \hat{u} = \frac{u}{(gH\sin\theta)^{1/2}}, \quad \hat{T} = \frac{T}{gd\cos\theta}, \quad \hat{\sigma}_z^f = \frac{\sigma_z^f}{\rho g d\cos\theta}. \tag{6.22j}$$

A restriction of $d\hat{u}/dZ \geq 0$ is imposed for the momentum equations in the direction of shear, i.e. Eq. (6.22b), Eq. (6.22e), and Eq. (6.22h). Shear rate cannot be negative because it will yield the kinetic/collisional shear stress negative, which implies that the stress would aid motion instead of resisting.

6.4.2.2 Numerical Solutions

The flow depth, *Z*, of inclined flow is divided into *N* nodes of *N*-1 equal segments. The equations of motions presented in Eq. (6.22) are then discretized using the finite difference technique. For interior nodes, the differential equations are discretized using central difference approximations. An example is shown in Eq. (6.23) for the first and second derivatives of dimensionless granular temperature at interior node i

$$\frac{d\hat{T}}{dZ} = \frac{\hat{T}_{i+1} - \hat{T}_{i-1}}{2 \cdot \Delta Z}, \tag{6.23a}$$

$$\frac{d^2\hat{T}}{dZ^2} = \frac{\hat{T}_{i+1} - 2\hat{T}_i + \hat{T}_{i-1}}{(\Delta Z)^2}, \tag{6.23b}$$

where $\Delta Z = 1/(N-1)$ is the distance between consecutive nodes. For the bottom surface boundary, the differential equations are discretized using forward difference approximations, as shown in Eq. (6.24) for the case of the derivative of the dimensionless granular temperature at the bottom boundary node 1

$$\frac{d\hat{T}}{dZ} = \frac{-3\hat{T}_1 + 4\hat{T}_2 - \hat{T}_3}{(2\Delta Z)}. \tag{6.24}$$

Finally for the top surface boundary, the differential equations are discretized using backward difference approximations, as shown in Eq. (6.25) for the case of the derivative of the dimensionless granular temperature at the free surface node *N*

$$\frac{d\hat{T}}{dZ} = \frac{3\hat{T}_N - 4\hat{T}_{N-1} + \hat{T}_{N-2}}{(2\Delta Z)}. \tag{6.25}$$

On the other hand, the integrals in the governing equations are approximated by the trapezoidal rule. An example is given in Eq. (6.26) for solid volume fraction,

$$\int_0^1 v_s dZ = \sum_{i=1}^{N-1} \frac{\Delta Z}{2}\left(v_{s_i} + v_{s_{i+1}}\right). \tag{6.26}$$

The discretized governing equations form a set of $3N$ nonlinear algebraic equations

$$E_{m=1,3N} = 0. \tag{6.27}$$

The systems of nonlinear equations are solved based on a modified form of the Newton-Raphson method. Starting with guessed values of the variables at the nodes $v_{s_{i=1,N}}$, $\hat{T}_{i=1,N}$, and $\hat{u}_{i=1,N}$, the new values of the variables at each iteration are calculated using Eq. (6.28)

$$\text{var}^{new} = \text{var}^{old} - J^{-1} \cdot E(\text{var}^{old}) \cdot \alpha, \tag{6.28a}$$

$$J_{m,n} = \frac{\partial E_{m=1,3N}}{\partial \text{var}_{n=1,3N}}, \tag{6.28b}$$

where $\text{var}_{n=1,3N}$ stands for the variables $(v_{s_{i=1,N}}, \hat{u}_{i=1,N}, \hat{T}_{i=1,N})$, J is the Jacobian matrix of E, and α is a modified factor which is introduced in this research to reduce the increment values $J^{-1} \cdot E(\text{var}^{old})$ so that the new calculated values are non-negative $(\text{var}^{new} \geq 0)$.

The iteration of the numerical solution continues until convergence is achieved. Two criteria are set for convergence in this research. The first criterion requires

that the largest value of the magnitudes of the residuals must be less than a tolerance value R_1 as

$$\max\left(\left|E_{m=1,3N}\left(\text{var}\right)\right|\right) < R_1 . \tag{6.29a}$$

The second convergence criterion is similar to Mohan et al. (1997), which is presented as

$$\sqrt{\sum_{m=1}^{3N}(E_m\left(\text{var}\right)/A_m)^2} < R_2 , \tag{6.29b}$$

where $E_m\left(\text{var}\right)$ is the residual of the m^{th} equation, A_{m} is the magnitude of the largest element of the m^{th} row of the Jacobian matrix, and R_2 is a tolerance value.

The developed numerical model for inclined flow is written in a MATLAB program and presented in Appendix B.

6.4.2.3 Model Predictions

Profiles of dense granular flow depend on the roughness of the basal boundary surface (see Sec. 2.2.5). The proposed model is used to predict the simulation experiments of inclined flows on a bumpy-rough boundary conducted by Silbert et al. (2001) and on a flat-frictional boundary conducted in this research.

6.4.2.3.1 Inclined Flow on a Bumpy-Rough Boundary

Silbert et al. (2001) conducted inclined flow simulations of thick piles of mono-disperse spherical particles on a bumpy-rough boundary. The simulation results for H=40d and $\theta = 26^0$ are chosen in this research for the verification of the proposed model. The values of parameters used in the simulation experiment and in the unified model are presented in Table 6.4. The simulation results and the model predictions are compared in Figure 6.8.

The comparison shows that the proposed model captures the typical behaviours of inclined granular flows on a rough boundary, which are characterized by low granular temperature, high solid volume fraction, and low slip velocity at the rough base, as discussed in Sec. 2.2.5. These flow profiles were mainly captured by using a high coefficient of specularity (φ) for the rough bottom boundary. The restitution coefficient used in the model was lower than the value used in the simulation experiment, in order to obtain better predictions. It is also interesting to note the variation of kinetic/collisional volume fraction (F_1) over the depth of flow. It reveals the three distinct regions of dense granular flow over rough boundary, as discussed by Louge (2003), namely the thin basal frictional region, the middle core region, and the thin top collisional region. In general, the variation of F_1 follows the variation of granular temperature.

TABLE 6.4: Simulation and Model Parameters

Parameter	Simulation Experiment	Model
H/*d* of flow	40	40
Inclination angle of plane	26^0	26^0
Particle density		2500 kg/m^3
Particle diameter		1 mm
Restitution coefficient (ε and ε_w)	0.88	0.6
Friction angle	$\mu_s = 0.5$ (static friction coefficient between particles)	$\phi_{cs} = \delta = 24.5^0$
Γ	N/A	0.9
λ	N/A	0.035
Specularity coefficient (φ)	N/A	0.7854
v_S^m	N/A	0.61
m_1, m_2, m_3, m_4, m_5	N/A	0.01, 250, 0.5, 1, 0.035
e^*	N/A	0.9
I_{cs}^*	N/A	10^{-5}
Tolerance value, R_1	N/A	0.01
Tolerance value, R_2	N/A	1.69E-06

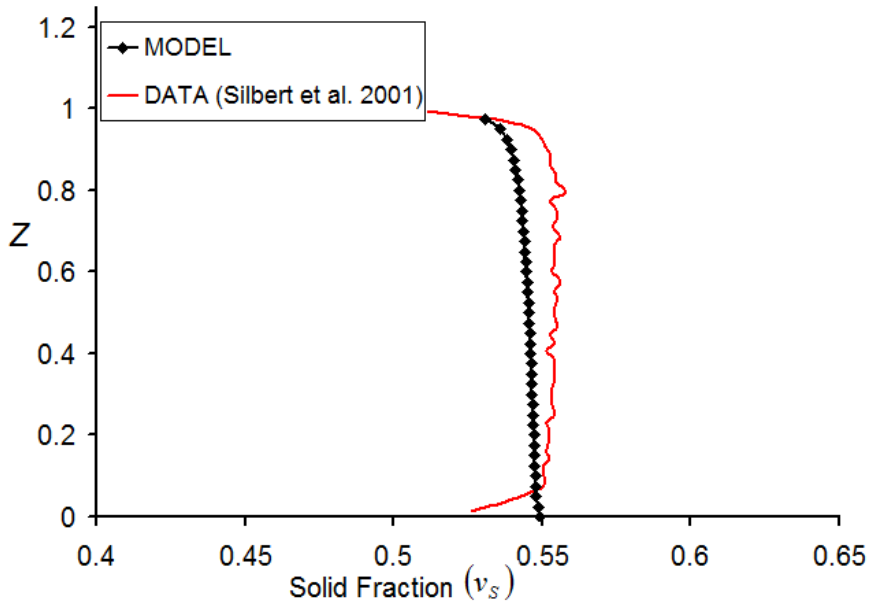

(a)

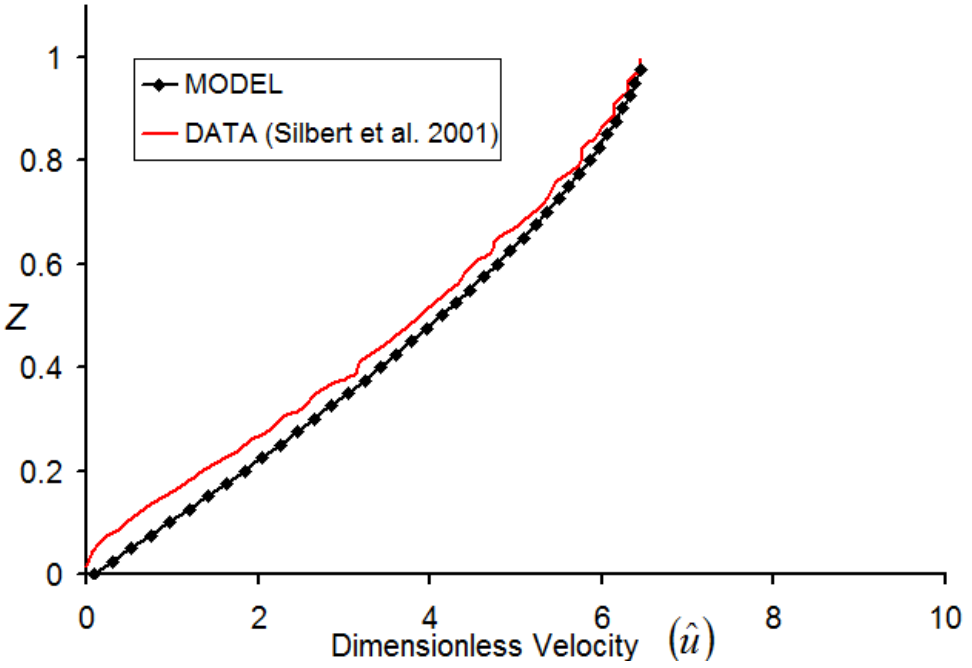
MODEL
DATA (Silbert et al. 2001)
Z
Dimensionless Velocity $(\hat{u})$
0
0.2
0.4
0.6
0.8
1
0
2
4
6
8
10

(b)

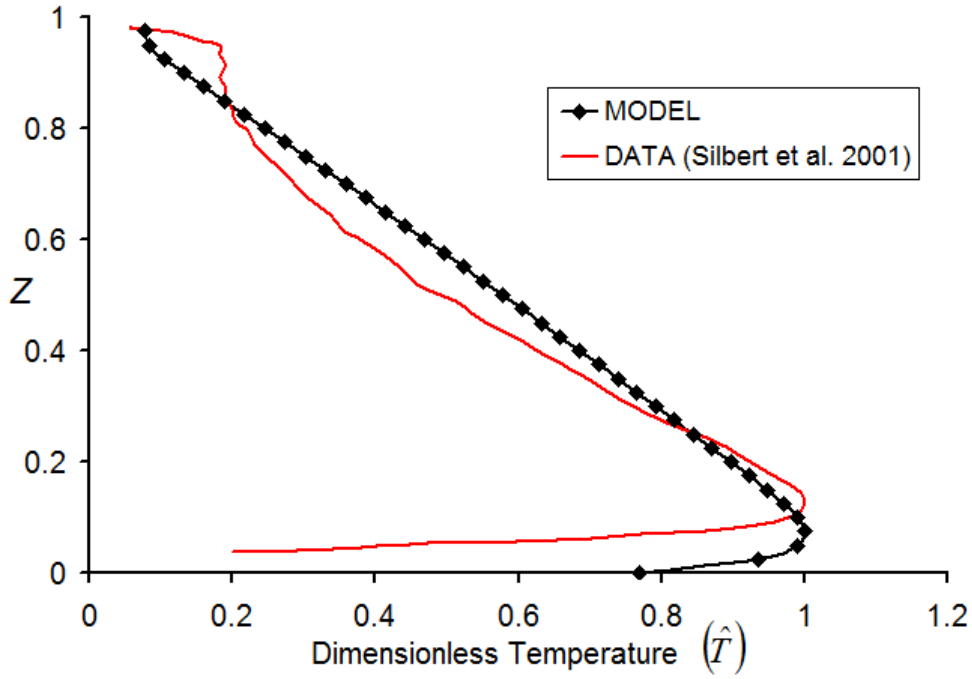
MODEL
DATA (Silbert et al. 2001)
Z
Dimensionless Temperature $(\hat{T})$
0
0.2
0.4
0.6
0.8
1
1.2

(c)

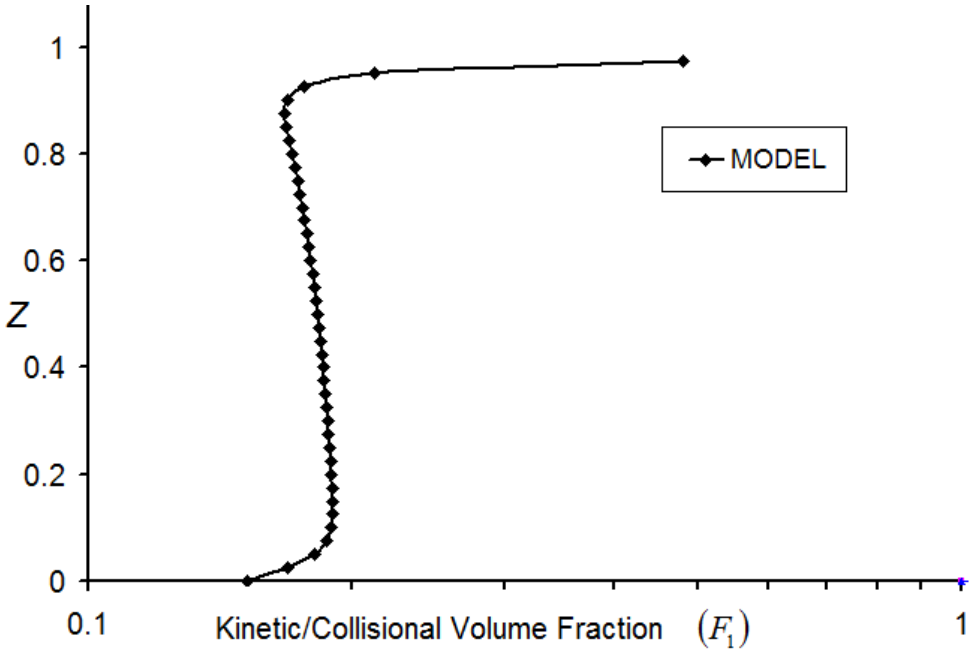

(d)

FIGURE 6.8: Prediction of inclined flow over rough boundary using the proposed unified model (data was taken from Silbert et al., 2001).[6]

6.4.2.3.2 Inclined Flow of 4 mm Mean Diameter Particles on Flat-Frictional Boundary

Inclined flow simulations of 4 mm mean diameter, slightly dispersed spherical particles were conducted in this research for a flat-frictional base which consisted of fixed particles arranged in a rectangular array (see Chapter 3). The simulation data are used here for verification of the proposed model. The values of parameters used in the simulation and in the model are presented in Table 6.5, while the simulation data and the model predictions are compared in Figure 6.9.

[6] Reprinted excerpt (extracted simulation data) with permission from L. E. Silbert, D. Ertas¸, G. S. Grest, T. C. Halsey, D. Levine, and S. J. Plimpton, Phys. Rev. E 64, 051302 (2001). Copyright (2001) by the American Physical Society. http://link.aps.org/abstract/PRE/v64/e051302

The proposed model has also captured the typical behaviours of inclined granular flows on a flat-frictional boundary, which is characterized by high granular temperature, low solid volume fraction, and large slip velocity at the frictional base, as discussed in Sec. 2.2.5. These flow profiles were mainly captured by using a low coefficient of specularity for the less roughness of the base. The restitution coefficient used in the model was also lower than the value used in the simulation experiment to obtain better prediction. The variation of the kinetic/collisional volume fraction (F_1) over the depth of the flow is also observed to be similar with the variation of granular temperature.

TABLE 6.5: Simulation and Model Parameters

Parameter	**Simulation Experiment**	**Model**
H/*d* of flow	19	19
Inclination angle of plane	23^0	23^0
Particle density	1095 kg/m^3	1095 kg/m^3
Particle diameter	4 mm	4 mm
Restitution coefficient (ε and ε_w)	0.75	0.65
Friction angle	$\mu_s = 0.6$ (static friction coefficient between particles)	$\phi_{cs} = \delta = 22.5^0$
Γ	N/A	0.9
λ	N/A	0.035
Specularity coefficient (φ)	N/A	0.2443
v_S^m	N/A	0.61
m_1, m_2, m_3, m_4, m_5	N/A	0.01, 250, 0.5, 1, 0.035
e^*	N/A	0.9
I_{cs}^*	N/A	10^{-5}
Tolerance value, R_1	N/A	0.001
Tolerance value, R_2	N/A	1.77E-07

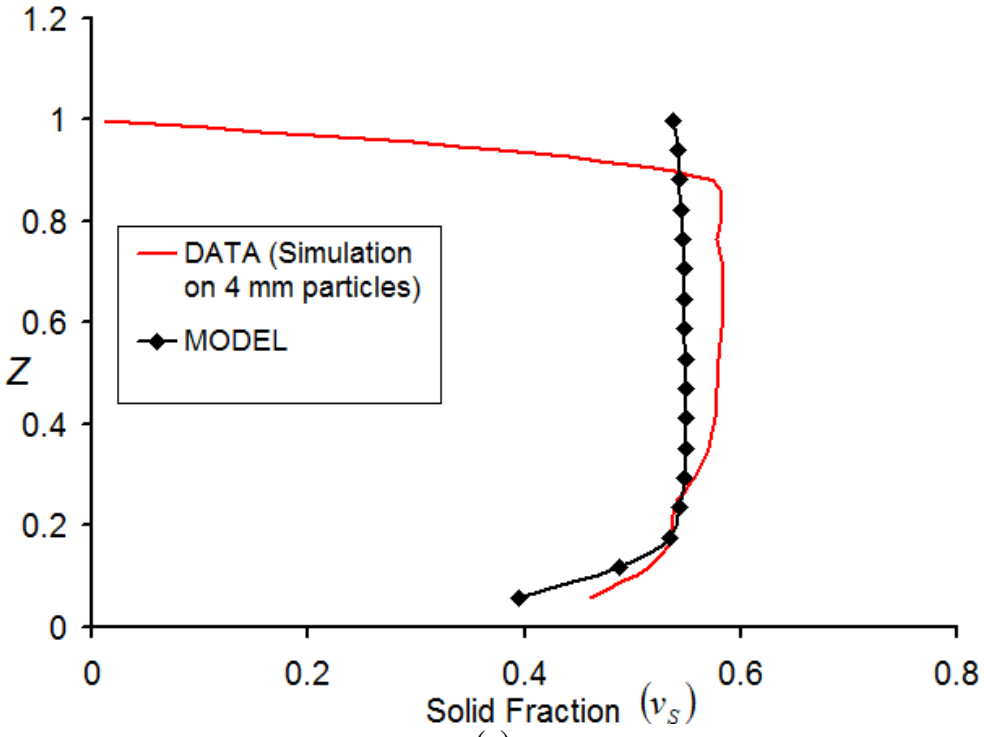
1.2
1
0.8
0.6
Z
0.4
0.2
0
0
0.2
0.4
0.6
0.8
DATA (Simulation on 4 mm particles)
MODEL
Solid Fraction (v_S)

(a)

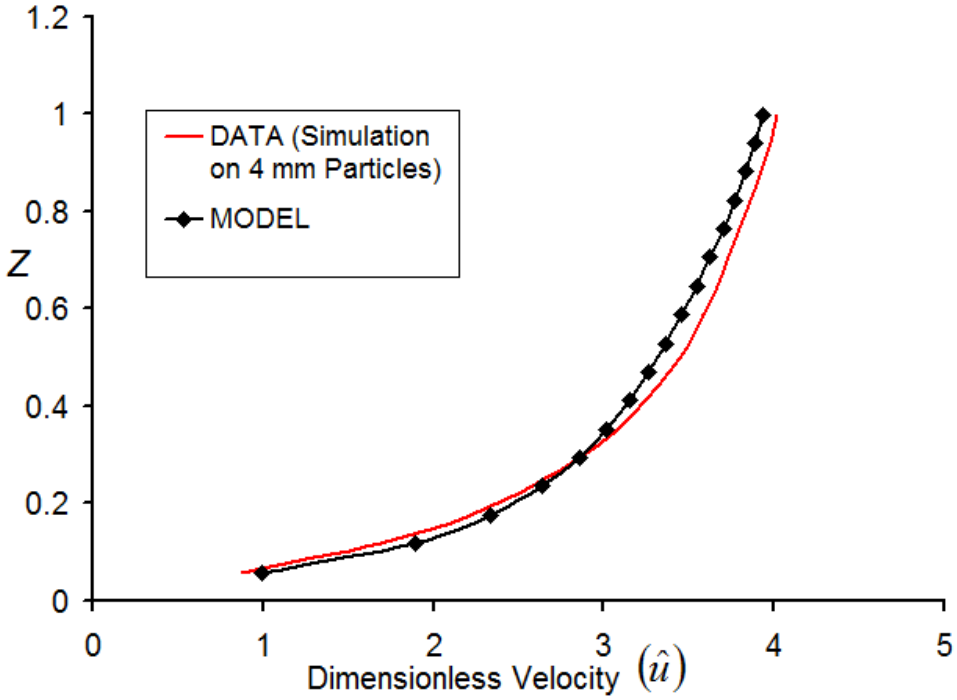
1.2
1
0.8
Z
0.6
0.4
0.2
0
0
1
2
3
4
5
DATA (Simulation on 4 mm Particles)
MODEL
Dimensionless Velocity $(\hat{u})$

(b)

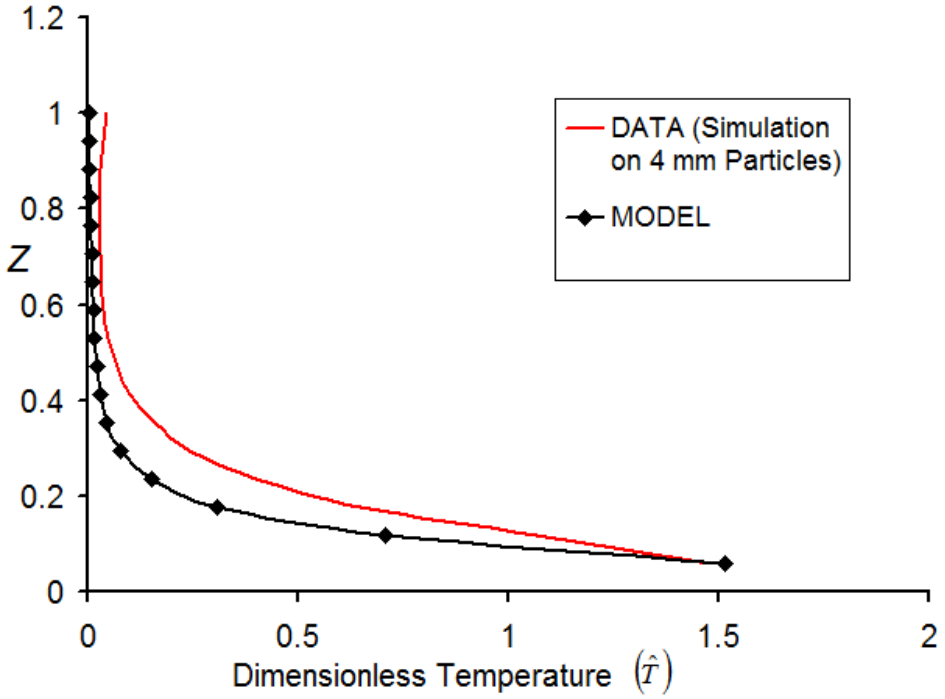

(c)

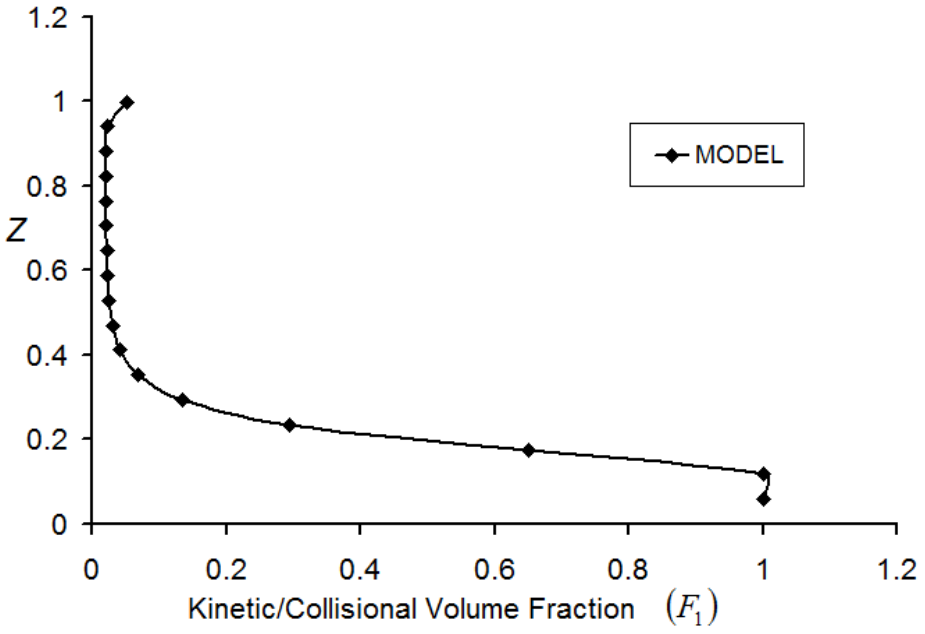

(d)

FIGURE 6.9: Prediction of inclined flow of 4 mm diameter particles over flat-frictional boundary using the proposed unified model.

6.4.2.3.3 Inclined Flow of 4 cm Mean Diameter Particles on a Flat-Frictional Boundary

Simulation experiments were also conducted on 4 cm mean diameter, slightly dispersed spherical particles in order to observe the flow behaviour of large particles at higher stress (see Chapter 3). The simulation data are used here to verify the proposed unified model. The values of the parameters used in the simulation and in the model are presented in Table 6.6. The simulation results and the model predictions are compared in Figure 6.10.

The 4 cm diameter particles exhibit similar flow behaviours to the 4 mm diameter particles, and are captured by the proposed unified model. Moreover, a variation of F_1 similar to the granular temperature is also observed here. Low value of the specularity coefficient (φ) was also used in modeling the flow of the 4 cm diameter particles, in order to represent the less roughness of the base. The restitution coefficient used in the model was closer to the actual value in the simulation experiment.

TABLE 6.6: Simulation and Model Parameters

Parameter	Simulation Experiment	Model
H/*d* of flow	27	27
Inclination angle of plane	23^0	23^0
Particle density	1095 kg/m^3	1095 kg/m^3
Particle diameter	4 cm	4 cm
Restitution coefficient (ε and ε_w)	0.75	0.7
Friction angle	$\mu_s = 0.6$ (static friction coefficient between particles)	$\phi_{cs} = \delta = 22.5^0$
Γ	N/A	0.9
λ	N/A	0.035
Specularity coefficient (φ)	N/A	0.2443
v_S^m	N/A	0.61
m_1, m_2, m_3, m_4, m_5	N/A	0.01, 250, 0.5, 1, 0.035
e^*	N/A	0.9
I_{cs}^*	N/A	10^{-5}
Tolerance value, R_1	N/A	0.001
Tolerance value, R_2	N/A	2.03E-07

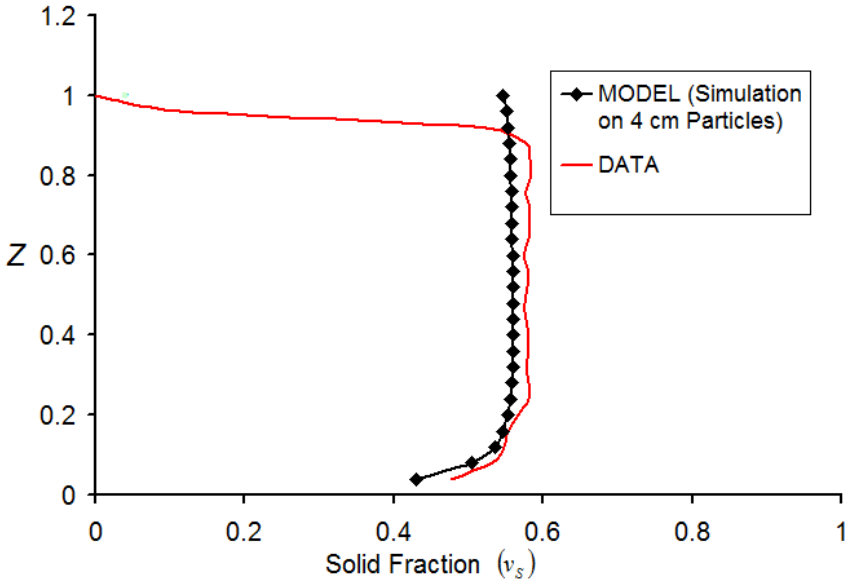

(a)

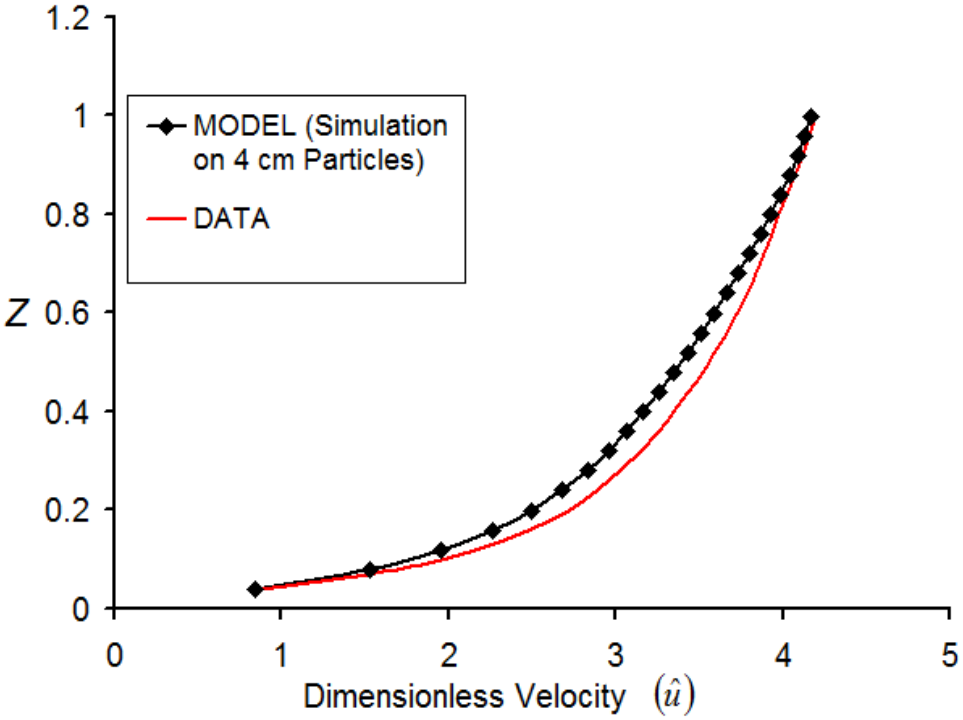
1.2
1
0.8
Z 0.6
0.4
0.2
0
0
1
2
3
4
5
MODEL (Simulation on 4 cm Particles)
DATA
Dimensionless Velocity $(\hat{u})$

(b)

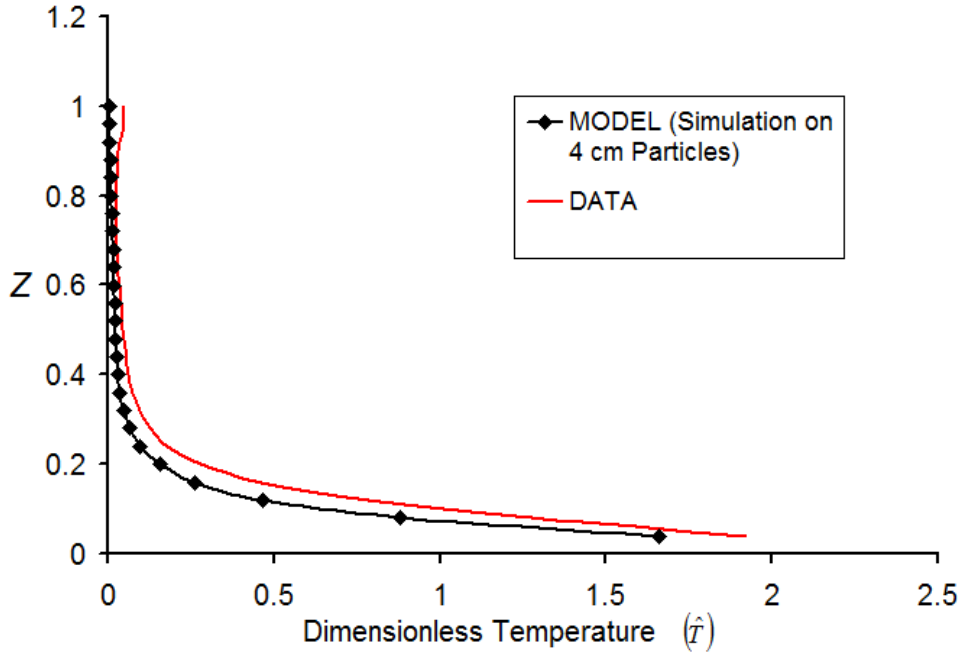
1.2
1
0.8
Z 0.6
0.4
0.2
0
0
0.5
1
1.5
2
2.5
MODEL (Simulation on 4 cm Particles)
DATA
Dimensionless Temperature $(\hat{T})$

(c)

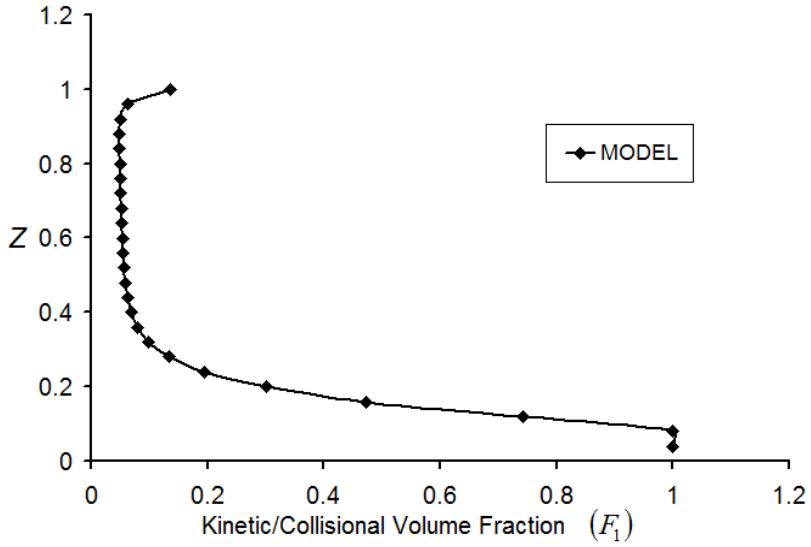

(d)

FIGURE 6.10: Prediction of inclined flow of 4 cm diameter particles over flat-frictional boundary using the proposed unified model.

6.4.2.4 Performance of Proposed Model for Inclined Flow

In general, the proposed unified model successfully captures the typical inclined flow profiles on flat-frictional and bumpy-rough boundaries. As reviewed in Chapter 2, the density, velocity, and granular temperature profiles of inclined flows depend mainly on the roughness of bottom boundary. The proposed model used low and high values of the parameter, specularity coefficient (φ), in order to represent the moderately rough and rough bottom boundaries. The restitution coefficients in the simulation experiments of inclined flow were high. However, slightly lower values of restitution coefficients were used in the proposed model in order to obtain a best fit of the experimental results. The other feature of the proposed model is that it is able to calculate the profile of the collisional volume fraction (F_1) which helps to identify quasi-static, collisional, and intermediate flow states. It also indicates the relative progress of intermediate flow states towards the collisional or quasi-static states. The depth profile of F_1 was similar to the profile of the granular temperature.

CHAPTER SEVEN

CONCLUSIONS AND RECOMMENDATIONS

7.1 Summary

In general, the research work presented in this thesis is categorized under the field of study for the investigation of granular flow behaviour and the development of a unified constitutive model to capture the complex behaviour of granular materials. This research is focused to dry granular materials in order to devote all the effort for a better understanding of how granular particles interact without considering the effect of interstitial fluid. To this end, it has been well understood that the flow interaction of granular particles consists of rate-independent rubbing friction and rate-dependent collisions. Nevertheless, the challenge is that the occurrence of the above flow or deformation mechanisms depends on the stress, density, particle size, and rate at which the granular material deforms. Some industrial processes, such as the processing of food grains and pharmaceutical particles, involve small size particles flowing under low stress and density. On the other hand, geotechnical problems, such as flow type landslides, occur under high stress and density, and involve a mixture of small soil particles and large rock fragments. The occurrence of rate-dependent collisional behaviour in geotechnical problems of granular flows has been a subject of interest for many years.

Shear experiments conducted by geotechnical scientists (Hungr & Morgenstern, 1984; Sassa, 2000) revealed the lack of rate dependent behaviors of granular flow at high stresses. As a result, many geotechnical flow analyses models (TITAN2D, DAN3D, RASH3D) do not include the collisional flow mechanism. On the contrary, the models have not been performing satisfactorily in predicting some dry debris flows and avalanches by considering only the rate-independent frictional mechanism (Hungr & Evans, 1996; Evans et al., 2001; Hungr et al.,

2007; Pirulli, 2009). Instead, the velocity dependent Voellmy model produced better predictions. In wet flows, the velocity dependent shear stress component of the Voellmy model has been attributed to capture the stress produced due to the turbulence of the pore water. In dry mass flows, however, the use of Voellmy model requires an explanation for the possible source of the rate-dependent shear resistance component. Moreover, the shear experiments conducted by geotechnical researchers were limited to small size particles, even though they covered the range of stresses and flow rates at which actual landslides would occur.

As the occurrence of collisional flow mechanism depends on particle inertia, both the flow rate and particle mass (or particle size and density) are equally important in the investigation of rate-dependent granular flow behaviour. Therefore, additional investigation on the relevance of collisional behaviour for large diameter particles is necessary to determine the consideration of collisional stress contribution in landslide analysis models. The occurrence of collisional behaviour at high stresses may also explain the better performance of Voellmy model in predicting dry debris flows and avalanches.

In this research, the occurrence of rate-dependent collisional flow behaviour for large size granular particles was assessed by conducting plane shear simulations at high stresses and flow rates. Detailed assessment of the relevance of collisional behaviour in snow, debris, and rock avalanches were also conducted for different flow depths, velocities, and void ratios that are required to produce the rate-dependent flow behaviour in the avalanches. By extending the plane shear simulations of large diameter particles to all ranges of stresses, void ratios, and flow rates, the critical state soil mechanics framework established for frictional flow behaviour has been extended, as originally presented by Campbell (2005), to capture the rate-dependent flow behaviour of granular materials. The extended framework has been shown to be effective in capturing the flow behaviours, understand flow progress, and develop and evaluate unified constitutive models.

The rate-dependent behaviour of granular material has been investigated mostly by conducting shear experiments and simulations on spherical particles. Some experiments on non-spherical particles have exhibited differences in the rate-dependent flow behaviour from the spherical particles. In this research, ring shear simulations of non-spherical particles were also conducted to observe the type of rate-dependent flow behaviours observed from physical experiments. As well, the general effects of particle shape on the extended critical state framework have been discussed.

Pure frictional and pure collisional granular flows have been successfully modeled using the theory of plasticity and kinetic theory of granular flow (KTGF), respectively. For intermediate flows, however, several unified models have been proposed to capture the simultaneous occurrence of the rate-independent frictional behaviour and the rate-dependent collisional behaviour in a flow. Most of the models are based on the assumption of Savage (1982), who proposed the total stress is equal to the sum of the frictional and the collisional stress. Understanding how the stress contributions from the two simultaneously occurring flow mechanisms combine to give a total stress is the main challenge in the development of a unified constitutive model for granular flows.

In this research, the unified models proposed by Savage (1982, 1998) and Louge (2003) have been selected for evaluation by predicting the extended critical state framework discussed above. The Savage (1982) model was chosen because it provided the basis for the most improved models developed after his original model. The Savage (1998) model was selected because it is not influenced by a restitution coefficient, which differentiates it from other unified models. On the other hand, Louge (2003) model was selected because it presents a different approach by considering that the shear works of both frictional and collisional stress contributions would produce granular temperature before changing to heat.

A new unified constitutive model has been also developed in this research by exploring the particle interactions inside a flow based on the microscopic description proposed by Sayed (1981), and by considering the analogy of the transformation from ice to water. The constitutive equation involves an empirical equation for a stress-coefficient which is suggested based on the experimentally observed variations of granular temperature with void ratio at different shear rates. The constitutive model was applied to predict the extended critical state framework and was also implemented in the equations of motion and solved for inclined granular flows. Equations of motion and boundary conditions similar to Johnson (1987) and Nott (1991) were used in this research, and the numerical model was used to predict inclined flow simulation experiments conducted by Silbert et al. (2001) and in this research.

7.2 Conclusions

As summarized in the previous section, the objectives of this research are focused on the relevance of rate-dependent collisional flow behaviour in geotechnical granular material flows, the review of the flow behaviour of geotechnical granular materials with the extension of critical state framework, and the development of a unified constitutive model for dry granular flows. The main findings of the research are outlined below.

1. Rapid flow landslides involving large-size particles, such as debris and rock avalanches, may be characterized by rate-dependent behaviour due to the collisional interaction of the particles in the flow in addition to the rubbing or sliding of particles over one another with long enduring contact. With the decrease in particle sizes, less flowing depths (or less confining stresses) are required to achieve the rate-dependent collisional interaction of particles.

2. As originally presented by Campbell (2005), a series of state lines have been obtained as a function of the dimensionless shear rate by plotting the rate-

dependent flow states in a void ratio versus a normal stress plot in the critical state framework. Following this finding, the entire critical state framework is extended in this research to capture rate-dependent flow states in addition to the rate-independent critical states by considering the characteristic shear velocity, $(\dot{\gamma}d)$, as a state variable in addition to the existing variables of void ratio, normal stress, and shear stress. In addition to the conventional critical state line, series of state lines are formed as functions of $\dot{\gamma}d$ in the void ratio versus vertical normal stress and shear stress versus vertical normal stress plots in the critical state framework. The series of state lines are referred to in this research as *supercritical state lines*. In the extended framework, the critical state line is the lowest bound state line. An additional plane is introduced in the framework by plotting the void ratio versus granular temperature as a function of $\dot{\gamma}d$. The conventional critical state framework has been used to identify contractive and dilative behaviours of soils and assessing flow liquefaction. Similarly, the extended critical state framework is useful for flow classification as quasi-static, collisional and intermediate regimes and for understanding flow progress. The extended framework is also useful in developing and evaluating unified constitutive models.

3. The flow behaviour of granular material and the extended critical state framework have been studied by using mainly the experimental results of mono-disperse spherical particles. Some experimental studies are available in the literature to investigate the flow behaviour of non-spherical particles. Ring shear simulations were also conducted in this research to observe the effects of particle shape in flow behaviour as obtained in physical experiments. The simulations reproduced some of the behaviour of non-spherical particles obtained in the experiments. In order for the simulations to fully capture the experimental results, the shape of individual particle used in the experiment must be synthesized precisely as a DEM particle, including the sharp edges and corners which are key features for particle interlocking that governs the behaviour of non-spherical particles.

4. The evaluation of selected unified models proposed by Savage (1982, 1998), and Louge (2003) was performed by predicting the extended critical state framework using the models. The main limitation obtained was that the Savage (1982, 1998) models did not capture the void ratio versus granular temperature plot of the extended critical state framework. The models predicted the granular temperatures in the collisional regime but showed that the trend of granular temperature would be unaffected as the flow progresses to the intermediate regime, while the measured values increased. In the Savage (1982) model, only the equations for the stresses are changed by combining the frictional and collisional stress contributions, whereas the equation for granular temperature remained unchanged from its expression in a pure collisional flow case. Thus, the granular temperature equation derived from kinetic theory was used to predict the entire flow. The Louge (2003) model, however, overcomes the above limitation by deriving the granular temperature assuming both frictional and collisional stress components would produce fluctuation energies before dissipating to heat, and substituting the total stress in the fluctuation energy equation.

5. Most of the existing constitutive models for granular materials mainly consist of simple additions of the frictional and collisional stress contributions based on the assumption of Savage (1982). A new unified constitutive model is developed in this research to overcome the assumption. The model combines the frictional and collisional stress contributions by using weighting functions, which are referred to in this research as stress coefficients. The frictional and collisional stress coefficients are inter-dependent. The model also overcomes the limitations of Savage's (1982, 1998) models in predicting granular temperatures. The assumption made by Louge (2003), which considers the frictional stress component in calculating the granular temperature, may be subject to criticism. In this research, the granular temperature equation is derived by taking conventional fluctuation energy equation (Johnson & Jackson, 1987), which considers only that the work of collisional shear stress

produces granular temperature, while the work of frictional shear stress directly dissipates to heat. The new proposed model captures the extended critical state framework and it is able to successfully predict the typical profiles of inclined flows over flat frictional and rough boundaries.

7.3 Recommendations for Further Research

1. The assessment of the relevance of rate-dependent collisional flow behaviour in geotechnical granular material flows was accomplished in this research using simulation experiments of plane shear flows. The lack of rate-dependent behaviour in previous laboratory experiments is attributed to the small particle sizes used in the experiments. Thus, the behaviour of large-size particles was investigated here using simulation experiments, as financial constraints limited the researcher's ability to purchase or manufacture a large-size ring shear apparatus. The assessment of rate-dependent flow behaviour by conducting laboratory experiments on large-size particles is left for future studies.

2. The rate-dependent flow behaviour of granular material is investigated mostly by using mono-disperse spherical particles. Some experiments and simulations on poly-disperse and non-spherical particles indicate their significant effects on flow behaviours. Geotechnical granular materials are characterized by poly-dispersity and non-spherical shapes. Future studies of the above type of materials in physical laboratory experiments and DEM simulations are required for a deeper understanding of the behaviour of geotechnical granular flows.

3. Unified constitutive models proposed by various researchers to date are evaluated using the flow behaviour of mono-disperse spherical granular materials. Future research work should strive to improve existing constitutive models to capture the flow behaviour of a wide variety of granular materials.

REFERENCES

Aarons, L., and Sundaresan, S. 2006. Shear flow of assemblies of cohesive and non-cohesive granular materials. Powder Technology, 169: 10-21.

Ahn, H. 1989. Experiments and analytical investigations of granular materials: shear flow and convective heat transfer. Ph.D. Thesis, California Institute of Technology, USA.

Ahn, H., Brennen, C. E., and Sabersky, R. H. 1991. Measurements of Velocity, Velocity Fluctuation, Density, and Stresses in Chute Flows of Granular Materials. Journal of Applied Mechanics, 58(3): 792-803.

Ancey, C. 2001. Dry granular flow down an inclined channel: Experimental investigations on the frictional-collisional regime. Physical Review E, 65: 011304 (1-19).

Ancey, C., and Evesque, P. 2000. Frictional-collisional regime for granular suspension flow down an inclined channel. Physical Review E, 62: 8349-8360.

Azanza, E., Chevoir, F., and Moucheront, P. 1999. Experimental study of collisional granular flows down an inclined plane. Journal of Fluid Mechanics, 400: 199-227.

Bagnold, R. A. 1954. Experiments on a gravity-free dispersion of large solid spheres in a Newtonian fluid under shear. Proceedings of the Royal Society of London, Series A, Mathematical and Physical Sciences, 225: 49-63.

Bartelt, P., Buser, O., and Platzer, K. 2006. Fluctuation-dissipation relations for granular snow avalanches. Journal of Glaciology, 52(179): 631-643.

Berzi, D., di Prisco, C. G., and Vescovi, D. 2011. Constitutive relations for steady, dense granular flows. Physical Review E, 84 (031301): 1-6.

Bridgewater, J. 1972. Stress velocity relationships for particulate solids. ASME, no. 72-MH-21.

Cagnoli, B., and Manga, M. 2004. Granular mass flows and Coulomb's friction in shear cell experiments: Implication for geophysical flows. Journal of Geophysical Research - Earth Surface, 109(F04005): 1-12.

Campbell, C. S. 2002. Granular shear flows at the elastic limit. Journal of Fluid Mechanics, 465: 261-291.

Campbell, C. S. 2005. Stress-controlled elastic granular shear flows. Journal of Fluid Mechanics, 539: 273-297.

Campbell, C. S. 2011. Elastic granular flows of ellipsoidal particles. Physics of Fluids 23, 013306:1-10

Casagrande, A. 1936. Characteristics of cohesionless soils affecting the stability of slopes and earth fills. Journal of Boston Society of Civil Engineers, Reprinted in Contributions to Soil Mechanics 1925-1940, Boston Society of Civil Engineers: 257-276.

Cassar, C., Nicolas, N., and Pouliquen, O. 2005. Submarine granular flows down inclined planes. Physics of Fluids, 17(103301): 1-11.

Chen, C.L. 1988. Generalized viscoplastic modeling of debris flow. Journal of Hydraulic Engineering, 114(3): 237-257.

Chen, H., and Lee, C.F. 2000. Numerical simulation of debris flows. Canadian Geotechnical Journal, 37: 146-160.

Cleary, P. W. 2008. The effect of particle shape on simple shear flows. Powder Technology, 179: 144-163.

Cruden, D.M., and Varnes, D.J. 1996. Landslide types and processes. In Landslide Investigation and Mitigation. Transportation Research Board, U.S. National Research Council, Special Report 247, Washington, D.C. pp. 36-75.

Daerr, A. 2001. Dynamical equilibrium of avalanches on a rough plane. Physics of Fluids, 13(7): 2115-2124.

Daerr, A., and Douady, S. 1999. Two types of avalanche behavior in granular media. Nature (London) 399: 241-243.

Da Cruz, F., Chevoir, F., Roux, J. N., and Iordanoff, I. 2004. Macroscopic friction of dry granular materials. Transient Processes in Tribology, Edited by G. Dalmaz, A. A. Lubrecht, D. Dowson, and M. Priest, p. 53-61, Amsterdam, Elsevier.

Da Cruz, F., Emam, S., Prochnow, M., Roux, J. N., and Chevoir, F. 2005. Rheophysics of dense granular materials: Discrete simulation of plane shear flows. Physical Review E, 72: 021309.

Delannay, R., Louge, M., Richard, P., Taberlet, N., and Valance, A. 2007. Towards a theoretical picture of dense granular flows down inclines. Nature Materials, 6: 99-108.

Denlinger, R.P., and Iverson, R.M. 2001. Flow of variably fluidized granular masses across three-dimensional terrain 2. Numerical predictions and experimental tests. Journal of Geophysical Research - Solid Earth, 106: 553-566.

Drake, T. G. 1988. Experimental flows of granular material. Ph.D. Thesis, University of California, Los Angeles.

Drake, T. G. 1990. Structural features in granular flows. Journal of Geophysical Research, 95: 8681-8696.

Drescher, A., and De Josselin de Jong, G. 1972. Photoelastic verification of a mechanical model for the flow of a granular material. Journal of the Mechanics and Physics of Solids, 20(5): 337-340.

EPOCH. 1993. The Temporal Occurrence and Forecasting of Landslides in the European Community (Ed: Flageollet, J. C.). Contract No. 90 0025, 3 Volumes.

Evans, S. G., Hungr, O., and Clague, J. J. 2001. Dynamics of the 1984 rock avalanche and associated distal debris flow on Mount Cayley, British Columbia, Canada: Implications for landslide hazard assessment on dissected volcanoes. Engineering Geology, 61:29-51.

Fang, C., Wang, Y., and Hutter, K. 2006. Shearing flows of a dry granular material – hypoplastic constitutive theory and numerical simulations. Int. J. Num. & Anal. Meth. in Geomech., 30: 1409 - 1437

Farrell, M., Lun, C. K. K., and Savage, S. B. 1986. A simple kinetic theory for granular flow of binary mixtures of smooth, inelastic, spherical particles. Acta Mechanica, 63: 45-60.

Fukuoka, H., and Sassa, K. 1991. High-speed high-stress ring shear tests on granular soils and clayey soils. Rice, Raymond M., technical coordinator. Proceedings of the IUFRO Technical Session on Geomorphic Hazards in Managed Forests, Montreal, Canada. Gen. Tech. Rep. PSW-GTR-130, Berkeley,

CA: Pacific Southwest Research Station, Forest Service, U.S. Department of Agriculture, 33-41.

Galas, S., Dalbey, K., Kumar, D., Sheridan, M., and Patra, A. 2007. Benchmarking TITAN2D mass flow model against a sand flow experiment and the 1903 frank slide. International Forum on Landslide Disaster Management, Hong Kong.

GDR MiDi. 2004. On dense granular flows. European Physical Journal E, 14: 341-365.

Gioia, G., Ott-Monsivais, S.E., and Hill, K.M. 2006. Fluctuating velocity and momentum transfer in dense granular flows. Physical Review Letters, 96(13): 138001.

Goldhirsch, I. 1999. Rapid granular flows: Kinetics and Hydrodynamics. In: Modeling in Applied Sciences: A Kinetic Theory Approach; N. Bellomo, M. Pulvirenti eds., Birkhauser, Boston, 201-213.

Gray, J.M.N.T., Wieland, M., and Hutter, K. 1999. Gravity-driven free surface flow of granular avalanches over complex basal topography. Proceedings of the Royal Society A: Mathematical, Physical and Engineering Sciences, 455: 1841-1874.

Hanes, D. M., and Inman, D. L. 1985a. Observations of rapidly flowing granular-fluid materials. Journal of Fluid Mechanics, 150: 357-380.

Hanes, D. M., and Inman D. L. 1985b. Experimental evaluation of a dynamic yield criterion for granular fluid flows. Journal of Geophysical Research, 90(B5): 3670-3674.

Hatano, T. 2007. Power-law friction in closely packed granular materials. Physical Review E, 75: 1-4.

Hatano, T. 2010. Critical Scaling of Granular Rheology. Progress of Theoretical Physics Supplement, No. 184:143-152.

Herrmann, H. J., Luding, S., Cafiero, C. 2001. Dynamics of granular systems. Physica A, 295: 93-100.

Highland, L. M. 2004. Landslide types and processes. U.S. Geological Survey Fact Sheet 2004-3072.

Horne, M. R. 1965b. The behaviour of an assembly of rotund, rigid, cohesionless particles, II. Proc. Roy. Soc. Series A 286, no. 1404: 79-97.

Horne, M. R. 1965a. The behaviour of an assembly of rotund, rigid, cohesionless particles, I. Proc. Roy. Soc. Series A 286, no. 1404: 62-78.

Howell, D. W., Veje, C. T., and Behringer, R. P. 1999. Fluctuations in Granular Media. Chaos, 9(3): 559- 572.

Hungr, O. 1995. A model for the runout analysis of rapid flow slides, debris flows, and avalanches. Canadian Geotechnical Journal, 32: 610-623.

Hungr, O., and Evans, S.G 1996. Rock avalanche runout prediction using a dynamic model. In Proceedings of the Seventh International Symposium on Landslides. Edited by K. Senneset. Trondheim. 17-21 June 1996. A.A.Balkema, Rotterdam, 1: 233-238.

Hungr, O., Evans, S.G, Bovis, M., and Hutchinson, J.N. 2001. A review of the classification of landslides of the flow type. Environmental & Engineering Geoscience, 7(3): 221-238.

Hungr, O., McKinnon, M., and McDougall, S. 2007. Two models for analysis of landslide motion: application to the 2007 Hong Kong benchmarking exercises. International Forum on Landslide Disaster Management, Hong Kong.

Hungr, O., and Morgenstern, N.R., 1984. High velocity ring shear tests on sand. Geotechnique, 34: 415-421

Itasca Consulting Group Inc. 2008. PFC3D - Particle Flow Code in 3 Dimensions. User's Guide, Version 4, Minneapolis, USA.

Jenkins, J. 1993. Hydraulic theory for a debris flow supported on a collisional shear layer. IAHR, Tokyo, 1993, pp. 1-12.

Jenkins, J. T., and Berzi, D. 2010. Dense inclined flows of inelastic spheres: Tests of an extension of kinetic theory. Granular Matter, 12: 151-158.

Jenkins, J.T., and Richman, M.W. 1985. Kinetic theory for plane flows of a dense gas of identical, rough, inelastic, circular disks. Physics of Fluids, 28: 3485-3494.

Jenkins, J. T., and Savage, S. B. 1983. A theory for the rapid flow of identical, smooth, nearly elastic, spherical particles. Journal of Fluid Mechanics, 130: 187-202.

Jenkins, J. T., and Zhang, C. 2002. Kinetic theory for identical, frictional, nearly elastic spheres. Physics of Fluids, 14(3): 1228-1235.

Ji, S., and Shen, H.H. 2005. Characteristics of temporal-spatial parameters in quasi-solid-fluid phase transition of granular materials. Chinese Science Bulletin, 51(6): 646-654.

Johnson, P. C. 1987. Frictional-collisional equations of motion for particulate flows with application to chutes and shear cells. Ph.D. Thesis, Department of Chemical Engineering, Princeton University.

Johnson, P. C., and Jackson, R. 1987. Frictional-collisional constitutive relations for granular materials, with application to plane shearing. Journal of Fluid Mechanics, 176: 67-93.

Jop, P., Forterre, Y., and Pouliquen, O. 2006. A constitutive law for dense granular flows. Nature, 441: 727-730.

Kaibori, M. 1986. Study on the movement of the slope failure materials. Ph.D. Thesis, Faculty of Agriculture, Kyoto University, Japan.

Kelfoun, K., and Druitt, T.H. 2005. Numerical modeling of the emplacement of Socompa rock avalanche, Chile. Journal of Geophysical Research - Solid Earth, 110: B12202.

Kumaran, V. 2008. Dense granular flow down an inclined plane - from kinetic theory to granular dynamics. Journal of Fluid Mechanics, 599: 120-168.

Kumaran, V. 2009. Dynamics of dense sheared granular flows. Part 1: Structure and diffusion. Journal of Fluid Mechanics, 632: 109-144.

Lan, Y., and Rosato, A. D. 1995. Macroscopic behavior of granular vibrating beds of smooth inelastic spheres. Physics of Fluids, 7: 1818-1831.

Lee, C. H., and Huang, C. J. 2010. Model of sheared granular material and application to surface-driven granular flows under gravity. Physics of Fluids, 22: 043307:1-10.

Liu, J., and Rosato, A. D., 2005. Migration of an Intruder in a Boundary Driven Granular Flow. Journal of Physics: Condensed Matter 17: S2609-S2622.

Lois, G., Lemaitre A., Carlson J. M. 2005. Numerical tests of constitutive laws for dense granular flows. Physical Review E, 72: 051303.

Louge, M. Y. 2003. Model for dense granular flows down bumpy inclines. Physical Review E, 67, 061303: 1-11.

Louge, M. Y., and Keast, S. C. 2001. On dense granular flows down flat frictional inclines. Physics of Fluids, 13(5): 1213–1233.

Lu, K., Brodsky, E. E., and Kavehpour, H. P. 2007. Shear-weakening of the transitional regime for granular flow. Journal of Fluid Mechanics, 587: 347-372.

Lu, L. S., and Hsiau, S. S. 2005. Mixing in vibrated granular beds with the effect of electrostatic force. Powder Technology, 160: 170-179.

Luding, S., Muller, M., and McNamara, S. 1998. The validity of "Molecular Chaos" in granular flows. World Congress on Particle Technology, Brighton, CD: ISBN 0-85295-401-9.

Lun, C. K. K. 1996. Granular dynamics of inelastic spheres in Couette flow. Physics of Fluids, 8(11): 2868-2883.

Lun, C. K. K., and Savage, S. B. 1987. A simple kinetic theory for granular flow of rough, inelastic, spherical particles. Journal of Applied Mechanics, 54: 47-53.

Lun, C. K. K., Savage, S. B., Jeffrey, D. J., and Chepurniy, N. 1984. Kinetic theories for granular flow: inelastic particles in Couette flow and slightly inelastic particles in a general flow field. Journal of Fluid Mechanics, 140: 223-256.

Martino, R., and Davies, T. R. 2003. Dynamic friction coefficient of a fluid-solid mixture. International Conference on Fast Slope Movements Prediction and Prevention for Risk Mitigation, Associazione Geotecnica Italiana, Naples, May 11-13, 357-360.

McDougall, S. 2006. A new continuum dynamic model for the analysis of extremely rapid landslide motion across complex 3D terrain. Ph.D. Thesis, Department of Earth and Ocean Sciences, University of British Columbia.

McTigue, D. F. 1978. A model for stresses in shear flow of a granular material. Proc. U.S.-Japan Seminar on Continuum Mechanical and Statistical Approaches in the Mechanics of Granular Materials: 266-271, Gakujutsu Bunken Kukyu-Kai.

Mills, P., Loggia, D., and Tixier, M. 1999. Model for a stationnary dense granular flow along an inclined wall. Europhysics Letters, 45(6): 733-738.

Mitarai, N., and Nakanishi, H. 2005. Bagnold scaling, density plateau, and kinetic theory analysis of dense granular flow. Physical Review Letters, 94(128001): 1-4.

Mitchell, J.K., Soga, K. 2005. Fundamentals of Soil Behavior, 3rd Edition. John Wiley & Sons, Hoboken.

Mohan, L. S., Nott, P. R., and Rao, K. K. 1997. Fully developed flow of coarse granular materials through a vertical channel. In: Chemical Engineering Science, 52(6): 913-933.

Natarajan, V. V. R., Hunt, M. L., and Taylor, E. D. 1995. Local measurements of velocity fluctuations and diffusion coefficients for a granular material flow. Journal of Fluid Mechanics, 304: 1-25.

Nott, P. R. 1991. Analysis of granular flow in aerated and vibrated chutes. PhD Thesis, Princeton University.

Ogawa, S. 1978. Multitemperature theory of granular materials. Proc. U.S.-Japan Seminar on Continuum Mechanical and Statistical Approaches in the Mechanics of Granular Materials: 208-217, Gakujutsu Bunken Kukyu-Kai.

Ogawa, S. A., Umemura, A., and Oshima, N. 1980. On the equations of fully fluidized granular materials. Journal of Applied Mathematics and Physics 31: 483-493.

Patton, J. S., Brennen, C. E., and Sabersky, R. H. 1987. Shear flows of rapidly flowing granular materials. Journal of Applied Mechanics, 54:801-805.

Perla, R., Cheng, T. T., and McClung, D. M. 1980. A two-parameter model of snow-avalanche motion. Journal of Glaciology, 26: 197-207.

Pierson, T.C., and Costa, J.E. 1987. A rheological classification of subaerial sediment water flows. Reviews in Engineering Geology, Geological Society of America, 7: 1-12.

Pirulli, M. 2005. Numerical modeling of landslide runout, a continuum mechanics approach. PhD Thesis, Department of Structural and Geotechnical Engineering, Politecnico di Torino, Italy.

Pirulli, M. 2009. The Thurwieser rock avalanche (Italian Alps): Description and dynamic analysis. Engineering Geology, 109: 80-92.

Pitman, E. B., Patra, A. K., Nichita, C. C., Bauer, A. C., Sheridan, M. F., and Bursik, M. I. 2003. Modeling geophysical mass flows. Geophysical Research Abstracts, 5, 07342.

Pouliquen, O. 1999. Scaling laws in granular fl ows down a bumpy inclined plane. Physics of Fluids, 11: 542-548.

Pudasaini, S. P., and Hutter, K. 2003. Rapid shear flows of dry granular masses down curved and twisted channels. Journal of Fluid Mechanics, 495: 193-208.

Pudasaini, S. P., and Hutter, K. 2007. Avalanche Dynamics: Dynamics of Rapid Flows of Dense Granular Avalanches. Springer Verlag

Reddy, K.A., and Kumaran, V. 2010. Dense granular flow down an inclined plane: a comparison between the hard particle model and soft particle simulations. Physics of Fluids, 22: 113302.

Reynolds, O. 1885. On the dilatancy of media composed of rigid particles in contact, with experimental illustrations. Phil. Mag., Series 5, 20: 469-481.

Rognon, P., Roux, J., Naaim, M., and Chevoir, F. 2007. Dense flows of bidisperse assemblies of disks down an inclined plane. Physics of Fluids, 19: 058101.

Rowe, P. W. 1962. The stress-dilatancy relation for static equilibrium of an assembly of particles in contact. Proc. Roy. Soc. Series A 269, no. 1339: 500-527.

Rowe, P. W. 1963. Stress-dilatancy, earth pressures, and slopes. Journal of the Soil Mechanics and Foundations, ASCE, 89(3): 37-61.

Sassa, K. 2000. Mechanism of flows in granular soils. In GeoEng 2000: An International Conference on Geotechnical and Geological Engineering. Melbourne, Australia. 9-24 November 2000. Technomic Publishing Company, Inc., Lancaster, Pennsylvania, Vol.1: Invited Papers, pp. 1671-1702.

Savage, S. B. 1982. Granular flows down rough inclines - review and extension. Mechanics of granular materials : new models and constitutive relations : proceedings of the U.S./Japan Seminar on New Models and Constitutive Relations in the Mechanics of Granular Materials, edited by Jenkins, J. T., and Satake, M., Ithaca, New York, August 23-27.

Savage, S. B. 1998. Analyses of slow high-concentration flows of granular materials. Journal of Fluid Mechanics, 377: 1-26.

Savage, S.B., and Hutter, K. 1989. The motion of a finite mass of granular material down a rough incline. Journal of Fluid Mechanics, 199: 177-215.

Savage, S. B., and Jeffrey, D. J. 1981. The stress tensor in a granular flow at high shear rates. Journal of Fluid Mechanics, 110: 255-272.

Savage, S. B. and Sayed M. 1984. Stresses developed by dry cohesionless granular materials sheared in an annular shear cell. Journal of Fluid Mechanics, 142: 391-430.

Sayed, M. 1981. Theoretical and Experimental Studies of the Flow of Cohesionless Granular Materials. Ph.D. Thesis, McGill University, Montreal, Canada.

Schofield, A. N., and Wroth, C.P. 1968. Critical state soil mechanics. London, England: McGraw-Hill, pp. 310.

Shen, H. H. 1981. Constitutive relationships for fluid-solid mixtures. Ph.D. Thesis, Clarkson College of Technology, USA.

Sheridan, M. F., Stinton, A. J., Patra, A., Pitman B., Bauer, A., and Nichita, C. 2003. Evaluating TITAN2D mass-flow model using the 1963 Little Tahoma Peak

Avalanches, Mount Rainier, Washington. Geophysical Research Abstracts, 5: 14695.

Silbert, L. E., Ertaş, D., Grest, G. S., Halsey, T. C., Levine, D., and Plimpton, S. J. 2001. Granular flow down an inclined plane: Bagnold scaling and rheology. Physical Review E, 64(51302): 1-14.

Silbert, L. E., Grest, G. S., and Plimpton, S. J. 2002. Boundary effects and self-organization in dense granular flows. Physics of Fluids, 14: 1-10.

Silbert, L. E., Landry, J. W., and Grest, G. S. 2003. Granular flow down a rough inclined plane; transition between thin and thick piles. Physics of Fluids, 15: 1-10.

Skinner, A. 1969. A note on the influence of interparticle friction on the shearing strength of a random assembly of spherical particles, Geotechnique, 19, 1: 150-157.

Takahashi, T. 2007. Debris flow: mechanics, prediction and countermeasures. Balkema-proceedings and monographs in engineering, water and earth sciences. Routledge.

Thompson, P. A., and Grest, G. S. 1991. Granular flow: friction and the dilatancy transition. Physical Review Letters, 67: 1751-1754.

Thornton, C. 2000. Numerical simulations of deviatoric shear deformation of granular media, Geotechnique, 50, 1:43-53.

Varnes, D.J. 1978. Slope movement types and processes. In Landslides Analysis and Control. Special Report 176, Transportation Research Board, National Academy of Sciences, Washington, D.C., pp. 11-33.

Vibert, C., Sassa, K., and Fukuoka, H. 1989. Friction characteristics of granular soils subjected to high speed shearing. Proceedings of the Japan-China symposium on landslides and debris flows, The Japan Landslide Society and The Japan Society of Erosion Control Engineering, Niigata and Tokyo, 1: 295-299.

Vidyapathi, M., Langroudi, K., Sun, J., Sundaresan, S., Tardos, G. I., and Subramaniam, S. 2012. Experimental and computational studies of dense granular flow: Transition from quasi-static to intermediate regime in a Couette shear device. Powder Technology, 220: 7-14.

Vilajosana, I., Khazaradze, G., Suriñach, E., Lied, E., and Kristensen, K. 2007. Snow avalanche speed determination using seismic methods. Cold Regions Science and Technology, 49: 2-10.

Wang, X. 2008. Geotechnical analysis of flow slides, debris flows, and related phenomena. Ph.D. Thesis, university of Alberta.

Wang, Y and Hutter, K. 1999. Shearing flows in a Goodman-Cowin type granular material – Theory and numerical results. Particulate Science and Technology, 17: 97 - 124.

Wieland, M., Gray, J.M.N.T., and Hutter, K. 1999. Channelized free-surface flow of cohesionless granular avalanches in a chute with shallow lateral curvature. Journal of Fluid Mechanics, 392: 73-100.

Wood, D. M. 1990. Soil behaviour and critical state soil mechanics. Cambridge University Press, pp. 462.

Wu, W. 2006. On high-order hypoplastic models for granular materials. Journal of Engineering Mathematics, 56: 23 - 34

Yan, Y., and Ji, S. 2009. Energy conservation in a granular shear flow and its quasi-solid-liquid transition. Particulate Science and Technology, 27(2): 126-138.

Yimsiri, S. 2001. Pre-failure deformation characteristics of soils: anisotropy and soil fabric, Ph.D. Dissertation, University of Cambridge, Cambridge, England.

APPENDIX A PFC CODES FOR FLOW SIMULATIONS

A.1 PFC CODE FOR PLANE SHEAR FLOW SIMULATION

```
Set Safety_fac  0.25 ; (Safety_fac is a PFC command used to reduce the computed
                       critical time step at the start of each cycle. Default value is
                       0.8 but recommended to use lower value when using the
                       Hertz contact model, especially under rapidly changing
                       conditions)

; INPUTS

def wall_inputs
d_     = 0.04          ; (Average particle diameter)
nx_    = 9             ; (Model size in x-direction, 9d)
ny_    = 9             ; (Model size in y-direction, 9d)
nz_    = 10            ; (Model size in z-direction, 10d including the boundary
                         particles)
s_     = 10000.0       ; (Prescribed vertical normal stress)
_alpha = 1.0           ; (It is f_R , see Eq. 3.4)
end

wall_inputs

def ball_inputs
n_          = 750              ; (number of particles excluding the boundary particles)
fb_         = 0.6                          ; (Friction coefficient at contact, μ_s)
pois_       = 0.34                         ; (Poisson's ratio)
shea_r      = 3.25e9/2.0/(1 + pois_)       ; (Shear modulus)
dampc_ = 0.75                              ; (Restitution coefficient, ε)
den_        = 1095.0                       ; (Particle density, ρ)
velo_       = -18.0                        ; (Shearing velocity, see Figure 3.1)
incr_       = 3.0                          ; (Shear velocity applied in 3 increments)
mc_modify1  = 15                           ; (see gradual_shearing function below)
mc_modify2  = 5000                         ; (see further_shearing function below)
cyc_        = 500                          ; (measurement sphere is updated every 500
                                             cycles, see gradual_shearing and
                                             further_shearing functions)
T_L = 2001                    ; (The initial ID no. for the top boundary particles)
T_U = T_L + nx_*ny_ - 1       ; (The final ID no. for the top boundary particles)
B_L = 1001                    ; (The initial ID no. for the bottom boundary particles)
B_U = B_L + nx_*ny_ - 1       ; (The final ID no. for the bottom boundary particles)
end

ball_inputs

def other_operations
x_ = nx_*d_
```

```
y_ = ny_*d_
z_ = nz_*d_
t_   = 0.00015                ; (Spacing b/n walls in the model to avoid their contact)
x_t = x_ - t_
y_t = y_ - t_
x_half = x_/2.0
y_half = y_/2.0
z_half = z_/2.0
r_ = d_/2.0
z_d = z_ - d_
r_m = z_half - 1.25*d_
end

other_operations

; MODEL CONSTRUCTION

plot add wall blue
plot add ball yellow   range id 1       n_
plot add ball green    range id T_L   T_U
plot add ball red      range id B_L   B_U
plot add measure blue                                  ; (plot measurement sphere)
plot show

; Construction of walls, id 1 is not used
wall id 2 face  (x_   0.0   0.0)  (x_   0.0    2.0)  (x_   y_    2.0)   (x_   y_    0.0)
wall id 3 face  (x_t  t_    z_)   (t_   t_     z_)   (t_   y_t   z_)    (x_t  y_t   z_)
wall id 4 face  (0.0  0.0   2.0)  (0.0  0.0    0.0)  (0.0  y_    0.0)   (0.0  y_    2.0)
wall id 5 face  (0.0  0.0   0.0)  (0.0  0.0    2.0)  (x_   0.0   2.0)   (x_   0.0   0.0)
wall id 6 face  (0.0  y_    0.0)  (x_   y_     0.0)  (x_   y_    2.0)   (0.0  y_    2.0)

; Assigning wall frictions (frictionless walls considered)
wall id 2 fric 0.0
wall id 3 fric 0.0 x  x_half  y  y_half  z  z_
wall id 4 fric 0.0
wall id 5 fric 0.0
wall id 6 fric 0.0

; Construction of boundary particles
def rough_surfacetop
zz =  z_ - r_
yy = -r_
loop m (1, ny_)
yy = yy + d_
xx = -r_
loop n (1, nx_)
```

```
xx = xx + d_
i = 2000 + (m-1)*nx_ + n
command
ball hertz id i x xx y yy z zz rad r_
endcommand
endloop
endloop
end

rough_surfacetop

prop dens den_ poiss pois_ shear shea_r range id T_L T_U
prop xvel 0.0 yvel 0.0 zvel 0.0 xspin 0.0 yspin 0.0 zspin 0.0 range id T_L  T_U
fix xspin yspin zspin x y z range id T_L  T_U

def rough_surfacebottom
zz =  r_
yy = -r_
loop m (1, ny_)
yy = yy + d_
xx = -r_
loop n (1, nx_)
xx = xx + d_
i = 1000 + (m-1)*nx_ + n
command
ball hertz id i x xx y yy z zz rad r_
endcommand
endloop
endloop
end

rough_surfacebottom

prop dens den_ poiss pois_ shear shea_r range id B_L  B_U
prop xvel 0.0 yvel 0.0 zvel 0.0 xspin 0.0 yspin 0.0 zspin 0.0 range id B_L  B_U
fix xspin yspin zspin x y z range id B_L  B_U

; Generation of particles
set random
gen hertz id 1       25 rad 0.008125  0.008125   x 0.0 x_ y 0.0 y_ z d_ z_d
gen hertz id 26      88 rad 0.0085      0.0085   x 0.0 x_ y 0.0 y_ z d_ z_d
gen hertz id 89     250 rad 0.009         0.009   x 0.0 x_ y 0.0 y_ z d_ z_d
gen hertz id 251    381 rad 0.0095        0.0095  x 0.0 x_ y 0.0 y_ z d_ z_d
gen hertz id 382    512 rad 0.01            0.01  x 0.0 x_ y 0.0 y_ z d_ z_d
gen hertz id 513    650 rad 0.0105        0.0105  x 0.0 x_ y 0.0 y_ z d_ z_d
gen hertz id 651    750 rad 0.01104     0.01104   x 0.0 x_ y 0.0 y_ z d_ z_d
```

```
prop dens den_ poiss pois_ shear shea_r range id 1 n_
ini rad mult 2 range id 1 n_
Cycle 4000
Solve
measure id 1 x x_half y y_half z  z_half  rad r_m
plot add measure blue
print measure 1
```

; CONSOLIDATION

; Assigning particle properties

```
prop fric fb_
prop damp 0.0
damp local 0.0

free z range id T_L  T_U      ; (free the top boundary particles for vertical motion)
```

; Defining servo-controlled wall and assigning vertical normal stress

```
def servo
while_stepping
swall_stress = w_zfob(find_wall(3))/(x_*y_)
sum_kn = 0.0
cp = contact_head
loop while cp # null
if c_ball2(cp) = find_wall(3)
sum_kn = sum_kn + c_hn(cp)
end_if
cp = c_next(cp)
end_loop
udz = _alpha*x_*y_/(tdel * sum_kn)*(swall_stress - s_)
 APV_ = 0.0
loop mQ(T_L, T_U)
APV_ = APV_ + b_zvel(find_ball(mQ))/(T_U - T_L + 1.0)
endloop
w_zvel(find_wall(3)) = udz + APV_
loop mr(T_L, T_U)
b_zvel(find_ball(mr)) = APV_
endloop
end

servo
```

; Defining Measurements

```
his swall_stress                                    ;  (History 1)
his APV_                                            ;  (History 2)
```

```
def volume_calculation
vol_me = 0.0
loop ac (1, n_)
vol_me = vol_me + 4.0/3.0*pi*(b_rad(find_ball(ac)))^3.0
endloop
end

volume_calculation

def Height_
Height_ = w_z(find_wall(3))
Void_R = (x_*y_*(w_z(find_wall(3))-d_) - (vol_me +
nx_*ny_*4.0/3.0*pi*r_^3))/(vol_me + nx_*ny_*4.0/3.0*pi*r_^3)
end

his Height_                    ;  (History 3)
his Void_R                     ;  (History 4)

History measure s11  id 1      ;  (History 5)
History measure s12  id 1      ;  (History 6)
History measure s21  id 1      ;  (History 7)
History measure s22  id 1      ;  (History 8)
History measure s13  id 1      ;  (History 9)
History measure s31  id 1      ;  (History 10)
History measure s23  id 1      ;  (History 11)
History measure s32  id 1      ;  (History 12)
History measure s33  id 1      ;  (History 13)
History measure ed11 id 1      ;  (History 14)
History measure ed12 id 1      ;  (History 15)
History measure ed21 id 1      ;  (History 16)
History measure ed22 id 1      ;  (History 17)
History measure ed31 id 1      ;  (History 18)
History measure ed13 id 1      ;  (History 19)
History measure ed23 id 1      ;  (History 20)
History measure ed32 id 1      ;  (History 21)
History measure ed33 id 1      ;  (History 22)
History measure coord id 1     ;  (History 23)

def VoidRatio_2
VoidRatio_2 = m_poros(find_meas(1))/(1.0 - m_poros(find_meas(1)))
end

History VoidRatio_2            ;  (History 24)
```

History measure sliding_fraction id 1 ; *(History 25)*

; Consolidating
Cycle 5000
Solve

; SHEARING

; Assigning viscous damping coefficients to particles
Damp viscous notension on

def damcoef
damcoef = abs(ln(dampc_)/sqrt(pi^2.0+(-1*ln(dampc_))^2.0))
end

Damp viscous normal damcoef shear damcoef

; Recording shearing time
set time 0.0

def real_time
real_time = time
end

his real_time ; *(History 26)*

; Replacing vertical walls with periodic boundaries
del wall 2 4 5 6
set periodic on 0.0 x_ 0.0 y_ 0.0 5.0

; Shearing by increasing the shear velocity gradually
def Gradual_shearing
vxx = 0.0
loop mm (1,incr_)
vxx = vxx + velo_/incr_
command
prop xvel vxx range id B_L B_U
fix x range id B_L B_U
endcommand
loop cb (1, mc_modify1)
z_newm = w_z(find_wall(3))/2.0
r_newm = z_newm - d_
if r_newm < x_half
command
measure id 1 x x_half y y_half z z_newm rad r_newm
endcommand

```
else
command
measure id 1 x x_half y y_half z z_newm rad x_half
endcommand
endif

command
print measure 1
cyc cyc_
endcommand
endloop
endloop
end

Gradual_shearing

; Further shearing after the required shearing velocity is reached
def Further_shearing
loop ms (1, mc_modify2)
z_newm = w_z(find_wall(3))/2.0
r_newm = z_newm - d_
if r_newm < x_half
command
measure id 1 x x_half y y_half z z_newm rad r_newm
endcommand
else
command
measure id 1 x x_half y y_half z z_newm rad x_half
endcommand
endif
command
print measure 1
cyc cyc_
endcommand
endloop
end

Further_shearing

; Measurements of solid fraction, and average and fluctuation velocities after flow is reached steady state

Call PFC_CODE_FOR_SOLIDFRACTIONANDVELOCITY_MEASUREMENTS.TXT
Further_shearing
```

A.2 PFC CODE FOR INCLINED FLOW SIMULATION

```
Set Safety_fac  0.35 ; (Safety_fac is a PFC command used to reduce the computed
                       critical time step at the start of each cycle. Default value is
                       0.8 but recommended to use lower value when using the
                       Hertz contact model, especially under rapidly changing
                       conditions)

; INPUTS

def wall_inputs
d_     = 0.04              ; (Average particle diameter)
nx_    = 7                 ; (Model size in x-direction, 7d)
ny_    = 4                 ; (Model size in y-direction, 4d)
nz_    = 50                ; (Model size in z-direction, 50d including the boundary
                             particles)
incl_  = 23                ; (Angle of inclined plane, θ)
end

wall_inputs

def ball_inputs
n_     = 825               ; (Number of particles)
fb_    = 0.6               ; (Friction coefficient at particles contact)
pois_  = 0.34              ; (Poisson's ratio)
shea_r = 3.25e9/2.0/(1 + pois_)   ; (Shear modulus)
dampc_ = 0.75              ; (Restitution coefficient)
den_   = 1095.0            ; (Particle density)
gravx_ = 9.81*sin(pi/180*incl_)   ; (Gravity in x-direction)
gravz_ = -9.81*cos(pi/180*incl_)  ; (Gravity in z-direction)
cyc_       = 5000000       ; (Number of cycles during shearing)
B_L = 2001                 ; (The initial ID no. for the bottom boundary
                             particles)
B_U = B_L + nx_*ny_ - 1    ; (The final ID no. for the bottom boundary
                             particles)
end

ball_inputs

def other_operations
x_ = nx_*d_
y_ = ny_*d_
z_ = nz_*d_
t_ = 0.00015               ; (Spacing b/n walls in the model to avoid their contact)
x_t = x_ - t_
y_t = y_ - t_
```

```
r_ = d_/2.0
z_d = z_ - d_
end

other_operations

; MODEL CONSTRUCTION

plo add wall blue
plo add ball yel   range id 1 n_
plo add ball red   range id B_L  B_U
plot show

; Construction of walls, id 1 is not used
wall id 2 face  (x_   0.0   0.0)  (x_   0.0   10.0)  (x_   y_   10.0)   (x_   y_   0.0)
wall id 3 face  (x_t  t_    z_)   (t_   t_    z_)     (t_   y_t  z_)     (x_t  y_t  z_)
wall id 4 face  (0.0  0.0   10.0)  (0.0  0.0   0.0)   (0.0  y_   0.0)    (0.0  y_   10.0)
wall id 5 face  (0.0  0.0   0.0)  (0.0  0.0   10.0)  (x_   0.0  10.0)   (x_   0.0  0.0)
wall id 6 face  (0.0  y_    0.0)  (x_   y_    0.0)   (x_   y_   10.0)   (0.0  y_   10.0)

; Assigning wall frictions (frictionless walls considered)
wall id 2 fric 0.0
wall id 3 fric 0.0  ; x  x_half  y  y_half  z  z_
wall id 4 fric 0.0
wall id 5 fric 0.0
wall id 6 fric 0.0

; Construction of boundary particles
def rough_surfacebottom
zz =  r_
yy = -r_
loop m (1, ny_)
yy = yy + d_
xx = -r_
loop n (1, nx_)
xx = xx + d_
i = 2000 + (m-1)*nx_ + n
command
ball hertz id i x xx y yy z zz rad r_
endcommand
endloop
endloop
end

rough_surfacebottom
```

```
prop dens den_ poiss pois_ shear shea_r range id B_L  B_U
prop xvel 0.0 yvel 0.0 zvel 0.0 xspin 0.0 yspin 0.0 zspin 0.0 range id B_L  B_U
fix xspin yspin zspin x y z range id B_L  B_U
```

; Generation of particles

```
set random
gen hertz id 1         27 rad 0.008125  0.008125  x 0.0 x_ y 0.0 y_ z d_ z_d
gen hertz id 28        98 rad 0.0085      0.0085    x 0.0 x_ y 0.0 y_ z d_ z_d
gen hertz id 99      275 rad 0.009        0.009     x 0.0 x_ y 0.0 y_ z d_ z_d
gen hertz id 276    419 rad 0.0095      0.0095    x 0.0 x_ y 0.0 y_ z d_ z_d
gen hertz id 420    563 rad 0.01          0.01      x 0.0 x_ y 0.0 y_ z d_ z_d
gen hertz id 564    716 rad 0.0105      0.0105    x 0.0 x_ y 0.0 y_ z d_ z_d
gen hertz id 717    825 rad 0.01104    0.01104   x 0.0 x_ y 0.0 y_ z d_ z_d

prop dens den_ poiss pois_ shear shea_r range id 1 n_

ini rad mult 2 range id 1 n_
Cycle 15000
Solve
```

; CONSOLIDATION

; Assigning particle properties

```
prop fric fb_
set gravity gravx_ 0  gravz_
prop damp 0.0
damp local 0.0
```

; Consolidating

```
Cycle 25000
Solve
```

; SHEARING

; Assigning viscous damping coefficients to particles

```
Damp viscous notension on

def damcoef
damcoef = abs(ln(dampc_)/sqrt(pi^2.0+(-1*ln(dampc_))^2.0))
end

Damp viscous normal damcoef shear damcoef
```

; Recording shearing time

```
set time 0.0
```

```
def real_time
real_time = time
end

his real_time                                   ; (History 1)

; Replacing vertical walls with periodic boundaries
del wall 2 3 4 5 6
set periodic on 0.0 x_ 0.0  y_ 0.0 10.0

; Measurements of solid fraction, and average and fluctuation velocities

Call PFC_CODE_FOR_ SOLIDFRACTIONANDVELOCITY _MEASUREMENTS.TXT

; Shearing
cyc cyc_
```

A.3 PFC CODE FOR MEASUREMENTS OF SOLID FRACTION, AVERAGE FLOW VELOCITY, AND FLUCTUATION VELOCITIES

; Solid fraction, average and velocity fluctuations after dividing the flow into layers of equal thickness, d_max (diameter of the largest particle)

; This program is for flow depth of up to 10 layers

; The red-bold lines are used only for plane shear simulations

```
Def Full_Ht
mc_modify2  = 1300
d_max = 2*b_rad(find_ball(750))        ; (The diameter of the largest particle)
end

Full_Ht

Def Depth_

Depth_  = w_z(find_wall(3))            ; (The height of flow, H)

; For Layer 1

zb_          = 0.0*d_max + d_
zt_          = 1.0*d_max + d_
W1_          = 0.0
W1_Vx        = 0.0
W1_Vx2       = 0.0
W1_Vy2       = 0.0
W1_Vz2       = 0.0
W1_VxVz = 0.0

loop aa (1, n_)

hb_     = b_z(find_ball(aa)) + b_rad(find_ball(aa)) - zb_

if hb_ > 0.0
if hb_ < 2.0*b_rad(find_ball(aa))
W1_     = W1_     + (abs(hb_))^2.0*(3.0*b_rad(find_ball(aa)) - hb_)
W1_Vx   = W1_Vx   +
b_xvel(find_ball(aa))*(abs(hb_))^2.0*(3.0*b_rad(find_ball(aa)) - hb_)
W1_Vx2  = W1_Vx2  +
(abs(b_xvel(find_ball(aa))))^2.0*(abs(hb_))^2.0*(3.0*b_rad(find_ball(aa)) - hb_)
W1_Vy2  = W1_Vy2  +
(abs(b_yvel(find_ball(aa))))^2.0*(abs(hb_))^2.0*(3.0*b_rad(find_ball(aa)) - hb_)
```

```
W1_Vz2  = W1_Vz2  +
(abs(b_zvel(find_ball(aa))))^2.0*(abs(hb_))^2.0*(3.0*b_rad(find_ball(aa)) - hb_)
W1_VxVz = W1_VxVz +
b_xvel(find_ball(aa))*b_zvel(find_ball(aa))*(abs(hb_))^2.0*(3.0*b_rad(find_
ball(aa)) - hb_)
end_if
end_if

if hb_ >= 2.0*b_rad(find_ball(aa))
if hb_ <= d_max
W1_     = W1_     + 4.0*(abs(b_rad(find_ball(aa))))^3.0
W1_Vx   = W1_Vx   + b_xvel(find_ball(aa))*4.0*(abs(b_rad(find_ball(aa))))^3.0
W1_Vx2  = W1_Vx2  +
(abs(b_xvel(find_ball(aa))))^2.0*4.0*(abs(b_rad(find_ball(aa))))^3.0
W1_Vy2  = W1_Vy2  +
(abs(b_yvel(find_ball(aa))))^2.0*4.0*(abs(b_rad(find_ball(aa))))^3.0
W1_Vz2  = W1_Vz2  +
(abs(b_zvel(find_ball(aa))))^2.0*4.0*(abs(b_rad(find_ball(aa))))^3.0
W1_VxVz = W1_VxVz +
b_xvel(find_ball(aa))*b_zvel(find_ball(aa))*4.0*(abs(b_rad(find_ball(aa))))^
3.0
end_if
end_if

if hb_ > d_max
if hb_ < d_max + 2.0*b_rad(find_ball(aa))
ht_     = zt_     - b_z(find_ball(aa)) + b_rad(find_ball(aa))
W1_     = W1_     + (abs(ht_))^2.0*(3.0*b_rad(find_ball(aa)) - ht_)
W1_Vx   = W1_Vx   +
b_xvel(find_ball(aa))*(abs(ht_))^2.0*(3.0*b_rad(find_ball(aa)) - ht_)
W1_Vx2  = W1_Vx2  +
(abs(b_xvel(find_ball(aa))))^2.0*(abs(ht_))^2.0*(3.0*b_rad(find_ball(aa)) - ht_)
W1_Vy2  = W1_Vy2  +
(abs(b_yvel(find_ball(aa))))^2.0*(abs(ht_))^2.0*(3.0*b_rad(find_ball(aa)) - ht_)
W1_Vz2  = W1_Vz2  +
(abs(b_zvel(find_ball(aa))))^2.0*(abs(ht_))^2.0*(3.0*b_rad(find_ball(aa)) - ht_)
W1_VxVz = W1_VxVz +
b_xvel(find_ball(aa))*b_zvel(find_ball(aa))*(abs(ht_))^2.0*(3.0*b_rad(find_
ball(aa)) - ht_)
end_if
end_if

endloop

; For Layer 2
```

```
zb_          = 1.0*d_max + d_
zt_          = 2.0*d_max + d_
W2_          = 0.0
W2_Vx        = 0.0
W2_Vx2       = 0.0
W2_Vy2       = 0.0
W2_Vz2       = 0.0
W2_VxVz = 0.0

loop aa (1, n_)

hb_     = b_z(find_ball(aa)) + b_rad(find_ball(aa)) - zb_

if hb_ > 0.0
if hb_ < 2.0*b_rad(find_ball(aa))
W2_     = W2_     + (abs(hb_))^2.0*(3.0*b_rad(find_ball(aa)) - hb_)
W2_Vx   = W2_Vx   +
b_xvel(find_ball(aa))*(abs(hb_))^2.0*(3.0*b_rad(find_ball(aa)) - hb_)
W2_Vx2  = W2_Vx2  +
(abs(b_xvel(find_ball(aa))))^2.0*(abs(hb_))^2.0*(3.0*b_rad(find_ball(aa)) - hb_)
W2_Vy2  = W2_Vy2  +
(abs(b_yvel(find_ball(aa))))^2.0*(abs(hb_))^2.0*(3.0*b_rad(find_ball(aa)) - hb_)
W2_Vz2  = W2_Vz2  +
(abs(b_zvel(find_ball(aa))))^2.0*(abs(hb_))^2.0*(3.0*b_rad(find_ball(aa)) - hb_)
W2_VxVz = W2_VxVz +
b_xvel(find_ball(aa))*b_zvel(find_ball(aa))*(abs(hb_))^2.0*(3.0*b_rad(find_
ball(aa)) - hb_)
end_if
end_if

if hb_ >= 2.0*b_rad(find_ball(aa))
if hb_ <= d_max
W2_     = W2_     + 4.0*(abs(b_rad(find_ball(aa))))^3.0
W2_Vx   = W2_Vx   + b_xvel(find_ball(aa))*4.0*(abs(b_rad(find_ball(aa))))^3.0
W2_Vx2  = W2_Vx2  +
(abs(b_xvel(find_ball(aa))))^2.0*4.0*(abs(b_rad(find_ball(aa))))^3.0
W2_Vy2  = W2_Vy2  +
(abs(b_yvel(find_ball(aa))))^2.0*4.0*(abs(b_rad(find_ball(aa))))^3.0
W2_Vz2  = W2_Vz2  +
(abs(b_zvel(find_ball(aa))))^2.0*4.0*(abs(b_rad(find_ball(aa))))^3.0
W2_VxVz = W2_VxVz +
b_xvel(find_ball(aa))*b_zvel(find_ball(aa))*4.0*(abs(b_rad(find_ball(aa))))^
3.0
end_if
end_if
```

```
if hb_ > d_max
if hb_ < d_max + 2.0*b_rad(find_ball(aa))
ht_     = zt_     - b_z(find_ball(aa)) + b_rad(find_ball(aa))
W2_     = W2_     + (abs(ht_))^2.0*(3.0*b_rad(find_ball(aa)) - ht_)
W2_Vx   = W2_Vx   +
b_xvel(find_ball(aa))*(abs(ht_))^2.0*(3.0*b_rad(find_ball(aa)) - ht_)
W2_Vx2  = W2_Vx2  +
(abs(b_xvel(find_ball(aa))))^2.0*(abs(ht_))^2.0*(3.0*b_rad(find_ball(aa)) - ht_)
W2_Vy2  = W2_Vy2  +
(abs(b_yvel(find_ball(aa))))^2.0*(abs(ht_))^2.0*(3.0*b_rad(find_ball(aa)) - ht_)
W2_Vz2  = W2_Vz2  +
(abs(b_zvel(find_ball(aa))))^2.0*(abs(ht_))^2.0*(3.0*b_rad(find_ball(aa)) - ht_)
W2_VxVz = W2_VxVz +
b_xvel(find_ball(aa))*b_zvel(find_ball(aa))*(abs(ht_))^2.0*(3.0*b_rad(find_
ball(aa)) - ht_)
end_if
end_if

endloop

; For Layer 3

zb_          = 2.0*d_max + d_
zt_          = 3.0*d_max + d_
W3_          = 0.0
W3_Vx        = 0.0
W3_Vx2       = 0.0
W3_Vy2       = 0.0
W3_Vz2       = 0.0
W3_VxVz = 0.0

loop aa (1, n_)

hb_     = b_z(find_ball(aa)) + b_rad(find_ball(aa)) - zb_

if hb_ > 0.0
if hb_ < 2.0*b_rad(find_ball(aa))
W3_     = W3_     + (abs(hb_))^2.0*(3.0*b_rad(find_ball(aa)) - hb_)
W3_Vx   = W3_Vx   +
b_xvel(find_ball(aa))*(abs(hb_))^2.0*(3.0*b_rad(find_ball(aa)) - hb_)
W3_Vx2  = W3_Vx2  +
(abs(b_xvel(find_ball(aa))))^2.0*(abs(hb_))^2.0*(3.0*b_rad(find_ball(aa)) - hb_)
W3_Vy2  = W3_Vy2  +
(abs(b_yvel(find_ball(aa))))^2.0*(abs(hb_))^2.0*(3.0*b_rad(find_ball(aa)) - hb_)
W3_Vz2  = W3_Vz2  +
(abs(b_zvel(find_ball(aa))))^2.0*(abs(hb_))^2.0*(3.0*b_rad(find_ball(aa)) - hb_)
```

W3_VxVz = W3_VxVz +
b_xvel(find_ball(aa))*b_zvel(find_ball(aa))*(abs(hb_))^2.0*(3.0*b_rad(find_
ball(aa)) - hb_)
end_if
end_if

if hb_ >= 2.0*b_rad(find_ball(aa))
if hb_ <= d_max
W3_ = W3_ + 4.0*(abs(b_rad(find_ball(aa))))^3.0
W3_Vx = W3_Vx + b_xvel(find_ball(aa))*4.0*(abs(b_rad(find_ball(aa))))^3.0
W3_Vx2 = W3_Vx2 +
(abs(b_xvel(find_ball(aa))))^2.0*4.0*(abs(b_rad(find_ball(aa))))^3.0
W3_Vy2 = W3_Vy2 +
(abs(b_yvel(find_ball(aa))))^2.0*4.0*(abs(b_rad(find_ball(aa))))^3.0
W3_Vz2 = W3_Vz2 +
(abs(b_zvel(find_ball(aa))))^2.0*4.0*(abs(b_rad(find_ball(aa))))^3.0
W3_VxVz = W3_VxVz +
b_xvel(find_ball(aa))*b_zvel(find_ball(aa))*4.0*(abs(b_rad(find_ball(aa))))^
3.0
end_if
end_if

if hb_ > d_max
if hb_ < d_max + 2.0*b_rad(find_ball(aa))
ht_ = zt_ - b_z(find_ball(aa)) + b_rad(find_ball(aa))
W3_ = W3_ + (abs(ht_))^2.0*(3.0*b_rad(find_ball(aa)) - ht_)
W3_Vx = W3_Vx +
b_xvel(find_ball(aa))*(abs(ht_))^2.0*(3.0*b_rad(find_ball(aa)) - ht_)
W3_Vx2 = W3_Vx2 +
(abs(b_xvel(find_ball(aa))))^2.0*(abs(ht_))^2.0*(3.0*b_rad(find_ball(aa)) - ht_)
W3_Vy2 = W3_Vy2 +
(abs(b_yvel(find_ball(aa))))^2.0*(abs(ht_))^2.0*(3.0*b_rad(find_ball(aa)) - ht_)
W3_Vz2 = W3_Vz2 +
(abs(b_zvel(find_ball(aa))))^2.0*(abs(ht_))^2.0*(3.0*b_rad(find_ball(aa)) - ht_)
W3_VxVz = W3_VxVz +
b_xvel(find_ball(aa))*b_zvel(find_ball(aa))*(abs(ht_))^2.0*(3.0*b_rad(find_
ball(aa)) - ht_)
end_if
end_if

endloop

; For Layer 4

zb_ = 3.0*d_max + d_
zt_ = 4.0*d_max + d_

```
W4_          = 0.0
W4_Vx        = 0.0
W4_Vx2       = 0.0
W4_Vy2       = 0.0
W4_Vz2       = 0.0
W4_VxVz = 0.0

loop aa (1, n_)

hb_     = b_z(find_ball(aa)) + b_rad(find_ball(aa)) - zb_

if hb_ > 0.0
if hb_ < 2.0*b_rad(find_ball(aa))
W4_     = W4_     + (abs(hb_))^2.0*(3.0*b_rad(find_ball(aa)) - hb_)
W4_Vx   = W4_Vx   +
b_xvel(find_ball(aa))*(abs(hb_))^2.0*(3.0*b_rad(find_ball(aa)) - hb_)
W4_Vx2  = W4_Vx2  +
(abs(b_xvel(find_ball(aa))))^2.0*(abs(hb_))^2.0*(3.0*b_rad(find_ball(aa)) - hb_)
W4_Vy2  = W4_Vy2  +
(abs(b_yvel(find_ball(aa))))^2.0*(abs(hb_))^2.0*(3.0*b_rad(find_ball(aa)) - hb_)
W4_Vz2  = W4_Vz2  +
(abs(b_zvel(find_ball(aa))))^2.0*(abs(hb_))^2.0*(3.0*b_rad(find_ball(aa)) - hb_)
W4_VxVz = W4_VxVz +
b_xvel(find_ball(aa))*b_zvel(find_ball(aa))*(abs(hb_))^2.0*(3.0*b_rad(find_
ball(aa)) - hb_)
end_if
end_if

if hb_ >= 2.0*b_rad(find_ball(aa))
if hb_ <= d_max
W4_     = W4_     + 4.0*(abs(b_rad(find_ball(aa))))^3.0
W4_Vx   = W4_Vx   + b_xvel(find_ball(aa))*4.0*(abs(b_rad(find_ball(aa))))^3.0
W4_Vx2  = W4_Vx2  +
(abs(b_xvel(find_ball(aa))))^2.0*4.0*(abs(b_rad(find_ball(aa))))^3.0
W4_Vy2  = W4_Vy2  +
(abs(b_yvel(find_ball(aa))))^2.0*4.0*(abs(b_rad(find_ball(aa))))^3.0
W4_Vz2  = W4_Vz2  +
(abs(b_zvel(find_ball(aa))))^2.0*4.0*(abs(b_rad(find_ball(aa))))^3.0
W4_VxVz = W4_VxVz +
b_xvel(find_ball(aa))*b_zvel(find_ball(aa))*4.0*(abs(b_rad(find_ball(aa))))^
3.0
end_if
end_if

if hb_ > d_max
if hb_ < d_max + 2.0*b_rad(find_ball(aa))
```

```
ht_     = zt_     - b_z(find_ball(aa)) + b_rad(find_ball(aa))
W4_     = W4_     + (abs(ht_))^2.0*(3.0*b_rad(find_ball(aa)) - ht_)
W4_Vx   = W4_Vx   +
b_xvel(find_ball(aa))*(abs(ht_))^2.0*(3.0*b_rad(find_ball(aa)) - ht_)
W4_Vx2  = W4_Vx2  +
(abs(b_xvel(find_ball(aa))))^2.0*(abs(ht_))^2.0*(3.0*b_rad(find_ball(aa)) - ht_)
W4_Vy2  = W4_Vy2  +
(abs(b_yvel(find_ball(aa))))^2.0*(abs(ht_))^2.0*(3.0*b_rad(find_ball(aa)) - ht_)
W4_Vz2  = W4_Vz2  +
(abs(b_zvel(find_ball(aa))))^2.0*(abs(ht_))^2.0*(3.0*b_rad(find_ball(aa)) - ht_)
W4_VxVz = W4_VxVz +
b_xvel(find_ball(aa))*b_zvel(find_ball(aa))*(abs(ht_))^2.0*(3.0*b_rad(find_
ball(aa)) - ht_)
end_if
end_if

endloop

; For Layer 5

zb_         = 4.0*d_max + d_
zt_         = 5.0*d_max + d_
W5_         = 0.0
W5_Vx       = 0.0
W5_Vx2      = 0.0
W5_Vy2      = 0.0
W5_Vz2      = 0.0
W5_VxVz = 0.0

loop aa (1, n_)

hb_     = b_z(find_ball(aa)) + b_rad(find_ball(aa)) - zb_

if hb_ > 0.0
if hb_ < 2.0*b_rad(find_ball(aa))
W5_     = W5_     + (abs(hb_))^2.0*(3.0*b_rad(find_ball(aa)) - hb_)
W5_Vx   = W5_Vx   +
b_xvel(find_ball(aa))*(abs(hb_))^2.0*(3.0*b_rad(find_ball(aa)) - hb_)
W5_Vx2  = W5_Vx2  +
(abs(b_xvel(find_ball(aa))))^2.0*(abs(hb_))^2.0*(3.0*b_rad(find_ball(aa)) - hb_)
W5_Vy2  = W5_Vy2  +
(abs(b_yvel(find_ball(aa))))^2.0*(abs(hb_))^2.0*(3.0*b_rad(find_ball(aa)) - hb_)
W5_Vz2  = W5_Vz2  +
(abs(b_zvel(find_ball(aa))))^2.0*(abs(hb_))^2.0*(3.0*b_rad(find_ball(aa)) - hb_)
```

```
W5_VxVz = W5_VxVz +
b_xvel(find_ball(aa))*b_zvel(find_ball(aa))*(abs(hb_))^2.0*(3.0*b_rad(find_
ball(aa)) - hb_)
end_if
end_if

if hb_ >= 2.0*b_rad(find_ball(aa))
if hb_ <= d_max
W5_    = W5_    + 4.0*(abs(b_rad(find_ball(aa))))^3.0
W5_Vx  = W5_Vx  + b_xvel(find_ball(aa))*4.0*(abs(b_rad(find_ball(aa))))^3.0
W5_Vx2 = W5_Vx2 +
(abs(b_xvel(find_ball(aa))))^2.0*4.0*(abs(b_rad(find_ball(aa))))^3.0
W5_Vy2 = W5_Vy2 +
(abs(b_yvel(find_ball(aa))))^2.0*4.0*(abs(b_rad(find_ball(aa))))^3.0
W5_Vz2 = W5_Vz2 +
(abs(b_zvel(find_ball(aa))))^2.0*4.0*(abs(b_rad(find_ball(aa))))^3.0
W5_VxVz = W5_VxVz +
b_xvel(find_ball(aa))*b_zvel(find_ball(aa))*4.0*(abs(b_rad(find_ball(aa))))^
3.0
end_if
end_if

if hb_ > d_max
if hb_ < d_max + 2.0*b_rad(find_ball(aa))
ht_    = zt_    - b_z(find_ball(aa)) + b_rad(find_ball(aa))
W5_    = W5_    + (abs(ht_))^2.0*(3.0*b_rad(find_ball(aa)) - ht_)
W5_Vx  = W5_Vx  +
b_xvel(find_ball(aa))*(abs(ht_))^2.0*(3.0*b_rad(find_ball(aa)) - ht_)
W5_Vx2 = W5_Vx2 +
(abs(b_xvel(find_ball(aa))))^2.0*(abs(ht_))^2.0*(3.0*b_rad(find_ball(aa)) - ht_)
W5_Vy2 = W5_Vy2 +
(abs(b_yvel(find_ball(aa))))^2.0*(abs(ht_))^2.0*(3.0*b_rad(find_ball(aa)) - ht_)
W5_Vz2 = W5_Vz2 +
(abs(b_zvel(find_ball(aa))))^2.0*(abs(ht_))^2.0*(3.0*b_rad(find_ball(aa)) - ht_)
W5_VxVz = W5_VxVz +
b_xvel(find_ball(aa))*b_zvel(find_ball(aa))*(abs(ht_))^2.0*(3.0*b_rad(find_
ball(aa)) - ht_)
end_if
end_if

endloop

; For Layer 6

zb_        = 5.0*d_max + d_
zt_        = 6.0*d_max + d_
```

```
W6_          = 0.0
W6_Vx        = 0.0
W6_Vx2       = 0.0
W6_Vy2       = 0.0
W6_Vz2       = 0.0
W6_VxVz = 0.0

loop aa (1, n_)

hb_     = b_z(find_ball(aa)) + b_rad(find_ball(aa)) - zb_

if hb_ > 0.0
if hb_ < 2.0*b_rad(find_ball(aa))
W6_     = W6_     + (abs(hb_))^2.0*(3.0*b_rad(find_ball(aa)) - hb_)
W6_Vx   = W6_Vx   +
b_xvel(find_ball(aa))*(abs(hb_))^2.0*(3.0*b_rad(find_ball(aa)) - hb_)
W6_Vx2  = W6_Vx2  +
(abs(b_xvel(find_ball(aa))))^2.0*(abs(hb_))^2.0*(3.0*b_rad(find_ball(aa)) - hb_)
W6_Vy2  = W6_Vy2  +
(abs(b_yvel(find_ball(aa))))^2.0*(abs(hb_))^2.0*(3.0*b_rad(find_ball(aa)) - hb_)
W6_Vz2  = W6_Vz2  +
(abs(b_zvel(find_ball(aa))))^2.0*(abs(hb_))^2.0*(3.0*b_rad(find_ball(aa)) - hb_)
W6_VxVz = W6_VxVz +
b_xvel(find_ball(aa))*b_zvel(find_ball(aa))*(abs(hb_))^2.0*(3.0*b_rad(find_
ball(aa)) - hb_)
end_if
end_if

if hb_ >= 2.0*b_rad(find_ball(aa))
if hb_ <= d_max
W6_     = W6_     + 4.0*(abs(b_rad(find_ball(aa))))^3.0
W6_Vx   = W6_Vx   + b_xvel(find_ball(aa))*4.0*(abs(b_rad(find_ball(aa))))^3.0
W6_Vx2  = W6_Vx2  +
(abs(b_xvel(find_ball(aa))))^2.0*4.0*(abs(b_rad(find_ball(aa))))^3.0
W6_Vy2  = W6_Vy2  +
(abs(b_yvel(find_ball(aa))))^2.0*4.0*(abs(b_rad(find_ball(aa))))^3.0
W6_Vz2  = W6_Vz2  +
(abs(b_zvel(find_ball(aa))))^2.0*4.0*(abs(b_rad(find_ball(aa))))^3.0
W6_VxVz = W6_VxVz +
b_xvel(find_ball(aa))*b_zvel(find_ball(aa))*4.0*(abs(b_rad(find_ball(aa))))^
3.0
end_if
end_if

if hb_ > d_max
if hb_ < d_max + 2.0*b_rad(find_ball(aa))
```

```
ht_     = zt_     - b_z(find_ball(aa)) + b_rad(find_ball(aa))
W6_     = W6_     + (abs(ht_))^2.0*(3.0*b_rad(find_ball(aa)) - ht_)
W6_Vx   = W6_Vx   +
b_xvel(find_ball(aa))*(abs(ht_))^2.0*(3.0*b_rad(find_ball(aa)) - ht_)
W6_Vx2  = W6_Vx2  +
(abs(b_xvel(find_ball(aa))))^2.0*(abs(ht_))^2.0*(3.0*b_rad(find_ball(aa)) - ht_)
W6_Vy2  = W6_Vy2  +
(abs(b_yvel(find_ball(aa))))^2.0*(abs(ht_))^2.0*(3.0*b_rad(find_ball(aa)) - ht_)
W6_Vz2  = W6_Vz2  +
(abs(b_zvel(find_ball(aa))))^2.0*(abs(ht_))^2.0*(3.0*b_rad(find_ball(aa)) - ht_)
W6_VxVz = W6_VxVz +
b_xvel(find_ball(aa))*b_zvel(find_ball(aa))*(abs(ht_))^2.0*(3.0*b_rad(find_
ball(aa)) - ht_)
end_if
end_if

endloop

; For Layer 7

zb_         = 6.0*d_max + d_
zt_         = 7.0*d_max + d_
W7_         = 0.0
W7_Vx       = 0.0
W7_Vx2      = 0.0
W7_Vy2      = 0.0
W7_Vz2      = 0.0
W7_VxVz = 0.0

loop aa (1, n_)

hb_     = b_z(find_ball(aa)) + b_rad(find_ball(aa)) - zb_

if hb_ > 0.0
if hb_ < 2.0*b_rad(find_ball(aa))
W7_     = W7_     + (abs(hb_))^2.0*(3.0*b_rad(find_ball(aa)) - hb_)
W7_Vx   = W7_Vx   +
b_xvel(find_ball(aa))*(abs(hb_))^2.0*(3.0*b_rad(find_ball(aa)) - hb_)
W7_Vx2  = W7_Vx2  +
(abs(b_xvel(find_ball(aa))))^2.0*(abs(hb_))^2.0*(3.0*b_rad(find_ball(aa)) - hb_)
W7_Vy2  = W7_Vy2  +
(abs(b_yvel(find_ball(aa))))^2.0*(abs(hb_))^2.0*(3.0*b_rad(find_ball(aa)) - hb_)
W7_Vz2  = W7_Vz2  +
(abs(b_zvel(find_ball(aa))))^2.0*(abs(hb_))^2.0*(3.0*b_rad(find_ball(aa)) - hb_)
```

W7_VxVz = W7_VxVz +
b_xvel(find_ball(aa))*b_zvel(find_ball(aa))*(abs(hb_))^2.0*(3.0*b_rad(find_
ball(aa)) - hb_)
end_if
end_if

if hb_ >= 2.0*b_rad(find_ball(aa))
if hb_ <= d_max
W7_ = W7_ + 4.0*(abs(b_rad(find_ball(aa))))^3.0
W7_Vx = W7_Vx + b_xvel(find_ball(aa))*4.0*(abs(b_rad(find_ball(aa))))^3.0
W7_Vx2 = W7_Vx2 +
(abs(b_xvel(find_ball(aa))))^2.0*4.0*(abs(b_rad(find_ball(aa))))^3.0
W7_Vy2 = W7_Vy2 +
(abs(b_yvel(find_ball(aa))))^2.0*4.0*(abs(b_rad(find_ball(aa))))^3.0
W7_Vz2 = W7_Vz2 +
(abs(b_zvel(find_ball(aa))))^2.0*4.0*(abs(b_rad(find_ball(aa))))^3.0
W7_VxVz = W7_VxVz +
b_xvel(find_ball(aa))*b_zvel(find_ball(aa))*4.0*(abs(b_rad(find_ball(aa))))^
3.0
end_if
end_if

if hb_ > d_max
if hb_ < d_max + 2.0*b_rad(find_ball(aa))
ht_ = zt_ - b_z(find_ball(aa)) + b_rad(find_ball(aa))
W7_ = W7_ + (abs(ht_))^2.0*(3.0*b_rad(find_ball(aa)) - ht_)
W7_Vx = W7_Vx +
b_xvel(find_ball(aa))*(abs(ht_))^2.0*(3.0*b_rad(find_ball(aa)) - ht_)
W7_Vx2 = W7_Vx2 +
(abs(b_xvel(find_ball(aa))))^2.0*(abs(ht_))^2.0*(3.0*b_rad(find_ball(aa)) - ht_)
W7_Vy2 = W7_Vy2 +
(abs(b_yvel(find_ball(aa))))^2.0*(abs(ht_))^2.0*(3.0*b_rad(find_ball(aa)) - ht_)
W7_Vz2 = W7_Vz2 +
(abs(b_zvel(find_ball(aa))))^2.0*(abs(ht_))^2.0*(3.0*b_rad(find_ball(aa)) - ht_)
W7_VxVz = W7_VxVz +
b_xvel(find_ball(aa))*b_zvel(find_ball(aa))*(abs(ht_))^2.0*(3.0*b_rad(find_
ball(aa)) - ht_)
end_if
end_if

endloop

; For Layer 8

zb_ = 7.0*d_max + d_
zt_ = 8.0*d_max + d_

```
W8_          = 0.0
W8_Vx        = 0.0
W8_Vx2       = 0.0
W8_Vy2       = 0.0
W8_Vz2       = 0.0
W8_VxVz = 0.0

loop aa (1, n_)

hb_     = b_z(find_ball(aa)) + b_rad(find_ball(aa)) - zb_

if hb_ > 0.0
if hb_ < 2.0*b_rad(find_ball(aa))
W8_     = W8_     + (abs(hb_))^2.0*(3.0*b_rad(find_ball(aa)) - hb_)
W8_Vx   = W8_Vx   +
b_xvel(find_ball(aa))*(abs(hb_))^2.0*(3.0*b_rad(find_ball(aa)) - hb_)
W8_Vx2  = W8_Vx2  +
(abs(b_xvel(find_ball(aa))))^2.0*(abs(hb_))^2.0*(3.0*b_rad(find_ball(aa)) - hb_)
W8_Vy2  = W8_Vy2  +
(abs(b_yvel(find_ball(aa))))^2.0*(abs(hb_))^2.0*(3.0*b_rad(find_ball(aa)) - hb_)
W8_Vz2  = W8_Vz2  +
(abs(b_zvel(find_ball(aa))))^2.0*(abs(hb_))^2.0*(3.0*b_rad(find_ball(aa)) - hb_)
W8_VxVz = W8_VxVz +
b_xvel(find_ball(aa))*b_zvel(find_ball(aa))*(abs(hb_))^2.0*(3.0*b_rad(find_
ball(aa)) - hb_)
end_if
end_if

if hb_ >= 2.0*b_rad(find_ball(aa))
if hb_ <= d_max
W8_     = W8_     + 4.0*(abs(b_rad(find_ball(aa))))^3.0
W8_Vx   = W8_Vx   + b_xvel(find_ball(aa))*4.0*(abs(b_rad(find_ball(aa))))^3.0
W8_Vx2  = W8_Vx2  +
(abs(b_xvel(find_ball(aa))))^2.0*4.0*(abs(b_rad(find_ball(aa))))^3.0
W8_Vy2  = W8_Vy2  +
(abs(b_yvel(find_ball(aa))))^2.0*4.0*(abs(b_rad(find_ball(aa))))^3.0
W8_Vz2  = W8_Vz2  +
(abs(b_zvel(find_ball(aa))))^2.0*4.0*(abs(b_rad(find_ball(aa))))^3.0
W8_VxVz = W8_VxVz +
b_xvel(find_ball(aa))*b_zvel(find_ball(aa))*4.0*(abs(b_rad(find_ball(aa))))^
3.0
end_if
end_if

if hb_ > d_max
if hb_ < d_max + 2.0*b_rad(find_ball(aa))
```

```
ht_     = zt_     - b_z(find_ball(aa)) + b_rad(find_ball(aa))
W8_     = W8_     + (abs(ht_))^2.0*(3.0*b_rad(find_ball(aa)) - ht_)
W8_Vx   = W8_Vx   +
b_xvel(find_ball(aa))*(abs(ht_))^2.0*(3.0*b_rad(find_ball(aa)) - ht_)
W8_Vx2  = W8_Vx2  +
(abs(b_xvel(find_ball(aa))))^2.0*(abs(ht_))^2.0*(3.0*b_rad(find_ball(aa)) - ht_)
W8_Vy2  = W8_Vy2  +
(abs(b_yvel(find_ball(aa))))^2.0*(abs(ht_))^2.0*(3.0*b_rad(find_ball(aa)) - ht_)
W8_Vz2  = W8_Vz2  +
(abs(b_zvel(find_ball(aa))))^2.0*(abs(ht_))^2.0*(3.0*b_rad(find_ball(aa)) - ht_)
W8_VxVz = W8_VxVz +
b_xvel(find_ball(aa))*b_zvel(find_ball(aa))*(abs(ht_))^2.0*(3.0*b_rad(find_
ball(aa)) - ht_)
end_if
end_if

endloop

; For Layer 9

zb_          = 8.0*d_max + d_
zt_          = 9.0*d_max + d_
W9_          = 0.0
W9_Vx        = 0.0
W9_Vx2       = 0.0
W9_Vy2       = 0.0
W9_Vz2       = 0.0
W9_VxVz = 0.0

loop aa (1, n_)

hb_     = b_z(find_ball(aa)) + b_rad(find_ball(aa)) - zb_

if hb_ > 0.0
if hb_ < 2.0*b_rad(find_ball(aa))
W9_     = W9_     + (abs(hb_))^2.0*(3.0*b_rad(find_ball(aa)) - hb_)
W9_Vx   = W9_Vx   +
b_xvel(find_ball(aa))*(abs(hb_))^2.0*(3.0*b_rad(find_ball(aa)) - hb_)
W9_Vx2  = W9_Vx2  +
(abs(b_xvel(find_ball(aa))))^2.0*(abs(hb_))^2.0*(3.0*b_rad(find_ball(aa)) - hb_)
W9_Vy2  = W9_Vy2  +
(abs(b_yvel(find_ball(aa))))^2.0*(abs(hb_))^2.0*(3.0*b_rad(find_ball(aa)) - hb_)
W9_Vz2  = W9_Vz2  +
(abs(b_zvel(find_ball(aa))))^2.0*(abs(hb_))^2.0*(3.0*b_rad(find_ball(aa)) - hb_)
```

W9_VxVz = W9_VxVz +
b_xvel(find_ball(aa))*b_zvel(find_ball(aa))*(abs(hb_))^2.0*(3.0*b_rad(find_
ball(aa)) - hb_)
end_if
end_if

if hb_ >= 2.0*b_rad(find_ball(aa))
if hb_ <= d_max
W9_ = W9_ + 4.0*(abs(b_rad(find_ball(aa))))^3.0
W9_Vx = W9_Vx + b_xvel(find_ball(aa))*4.0*(abs(b_rad(find_ball(aa))))^3.0
W9_Vx2 = W9_Vx2 +
(abs(b_xvel(find_ball(aa))))^2.0*4.0*(abs(b_rad(find_ball(aa))))^3.0
W9_Vy2 = W9_Vy2 +
(abs(b_yvel(find_ball(aa))))^2.0*4.0*(abs(b_rad(find_ball(aa))))^3.0
W9_Vz2 = W9_Vz2 +
(abs(b_zvel(find_ball(aa))))^2.0*4.0*(abs(b_rad(find_ball(aa))))^3.0
W9_VxVz = W9_VxVz +
b_xvel(find_ball(aa))*b_zvel(find_ball(aa))*4.0*(abs(b_rad(find_ball(aa))))^
3.0
end_if
end_if

if hb_ > d_max
if hb_ < d_max + 2.0*b_rad(find_ball(aa))
ht_ = zt_ - b_z(find_ball(aa)) + b_rad(find_ball(aa))
W9_ = W9_ + (abs(ht_))^2.0*(3.0*b_rad(find_ball(aa)) - ht_)
W9_Vx = W9_Vx +
b_xvel(find_ball(aa))*(abs(ht_))^2.0*(3.0*b_rad(find_ball(aa)) - ht_)
W9_Vx2 = W9_Vx2 +
(abs(b_xvel(find_ball(aa))))^2.0*(abs(ht_))^2.0*(3.0*b_rad(find_ball(aa)) - ht_)
W9_Vy2 = W9_Vy2 +
(abs(b_yvel(find_ball(aa))))^2.0*(abs(ht_))^2.0*(3.0*b_rad(find_ball(aa)) - ht_)
W9_Vz2 = W9_Vz2 +
(abs(b_zvel(find_ball(aa))))^2.0*(abs(ht_))^2.0*(3.0*b_rad(find_ball(aa)) - ht_)
W9_VxVz = W9_VxVz +
b_xvel(find_ball(aa))*b_zvel(find_ball(aa))*(abs(ht_))^2.0*(3.0*b_rad(find_
ball(aa)) - ht_)
end_if
end_if

endloop

; For Layer 10

zb_ = 9.0*d_max + d_
zt_ = 10.0*d_max + d_

```
W10_          = 0.0
W10_Vx      = 0.0
W10_Vx2    = 0.0
W10_Vy2    = 0.0
W10_Vz2    = 0.0
W10_VxVz = 0.0

loop aa (1, n_)

hb_     = b_z(find_ball(aa)) + b_rad(find_ball(aa)) - zb_

if hb_ > 0.0
if hb_ < 2.0*b_rad(find_ball(aa))
W10_     = W10_     + (abs(hb_))^2.0*(3.0*b_rad(find_ball(aa)) - hb_)
W10_Vx   = W10_Vx   +
b_xvel(find_ball(aa))*(abs(hb_))^2.0*(3.0*b_rad(find_ball(aa)) - hb_)
W10_Vx2  = W10_Vx2  +
(abs(b_xvel(find_ball(aa))))^2.0*(abs(hb_))^2.0*(3.0*b_rad(find_ball(aa)) - hb_)
W10_Vy2  = W10_Vy2  +
(abs(b_yvel(find_ball(aa))))^2.0*(abs(hb_))^2.0*(3.0*b_rad(find_ball(aa)) - hb_)
W10_Vz2  = W10_Vz2  +
(abs(b_zvel(find_ball(aa))))^2.0*(abs(hb_))^2.0*(3.0*b_rad(find_ball(aa)) - hb_)
W10_VxVz = W10_VxVz +
b_xvel(find_ball(aa))*b_zvel(find_ball(aa))*(abs(hb_))^2.0*(3.0*b_rad(find_
ball(aa)) - hb_)
end_if
end_if

if hb_ >= 2.0*b_rad(find_ball(aa))
if hb_ <= d_max
W10_     = W10_     + 4.0*(abs(b_rad(find_ball(aa))))^3.0
W10_Vx   = W10_Vx   +
b_xvel(find_ball(aa))*4.0*(abs(b_rad(find_ball(aa))))^3.0
W10_Vx2  = W10_Vx2  +
(abs(b_xvel(find_ball(aa))))^2.0*4.0*(abs(b_rad(find_ball(aa))))^3.0
W10_Vy2  = W10_Vy2  +
(abs(b_yvel(find_ball(aa))))^2.0*4.0*(abs(b_rad(find_ball(aa))))^3.0
W10_Vz2  = W10_Vz2  +
(abs(b_zvel(find_ball(aa))))^2.0*4.0*(abs(b_rad(find_ball(aa))))^3.0
W10_VxVz = W10_VxVz +
b_xvel(find_ball(aa))*b_zvel(find_ball(aa))*4.0*(abs(b_rad(find_ball(aa))))^
3.0
end_if
end_if

if hb_ > d_max
```

```
if hb_ < d_max + 2.0*b_rad(find_ball(aa))
ht_     = zt_     - b_z(find_ball(aa)) + b_rad(find_ball(aa))
W10_    = W10_    + (abs(ht_))^2.0*(3.0*b_rad(find_ball(aa)) - ht_)
W10_Vx  = W10_Vx  +
b_xvel(find_ball(aa))*(abs(ht_))^2.0*(3.0*b_rad(find_ball(aa)) - ht_)
W10_Vx2 = W10_Vx2 +
(abs(b_xvel(find_ball(aa))))^2.0*(abs(ht_))^2.0*(3.0*b_rad(find_ball(aa)) - ht_)
W10_Vy2 = W10_Vy2 +
(abs(b_yvel(find_ball(aa))))^2.0*(abs(ht_))^2.0*(3.0*b_rad(find_ball(aa)) - ht_)
W10_Vz2 = W10_Vz2 +
(abs(b_zvel(find_ball(aa))))^2.0*(abs(ht_))^2.0*(3.0*b_rad(find_ball(aa)) - ht_)
W10_VxVz = W10_VxVz +
b_xvel(find_ball(aa))*b_zvel(find_ball(aa))*(abs(ht_))^2.0*(3.0*b_rad(find_
ball(aa)) - ht_)
end_if
end_if

endloop

end

; History of measurements

His Depth_
His W1_
His W1_Vx
His W1_Vx2
His W1_Vy2
His W1_Vz2
His W1_VxVz
His W2_
His W2_Vx
His W2_Vx2
His W2_Vy2
His W2_Vz2
His W2_VxVz
His W3_
His W3_Vx
His W3_Vx2
His W3_Vy2
His W3_Vz2
His W3_VxVz
His W4_
His W4_Vx
His W4_Vx2
His W4_Vy2
```

His W4_Vz2
His W4_VxVz
His W5_
His W5_Vx
His W5_Vx2
His W5_Vy2
His W5_Vz2
His W5_VxVz
His W6_
His W6_Vx
His W6_Vx2
His W6_Vy2
His W6_Vz2
His W6_VxVz
His W7_
His W7_Vx
His W7_Vx2
His W7_Vy2
His W7_Vz2
His W7_VxVz
His W8_
His W8_Vx
His W8_Vx2
His W8_Vy2
His W8_Vz2
His W8_VxVz
His W9_
His W9_Vx
His W9_Vx2
His W9_Vy2
His W9_Vz2
His W9_VxVz
His W10_
His W10_Vx
His W10_Vx2
His W10_Vy2
His W10_Vz2
His W10_VxVz

A.4 PFC CODE FOR RING SHEAR FLOW SIMULATION

```
Set Safety_fac  0.35 ; (Safety_fac is a PFC command used to reduce the computed
                        critical time step at the start of each cycle. Default value is
                        0.8 but recommended to use lower value when using the
                        Hertz contact model, especially under rapidly changing
                        conditions)

; INPUTS

def Apparatus_dimensions_inputs
d_          = 0.005                    ; (Average particle diameter)
nr_         = 4.0                      ; (Ring thickness,4d)
t_          = nr_*d_                   ; (Ring thickness)
nz_         = 12.0                     ; (Initial ring height,12d)
H_          = nz_*d_                   ; (Initial ring height)
rad_avg     = 30.0*d_                  ; (Average ring diameter, (Ri + Ro)/2)
rad_in      = rad_avg - t_/2.0         ; (Inside ring diameter, Ri)
rad_out     = rad_avg + t_/2.0         ; (Outside ring diameter, Ro)
end

Apparatus_dimensions_inputs

def balls_and_clumps_inputs
n_          = 6665                     ; (Number of particles)
rad_mult    = 2.0
pois_       = 0.34                     ; (Poisson's ratio of particles)
shea_r      = 3.25e9/2.0/(1 + pois_)   ; (Shear Modulus of particles)
fb_         = 0.6                      ; (Friction coefficient at particles contact)
den_        = 1095.0                   ; (Particles density)
dampc_      = 0.75                     ; (Restitution coefficient, ε)
frac_cl     = 1.0                      ; (Fraction of angular particles over total
                                         particles (spherical + angular); in this
                                         case all particles are angular)

if n_*frac_cl - int(n_*frac_cl) >= 0.5
n_cl        = int(n_*frac_cl) + 1
else
n_cl        = int(n_*frac_cl)
end_if
n_cl2       = n_cl + 2
n_ball      = n_ - n_cl
end

balls_and_clumps_inputs

def wall_inputs
```

```
z_   = 20.0*H_                          ; (Height of vertical walls)
s_   = 150000.0                         ; (Prescribed vertical normal stress)
_alpha = 4.25                           ; (the coefficient  f_s , see Eq. 3.7)
end

wall_inputs

def other_operations_and_inputs
nrad_out    = -1.0*rad_out
r_          = d_/2.0
H_d         = H_ - d_
AA_         = pi*(rad_out^2.0 - rad_in^2.0)
Rad_Velo  = 20.0                        ; (Prescribed angular velocity, ω_z)
incr_       = 4.0                       ; (Angular velocity applied in 4
increments)
cyc_        = 3000000                   ; (See further_shearing at the end)
end

other_operations_and_inputs

; MODEL CONSTRUCTION

Plot add wall blue
Plot add ball yellow    range  id 1 n_
Plot add clump green  range  id 1 2

def plot_clumps
if n_cl > 0.0
command
Plot add clump red range  id 3 n_cl2
endcommand
end_if
end

plot_clumps

Plot show

; Construction of vertical cylindrical walls
wall id 1  type cyl end1 0.0 0.0 0.0 end2 0.0 0.0 z_  rad rad_in  rad_in
wall id 2  type cyl end1 0.0 0.0 0.0 end2 0.0 0.0 z_  rad rad_out rad_out

; Assigning of wall frictions (frictionless walls considered)
wall id 1 fric 0.0
wall id 2 fric 0.0
```

```
; Construction of boundary plates
def rough_topsurface
T_L = 10001                    ; (The initial ID no. for the top boundary particles)
T_U = 10000                    ; (The final ID no. for the top boundary particles)
zz =  H_ - r_
rr = rad_out + r_
loop m (1, nr_)
rr = rr - d_
PL_ =(rr^2.0 - r_^2.0)^0.5
ratio_ = r_/PL_
incr1_ = 2.0*atan(ratio_)
num_  = int(2.0*pi/incr1_)
incr2_ = 2.0*pi/num_
loop n (1, num_)
teta_ = incr2_*(n-1)
xx    = rr*cos(teta_)
yy    = rr*sin(teta_)
a_ = T_U + n
command
ball hertz id a_ x xx y yy z zz rad r_
endcommand
endloop
T_U = T_U + num_
endloop
n_contact_balls = T_U - T_L + 1
end

rough_topsurface

; Assigning properties for top boundary particles
prop dens den_ poiss pois_ shear shea_r range id T_L  T_U
prop fric fb_

; Changing top boundary particles into clump/plate
def making_topclump
z_1 = H_ - d_
z_2 = H_
command
clump add id 1 range z z_1 z_2
endcommand
end

making_topclump

; Assigning properties for top boundary clump
```

```
clump prop permanent full on update_cycle 1 xvel 0.0 yvel 0.0 zvel 0.0 xspin 0.0
yspin 0.0 zspin 0.0 range id 1
clump fix xspin yspin zspin x y z range id 1

def rough_bottomsurface
B_L = 20001                    ; (The initial ID no. for the bottom boundary particles)
B_U = 20000                    ; (The final ID no. for the bottom boundary particles)
zz =  r_
rr = rad_out + r_
loop m (1, nr_)
rr = rr - d_
PL_ =(rr^2.0 - r_^2.0)^0.5
ratio_ = r_/PL_
incr1_ = 2.0*atan(ratio_)
num_  = int(2.0*pi/incr1_)
incr2_ = 2.0*pi/num_
loop n (1, num_)
teta_ = incr2_*(n-1)
xx    = rr*cos(teta_)
yy    = rr*sin(teta_)
b_ = B_U + n
command
ball hertz id b_ x xx y yy z zz rad r_
endcommand
endloop
B_U = B_U + num_
endloop
end

rough_bottomsurface

; Assigning properties for bottom boundary particles
prop dens den_ poiss pois_ shear shea_r  range id B_L  B_U
prop fric fb_

; Changing bottom boundary particles into clump/plate
def making_bottomclump
z_1 = 0.0
z_2 = d_
command
clump add id 2 range z z_1 z_2
endcommand
end

making_bottomclump
```

; Assigning properties for bottom boundary clump
clump prop permanent full on update_cycle 1 xvel 0.0 yvel 0.0 zvel 0.0 xspin 0.0 yspin 0.0 zspin 0.0 range id 2
clump fix xspin yspin zspin x y z range id 2
; Generation of particles
set random

Def Filtering_balls
_brad = fc_arg(0)
_xpos = fc_arg(1)
_ypos = fc_arg(2)
_zpos = fc_arg(3)
_rxy = sqrt(_xpos*_xpos+_ypos*_ypos)
if (_rxy+_brad) > rad_in
if (_rxy+_brad) < rad_out
_skip = 0
else
_skip = 1
end_if
else
_skip = 1
end_if
Filtering_balls = _skip
END

gen hertz id 1 222 rad 0.001015625 0.001015625 x nrad_out rad_out y nrad_out rad_out z d_ H_d Filter Filtering_balls
gen hertz id 223 778 rad 0.0010625 0.0010625 x nrad_out rad_out y nrad_out rad_out z d_ H_d Filter Filtering_balls
gen hertz id 779 2222 rad 0.001125 0.001125 x nrad_out rad_out y nrad_out rad_out z d_ H_d Filter Filtering_balls
gen hertz id 2223 3388 rad 0.0011875 0.0011875 x nrad_out rad_out y nrad_out rad_out z d_ H_d Filter Filtering_balls
gen hertz id 3389 4554 rad 0.00125 0.00125 x nrad_out rad_out y nrad_out rad_out z d_ H_d Filter Filtering_balls
gen hertz id 4555 5776 rad 0.0013125 0.0013125 x nrad_out rad_out y nrad_out rad_out z d_ H_d Filter Filtering_balls
gen hertz id 5777 6665 rad 0.00138 0.00138 x nrad_out rad_out y nrad_out rad_out z d_ H_d Filter Filtering_balls

prop dens den_ poiss pois_ shear shea_r range id 1 n_
ini rad mult rad_mult range id 1 n_
Cycle 4000
Solve

; Replacing spherical particles with angular particles

```
def Clump_replacement
if n_cl > 0.0
command
clump template make angular_particle 3 radii 0.003 0.003 0.003 pos (0.00075,
0.0, 0.0) (0.00525, 0.0, 0.0) (0.003, 0.0, 0.0052)
clump replace 1 angular_particle frac_cl
clump prop permanent full on update_cycle 1
endcommand
end_if
end

Clump_replacement

cyc 10000
solve

; CONSOLIDATION

; Assigning particle properties
prop fric fb_
prop damp  0.0
damp local 0.0

clump free z range id 1            ; (free the top boundary plate for vertical motion)

; Defining servo-controlled plate and assigning vertical normal stress
def servo
while_stepping
swall_stress  = cl_zfob(find_clump(1))/AA_
fra_ction = (swall_stress - s_)/s_
if abs(fra_ction) < 1.0
udz = _alpha*Rad_Velo*rad_avg*fra_ction
else
udz = _alpha*Rad_Velo*rad_avg*fra_ction/abs(fra_ction)
endif
cl_zvel(find_clump(1)) = udz
end

servo

; Defining Measurements
his swall_stress                                    ; (History 1)
his udz                                             ; (History 2)

def Volume_calculation
V_b  = 0.0
```

```
V_cl = 0.0
if n_ball > 0.0
loop q (1, n_ball)
V_b = V_b + 4.0/3.0*pi*(b_rad(find_ball(q)))^3.0
endloop
end_if
if n_cl > 0.0
loop p (3, n_cl2)
cl_volgiven(find_clump(p)) = 0.0
V_cl = V_cl + cl_vol(find_clump(p))
endloop
end_if
end

volume_calculation

def Height_
Height_    = cl_z(find_clump(1)) + d_/2.0
w_VPos     = cl_z(find_clump(1)) + r_
Void_R     = (AA_*(w_VPos -   d_) - (V_b + V_cl +
n_contact_balls*4.0/3.0*pi*r_^3.0))/(V_b + V_cl +
n_contact_balls*4.0/3.0*pi*r_^3.0)
Void_R1    = (AA_*(w_VPos - 2*d_) - (V_b + V_cl))/(V_b + V_cl)
shear_rate = cl_rzvel(find_clump(2))*rad_avg/(w_VPos - d_)
end

his Height_                                          ; (History 3)
his Void_R                                           ; (History 4)
his shear_rate                                       ; (History 5)

; Consolidating
Cycle 500000
Solve   average 0.045 maximum 0.045

; SHEARING

; Measuring shear stress
def Shear_stress
Shear_stress  = 3.0*cl_zmom(find_clump(1))/(2.0*pi*(rad_out^3.0 - rad_in^3.0))
end

his Shear_stress                                     ; (History 6)

; Recording shearing time
set time 0.0
```

```
def real_time
real_time = time
end
his real_time                                          ; (History7)

; Assigning viscous damping coefficients to particles
Damp viscous notension on

def damcoef
damcoef = abs(ln(dampc_)/sqrt(pi^2.0+(-1.0*ln(dampc_))^2.0))
end

Damp viscous normal damcoef shear damcoef

; Shearing by increasing the angular velocity gradually
def Gradual_shearing
loop mm (1,incr_)
wzz = wzz + Rad_Velo/incr_
command
clump prop zspin wzz range id 2
clump fix  zspin     range id 2
cyc 5000
endcommand
endloop
end

Gradual_shearing

; Further shearing after the required angular velocity is reached
def Further_shearing
command
cycle  cyc_
endcommand
end

Further_shearing
```

APPENDIX B MATLAB CODE FOR INCLINED FLOW

```
function [] = Existing_Model()

%INPUT PARAMETERS

Iteration_ = 1000 ;

NewtonRaphsonModifier = 0.05 ;   % It is α, see Eq. 6.28(a)

s    = 0.78539816 ;              % It is the specularity coefficient, φ

ew   = 0.6 ;                     % Wall-ball restitution coefficient

e    = 0.6 ;                     % Ball-ball resitution coefficient

nu   = (1+e)/2 ;

del  = 24.5 ;                    % Friction angle at the boundary, δ

fi   = 24.5 ;                    % Critical state friction angle, ϕcs

den  = 2500 ;                    % Particle density

t    = 26.0;                     % Angle of inclined plane, Θ

n    = 40;                       % No. of nodes, N

dZ   = 0.025641;                 % 1/(n-1), Z=z/H varies from 0 to 1

h    = 39.0;                     % h is H/d

dia  = 0.001;                    % Particle diameter

gra  = 9.81;                     % Acceleration of gravity

vm   = 0.61;                     % Maximum close packing solid volume↙
fraction

m1   = 0.01;

m2   = 250;

m3   = 0.5;
```

```
m4   = 1;

m5   = 0.035;

v1   = 0.5263;                    % Random loose packing solid volume↙
fraction

I    = 0.00001;                   % It is the I value at the quasi-static -↙
intermediate boundary


AA = n + 1;

BB = 2*n;

CC = 2*n + 1;

DD = 3*n;


gv = dlmread('INITIALVALUES.txt','\t')      % Importing initial guessed values

format long


for hp = 1:Iteration_

% EVALUATED FUNCTIONS

% Scaling factor for velocity inputs

kd      =  sqrt(gra*sin(pi/180*t)/(h*dia))*dia;

% Kinetic theory functions of void ratio

go         =@(v) (1-(v/vm)^(1/3))^-1;

dgo        =@(v) go(v)^2*(3*vm*(v/vm)^(2/3))^-1;

ddgo       =@(v) 2/(3*vm)*go(v)*dgo(v)*(v/vm)^(-2/3) - 2*go(v)^2/(9*vm^2)*↙
(v/vm)^(-5/3);

dddgo    =@(v) 2/(3*vm)*(go(v)*dgo(v)*-2/3*(v/vm)^(-5/3)/vm + (v/vm)^(-2↙
/3)*(dgo(v)^2+go(v)*ddgo(v))) - 2/(9*vm^2)*(2*go(v)*dgo(v)*(v/vm)^(-5/3) +↙
go(v)^2*-5/3*(v/vm)^(-8/3)/vm);
```

```
g1      =@(v)  v*(1+4*nu*v*(1-(v/vm)^(1/3))^-1);

dg1     =@(v) (1 + 4*nu*(2*v*(1-(v/vm)^(1/3))^-1 + v^2*(3*vm*(v/vm)^↙
(2/3)*(1-(v/vm)^(1/3))^2)^-1));

g2      =@(v) 5*pi^.5/96*(1/(nu*(2-nu)*go(v)) + 8/5*(3*nu-1)/(2-nu)*v +↙
64/25*nu*((3*nu-2)/(2-nu)+12/pi)*v^2*go(v));

dg2     =@(v) (5*pi^.5/96*(-1*dgo(v)/(nu*(2-nu)*go(v)^2) + 8/5*(3*nu-1)/(2-↙
nu) + 64/25*nu*((3*nu-2)/(2-nu)+12/pi)*(2*v*go(v)+v^2*dgo(v))));

g3      =@(v) 25*sqrt(pi)/(16*nu*(41-33*nu))*(1/go(v)+12/5*nu*(1+nu*↙
(4*nu-3))*v + 16/25*nu^2*(9*nu*(4*nu-3)+4/pi*(41-33*nu))*v^2*go(v));

dg3     =@(v) 25*sqrt(pi)/(16*nu*(41-33*nu))*(-1*dgo(v)/go(v)^2+12/5*nu*↙
(1+nu*(4*nu-3)) + 16/25*nu^2*(9*nu*(4*nu-3)+4/pi*(41-33*nu))*(2*v*go(v)↙
+v^2*dgo(v)));

ddg3    =@(v) 25*sqrt(pi)/(16*nu*(41-33*nu))*((-1*ddgo(v)*go(v)^2+2*go↙
(v)*dgo(v)^2)/go(v)^4 + 16/25*nu^2*(9*nu*(4*nu-3)+4/pi*(41-33*nu))*(2*go↙
(v)+4*v*dgo(v)+v^2*ddgo(v)));

g4      =@(v) 15*sqrt(pi)/4*(2*nu-1)*(nu-1)/(41-33*nu)*(1/(v*go(v))↙
+12/5*nu)*(2*v*go(v)+v^2*dgo(v));

dg4     =@(v) 15*sqrt(pi)/4*(2*nu-1)*(nu-1)/(41-33*nu)*((1/(v*go(v))↙
+12/5*nu)*(2*go(v)+4*v*dgo(v)+v^2*ddgo(v)) - (2*v*go(v)+v^2*dgo(v))*(go↙
(v)+v*dgo(v))/(v*go(v))^2);

ddg4    =@(v) 15*sqrt(pi)/4*(2*nu-1)*(nu-1)/(41-33*nu)*(-2*(go(v)+v*dgo↙
(v))/(v*go(v))^2*(2*go(v)+4*v*dgo(v)+v^2*ddgo(v))+(1/(v*go(v))+12/5*nu)*↙
(6*dgo(v)+6*v*ddgo(v)+v^2*dddgo(v)) ...
        -(2*v*go(v)+v^2*dgo(v))*(((2*dgo(v)+v*ddgo(v))*(v*go(v))^2-↙
2*v*go(v)*(go(v)+v*dgo(v))^2)/(v*go(v))^4));

g5      =@(v) 48/pi^.5*(1+e)/2*(1-(1+e)/2)*v^2*(1-(v/vm)^(1/3))^-1;

dg5     =@(v) 48/pi^.5*(1+e)/2*(1-(1+e)/2)*(2*v*(1-(v/vm)^(1/3))^-1 + v^2*↙
(3*vm*(v/vm)^(2/3)*(1-(v/vm)^(1/3))^2)^-1);

% Collisonal shear stress coefficient B1

B1      =@(v,r)  ((m1+m2*(r*kd)^m3) + m4*max(0,(v-v1)/abs(v-v1))*exp↙
(((1-v1)/v1-(1-v)/v)/m5))/(m1+m2*(r*kd)^m3);

dB1v    =@(v,r)  (m4*max(0,(v-v1)/abs(v-v1))*exp(((1-v1)/v1-(1-v)/v)/m5))/↙
(m1+m2*(r*kd)^m3)/(m5*v^2);
```

```
dB1u      =@(v,r,dr) max(0,(v-v1)/abs(v-v1))*-1*m4*exp(((1-v1)/v1-(1-v)/v)↙
/m5)*m2*m3*(r*kd)^(m3-1)/(m1+m2*(r*kd)^m3)^2*(dr*kd);

B1b       =@(v,r)    B1(v,r);      % It is B1 used in the boundary conditions.
dB1bv     =@(v,r)    dB1v(v,r);
dB1bu     =@(v,r,dr) dB1u(v,r,dr);

g2B1      =@(v,r)    g2(v)*B1(v,r);

dg2B1v    =@(v,r)    dg2(v)*B1(v,r) + g2(v)*dB1v(v,r);

dg2B1u    =@(v,r,dr) g2(v)*dB1u(v,r,dr);

% Collisional volume fraction Fc (or F1)  .....(A)

B2_x      =@(v,x)   (1-x)*10^(1/m5*((1-v)/v-((1-x)/(v-x*v1)-1))) ;

ss_x      =@(v,r,x)   B2_x(v,x)*tan(pi/180*fi)*10^(((1-v1)/v1-(1-v)/v)/m5) +↙
B1(v,r)^1.5*den*g2(v)^1.5/g5(v)^0.5*(r*kd)^2;

options   = optimset('TolFun',1e-50,'display','off','LargeScale','off');

ForFc     =@(v,r,x)    B1(v,r) - (x^(2/3)*g5(v)*g2(v1))^(1/3) * (r*kd*sqrt(den)↙
*ss_x(v,r,x) - B2_x(v,x)*tan(pi/180*fi)*10^(((1-v1)/v1-(1-v)/v)/m5)*I*sqrt↙
(ss_x(v,r,x)))^(4/9) / ...
                  (g2(v)*g5(v1)^(1/9)*(den*(r*kd)^2)^(2/3));


% SHEAR RATES AND THEIR DIFFERENTIALS FOR B1 AND B2↙
CALCUALTIONS

rN    =@(n)    (3*gv(2*n,1)-4*gv(2*n-1,1)+gv(2*n-2,1))/(2*dZ);

drNN  =        3/(2*dZ);

drN1  =       -4/(2*dZ);

drN2  =        1/(2*dZ);


ri    =@(n,i)  (gv(n+i+1,1)-gv(n+i-1,1))/(2*dZ);

dri1  =       1/(2*dZ);

dri_1 =      -1/(2*dZ);
```

```
r1    =@(n)    (-3*gv(n+1,1)+4*gv(n+2,1)-gv(n+3,1))/(2*dZ);

dr11  =      -3/(2*dZ);

dr12  =       4/(2*dZ);

dr13  =      -1/(2*dZ);


% Collisional volume fraction Fc (or F1)  .....(B)

Fc(1,1)  =  max(0,(gv(1,1)-v1)/abs(gv(1,1)-v1))*fsolve(@(x) ForFc(gv(1,1),r1↙
(n),x),0.0,options) +  max(0,(v1-gv(1,1))/abs(v1-gv(1,1)));

Fc(n,1)  =  max(0,(gv(n,1)-v1)/abs(gv(n,1)-v1))*fsolve(@(x) ForFc(gv(n,1),rN↙
(n),x),0.0,options) +  max(0,(v1-gv(n,1))/abs(v1-gv(n,1)));

for az     = 2:n-1

Fc(az,1)  =  max(0,(gv(az,1)-v1)/abs(gv(az,1)-v1))*fsolve(@(x) ForFc(gv(az,↙
1),ri(n,az),x),0.0,options) +  max(0,(v1-gv(az,1))/abs(v1-gv(az,1)));

end

B2            =@(v,f)      (1-Fc(f,1))*10^(1/m5*((1-v)/v-((1-Fc(f,1))/(v-Fc(f,1)↙
*v1)-1))) ;

ss            =@(v,r,f)      B2(v,f)*tan(pi/180*fi)*10^(((1-v1)/v1-(1-v)/v)/m5) +↙
B1(v,r)^1.5*den*g2(v)^1.5/g5(v)^0.5*(r*kd)^2;

dB2v_dxv  =@(v,dxv,f)  10^(1/m5*((1-v)/v-((1-Fc(f,1))/(v-Fc(f,1)*v1)-1)))*(-1↙
*dxv+(1-Fc(f,1))*log(10)*1/m5*(-1/v^2+(dxv*(v-Fc(f,1)*v1)+(1-Fc(f,1))*(1-↙
v1*dxv))/(v-Fc(f,1)*v1)^2));

dssv_dxv   =@(v,r,dxv,f)  dB2v_dxv(v,dxv,f)*tan(pi/180*fi)*10^(((1-v1)/v1-↙
(1-v)/v)/m5) + B2(v,f)*tan(pi/180*fi)*10^(((1-v1)/v1-(1-v)/v)/m5)*log(10)/↙
(m5*v^2) + ...
                  dB1v(v,r)*den*g2(v)*(r*kd)^2*sqrt(B1(v,r)*g2(v)/g5(v)) + B1↙
(v,r)*den*(r*kd)^2*(3/2*g2(v)^0.5*dg2(v)*sqrt(B1(v,r)/g5(v)) + g2(v)^1.5/g5↙
(v)*(dB1v(v,r)*g5(v)^0.5/(2*B1(v,r)^0.5)-dg5(v)*B1(v,r)^0.5/(2*g5(v)^0.5)));

FordFcv    =@(v,r,dxv,f)  dB1v(v,r) - B1(v,r)*((2/3*Fc(f,1)^(-1/3)*dxv*g5(v)↙
+Fc(f,1)^(2/3)*dg5(v))/(3*Fc(f,1)^(2/3)*g5(v)) - dg2(v)/g2(v) + ...
                  4*(r*kd*sqrt(den)*dssv_dxv(v,r,dxv,f)-I*(0.5*ss(v,r,f)^(-0.5)↙
*dssv_dxv(v,r,dxv,f)*B2(v,f)*tan(pi/180*fi)*10^(((1-v1)/v1-(1-v)/v)/m5)+ ss↙
(v,r,f)^(0.5)*(dB2v_dxv(v,dxv,f)*tan(pi/180*fi)*10^(((1-v1)/v1-(1-v)/v)/m5) ...
```

```
                + B2(v,f)*tan(pi/180*fi)*10^(((1-v1)/v1-(1-v)/v)/m5)*log(10)/↙
(m5*v^2))))/(9*(r*kd*sqrt(den)*ss(v,r,f)-B2(v,f)*tan(pi/180*fi)*10^(((1-v1)↙
/v1-(1-v)/v)/m5)*I*ss(v,r,f)^0.5)));


dFcv(1,1) = max(0,(gv(1,1)-v1)/abs(gv(1,1)-v1))*fsolve(@(dxv) FordFcv(gv↙
(1,1),r1(n),dxv,1),0.0,options);

dFcv(n,1) = max(0,(gv(n,1)-v1)/abs(gv(n,1)-v1))*fsolve(@(dxv) FordFcv(gv↙
(n,1),rN(n),dxv,n),0.0,options);

for az = 2:n-1

dFcv(az,1) = max(0,(gv(az,1)-v1)/abs(gv(az,1)-v1))*fsolve(@(dxv) FordFcv↙
(gv(az,1),ri(n,az),dxv,az),0.0,options);

end


dB2u_dxu =@(v,dxu,f) 10^(1/m5*((1-v)/v-((1-Fc(f,1))/(v-Fc(f,1)*v1)-1)))*↙
(-1*dxu+(1-Fc(f,1))*log(10)/m5*((dxu*(v-Fc(f,1)*v1)-(1-Fc(f,1))*(v1*dxu))/↙
(v-Fc(f,1)*v1)^2));

dssu_dxu =@(v,r,dr,dxu,f) dB2u_dxu(v,dxu,f)*tan(pi/180*fi)*10^(((1-v1)↙
/v1-(1-v)/v)/m5) + den*g2(v)^1.5/g5(v)^0.5*(3/2*B1(v,r)^0.5*dB1u(v,r,dr)*↙
(r*kd)^2 + B1(v,r)^1.5*2*(r*kd)*(dr*kd));

FordFcu =@(v,r,dr,dxu,f) dB1u(v,r,dr) - B1(v,r)*((2*dxu)/(9*Fc(f,1)) - 4/3*↙
(dr*kd)/(r*kd) + 4/9*(sqrt(den)*((dr*kd)*ss(v,r,f)+(r*kd)*dssu_dxu(v,r,dr,dxu,↙
f)) - ...
                I*tan(pi/180*fi)*10^(((1-v1)/v1-(1-v)/v)/m5)*(dB2u_dxu(v,↙
dxu,f)*sqrt(ss(v,r,f))+B2(v,f)*dssu_dxu(v,r,dr,dxu,f)/(2*sqrt(ss(v,r,f)))))/((r*kd)↙
*sqrt(den)*ss(v,r,f)-B2(v,f)*tan(pi/180*fi)*10^(((1-v1)/v1-(1-v)/v)/m5)*I*sqrt↙
(ss(v,r,f))));

dFcu(1,1) = max(0,(gv(1,1)-v1)/abs(gv(1,1)-v1))*fsolve(@(dxu) FordFcu(gv↙
(1,1),r1(n),dr11,dxu,1),0.0,options);

dFcu(1,2) = max(0,(gv(1,1)-v1)/abs(gv(1,1)-v1))*fsolve(@(dxu) FordFcu(gv↙
(1,1),r1(n),dr12,dxu,1),0.0,options);

dFcu(1,3) = max(0,(gv(1,1)-v1)/abs(gv(1,1)-v1))*fsolve(@(dxu) FordFcu(gv↙
(1,1),r1(n),dr13,dxu,1),0.0,options);

dFcu(n,3) = max(0,(gv(n,1)-v1)/abs(gv(n,1)-v1))*fsolve(@(dxu) FordFcu(gv↙
(n,1),rN(n),drNN,dxu,n),0.0,options);
```

```
dFcu(n,1) = max(0,(gv(n,1)-v1)/abs(gv(n,1)-v1))*fsolve(@(dxu) FordFcu(gv↙
(n,1),rN(n),drN1,dxu,n),0.0,options);

dFcu(n,2) = max(0,(gv(n,1)-v1)/abs(gv(n,1)-v1))*fsolve(@(dxu) FordFcu(gv↙
(n,1),rN(n),drN2,dxu,n),0.0,options);


for az = 2:n-1

dFcu(az,1) = max(0,(gv(az,1)-v1)/abs(gv(az,1)-v1))*fsolve(@(dxu) FordFcu↙
(gv(az,1),ri(n,az),dri1,dxu,az),0.0,options);

dFcu(az,2) = max(0,(gv(az,1)-v1)/abs(gv(az,1)-v1))*fsolve(@(dxu) FordFcu↙
(gv(az,1),ri(n,az),dri_1,dxu,az),0.0,options);

end

% Frictional normal & shear stresses coefficient B2

%B2      =@(v,f)      is calculated above

dB2v    =@(v,f)      10^(1/m5*((1-v)/v-((1-Fc(f,1))/(v-Fc(f,1)*v1)-1)))*(-1↙
*dFcv(f,1)+(1-Fc(f,1))*log(10)*1/m5*(-1/v^2+(dFcv(f,1)*(v-Fc(f,1)*v1)+(1-Fc↙
(f,1))*(1-v1*dFcv(f,1)))/(v-Fc(f,1)*v1)^2));

dB2u    =@(v,co,f)   10^(1/m5*((1-v)/v-((1-Fc(f,1))/(v-Fc(f,1)*v1)-1)))*(-1↙
*dFcu(f,co)+(1-Fc(f,1))*log(10)/m5*((dFcu(f,co)*(v-Fc(f,1)*v1)-(1-Fc(f,1))*↙
(v1*dFcu(f,co)))/(v-Fc(f,1)*v1)^2));


NfB2    =@(v,f)      B2(v,f)*10^(((1-v1)/v1-(1-v)/v)/m5)/(den*gra*dia*cos↙
(t*pi/180));

dNfB2v  =@(v,f)      10^(((1-v1)/v1-(1-v)/v)/m5)*(dB2v(v,f) + B2(v,f)*log↙
(10)/(m5*v^2))/(den*gra*dia*cos(t*pi/180));

dNfB2u  =@(v,co,f)   10^(((1-v1)/v1-(1-v)/v)/m5)*dB2u(v,co,f)/↙
(den*gra*dia*cos(t*pi/180));

% Collisonal normal stress coefficient B3

dssv    =@(v,r,f)    dB2v(v,f)*tan(pi/180*fi)*10^(((1-v1)/v1-(1-v)/v)/m5) +↙
B2(v,f)*tan(pi/180*fi)*10^(((1-v1)/v1-(1-v)/v)/m5)*log(10)/(m5*v^2) + ...
                dB1v(v,r)*den*g2(v)*(r*kd)^2*sqrt(B1(v,r)*g2(v)/g5(v)) + B1(v,↙
r)*den*(r*kd)^2*(3/2*g2(v)^0.5*dg2(v)*sqrt(B1(v,r)/g5(v)) + g2(v)^1.5/g5(v)*↙
(dB1v(v,r)*g5(v)^0.5/(2*B1(v,r)^0.5)-dg5(v)*B1(v,r)^0.5/(2*g5(v)^0.5)));
```

```
dssu      =@(v,r,dr,co,f)  dB2u(v,co,f)*tan(pi/180*fi)*10^(((1-v1)/v1-(1-v)/v)↙
/m5) + den*g2(v)^1.5/g5(v)^0.5*(3/2*B1(v,r)^0.5*dB1u(v,r,dr)*(r*kd)^2 + B1↙
(v,r)^1.5*2*(r*kd)*(dr*kd));

B3        =@(v,r,f)     Fc(f,1)^(1/3)*g1(v1)*g5(v)*(ss(v,r,f)*(r*kd)*sqrt(den) -↙
B2(v,f)*tan(pi/180*fi)*10^(((1-v1)/v1-(1-v)/v)/m5)*I*sqrt(ss(v,r,f)))^(2/3)/(B1↙
(v,r)*g1(v)*g2(v)*g5(v1)^(2/3)*den*(r*kd)^2) ;

dB3v     =@(v,r,f)     B3(v,r,f)*((dFcv(f,1)/(3*Fc(f,1)) + dg5(v)/g5(v)) - (dB1v↙
(v,r)*g1(v)*g2(v)+B1(v,r)*g1(v)*dg2(v)+B1(v,r)*dg1(v)*g2(v))/(B1(v,r)*g1(v)↙
*g2(v)) + ...
                2*(r*kd*sqrt(den)*dssv(v,r,f)-I*(0.5*ss(v,r,f)^(-0.5)*dssv(v,r,f)↙
*B2(v,f)*tan(pi/180*fi)*10^(((1-v1)/v1-(1-v)/v)/m5)+ ss(v,r,f)^(0.5)*(dB2v(v,↙
f)*tan(pi/180*fi)*10^(((1-v1)/v1-(1-v)/v)/m5) ...
                + B2(v,f)*tan(pi/180*fi)*10^(((1-v1)/v1-(1-v)/v)/m5)*log(10)/↙
(m5*v^2))))/(3*(r*kd*sqrt(den)*ss(v,r,f)-B2(v,f)*tan(pi/180*fi)*10^(((1-v1)↙
/v1-(1-v)/v)/m5)*I*ss(v,r,f)^0.5)));

dB3u     =@(v,r,dr,co,f)  B3(v,r,f)*(dFcu(f,co)/(3*Fc(f,1)) - (dB1u(v,r,dr)*↙
(r*kd)^2 + B1(v,r)*2*(r*kd)*(dr*kd))/(B1(v,r)*(r*kd)^2) + 2/3*(sqrt(den)*↙
((dr*kd)*ss(v,r,f)+(r*kd)*dssu(v,r,dr,co,f)) - ...
                I*tan(pi/180*fi)*10^(((1-v1)/v1-(1-v)/v)/m5)*(dB2u(v,co,f)*sqrt↙
(ss(v,r,f))+B2(v,f)*dssu(v,r,dr,co,f)/(2*sqrt(ss(v,r,f)))))/((r*kd)*sqrt(den)*ss(v,r,↙
f)-B2(v,f)*tan(pi/180*fi)*10^(((1-v1)/v1-(1-v)/v)/m5)*I*sqrt(ss(v,r,f))));

g1B3     =@(v,r,f)     g1(v)*B3(v,r,f);

dg1B3v   =@(v,r,f)     dg1(v)*B3(v,r,f) + g1(v)*dB3v(v,r,f);

dg1B3u   =@(v,r,dr,co,f)  g1(v)*dB3u(v,r,dr,co,f)  ;


%JACOBIAN MATRIX

%At First Node

%Energy equation

J(1,1)     = dg3(gv(1,1))*(-3*gv(2*n+1,1)+4*gv(2*n+2,1)-gv(2*n+3,1))/(2*dZ)-↙
h*(1-ew^2)*gv(2*n+1,1)*pi*3^.5/4/vm*(go(gv(1,1))+gv(1,1)*dgo(gv(1,1))) ...
          + 2/3*h^2*tan(t*pi/180)*(s)*pi*3^.5/4/vm*gv(n+1,1)^2*(B1b(gv(1,1),↙
r1(n))*(go(gv(1,1))+gv(1,1)*dgo(gv(1,1))) + gv(1,1)*go(gv(1,1))*dB1bv(gv↙
(1,1),r1(n))) ...
          + g4(gv(1,1))*gv(2*n+1,1)*-3/(2*dZ) + dg4(gv(1,1))*gv(2*n+1,1)*(-3↙
*gv(1,1)+4*gv(2,1)-gv(3,1))/(2*dZ);

J(1,2)     = g4(gv(1,1))*gv(2*n+1,1)*4/(2*dZ);
```

```
J(1,3)     = g4(gv(1,1))*gv(2*n+1,1)*-1/(2*dZ);

J(1,2*n+1) = g3(gv(1,1))*-3/(2*dZ)-h*(1-ew^2)*pi*3^.5*gv(1,1)*go(gv(1,1))↙
/4/vm + g4(gv(1,1))*(-3*gv(1,1)+4*gv(2,1)-gv(3,1))/(2*dZ);

J(1,2*n+2) = g3(gv(1,1))*2/dZ;

J(1,2*n+3) = g3(gv(1,1))*-1/(2*dZ);

J(1,n+1)   = 2/3*h^2*tan(t*pi/180)*(s)*B1b(gv(1,1),r1(n))*pi*3^.5*gv(1,1)*go↙
(gv(1,1))/4/vm*2*gv(n+1,1) + 2/3*h^2*tan(t*pi/180)*(s)*dB1bu(gv(1,1),r1(n),↙
dr11)*pi*3^.5*gv(1,1)*go(gv(1,1))/4/vm*(gv(n+1,1))^2;

J(1,n+2)   = 2/3*h^2*tan(t*pi/180)*(s)*dB1bu(gv(1,1),r1(n),dr12)*pi*3^.5*gv↙
(1,1)*go(gv(1,1))/4/vm*(gv(n+1,1))^2;

J(1,n+3)   = 2/3*h^2*tan(t*pi/180)*(s)*dB1bu(gv(1,1),r1(n),dr13)*pi*3^.5*gv↙
(1,1)*go(gv(1,1))/4/vm*(gv(n+1,1))^2;

%Z-Momentum equation

J(2,1)     = 1/h*(dNfB2v(gv(1,1),1)+dg1B3v(gv(1,1),r1(n),1)*gv(2*n+1,1))-↙
dZ/2;

for mm = 2:n-1;

J(2,mm) = -dZ;

end

J(2,n)     = -dZ/2 - 1/h*pi/(9*vm)*(gv(n,1)/vm)^(-1/3);

J(2,2*n+1) = 1/h*g1B3(gv(1,1),r1(n),1);

J(2,n+1)   = 1/h*(dNfB2u(gv(1,1),1,1) + dg1B3u(gv(1,1),r1(n),dr11,1,1)*gv↙
(2*n+1,1));

J(2,n+2)   = 1/h*(dNfB2u(gv(1,1),2,1) + dg1B3u(gv(1,1),r1(n),dr12,2,1)*gv↙
(2*n+1,1));

J(2,n+3)   = 1/h*(dNfB2u(gv(1,1),3,1) + dg1B3u(gv(1,1),r1(n),dr13,3,1)*gv↙
(2*n+1,1));

%X-Momentum equation

if NfB2(gv(1,1),1)*tan(fi*pi/180)/tan(t*pi/180) <=  (2/3*(h/tan(t*pi/180))^.5*↙
```

```
(s)*B1b(gv(1,1),r1(n))*pi*3^.5*gv(1,1)*go(gv(1,1))/(4*vm)*gv(2*n+1,1)^.↙
5*gv(n+1,1)+NfB2(gv(1,1),1)*tan(del*pi/180)/tan(t*pi/180));

   J(3,1)     = dNfB2v(gv(1,1),1)*tan(fi*pi/180)/tan(t*pi/180)+ dg2B1v(gv(1,1),↙
r1(n))*gv(2*n+1,1)^.5/(h*tan(t*pi/180))^.5*(-3*gv(n+1,1)+4*gv(n+2,1)-gv↙
(n+3,1))/(2*dZ) ...
   -dNfB2v(gv(1,1),1)*tan(del*pi/180)/tan(t*pi/180)-2/3*(h/tan(t*pi/180))^.5*↙
(s)*pi*3^.5*gv(2*n+1,1)^.5*gv(n+1,1)/(4*vm)*(B1b(gv(1,1),r1(n))*(gv(1,1)↙
*dgo(gv(1,1))+go(gv(1,1))) + gv(1,1)*go(gv(1,1))*dB1bv(gv(1,1),r1(n)));

   J(3,2*n+1) = g2B1(gv(1,1),r1(n))/(h*tan(t*pi/180))^.5*(-3*gv(n+1,1)+4*gv↙
(n+2,1)-gv(n+3,1))/(2*dZ)/(2*gv(2*n+1,1)^.5)-2/3*(h/tan(t*pi/180))^.5*(s)↙
*B1b(gv(1,1),r1(n))*pi*3^.5*gv(1,1)*go(gv(1,1))/(4*vm)*gv(n+1,1)/(2*gv↙
(2*n+1,1)^.5);

   J(3,n+1)   = g2B1(gv(1,1),r1(n))*gv(2*n+1,1)^.5/(h*tan(t*pi/180))^.5*-3/↙
(2*dZ) + (-3*gv(n+1,1)+4*gv(n+2,1)-gv(n+3,1))/(2*dZ)*gv(2*n+1,1)^.5/(h*tan↙
(t*pi/180))^.5*dg2B1u(gv(1,1),r1(n),dr11) + dNfB2u(gv(1,1),1,1)*(tan↙
(fi*pi/180)/tan(t*pi/180) - tan(del*pi/180)/tan(t*pi/180)) -  2/3*(h/tan↙
(t*pi/180))^.5*(s)*pi*3^.5*gv(1,1)*go(gv(1,1))/(4*vm)*gv(2*n+1,1)^.5*(B1b↙
(gv(1,1),r1(n)) + gv(n+1,1)*dB1bu(gv(1,1),r1(n),dr11));

   J(3,n+2)   = g2B1(gv(1,1),r1(n))*gv(2*n+1,1)^.5/(h*tan(t*pi/180))^.5*4/↙
(2*dZ)  + (-3*gv(n+1,1)+4*gv(n+2,1)-gv(n+3,1))/(2*dZ)*gv(2*n+1,1)^.5/↙
(h*tan(t*pi/180))^.5*dg2B1u(gv(1,1),r1(n),dr12) + dNfB2u(gv(1,1),2,1)*(tan↙
(fi*pi/180)/tan(t*pi/180) - tan(del*pi/180)/tan(t*pi/180)) -  2/3*(h/tan↙
(t*pi/180))^.5*(s)*pi*3^.5*gv(1,1)*go(gv(1,1))/(4*vm)*gv(2*n+1,1)^.5*gv↙
(n+1,1)*dB1bu(gv(1,1),r1(n),dr12);

   J(3,n+3)   = g2B1(gv(1,1),r1(n))*gv(2*n+1,1)^.5/(h*tan(t*pi/180))^.5*-1/↙
(2*dZ) + (-3*gv(n+1,1)+4*gv(n+2,1)-gv(n+3,1))/(2*dZ)*gv(2*n+1,1)^.5/(h*tan↙
(t*pi/180))^.5*dg2B1u(gv(1,1),r1(n),dr13) + dNfB2u(gv(1,1),3,1)*(tan↙
(fi*pi/180)/tan(t*pi/180) - tan(del*pi/180)/tan(t*pi/180)) -  2/3*(h/tan↙
(t*pi/180))^.5*(s)*pi*3^.5*gv(1,1)*go(gv(1,1))/(4*vm)*gv(2*n+1,1)^.5*gv↙
(n+1,1)*dB1bu(gv(1,1),r1(n),dr13);

else

   J(3,n+1)   = -3/(2*dZ)*g2B1(gv(1,1),r1(n))*gv(2*n+1,1)^.5/(h*tan(t*pi/180))↙
^.5 + (-3*gv(n+1,1)+4*gv(n+2,1)-gv(n+3,1))/(2*dZ)*gv(2*n+1,1)^.5/(h*tan↙
(t*pi/180))^.5*dg2B1u(gv(1,1),r1(n),dr11);

   J(3,n+2)   =  4/(2*dZ)*g2B1(gv(1,1),r1(n))*gv(2*n+1,1)^.5/(h*tan(t*pi/180))↙
^.5 + (-3*gv(n+1,1)+4*gv(n+2,1)-gv(n+3,1))/(2*dZ)*gv(2*n+1,1)^.5/(h*tan↙
(t*pi/180))^.5*dg2B1u(gv(1,1),r1(n),dr12);

   J(3,n+3)   = -1/(2*dZ)*g2B1(gv(1,1),r1(n))*gv(2*n+1,1)^.5/(h*tan(t*pi/180))↙
```

```
^.5 + (-3*gv(n+1,1)+4*gv(n+2,1)-gv(n+3,1))/(2*dZ)*gv(2*n+1,1)^.5/(h*tan↙
(t*pi/180))^.5*dg2B1u(gv(1,1),r1(n),dr13);

   J(3,1)     = (-3*gv(n+1,1)+4*gv(n+2,1)-gv(n+3,1))/(2*dZ)*dg2B1v(gv(1,1),r1↙
(n))*gv(2*n+1,1)^.5/(h*tan(t*pi/180))^.5;

   J(3,2*n+1) = (-3*gv(n+1,1)+4*gv(n+2,1)-gv(n+3,1))/(2*dZ)*g2B1(gv(1,1),↙
r1(n))/(2*gv(2*n+1,1)^.5)/(h*tan(t*pi/180))^.5;

end

%At Last Node

%Energy equation

J(3*n-2,3*n)    = 3/(2*dZ)*g3(gv(n,1)) + g4(gv(n,1))*(3*gv(n,1)-4*gv(n-1,1)↙
+gv(n-2,1))/(2*dZ);

J(3*n-2,3*n-1)  = -4/(2*dZ)*g3(gv(n,1));

J(3*n-2,3*n-2)  = 1/(2*dZ)*g3(gv(n,1));

J(3*n-2,n)      = (3*gv(3*n,1)-4*gv(3*n-1,1)+gv(3*n-2,1))/(2*dZ)*dg3(gv(n,1))↙
+ dg4(gv(n,1))*gv(3*n,1)*(3*gv(n,1)-4*gv(n-1,1)+gv(n-2,1))/(2*dZ) ...
               + g4(gv(n,1))*gv(3*n,1)*3/(2*dZ);

J(3*n-2,n-1)    = g4(gv(n,1))*gv(3*n,1)*-4/(2*dZ);

J(3*n-2,n-2)    = g4(gv(n,1))*gv(3*n,1)*1/(2*dZ);

%Z-Momentum equation

J(3*n-1,n)      = 1/h*(dNfB2v(gv(n,1),n) + gv(3*n,1)*dg1B3v(gv(n,1),rN(n),n) -↙
pi/(9*vm)*(gv(n,1)/vm)^(-1/3));

J(3*n-1,3*n)    = 1/h*g1B3(gv(n,1),rN(n),n);

J(3*n-1,2*n)    = 1/h*(dNfB2u(gv(n,1),3,n) + dg1B3u(gv(n,1),rN(n),drNN,3,n)↙
*gv(3*n,1));

J(3*n-1,2*n-1)  = 1/h*(dNfB2u(gv(n,1),1,n) + dg1B3u(gv(n,1),rN(n),drN1,1,n)↙
*gv(3*n,1));

J(3*n-1,2*n-2)  = 1/h*(dNfB2u(gv(n,1),2,n) + dg1B3u(gv(n,1),rN(n),drN2,2,n)↙
*gv(3*n,1));

%X-Momentum equation
```

```
if NfB2(gv(n,1),n)*tan(fi*pi/180) <= tan(t*pi/180)*pi/6*(gv(n,1)/vm)^(2/3);

  J(3*n,n)     = dNfB2v(gv(n,1),n)*tan(fi*pi/180) + (gv(3*n,1)/h)^.5*tan↙
(t*pi/180)^.5*dg2B1v(gv(n,1),rN(n))*(3*gv(2*n,1)-4*gv(2*n-1,1)+gv(2*n-↙
2,1))/(2*dZ) ...
              - tan(t*pi/180)*pi/(9*vm)*(gv(n,1)/vm)^(-1/3);

  J(3*n,3*n)   = g2B1(gv(n,1),rN(n))*(tan(t*pi/180)/h)^.5*(3*gv(2*n,1)-4*gv↙
(2*n-1,1)+gv(2*n-2,1))/(2*dZ)/(2*gv(3*n,1)^.5);

  J(3*n,2*n)   = dNfB2u(gv(n,1),3,n)*tan(fi*pi/180) + g2B1(gv(n,1),rN(n))*↙
(gv(3*n,1)*tan(t*pi/180)/h)^.5*3/(2*dZ) + (3*gv(2*n,1)-4*gv(2*n-1,1)+gv↙
(2*n-2,1))/(2*dZ)*(gv(3*n,1)*tan(t*pi/180)/h)^.5*dg2B1u(gv(n,1),rN(n),↙
drNN);

  J(3*n,2*n-1) = dNfB2u(gv(n,1),1,n)*tan(fi*pi/180) + g2B1(gv(n,1),rN(n))*↙
(gv(3*n,1)*tan(t*pi/180)/h)^.5*-2/dZ    + (3*gv(2*n,1)-4*gv(2*n-1,1)+gv(2*n-↙
2,1))/(2*dZ)*(gv(3*n,1)*tan(t*pi/180)/h)^.5*dg2B1u(gv(n,1),rN(n),drN1);

  J(3*n,2*n-2) = dNfB2u(gv(n,1),2,n)*tan(fi*pi/180) + g2B1(gv(n,1),rN(n))*↙
(gv(3*n,1)*tan(t*pi/180)/h)^.5/(2*dZ)   + (3*gv(2*n,1)-4*gv(2*n-1,1)+gv(2*n-↙
2,1))/(2*dZ)*(gv(3*n,1)*tan(t*pi/180)/h)^.5*dg2B1u(gv(n,1),rN(n),drN2);

else

   J(3*n,2*n)  =  3*g2B1(gv(n,1),rN(n))*(gv(3*n,1)*tan(t*pi/180)/h)^.5/(2*dZ)↙
+ (3*gv(2*n,1)-4*gv(2*n-1,1)+gv(2*n-2,1))/(2*dZ)*(gv(3*n,1)*tan(t*pi/180)↙
/h)^.5*dg2B1u(gv(n,1),rN(n),drNN);

   J(3*n,2*n-1) = -4*g2B1(gv(n,1),rN(n))*(gv(3*n,1)*tan(t*pi/180)/h)^.5/↙
(2*dZ)  + (3*gv(2*n,1)-4*gv(2*n-1,1)+gv(2*n-2,1))/(2*dZ)*(gv(3*n,1)*tan↙
(t*pi/180)/h)^.5*dg2B1u(gv(n,1),rN(n),drN1);

   J(3*n,2*n-2) =  1*g2B1(gv(n,1),rN(n))*(gv(3*n,1)*tan(t*pi/180)/h)^.5/↙
(2*dZ)  + (3*gv(2*n,1)-4*gv(2*n-1,1)+gv(2*n-2,1))/(2*dZ)*(gv(3*n,1)*tan↙
(t*pi/180)/h)^.5*dg2B1u(gv(n,1),rN(n),drN2);

   J(3*n,n)    =  dg2B1v(gv(n,1),rN(n))*(gv(3*n,1)*tan(t*pi/180)/h)^.5*(3*gv↙
(2*n,1)-4*gv(2*n-1,1)+gv(2*n-2,1))/(2*dZ);

   J(3*n,3*n)  =  g2B1(gv(n,1),rN(n))*(tan(t*pi/180)/h)^.5/(2*gv(3*n,1)^.5)*↙
(3*gv(2*n,1)-4*gv(2*n-1,1)+gv(2*n-2,1))/(2*dZ);


end
```

```
%At Middle Nodes

%Energy equation

for i = 2:n-1;

   b = 3*i-2;

   J(b,i)   = ddg3(gv(i,1))*(gv(i+1,1)-gv(i-1,1))/(2*dZ)*gv(2*n+i,1)^.5*(gv↙
(2*n+i+1,1)-gv(2*n+i-1,1))/(2*dZ) ...
            + dg3(gv(i,1))/(2*gv(2*n+i,1)^.5)*((gv(2*n+i+1,1)-gv(2*n+i-1,1))/↙
(2*dZ))^2 + dg3(gv(i,1))*gv(2*n+i,1)^.5*(gv(2*n+i+1,1)-2*gv(2*n+i,1)+gv↙
(2*n+i-1,1))/dZ^2 ...
            + h*tan(t*pi/180)*dg2B1v(gv(i,1),ri(n,i))*gv(2*n+i,1)^.5*((gv(n+i+1,↙
1)-gv(n+i-1,1))/(2*dZ))^2 - h^2*dg5(gv(i,1))*gv(2*n+i,1)^1.5 ...
            + ddg4(gv(i,1))*((gv(i+1,1)-gv(i-1,1))/(2*dZ))^2*gv(2*n+i,1)^1.5 +↙
dg4(gv(i,1))*3/2*gv(2*n+i,1)^0.5*(gv(i+1,1)-gv(i-1,1))/(2*dZ)*(gv(2*n+i+1,1)↙
-gv(2*n+i-1,1))/(2*dZ) ...
            + dg4(gv(i,1))*gv(2*n+i,1)^1.5*(gv(i+1,1)-2*gv(i,1)+gv(i-1,1))/dZ^2↙
+ g4(gv(i,1))*gv(2*n+i,1)^1.5*-2/dZ^2;

   J(b,i+1) = dg3(gv(i,1))*gv(2*n+i,1)^.5*(gv(2*n+i+1,1)-gv(2*n+i-1,1))/↙
(2*dZ)^2 + dg4(gv(i,1))*gv(2*n+i,1)^1.5*2*(gv(i+1,1)-gv(i-1,1))/(2*dZ)*1/↙
(2*dZ) ...
            + g4(gv(i,1))*3/2*gv(2*n+i,1)^0.5*1/(2*dZ)*(gv(2*n+i+1,1)-gv↙
(2*n+i-1,1))/(2*dZ) + g4(gv(i,1))*gv(2*n+i,1)^1.5*1/(dZ^2);

   J(b,i-1) = dg3(gv(i,1))*gv(2*n+i,1)^.5*(gv(2*n+i+1,1)-gv(2*n+i-1,1))/↙
(2*dZ)^2*-1 + dg4(gv(i,1))*gv(2*n+i,1)^1.5*2*(gv(i+1,1)-gv(i-1,1))/(2*dZ)*-↙
1/(2*dZ) ...
            + g4(gv(i,1))*3/2*gv(2*n+i,1)^0.5*-1/(2*dZ)*(gv(2*n+i+1,1)-gv↙
(2*n+i-1,1))/(2*dZ) + g4(gv(i,1))*gv(2*n+i,1)^1.5*1/(dZ^2);

   J(b,2*n+i)   = dg3(gv(i,1))*(gv(i+1,1)-gv(i-1,1))/(2*dZ)*(gv(2*n+i+1,1)-gv↙
(2*n+i-1,1))/(2*dZ)/(2*gv(2*n+i,1)^.5) ...
   + g3(gv(i,1))*((gv(2*n+i+1,1)-gv(2*n+i-1,1))/(2*dZ))^2*(-gv(2*n+i,1)^-1.5↙
/4) + g3(gv(i,1))/(2*gv(2*n+i,1)^.5)*(gv(2*n+i+1,1)-2*gv(2*n+i,1)+gv(2*n+i-↙
1,1))/dZ^2 ...
   + h*tan(t*pi/180)*g2B1(gv(i,1),ri(n,i))*((gv(n+i+1,1)-gv(n+i-1,1))/(2*dZ))↙
^2/(2*gv(2*n+i,1)^.5) - h^2*g5(gv(i,1))*1.5*gv(2*n+i,1)^.5 + g3(gv(i,1))*gv↙
(2*n+i,1)^.5*(-2/dZ^2) ...
   + dg4(gv(i,1))*((gv(i+1,1)-gv(i-1,1))/(2*dZ))^2*3/2*gv(2*n+i,1)^0.5 + g4(gv↙
(i,1))*3/2*1/2*gv(2*n+i,1)^-0.5*(gv(i+1,1)-gv(i-1,1))/(2*dZ)*(gv(2*n+i+1,1)-↙
gv(2*n+i-1,1))/(2*dZ)...
   + g4(gv(i,1))*3/2*gv(2*n+i,1)^0.5*(gv(i+1,1)-2*gv(i,1)+gv(i-1,1))/dZ^2;

   J(b,2*n+i+1) = dg3(gv(i,1))*(gv(i+1,1)-gv(i-1,1))/(2*dZ)*gv(2*n+i,1)^.5/↙
```

```
(2*dZ) + g3(gv(i,1))/gv(2*n+i,1)^.5*(gv(2*n+i+1)-gv(2*n+i-1))/(2*dZ)^2 ...
      + g3(gv(i,1))*gv(2*n+i,1)^.5/dZ^2 + g4(gv(i,1))*3/2*gv(2*n+i,1)^0.5*1/↙
(2*dZ)*(gv(i+1,1)-gv(i-1,1))/(2*dZ);

   J(b,2*n+i-1) = dg3(gv(i,1))*(gv(i+1,1)-gv(i-1,1))/(2*dZ)*gv(2*n+i,1)^.5/↙
(2*dZ)*-1 + g3(gv(i,1))/gv(2*n+i,1)^.5*(gv(2*n+i+1)-gv(2*n+i-1))/(2*dZ)^2*-↙
1 ...
      + g3(gv(i,1))*gv(2*n+i,1)^.5/dZ^2 + g4(gv(i,1))*3/2*gv(2*n+i,1)^0.5*-1/↙
(2*dZ)*(gv(i+1,1)-gv(i-1,1))/(2*dZ);

   J(b,n+i+1)   = h*tan(t*pi/180)*g2B1(gv(i,1),ri(n,i))*gv(2*n+i,1)^.5*2*(gv↙
(n+i+1,1)-gv(n+i-1,1))/(2*dZ)^2    + h*tan(t*pi/180)*gv(2*n+i,1)^.5*((gv↙
(n+i+1,1)-gv(n+i-1,1))/(2*dZ))^2*dg2B1u(gv(i,1),ri(n,i),dri1);

   J(b,n+i-1)   = h*tan(t*pi/180)*g2B1(gv(i,1),ri(n,i))*gv(2*n+i,1)^.5*2*(gv↙
(n+i+1,1)-gv(n+i-1,1))/(2*dZ)^2*-1 + h*tan(t*pi/180)*gv(2*n+i,1)^.5*((gv↙
(n+i+1,1)-gv(n+i-1,1))/(2*dZ))^2*dg2B1u(gv(i,1),ri(n,i),dri_1);

end

%Z-Momentum equation

for i = 2:n-1;

   c = 3*i-1;

   J(c,i)      = 1/h*(dNfB2v(gv(i,1),i)+gv(2*n+i,1)*dg1B3v(gv(i,1),ri(n,i),i)) -↙
dZ/2;

   for nn = i+1:n-1;

   J(c,nn)     = -dZ;

   end

   J(c,n)      = -dZ/2 + 1/h*-pi/(9*vm)*(gv(n,1)/vm)^(-1/3);

   J(c,2*n+i)  = 1/h*g1B3(gv(i,1),ri(n,i),i);

   J(c,n+i+1)  = 1/h*(dNfB2u(gv(i,1),1,i) +gv(2*n+i,1)*dg1B3u(gv(i,1),ri(n,i),↙
dri1,1,i));

   J(c,n+i-1)  = 1/h*(dNfB2u(gv(i,1),2,i)+gv(2*n+i,1)*dg1B3u(gv(i,1),ri(n,i),↙
dri_1,2,i));

end
```

```
%X-Momentum equation

for i = 2:n-1

   d = 3*i;

   sum1 = 0;

   for kk = i:n-1

   sum1 = sum1 + dZ/2*(gv(kk,1)+gv(kk+1,1));

   end

if NfB2(gv(i,1),i)*tan(fi*pi/180) <= (h*tan(t*pi/180)*sum1 + tan(t*pi/180)↙
*pi/6*(gv(n,1)/vm)^(2/3));

   J(d,i)     = dNfB2v(gv(i,1),i)*tan(fi*pi/180) + (gv(2*n+i,1)*tan(t*pi/180)/h)^.↙
5*dg2B1v(gv(i,1),ri(n,i))*(gv(n+i+1,1)-gv(n+i-1,1))/(2*dZ) ...
            - h*tan(t*pi/180)*dZ/2;

  for ll  = i+1:n-1

  J(d,ll)     = -h*tan(t*pi/180)*dZ;

  end

  J(d,n)      = -h*tan(t*pi/180)*dZ/2 - tan(t*pi/180)*pi/(9*vm)*(gv(n,1)/vm)^(-1↙
/3);

  J(d,2*n+i)  = g2B1(gv(i,1),ri(n,i))*(tan(t*pi/180)/h)^.5*(gv(n+i+1,1)-gv(n+i-↙
1,1))/(2*dZ)/(2*gv(2*n+i,1)^.5);

  J(d,n+i+1)  = dNfB2u(gv(i,1),1,i)*tan(fi*pi/180)  + g2B1(gv(i,1),ri(n,i))*(gv↙
(2*n+i,1)*tan(t*pi/180)/h)^.5/(2*dZ)    + (gv(2*n+i,1)*tan(t*pi/180)/h)^.5*(gv↙
(n+i+1,1)-gv(n+i-1,1))/(2*dZ)*dg2B1u(gv(i,1),ri(n,i),dri1);

  J(d,n+i-1)  = dNfB2u(gv(i,1),2,i)*tan(fi*pi/180) + g2B1(gv(i,1),ri(n,i))*(gv↙
(2*n+i,1)*tan(t*pi/180)/h)^.5/(2*dZ)*-1 + (gv(2*n+i,1)*tan(t*pi/180)/h)^.5*↙
(gv(n+i+1,1)-gv(n+i-1,1))/(2*dZ)*dg2B1u(gv(i,1),ri(n,i),dri_1);

else

  J(d,n+i+1)  = g2B1(gv(i,1),ri(n,i))*(gv(2*n+i,1)*tan(t*pi/180)/h)^.5*1/(2*dZ)↙
+ (gv(2*n+i,1)*tan(t*pi/180)/h)^.5*(gv(n+i+1,1)-gv(n+i-1,1))/(2*dZ)*dg2B1u↙
(gv(i,1),ri(n,i),dri1);
```

```
  J(d,n+i-1)  = g2B1(gv(i,1),ri(n,i))*(gv(2*n+i,1)*tan(t*pi/180)/h)^.5*-1/(2*dZ)↙
+ (gv(2*n+i,1)*tan(t*pi/180)/h)^.5*(gv(n+i+1,1)-gv(n+i-1,1))/(2*dZ)*dg2B1u↙
(gv(i,1),ri(n,i),dri_1);

  J(d,i)      = dg2B1v(gv(i,1),ri(n,i))*(gv(2*n+i,1)*tan(t*pi/180)/h)^.5*(gv↙
(n+i+1,1)-gv(n+i-1,1))/(2*dZ);

  J(d,2*n+i)  = g2B1(gv(i,1),ri(n,i))*(tan(t*pi/180)/h)^.5/(2*gv(2*n+i,1)^.5)*↙
(gv(n+i+1,1)-gv(n+i-1,1))/(2*dZ);

end

end

%GOVERNING EQUATIONS

% At First Node

%Energy equation

E(1,1)        = g3(gv(1,1))*(-3*gv(2*n+1,1)+4*gv(2*n+2,1)-gv(2*n+3,1))/↙
(2*dZ) - h*(1-ew^2)*gv(2*n+1,1)*pi*3^.5*gv(1,1)*go(gv(1,1))/(4*vm) ...
           + 2/3*h^2*tan(t*pi/180)*(s)*B1b(gv(1,1),r1(n))*pi*3^.5*gv(1,1)*go↙
(gv(1,1))*gv(n+1,1)^2/(4*vm) + g4(gv(1,1))*gv(2*n+1,1)*(-3*gv(1,1)+4*gv↙
(2,1)-gv(3,1))/(2*dZ);

%Z-Momentum equation

   sum2 = 0;

   for km = 1:n-1

   sum2 = sum2 + dZ/2*(gv(km,1)+gv(km+1,1));

   end

E(2,1)        = 1/h*(NfB2(gv(1,1),1)+g1B3(gv(1,1),r1(n),1)*gv(2*n+1,1)-pi/6*↙
(gv(n,1)/vm)^(2/3)) - sum2;

%X-Momentum equation

if NfB2(gv(1,1),1)*tan(fi*pi/180)/tan(t*pi/180) <=  (2/3*(h/tan(t*pi/180))^.5*↙
(s)*B1b(gv(1,1),r1(n))*pi*3^.5*gv(1,1)*go(gv(1,1))/(4*vm)*gv(2*n+1,1)^.↙
5*gv(n+1,1)+NfB2(gv(1,1),1)*tan(del*pi/180)/tan(t*pi/180))

E(3,1)        = NfB2(gv(1,1),1)*tan(fi*pi/180)/tan(t*pi/180)+ g2B1(gv(1,1),r1↙
(n))*gv(2*n+1,1)^.5/(h*tan(t*pi/180))^.5*(-3*gv(n+1,1)+4*gv(n+2,1)-gv(n+3,↙
```

```
1))/(2*dZ) ...
            - NfB2(gv(1,1),1)*tan(del*pi/180)/tan(t*pi/180) - 2/3*(h/tan↙
(t*pi/180))^.5*(s)*B1b(gv(1,1),r1(n))*pi*3^.5*gv(2*n+1,1)^.5*gv(n+1,1)*gv↙
(1,1)*go(gv(1,1))/(4*vm);

else

E(3,1)        = (-3*gv(n+1,1)+4*gv(n+2,1)-gv(n+3,1))/(2*dZ)*g2B1(gv(1,1),r1↙
(n))*gv(2*n+1,1)^.5/(h*tan(t*pi/180))^.5;

end

%At Last Node

%Energy equation

E(3*n-2,1)    = (3*gv(3*n,1)-4*gv(3*n-1,1)+gv(3*n-2,1))/(2*dZ)*g3(gv(n,1)) +↙
(3*gv(n,1)-4*gv(n-1,1)+gv(n-2,1))/(2*dZ)*gv(3*n,1)*g4(gv(n,1));

%Z-Momentum equation

E(3*n-1,1)    = 1/h*(NfB2(gv(n,1),n) + g1B3(gv(n,1),rN(n),n)*gv(3*n,1) - pi/6*↙
(gv(n,1)/vm)^(2/3));

%X-Momentum equation

if NfB2(gv(n,1),n)*tan(fi*pi/180) <= tan(t*pi/180)*pi/6*(gv(n,1)/vm)^(2/3);

E(3*n,1)      = NfB2(gv(n,1),n)*tan(fi*pi/180) + g2B1(gv(n,1),rN(n))*(gv(3*n,↙
1)/h)^.5*tan(t*pi/180)^.5*(3*gv(2*n,1)-4*gv(2*n-1,1)+gv(2*n-2,1))/(2*dZ) ...
            - tan(t*pi/180)*pi/6*(gv(n,1)/vm)^(2/3) ;

else

E(3*n,1)      = g2B1(gv(n,1),rN(n))*(gv(3*n,1)*tan(t*pi/180)/h)^.5*(3*gv(2*n,↙
1)-4*gv(2*n-1,1)+gv(2*n-2,1))/(2*dZ);

end

%At Middle Nodes

%Energy equation

for i = 2:n-1

   b = 3*i-2;
```

```
   E(b,1)   = dg3(gv(i,1))*(gv(i+1,1)-gv(i-1,1))/(2*dZ)*gv(2*n+i,1)^.5*(gv↙
(2*n+i+1,1)-gv(2*n+i-1,1))/(2*dZ) ...
            + g3(gv(i,1))/(2*gv(2*n+i,1)^.5)*((gv(2*n+i+1,1)-gv(2*n+i-1,1))/↙
(2*dZ))^2 + g3(gv(i,1))*gv(2*n+i,1)^.5*(gv(2*n+i+1,1)-2*gv(2*n+i,1)+gv↙
(2*n+i-1,1))/dZ^2 ...
            + h*tan(t*pi/180)*g2B1(gv(i,1),ri(n,i))*gv(2*n+i,1)^.5*((gv(n+i+1,1)-↙
gv(n+i-1,1))/(2*dZ))^2 - h^2*g5(gv(i,1))*gv(2*n+i,1)^1.5 ...
            + dg4(gv(i,1))*gv(2*n+i,1)^1.5*((gv(i+1,1)-gv(i-1,1))/(2*dZ))^2 + g4↙
(gv(i,1))*3/2*gv(2*n+i,1)^0.5*(gv(2*n+i+1,1)-gv(2*n+i-1,1))/(2*dZ)*(gv(i+1,↙
1)-gv(i-1,1))/(2*dZ) ...
            + g4(gv(i,1))*gv(2*n+i,1)^1.5*(gv(i+1,1)-2*gv(i,1)+gv(i-1,1))/dZ^2;

end

%Z-Momentum equation

for i = 2:n-1;

   c = 3*i-1;

   sum3 = 0;

   for kr = i:n-1

   sum3 = sum3 + dZ/2*(gv(kr,1)+gv(kr+1,1));

   end

   E(c,1)   = 1/h*(NfB2(gv(i,1),i)+gv(2*n+i,1)*g1B3(gv(i,1),ri(n,i),i)-pi/6*(gv↙
(n,1)/vm)^(2/3)) - sum3;

end

%X-Momentum equation

for i = 2:n-1

   d = 3*i;

   sum4 = 0;

   for kl = i:n-1

   sum4 = sum4 + dZ/2*(gv(kl,1)+gv(kl+1,1));

   end
```

```
if NfB2(gv(i,1),i)*tan(fi*pi/180) <= (h*tan(t*pi/180)*sum4 + tan(t*pi/180)*pi/6*(gv(n,1)/vm)^(2/3));

    E(d,1)   = NfB2(gv(i,1),i)*tan(fi*pi/180) + g2B1(gv(i,1),ri(n,i))*(gv(2*n+i,1)*tan(t*pi/180)/h)^.5*(gv(n+i+1,1)-gv(n+i-1,1))/(2*dZ) ...
             - h*tan(t*pi/180)*sum4 - tan(t*pi/180)*pi/6*(gv(n,1)/vm)^(2/3);

else

    E(d,1)   = g2B1(gv(i,1),ri(n,i))*(gv(2*n+i,1)*tan(t*pi/180)/h)^.5*(gv(n+i+1,1)-gv(n+i-1,1))/(2*dZ);

end

end


%SOLUTION

stopp = abs(E(1,1));

for bm = 2:3*n;

stopp = max(stopp,abs(E(bm,1)));      % Finding the largest value of the magnitudes of the residuals

end

 if stopp < 0.01;                     % 0.01 is the tolerance R1

 break;

 else

JI=inv(J);

Inc=JI*-E;

gv = gv + Inc*NewtonRaphsonModifier

 end;

end

gv

Fc
```

```
E

stopp

hp

%CRITERION TWO

absJ     = abs(J);

TabsJ    = transpose(absJ);

MTabsJ   = max(TabsJ);

TMTabsJ  = transpose(MTabsJ);

sum5  = 0;

for z1 = 1:3*n

sum5 = sum5 + (E(z1,1)/TMTabsJ(z1,1))^2;

end

criteria_ = sum5^0.5                    % Calculation of the second tolerance R2

end
```